Bird, Hugh J.A. (2021) *Low-order methods for the unsteady aerodynamics of finite wings.* PhD thesis.

Low-order methods for the unsteady aerodynamics of finite wings

Hugh J. A. Bird
MEng

Submitted in fulfilment of the requirements for the
Degree of Doctor of Philosophy

School of Engineering
College of Science and Engineering
University of Glasgow

June 2021

Declaration

I certify that the thesis presented here for examination for a PhD degree of the University of Glasgow is solely my own work other than where I have clearly indicated that it is the work of others (in which case the extent of any work carried out jointly by me and any other person is clearly identified in it) and that the thesis has not been edited by a third party beyond what is permitted by the University's PGR Code of Practice.

The copyright of this thesis rests with the author. No quotation from it is permitted without full acknowledgement.

I declare that the thesis does not include work forming part of a thesis presented successfully for another degree.

I declare that this thesis has been produced in accordance with the University of Glasgow's Code of Good Practice in Research.

I acknowledge that if any issues are raised regarding good research practice based on review of the thesis, the examination may be postponed pending the outcome of any investigation of the issues.

Hugh J. A. Bird
June 2021

Dedicated to

Archibald Thomas Graham Ferguson
1928 - 2020

Abstract

The development of modern unmanned aerial vehicles, high-altitude long-endurance drones, wind turbines, energy harvesting devices and micro air vehicles all require the consideration of unsteady aerodynamics. Unsteady flow simulation is not only more computationally expensive than steady simulations, but the unsteadiness expands the range of relevant parameters to be considered. This makes the use of traditional unsteady computational fluid dynamics methods too computationally expensive for many applications.

Low-order methods provide an alternative. By neglecting less important aspects of the problem being solved, the cost of obtaining a solution can be greatly reduced. However, currently available low-order methods are limited by being either too narrow in the phenomena they model, still too computationally expensive, or not sufficiently well understood to be used with confidence. In this dissertation, low-order methods for the unsteady aerodynamics of finite wings are investigated. Uncertainties around Unsteady Lifting-Line Theory (ULLT) are resolved and new methods are derived where existing methods are either too slow or do not exist.

This thesis primarily studies ULLT. ULLT allows a problem to be modelled as interacting two-dimensional problems, reducing the cost of obtaining a solution. This approach is applied to Euler cases and low Reynolds number ($\mathrm{Re} = 10\,000$) cases for both sinusoidal oscillation kinematics and arbitrary kinematics. Small and large amplitude kinematics are investigated, with large amplitudes introducing additional complications including leading-edge vortex structures.

Frequency-domain problems are initially considered in the Euler regime using frequency-domain ULLT. It is shown that existing methods produce good solutions when the assumptions made in their derivation are satisfied. For low Reynolds number cases, where their assumptions are violated, they still provide reasonable accuracy, even in the presence of aerodynamic non-linearities. Frequency-domain methods are then applied to time-domain problems using a new, low-computational-cost method. It is shown how Fourier transforms can be used to obtain solutions for arbitrary input kinematics. Some of the limitations of this method are then alleviated with a new time-marching geometrically non-linear ULLT. However, this method cannot model the leading-edge vortex. For that, another new method is obtained, based on the 3D vortex particle method.

Publications

Journal Articles in Review

H.J.A. Bird and K. Ramesh, *Unsteady lifting-line theory and the influence of wake vorticity on aerodynamic loads*, Theoretical and Computational Fluid Dynamics, 2021. [1]

H.J.A. Bird, K. Ramesh, S. Ōtomo and I.M. Viola, *Usefulness of inviscid linear unsteady lifting-line theory for viscous large-amplitude problems*, AIAA Journal, 2021. [2]

H.J.A. Bird and K. Ramesh, *Applying frequency-domain unsteady lifting-line theory to time-domain problems*, AIAA Journal, In review. [3]

Publications in Conference Proceedings

H.J.A. Bird and K. Ramesh, *Theoretical and computational studies of a rectangular finite wing oscillating in pitch and heave*, 6th European Conference on Computational Mechanics (ECCM 6) 7th European Conference on Computational Fluid Dynamics (ECFD 7), 2018. [4]

H.J.A. Bird, S. Ōtomo, K. Ramesh and I.M. Viola, *A Geometrically Non-Linear Time-Domain Unsteady Lifting-Line Theory* , AIAA Scitech 2019 Forum, American Institute of Aeronautics and Astronautics, 2019. [5]

H.J.A. Bird, K. Ramesh, S. Ōtomo and I.M. Viola, *Leading Edge Vortex Formation on Finite Wings Using Vortex Particles* , AIAA Scitech 2021 Forum, American Institute of Aeronautics and Astronautics, 2021. [6]

Acknowledgements

First and foremost, I'd like to thank my PhD supervisor Dr. Kiran Ramesh. In a world where allegedly some supervisors are better than others, I count myself lucky to be his student. In exchange for his patience, his insight and his perpetual friendliness I suspect I'll have been the cause of any early grey hairs.

I've also have the opportunity to work with some very capable people. I've co-authored papers with Dr. Ignazio Maria Viola and Shūji Ōtomo. Ignazio's eye for detail never fails to amaze me, and Shūji's experimental work underpins much of this thesis. I've not formally collaborated with research group sibling Alfonso Martínez, but he deserves a mention. He adds an upbeat tone to our weekly research group meetings and is an excellent cook. On the administrative side, I'd like to thank Julia Deans. Her patience with regards to incorrectly completed forms astounds me.

No acknowledgment section would be complete without mentioning family. To my nuclear family, my dogs, Auntie Joan and Grandma Ferguson, thank you. I also feel I may as well list Matthew Johnston and Pia Hüsch here, because they may as well be family. Matthew has made me thankful for unlimited minutes mobile contracts and Pia has probably spent more time with me than anyone else over the last few years.

As a result of the unusual events of the last year, I feel indebted to a great many of my friends. They have entertained me, endured me and generally kept me sane though the highs and the lows. I daren't list everyone for fear of forgetting individuals, but I can never resist the opportunity to single out Robert Platten, a man of infectiously good spirit.

Finally, I should also thank you, the taxpayer. The work presented would not have been possible without the support of the UK's Engineering and Physical Sciences Research Council through a DTA studentship (project reference 1944318) and the Cirrus UK National Tier-2 HPC service at EPCC (http://www.cirrus.ac.uk).

Contents

List of Tables

List of Figures

Chapter 1

Introduction

> According to all known laws of aviation, there is no way a bee should be able to fly. Its wings are too small to get its fat little body off the ground.
>
> *Bee Movie [7]*

Some might consider it remarkable that over a century after the Wright Flyer first took flight, engineers remain hesitant to embrace the potential of unsteady aerodynamics. Whilst the *Bee Movie* [7], released in 2007, did not give researchers sufficient credit for their understanding, it did provide a hint as to why this is the case: unsteady aerodynamics for finite wings can be difficult to understand and to simulate.

Unsteadiness represents a problem rather than a solution in many areas. Early methods for unsteady aerodynamics were often related to the analysis of flutter or gusts. By and large, unsteady flow about wings was not used for aerodynamic purposes.

The reason for this is the high cost of analysing unsteady aerodynamics problems. Tools such as unsteady Computational Fluid Dynamics (CFD) are computationally expensive and require significant expertise to use. Alternative low-order methods are popular. These low-order methods solve an easier problem by removing flow-phenomena and simplifying geometry. Consequently, they can be orders of magnitude faster than CFD. Unfortunately, currently used methods don't include all relevant flow phenomena, are insufficiently well understood, or are still to slow for solving practical problems.

The lack of fast analysis tools is become increasingly problematic. They're needed to analyse the encounters of low-flying Unmanned Aerial Vehicles (UAVs) with gusts, and to model the interacting aerodynamics, structural dynamics and flight dynamics of increasingly flexible modern aeroplanes and High Altitude Long Endurance drones. For wind turbines with long, slender and flexible blades aeroelasticity is a growing analysis problem. And unsteady flow has the opportunity to lead to oscillating renewable energy harvesting devices which do less damage to then environment than traditional turbines, and to Micro Air Vehicles (MAVs) that are ultra-manoeuvrable due to their insect-like flapping flight. The analysis problem that complicates these applications is that of the unsteady aerodynamics of finite wings, and the limitation of current methods be it in computational cost (CFD) or capability and uncertainty (low-order methods).

This thesis, on low-order methods for the unsteady aerodynamics of finite wings, aims to reduce uncertainty in the use of unsteady lifting-line theory, and introduce new low-order methods by which problems involving finite wings may be studied. This introductory chapter continues with a review of the state of the art in Sec. 1.1. This allows the research objectives to be outlined in Sec. 1.2, immediately followed by a summary of the original contributions and publications linked to this dissertation in Sec. 1.3. The dissertation is outlined in Sec. 1.4.

1.1 Literature Review

1.1.1 Motivation and Applications

It is hard to overstate the importance of Unmanned Aerial Vehicles (UAVs) or drones. Persistent surveillance capabilities have been credited with influencing the outcome of the recent wars. Paraphrasing *The Economist* [8], '... drones helped Azerbaijan thrash Armenia in [the 2020 Nagorno-Karabakh war] last year.' Persistent drone surveillance is also of increasing importance for domestic policing, with UAVs being used in high crime cities such as Ciudad Juárez, and trialled in St Louis and Baltimore [9]. Cargo drones are also delivering medical supplies in remote areas, with *Bloomberg* [10] reporting that Zipline have been using drones to supply COVID-19 vaccines to Rwanda and Ghana, *The Guardian* [11] reporting drone deliveries of personal protective equipment and coronavirus test kits to the Isle of Mull in Scotland's Inner Hebrides, and blood delivery being assessed by Gilmore *et al.* [12] of the RAND Cooperation. Cargo delivery drones for consumers are also being trialled, with the American Federal Aviation Administration [13] having approved the use of hybrid multirotor / fixed wing drones such as that of Google subsidiary Wing for the delivery of food and over-the-counter pharmaceuticals directly to homes in Christiansburg in Virginia, United States.

For surveillance purposes, drones are often of the medium altitude long endurance kind, capable of staying aloft for tens of hours. However, the prevalence of High Altitude Long Endurance (HALE) UAVs is increasing. Capable of staying aloft indefinitely, they represent a low-cost, mobile, recoverable alternative to satellites, according to Gonzalo *et al.* [14]. Consequently, they are of interest to the telecommunications industry, with companies such as Facebook [15] and Softbank [16] aiming to produce HALE aircraft to extend wireless internet access to more remote parts of the world. HALE aircraft are also being considered by militaries for surveillance and communication, and for wildfire monitoring, according to *Aviation Week* [17].

Drones present challenges however. UAVs often operate at relatively low altitudes, and modern applications suggest their use in urban areas. In these applications gusts present a problem in both testing and operation, according to Williams and Harris [18]. This gust problem has lead to the North Atlantic Treaty Organization (NATO) to form a task group [19] dedicated to the rigid wings of UAVs encountering gusts [20].

High Altitude Long Endurance drones are capable of staying aloft potentially indefinitely largely due to their extraordinary flight efficiency. This is achieved through lightweight structures and very high aspect ratio wings. Consequently, their wings are flexible. This structural flexibility results in structural frequencies coinciding with those of the flight dynamics, making for a difficult to analyse problem. NASA's prototype HALE aeroplane, named Helios, crashed after turbulence caused it to flex into an unanticipated configuration, followed by divergent flight dynamics. Following the crash, Noll *et al.*'s report [21] cited the challenge of modelling flight dynamics, including the interaction of unsteady aerodynamics, control systems, environment and flexible structure. The report recommended the development of more advanced methods for multidisciplinary analysis. This lead to an explosion in the volume of research into the flight dynamics of HALE aeroplanes, including the work of Murua *et al.* [22], Su and Cesnik [23, 24], Simpson [25] and many others [26, 27, 28, 29, 30, 31, 32, 33, 34, 35, 36, 37]. Work has also been conducted into low-Reynolds number aerodynamics for HALE aircraft by NATO working group AVT-101 [38]. A particular challenge in such work is the aerodynamic model. The computational cost of CFD requires that low-order methods—typically the Unsteady Vortex Lattice Method (UVLM)—be used. Simpson [25] and Murua [22] both noted that the lack of aerodynamic non-linearities in available in current low-order models left their work unable to model 'critical' phenomena [22]. Murua [22] dedicated two pages of his PhD thesis to how the computational cost of unsteady aerodynamic analysis can create a 'severe limitation'. Afonso *et al.* [37] also reached this conclusion in a review of aeroelasticity for high-aspect ratio wings. Evidently, current low-order models for the unsteady aerodynamics of finite wings are too expensive computationally, and too narrow in their applicability.

What is a problem for current HALE drone engineers is becoming a problem for those working in other areas. For commercial aircraft operators, increasing aircraft efficiency leads to reduced ownership cost and reduced environmental impact. An avenue by which this can be achieved is reducing drag, by using higher aspect ratio wings, and reducing aircraft weight, potentially at the cost of increased flexibility. This phenomenon is already visible in the notably flexible composite wings of Boeing's 787 and Airbus's A350.

This increasing flexibility is likely to be exacerbated by the morphing aeroplane concept. Instead of using rigid control surfaces, morphing aircraft flex [39] or use complex mechanical actuators to change shape (active morphing). Morphing allows increased efficiency compared to control surfaces, but leads to increased flexibility. Beaverstock *et al.* [40] reviewed morphing aircraft. Aeroelasticity is likely to remain a central challenge as aircraft configurations change to meet challenges in the future, as described by Livne and Weisshaar [41].

The flexible wings that are problematic for aeroplane designers are also a problem for wind turbine manufacturers. A central element to the increasing affordability of wind energy has been the growth in the size of wind turbines. Increasing wind turbine size allows better efficiency, and the growth of off-shore wind farms means that the transport and erection of large turbine components is now less of a problem. Hansen *et al.* [42] pointed out that aeroelasticity is a major challenge for wind turbine designers. Aerodynamic nonlinearity is important because many turbines are stall regulated. They also noted that wind turbines are exposed to a large range of environmental conditions and wind farm configurations, so the number of analysis cases is large. Consequently, the cost of analysis is important.

Unsteady methods are also needed for the analysis of novel energy harvesting devices. Rostami and Armandei [43] described how renewable energy can be harvested using vortex-induced motions. Energy can be extracted from a flow using a flapping wing, reducing damage to the environment in comparison to turbines.

Fixed-wing UAVs have so far been a topic central to the motivation of the current thesis. Micro Air Vehicles (MAVs) provide another motivation. Whilst once humanity wished it could fly like birds, many are now tempted by the thought of insect-like flight. House flies demonstrate enormous manoeuvrability, being capable of landing on the ceiling for example. The high lift that insect flight manages to produce is attributed to unsteady leading-edge vortex structures [44], although the stability of the leading-edge vortex is not well understood. The need to better understand and model flapping flight for MAVs has lead to several NATO working groups (AVT-101 [38], AVT-149 [45], AVT-184 [46] and AVT-202 [47]).

Low-order methods for the unsteady aerodynamics of finite wings are needed for aircraft design, renewable energy and micro air vehicles. Current low-order methods are too computationally expensive for design, optimization or real-time simulation and control, or they fail to include important flow phenomena.

Having established a motivation, the state of the art will be examined in Sections 1.1.2 to 1.1.9.

1.1.2 Introduction to potential flow

Exact analytical solutions of the Navier-Stokes equations are rare. This has lead to the use of Computational Fluid Dynamics (CFD), where approximate numerical solutions are obtained. Unfortunately CFD is a computationally expensive method for steady flow, and even more expensive for unsteady problems. This expense has limited its use for flexible aircraft. For example, aeroelastic studies of flexible wings using CFD usually study static aeroelasticity [48, 49, 50]. For unsteady analysis, low-order methods are used.

Low-order methods discard elements of the problem to make it easier to solve. A common assumption is that the flow is incompressible and inviscid and can therefore be modelled using potential flow. Geometric assumptions are common, with wings and aerofoils often assumed to be thin, or existing only as a boundary condition on a plane. Phenomena are often modelled explicitly. This means that the mathematical model includes terms to represent the individual phenomena. The best known example of this is perhaps the Kutta condition, which describes how a fluid cannot flow around the sharp trailing edge of an aerofoil. Consequently, the bound vorticity of the aerofoil must result in the trailing edge being a stagnation point. Low-order methods often explicitly include this flow feature. By simplifying the problem, it can be solved analytically or at greatly reduced computational cost.

Inviscid, incompressible problems are often solved using the method of potential flow. An introduction to potential flow based models is given by Katz and Plotkin [51]. Potential flow models are typically solved as the sum of perturbations to a uniform flow. These perturbations influence the entire domain, although their influence tends to zero infinitely far from the perturbation. As a consequence, potential flow models do not require a mesh and can model infinite domains— ideal for external aerodynamics.

The summation of perturbations, typically vortices, can lead to the idea of causality. For example, it is common to state that the starting vortex of an aerofoil induces a downwash on the aerofoil. However, strictly this isn't correct. A representation of a flowfield in terms of velocity is equivalent to one in terms of perturbations. Neither causes the other, although for the purposes of low-order modelling, the perturbation representation is more useful.

Potential flow doesn't strictly model unsteady flow. The potential solution at any point in time is independent of time. To model time, perturbations representing the wake are allowed to convect at the local velocity. The forces on bodies are obtained from the circulatory part of the solution and the acceleratory part, also known as added mass. The circulatory part refers to the force due to circulation about the body at a point in time. The acceleratory part refers to forces due to the change in the potential field, and is only present in unsteady problems. For further discussion of the circulatory and acceleratory part of the solution, see Katz and Plotkin [51].

Potential flow problems can have exact analytical solutions in 2D, but not usually in 3D. There is therefore a considerable body of literature dedicated to finding a means by which to model the flow about both aerofoils and finite wings. Purely numerical methods allow the surface of a general body to be modelled in both 2D and 3D. Since a perturbation affects the entire domain in a potential flow model, the numerical cost of these models is not insignificant, though they remain far faster than CFD. Often however, this cost can be significantly reduced by using further assumptions such that a solution can be obtained at least partially using analytical means.

In Sec. 1.1.3, analytical solutions to 2D unsteady aerofoil problems are described. This is a precursor to Sec. 1.1.4 which reviews the state of analytical lifting-line theories. These are effectively a means to apply 2D solutions to 3D problems.

Analytical solutions can be challenging to find. Consequently, numerical solutions are often needed for more general problems. Numerical solutions for 2D problems are reviewed in Sec. 1.1.5, followed by a description of numerical lifting-line theories in Sec. 1.1.6. These LLTs whilst having numerical elements, do not compute the complete 3D interaction of a wing, reducing numerical cost in comparison to full 3D methods.

Lifting-line theory has not yet reached a point where it is capable of successfully modelling important aerodynamic non-linearities. Consequently, fully 3D methods are required for some problems. The challenging flow phenomena, and in particular Leading-Edge Vortices (LEVs) for the 2D problem are discussed in Sec. 1.1.7. This is followed by a discussion of these vortex structures applied to finite wings in Sec. 1.1.8. Fully 3D methods by which such problems may be attacked, including the Unsteady Vortex Lattice Method (UVLM) and the Vortex Particle Method (VPM), are discussed in Sec. 1.1.9.

1.1.3 Analytical methods for flow about an aerofoil

Low-order 3D solutions such as strip theory and lifting-line theory are effectively an extension of 2D methods that allow them to be applied to 3D problems. Consequently, before lifting-line theory is discussed, this section reviews 2D methods.

Potential flow methods have been used in conjunction with conformal mapping techniques to obtain analytical solutions for flat plates and thin aerofoils for steady and unsteady problems, and for more complex thick aerofoil geometries for steady flows. See Katz and Plotkin [51].

For unsteady flows, the first analytical solution was that of Wagner [52], who derived the response of an impulsively started aerofoil. The model assumed potential flow, a thin aerofoil and small-amplitude kinematics. A key element to the analysis was the vortex sheet representing the aerofoil wake, not present in the steady solution. The wake sheet is essential to satisfy the Kelvin condition that stipulates that circulation within a contour that is free to convect with a fluid should remain constant. This unsteady wake induces a downwash on the aerofoil, reducing the circulatory lift it creates.

The incidental response obtained by Wagner could be applied to arbitrary pitch and heave kinematics using the Duhamel integral method [53]. This involves the summation of the response to small step-changes that represent the change of kinematics with respect to time. This is admissible because Wagner's method, and those like it, are linear.

Unfortunately, the function central to Wagner's solution, Wagner's function, is difficult to evaluate. Whilst Wagner gave some numerical values, Küssner [54] derived a slowly convergent series, and Garrick [55] gave an early approximation.

Theodorsen [56] solved a similar problem to Wagner, but instead applied to aerofoils oscillating harmonically with kinematics perpendicular to the free stream, for example pitch or heave. His method was intended for the analysis of flutter, and demonstrated how the circulatory part of the solution was impacted by the oscillating wake. This relationship was represented by what is known as Theodorsen's function, $C(k)$, which can be written in terms of well studied special functions. Garrick [55] found that Theodorsen's solution was the frequency-domain equivalent to Wagner's time-domain solution. Since Theodorsen's function is much easier to evaluate than Wagner's function, it was possible to obtain better approximations of Wagner's function by taking the inverse Laplace transform of a function that approximated Theodorsen's function [57, 58, 59, 60, 61].

The impact of gusts on an aerofoil were also a subject of interest. Research included Sears' [62] work on the influence of an oscillating gust on a thin aerofoil, and Küssner's [54] response to a sharp edge gust. These are the gust equivalents to Theodorsen's work and Wagner's work respectively. The similarity of all of these problems allows for more general solutions. Kárman and Sears [63] reproduced Theodorsen's [56] frequency-domain result and Küssner's time-domain result. For frequency-domain problems, the solution of Küssner and Schwarz [64] (see Appendix B.2) allows the solution of any oscillatory problem involving vertical velocity boundary conditions on the aerofoil surface, linking it to the oscillating pressure distribution on the aerofoil.

The family of solutions for unsteady thin aerofoil theory continues into non-vertical asymptotically small displacements. Isaacs [65] produced a method for surging aerofoils and Greenberg [66] a method for harmonic motion in a pulsating stream. For discussions of classical unsteady thin aerofoil models see Bisplinghoff *et al.* [67], Newman [68], Ashley and Landahl [69] and Fung [70]. More modern extensions to unsteady thin aerofoil theory include the corrections of Sears's solution to account for gust distortion by Goldstein and Atassi [71] and Atassi [72]; an analysis of vorticity distributions by Epps and Roesler [73]; a viscous extension to Theodorsen's work by Taha and Rezaei [74]; and an analysis of leading-edge suction and stagnation point by Ramesh [75].

Having discussed unsteady solutions to 2D aerofoil problems, they can now be applied to 3D problems using lifting-line theory in the next section.

1.1.4 Analytical lifting-line theory

An easy way to model the aerodynamics of a complete wing is to apply a 2D method to chordwise strips and sum the result. This method, known as strip theory [53], is widely used due to its simplicity. Unfortunately, it neglects important 3D effects.

Lifting-Line Theory (LLT) is similar, insomuch that a 2D method is applied to chordwise strips on the wing. However, this 2D 'inner' method is enhanced with a 3D correction, by which 3D effects can be accounted for. This correction is obtained from a 3D model in the 'outer' domain, which has been simplified by removing the chord-scale detail of the wing surface. The outer 3D model depends on the inner 2D models for the detail, and in turn provides a 3D correction to these inner models.

The idea of the lifting-line theory is credited to Prandtl [76], although the concept was introduced by Lanchester [77]. Prandtl introduced a method for straight wings in steady flow. The spanwise vorticity was contained within the inner 2D solution, and the streamwise vorticity resulting from the change of bound circulation with respect to span existed only in the outer domain. This streamwise vorticity including the wing tip vortex is trailed due to Helmholtz's theorems. Since no component of the wake is shared between the 2D inner solution and outer 3D solution, Prandtl's lifting-line theory is relatively easy to obtain.

The asymptotic method on which lifting-line theory is based is known as separation of length-scales [78]. The idea is that important length-scales in the problem are sufficiently different that it can be decomposed into simpler, interacting problems. The mathematics of lifting-line theory were formalised by Van Dyke [79]. Van Dyke formally derived his lifting-line theory using the Matched Asymptotic Expansion (MAE) technique [78]. He also noted an often neglected limitation of the method: separation of length-scales requires that the inner solution change in outer problem on the length-scale of the outer problem. In other words, the 2D solution must change slowly with respect to span. The consequence of this is that lifting-line theory should theoretically not be applied to rectangular or elliptic wings, only pointed, cusped and lenticular wings.

LLT has remained prevalent as a low-order tool, and Prandtl's theory [76] has been extended a number of times. Early extensions for curved wings by Thurber [80] and swept straight wings by Cheng [81] used the MAE technique [78]. Kida and Miyai [82] obtained a solution which corrected a mistake in Van Dyke's work [79] by avoiding the MAE and instead asymptotically inverting the integral form of the problem. Guermond built upon Kida and Miyai's work to obtain a steady solution for swept curved wings [83] using a systematic method [84] that would later be reapplied to the unsteady problem [85].

Prandtl's method [76] works by reducing a complicated multidimensional wake integral into a single integral equation. Lifting-line methods follow Prandtl's methodology for this procedure, but alternative procedures are possible. The most notable results of such alternative procedures are those of Weissinger [86] and Reissner [87]. Such methods lack the consistent rationality of lifting-line theory, but were popular due to their early applicability to swept wings. See Ashley and Landahl [69].

Whilst Jones [57, 88] provided early approximate solutions to the incidental response of a finite wing, early Unsteady Lifting-Line Theories (ULLTs) were usually in the frequency domain. This allowed the solution to be solved as a complex variable with respect to span. Early work was motivated by the desire to analyse the forces on helicopter blades in forward flight [89, 90]. The early methods of James [91] and Van Holten [89, 90] considered a straight wing in unsteady motion using the MAE approach of Van Dyke [78]. Both methods assumed uniform downwash, and Van Holten points out that Weissinger's method [86] is invalid for unsteady problems. Both Van Holten [90] and James's [91] work contain erroneous logarithmic singularities. This was pointed out by Ahmadi and Widnall [92], in addition to other limitations that suggest the methods are suitable for only low frequency problems.

The frequency of oscillation, and consequently the wake wavelength can be related to the two length-scales (chord and span) of the wing geometry. This allowed Cheng [93] to suggest five frequency domains, Domains I to V, which can be used to assess the validity of a ULLT. In Domain I, the wake wavelength is greater than the span-scale. In Domain II, it is of the span-scale. In Domain III, the wake wavelength is less than the span-scale but more than the chord scale. In Domain IV, it is of the chord-scale. And in Domain V, the wake wavelength is less than the chord scale.

Ahmadi and Widnall suggested that the work of James [91] and Van Holten [89] was only asymptotically valid for when the wake wavelength was larger than the span-scale (Domain I) due to the assumption of uniform downwash. At such low oscillation frequencies, quasi-steady aerodynamic theory is adequate anyway [92]. All of James [91], Van Holten [89], Ahmadi and Widnall [92] pointed out that at very high frequency, in Domain V, where the wake wavelength is smaller than the chord-scale, three-dimensional effects are small. Consequently, the difference in results obtained between ULLT and strip theory should be small. An important aside is that forces on a wing depend on oscillation frequency. An assumed wing loading distribution based on steady results cannot accurately be applied to unsteady problems.

Ahmadi and Widnall's method [92] is suitable for Domains I-II since sinusoidal downwash is assumed. Sclavounos [94] derives a method suitable for Domains I-IV, again limited to straight wings. Dragos [95] obtained a solution where the wing is not assumed to be thin, but its applicability is unclear. MAE based research into curved and swept wings is limited. Cheng and Murillo [96] derived a method suitable for curved wings in Domains I-II, and applied it to a swimming propulsion problem.

These methods were all based on the method of matched asymptotic expansion of

Van Dyke [78]. By using a different method [84], Guermond and Sellier [85] were able to obtain a frequency domain unsteady lifting-line theory suitable for curved and swept wings at all frequencies (Domains I-V). This was effectively an unsteady extension of their earlier steady LLT [83]. This method avoids the need for solving integro-differential equations, and instead obtains the first-order 3D correction directly from the zero-eth order 2D solution via a series of integrals. The solution at any point on the wing can be obtained purely by integration. Unfortunately, for rectangular and elliptic wings these integrals suggest singular 3D corrections at the wing tip. For rectangular wings, this singularity is not integrable (see Appendix A.1.1). For elliptic wings it is, although the solution obtained is evidently incorrect. This result agrees with the earlier work of Van Dyke [79]. Consequently, the most advanced, easily applicable frequency-domain ULLT is that of Sclavounos [94].

Unsteady lifting-line theories have also been constructed in the time domain. Constructing a time-domain ULLT is difficult, because (as with the 2D methods of Theodorsen [56] and Wagner [52]) the solution must take the form of a function with respect to time instead of an oscillation amplitude and phase. From an analytical perspective it is tempting to attempt to find the indicial response of a wing. As with Wagner's method [52], this could then be applied to general time-domain kinematics using the Duhamel integral [53]. Obtaining an approximation of Wagner's function is difficult. Obtaining the response of a wing, which is variable due to the geometry of the wing, is consequently more difficult still.

The earliest result for indicial response was that of Jones [57, 88], using a simplified model and elliptic wing geometry. A more modern method is that of Boutet and Dimitriadis [97], where a Prandtl-like pseudosteady wake was used in combination with a Wagner-based [52] inner 2D solution. The interaction of the wake with the wing is computed using a Duhamel integral to obtain an indicial response.

Analytical unsteady lifting-line theory is subject to the same restrictions as the inner solutions that it is based upon. The models are linear and model only small-amplitude kinematics in the plane of the inner solutions (although this can vary with respect to span). However, they can theoretically be applied to both problems involving the movement of the wing, and gust problems. Analytical frequency-domain ULLT is more advanced than its time-domain counterpart where simplified wake models are used. ULLTs often have not been comprehensively compared to experimental or computational data, and the impact of wake model choices, theoretical asymptotic limitations, and wing planform limitations are unclear.

In order to create more general LLTs, more general inner solutions are required. In the next section, these numerical 2D aerofoil analysis methods are described.

1.1.5 Numerical methods for flow about an aerofoil

Two-dimensional problems are often solved using potential flow theory, where inviscid, incompressible flow is assumed. Such problems can be solved analytically using conformal mapping for some geometries. Otherwise, distributions of singularities can be placed on the aerofoil surface to form panel methods [51], or inside the aerofoil in the case of faster-converging modern methods [98]. For steady cases, these can be augmented using integral boundary layer theory [99]. This has resulted in popular aerofoil solvers such as Drela's XFoil [100]. For faster solutions, the aerofoil is assumed to be thin, leading to thin aerofoil theory [51]. This assumption is typically used for unsteady problems.

Whilst classical unsteady thin aerofoil theory (e.g. Theodorsen [56] and Wagner [52]) has stood the test of time, two assumptions prove problematic for some modern applications. Firstly, the geometric linearity of the method, where it is assumed that displacements are small and that the wake is planar. This shortcoming will be addressed in this section. And secondly the assumption that all vorticity is shed from the trailing edge. This aerodynamic non-linearity will be discussed in Sec. 1.1.7.

The problem of geometric non-linearity can be solved numerically using several approaches. Katz and Plotkin [51] described an unsteady vortex lattice method where a linear system is solved to find the correct point-vortex strengths to satisfy the no-penetration velocity boundary condition. The vortex particle wake is allowed to convect freely. Katz and Plotkin also described panel methods by which a thick aerofoil method could be constructed. Yan *et al.* [101] applied conformal mapping techniques to transform the thin aerofoil to a circle, allowing the velocity boundary condition to be satisfied using the Milne-Thompson theorem [51]. Ramesh *et al.* [102] satisfied the no-penetration velocity boundary condition using a Glauert-Fourier series expansion of vorticity, avoiding the need to solve for the chordwise vorticity distribution.

None of these approaches are flawless. According to Roesler and Epps [103], care must be taken in the setup of unsteady vortex lattice methods (such as that of Katz and Plotkin [51]) lest the solution converge to the incorrect result, and the vorticity distribution is very sensitive to nearby vortex particles. The conformal mapping of Yan *et al.* [101] is tiresome and limits the geometry and boundary conditions of the aerofoil model. Ramesh *et al.*'s [102] use of the Glauert-Fourier series chordwise vorticity, though elegant for other reasons, is troublesome since it incorrectly enforces zero vorticity at the trailing edge. Whilst it matches the Glauert-Fourier pressure distribution used by Küssner and Schwarz [64] at the leading edge, unsteady effects mean that it does not match at the trailing edge, breaking the Kutta condition. As a consequence, the solutions obtained using the method typically have some small error.

Currently, these numerical 2D solutions are not used in unsteady lifting-line theory. However, numerical ULLTs exist both for steady and unsteady cases, suggesting that such a method would be possible. These numerical ULLTs are examined in the next section.

1.1.6 Numerical lifting-line theory

Numerical extensions to steady lifting-line theory are plentiful. Guermond's method for curved and and swept wings was transformed into a more numerically amenable form by Devinant [104]. Sivells and Neely [105] devised a method for non-linear sectional data, Valarezo and Chin [106] investigated multi-element wings, Gallay and Laurendau [107] suggested a method suitable for post-stall flow and Ben-Gida *et al.* [108] suggested a method to model steady leading-edge vortex formation on swept wings. Caprace *et al.* [109] suggested a method by which singularities could be modified using Gaussian smoothing.

For ULLT, numerical methods have proven more popular in the time domain than the frequency domain, no doubt due to the aforementioned analytical difficulty. An early numerical method was that of Phlips *et al.* [110], where a numerical approximation of the wake was used to model flapping flight. Nabawy and Crowthe[111] constructed a Prandtl-like method for analysing insect-like hovering flight.

The greatest advance came when Devinant [112] created a method that numerically applied a simplified version of Guermond and Sellier's frequency-domain method [85] to time-domain problems. Two simplifications were necessary. Firstly, the wing had to be straight, to avoid the complexities of the spanwise interaction of the 2D solutions for which the outer domain does not account. And secondly, the downwash model was simplified, asymptotically limiting the method to Domains I-IV. Critically however, Devinant correctly accounted for the components of the wake that could be found in both the 2D inner domain and 3D outer domain.

As with steady LLT, numerical methods allow more complex inner solutions to be used. For example, Parenteau *et al.* [113] integrate Reynolds averaged Navier-Stokes solutions into a ULLT. Unlike the steady case however, ULLT demands matching of the inner and outer solutions. The challenge of this matching procedure led Parenteau's method to only be suitable for low frequency problems. Likewise, Ramesh *et al.* [114] integrated a geometrically non-linear discrete vortex particle based inner solution [102] with a psuedosteady wake to study the flutter of a cantilevered plate.

Unsteady lifting-line theory also introduces the possibility of adding complexity to the 3D outer domain. This is popular in applications such as wind-turbine modelling, where resolving the chord-scale of a wind turbine is challenging for simulations involving a turbine array. To this end, Backaert *et al.* [115] and Caprace *et al.* [116] integrated lifting-line theory into a vortex particle-mesh method. Sugar-Gabor [117] created a method which was applied to kinematics out of the plane of the 2D inner solution by only accounting for the wake in the outer domain, thereby avoiding the challenge of matching.

To summarise, lifting-line theory allows 2D models to be applied to 3D problems. For unsteady problems, small-amplitude linear frequency-domain ULLTs are well developed. Time-domain ULLTs are less well developed, with more analytically based ULLTs limited to low frequency wakes. Numerical time-domain ULLTs are better developed. Steady LLTs are often enhanced using more complex 2D models. For unsteady problems, this is complicated by the need to match components of the inner 2D and outer 3D wakes.

Whilst numerical LLT holds promise, integration of more complex 2D phenomena may be challenging. In particular the leading-edge vortex structure. This is reviewed in the next section.

1.1.7 Aerodynamic non-linearities in two dimensions

The potential flow model neglects viscosity, and as a consequence must explicitly enforce the Kutta condition. However, viscosity leads to other flow phenomena which must also be explicitly added to low-order models if flow is to be accurately modelled.

For steady flow, the inclusion of the viscous boundary layer to model stall in potential flow based models is well established. By modelling the boundary layer using integral boundary layer methods [99], an equivalent inviscid problem can be iteratively obtained. This has led to aerofoil solvers such as Drela's XFoil [100] that remain popular for their ease of use, accuracy and speed.

As ever, the unsteady case is more complicated. For helicopters, the phenomenon of dynamic stall is most pertinent. As described by McCroskey [118, 119], dynamic stall occurs when a vortex like disturbance travels over the upper surface of the wing from the trailing edge. It creates a 'highly-nonlinear fluctuating pressure field' [118].

Alternatively, instead of separation travelling from trailing to leading edge, separation can occur at the leading edge spontaneously. This leads to a leading-edge shear layer, which rolls up to form a Leading-Edge Vortex (LEV). It is thought that this LEV is central to the ability of insects to generate higher lift coefficients than would be possible for fixed wings in steady flow at low Reynolds numbers [44]. Consequently, the modelling of LEVs is essential in the development of MAVs.

The LEV has been studied extensively for 2D problems, both experimentally and with CFD. McGowan *et al.* [120] and Ol *et al.* [121] both studied the LEV experimentally and computationally, with comparison to the theoretical small-amplitude oscillating model of Theodorsen [56] (see Sec. 1.1.3). They found that CFD could predict experimental results with good accuracy, including the forces on the aerofoil. In some cases, Theodorsen's method can provide a good estimate of the forces despite the assumptions in its derivation being severely violated. Ōtomo *et al.* [122] applied Theodorsen's method to CFD results for periodic but non-sinusoidal problems involving LEVs using Fourier methods. Again, Theodorsen's method belied its assumptions.

Several factors influence LEV formation. Benton and Visbal [123] found that increased leading-edge radius and the addition of leading edge droop delayed the onset of LEV formation. Widmann and Tropea [124] found that the mechanism of LEV detachment changed with chord length and free stream velocity.

Further CFD simulations of plunging aerofoils were completed by Visbal [125], and Garmann and Visbal [126] for aerofoils undergoing pitch-ramp manoeuvres. Granlund, Ol and Bernal [127] experimentally investigated LEV formation for a pitch ramp manoeuvre. Beckwith and Babinsky [128], and Pitt Ford and Babinsky [129, 130] experimentally investigated LEV formation on a plate accelerated from rest, examining the circulation contained within the LEV. Stevens *et al.* [131] compared the flow topology and the force history of both CFD and experiments for accelerating flat plates. Visbal and Garmann [132] demonstrated how experimental features can lead to uncertainty when comparing CFD and experimental results.

For gusts, setting up CFD simulations is challenging, so almost all literature refers to experiment. Andreu-Angulo *et al.* [133] and Biler *et al.* [134] examined the effect of vertical gusts on a flat plate. Gehlert and Babinsky experimentally examined the effects of gusts on a cylinder. Mulleners *et al.* [135] examined the response of a plate to a streamwise gust encounter. Kay *et al.* [136] examined an aerofoil in turbulent flow. They found that the effects were similar to those found for a pitching aerofoil, except that the results were not so repeatable. Young and Smyth [137] examined oscillating gusts, and found that Atassi's solution [72] (see Sec. 1.1.3) provides a good solution except for very large amplitude gusts.

Attempts to model the leading-edge vortex in a low-order model are numerous. According to Darakananda and Eldredge [138], models that include the leading-edge vortex can be separated into two groups. Firstly, the group that has continuous shedding of some kind of vortex element. Katz [139] derived a model where discrete vortex particles were shed from some point on the chord of a thin aerofoil as well as the trailing edge. Jones [140] modelled a plate with separation on both edges where a bound vortex sheet was used for the wake instead of discrete particles. Both Sarpkaya [141] and Ansari *et al.* [142] shed discrete vortices from both edges of a plate and satisfied the boundary conditions by using the Milne-Thompson theorem [51] combined with conformal mapping. These models depend on the interaction of discrete vortex elements for the formation of large vortices. The large vortex structures that form are comprised of a large number of vortex elements. A second set of methods attempt to model this large vortex structure and its feeding shear layer explicitly using only a small number of elements rather than let the LEV form implicitly [143, 144].

However, the challenge of LEV shedding is in predicting when a leading-edge shear layer should be shed, and how strong it should be. The aforementioned models assumed that a shear layer is being shed continuously. Ramesh *et al.* [145] found that for any given aerofoil geometry and Reynolds number, an aerofoil could only provide so much leading-edge suction. Once this maximum leading-edge suction had been reached, separation occurs [146, 147, 148]. This suction could be linked to thin aerofoil theory via the leading-edge pressure/vorticity singularity to obtain the Leading Edge Suction Parameter (LESP). From this, Ramesh *et al.* derived the so-called Leading-edge suction parameter modulated Discrete Vortex Model (LDVM), which provided a means by which unsteady problems involving LEVs could be simulated quickly and reliably. Further developments of the model have centred around increasing the complexity of the LESP criterion to better reflect experimental results [146].

The LEV has proven to be an important vortex structure in 2D, and, unlike dynamic stall, there are low-order methods by which it can be modelled. In 3D, the structure becomes more complicated, as discussed in the next section.

1.1.8 Aerodynamic non-linearities in three dimensions

Unsteady viscous phenomena that occur in 2D such as dynamic stall and the formation of leading-edge vortices also occur in 3D. In 2D, modelling dynamic stall where separation starts at the trailing edge using low-order methods remains difficult, but effective models for leading-edge separation exist. It would be futile to attempt to model dynamic stall in 3D before it was successfully managed in 2D, so this review will focus exclusively on LEV based problems.

But first, earlier work on vortex-formation on wings must be briefly discussed. Rectangular plates oscillating at small amplitude are studied experimentally by Freymuth [149], Buchholz and Smits [150, 151], Ellenrieder *et al.* [152] and Parker [153]. Blondeaux *et al.* [154] recreated Freymuth's experiment in CFD. Visualisation shows the vortex structures in the wake which demonstrate the formation of interlocking vortex rings. However, as sketched by Ellenreider *et al.*, these rings can include structures in the shape of an '8', due to the merging of vortex filaments (a viscous phenomenon).

For large-amplitude pitch and plunge kinematics, leading-edge vortex arch structures often form, although the exact form of the arch depends on the wing planform and kinematics. The leading-edge vortex is often connected ('pinned') to the wing at the leading edge corners. This is sketched by Chiereghin *et al.* [155] for both pitching and plunging rectangular swept and unswept wings. These arches can be seen on rectangular flat plates in the work of Visbal [156] using CFD, and Yilmaz *et al.* [157], Yilmaz and Rockwell [158, 159] and Visbal *et al.* [160] experimentally. These plates either have squared edges or tight radii, so cannot support much leading-edge suction, meaning leading-edge separation occurs easily. Wings with an aerofoil section can support greater leading-edge suction, and similar LEV arches are observed, for example in the CFD of Visbal and Garmann [161, 162] and the experiments of Chiereghin *et al.* [155]. Different planforms result in different arch structures. Swept rectangular wings are studied by Chiereghin *et al.* [155] experimentally and by Visbal and Garmann [163] using CFD. On sweptback wings, a separate LEV arch structure may form on each half of the wing. Yilmaz and Rockwell also experimentally studied elliptic plates [159], where the LEV is not pinned to the leading- edge corners, instead merging with the tip vortex. The dynamic stall of wings of more arbitrary shape is studied by Spentzos *et al.* [164], where CFD is performed and compared to other published experimental results.

Insect-like flight is reviewed by Shyy *et al.* [165] and typically involves more complex kinematics. Ellington *et al.* [44] originally attributed the high lift coefficients found in insect flight to the leading-edge vortex. However, the stability of the structure on insect wings is a topic of contention [166]. Shyy *et al.* [167] suggested that it is stabilised by the tip vortices, supported by Birch and Dickinson [168]. Dickinson [169] suggested that wing rotation has a strong influence, and Lentink and Dickinson [170] suggested that rotational acceleration has a strong influence. Harbig *et al.* [166] investigated the advance ratio of the kinematics and the aspect ratio of the wing. Bhat *et al.* [171] also studied kinematics.

Given the additional complexity of LEVs on 3D wings, it might be expected that the popular LESP criterion of Ramesh *et al.* [145] (see Sec. 1.1.7), derived in 2D, would be insufficiently complicated. However, Hirato *et al.* [172] have applied the concept to a variety of rectangular tipped straight and swept wings and found that the concept holds.

In 3D, LEVs form complex structures depending on the planform of the wing and the kinematics. For rectangular-tipped wings, an arch attached to the leading edge is often formed. For elliptic wings, this arch often merges with the tip vortex. This arch structure is convected into the wake where it interacts with the trailing-edge wake. The vortex structures in the wing evolve, often merging. Despite this complexity, it would appear that the leading-edge suction parameter of Ramesh *et al.* [145, 172] still holds.

In order to model the evolution of the leading-edge vortex structure, a fully 3D solver must be used. Fortunately, the challenge of predicting LEV formation appears to be solvable using the LESP criterion as a basis. In the next section, low-order 3D methods with which such a solver may be constructed are reviewed.

1.1.9 Three dimensional methods for finite wings

Early steady finite-wing analysis was based upon Prantdtl's LLT [76]. It was thought that greater fidelity could be obtained using multiple lines, resulting in Falkner's vortex lattice theory [173], which depended upon multiple horseshoe vortices. Vortex lattice methods have remained popular, and attempts made to extend them to include stall, for example by Santos and Marques [174] using a Kirchoff-based correction.

To model thick bodies and non-lifting surfaces, panel methods [51, 175] gained popularity. Their early usage is generally attributed to Hess [176]. Panel methods discretise the surface of the body such that a distribution of singularities can be applied. Usually, a no-penetration velocity boundary condition is applied at collocation points on the surface.

Panel methods can be used for unsteady problems. For example Willis *et al.* [177] used the method, accelerating the surface panel solver using the pre-computed fast Fourier transform method [178]. However, the additional computational cost of unsteady panel methods in comparison to unsteady vortex lattice methods make them uncommon.

Unsteady vortex lattice methods remain popular due to their simplicity. Like its 2D counter part, the method is easy to incorrectly setup [103]. It has been used for the study of high altitude long endurance aeroplane flight dynamics by Murua [179] and Simpson [180], the analysis of tidal turbines with periodic wakes by Smyth *et al.* [181] and of wind turbines with viscous coupling by Nelson and Kouh [182]. The response of a wing to gusts of different frequencies was studied by Smyth *et al.* [183]. A non-linear frequency-domain solver was proposed by Parentau and Laurendeau [184], cambered wing drag analysis was studied by Lambert and Dimitriadis [185], and post-stall analysis was attempted by Mukherjee and Gopalarathnam [186] using a decambering approach. Hirato *et al.* [187] added a leading edge vortex lattice wake to the UVLM model to simulate leading-edge vortices in 3D. Their model used Aggarwal's [188] relation of the vortex lattice to the leading-edge suction having established the validity of the leading-edge suction parameter as a criterion for leading edge vortex shedding using CFD [172] (see Sec. 1.1.8).

The unsteady vortex lattice method has its limits however. There are three main problems. Firstly, typically the vortex filament fragments used are singular. This results in infinite velocities that can become problematic. Secondly, it can be difficult to account for distortion in the vortex lattice. When a filament fragment in the wake becomes too long, it no longer properly represents the solution. And thirdly, it can be difficult to model viscosity. Viscosity is required to model phenomena such as filament merging. Whilst these problems can all be mitigated with additional complexity and *ad-hoc* methods, Winckelmans *et al.* [189] suggested that the Vortex Particle Method (VPM) should be used instead.

The VPM lumps vorticity into a point. Vortex particles (also known vortex sticks) can convect freely, increasing or decreasing in vorticity as they 'stretch'. Singular particles lack the connectivity and continuity of vortex filaments. As a consequence, they do not create a solenoidal vorticity field - Helmholz's theorem can be violated. This problem can be fixed using regularised vortex particles, sometimes know as vortex blobs. Instead of being vorticity singularities, the vorticity is spread out. A variety of regularisation schemes exist, the choice of which affects computation cost and convergence characteristics, as demonstrated by Wee *et al.* [190]. So long as these particles are sufficiently tightly spaced, they can represent continuous vortex filaments. Since vorticity is no longer concentrated at singular points, the induced velocity as a vortex particle is approached no longer tends to infinity, aiding the stability of a simulation. The regularised vortex particle methods are preferred since the convergence of the method is proven [191].

Natural convection results in the stretching of vortex filaments. For a solver based on straight vortex particle fragments, the vertices of the filament may spread out such that the straight fragments no longer represent the correct geometry of the filament, and the filament would have to be subdivided. For vortex particle methods, redistribution methods can be used. The vortex particles are projected onto an appropriately sized grid. In these cases, the solver is semi-Lagrangian. This also gives an opportunity to resize the vortex core, permitting different discretisation fidelities in different parts of the flow-field, as described by Cottet *et al.* [192]. Methods where particle methods are combined with grids are known as Vortex Particle-Mesh methods and Vortex In Cell [193] methods, and are becoming increasingly popular due to their computation efficiency.

Viscosity plays a role in the development of vortex structures. The merger of filaments is a viscous phenomenon. Whilst it is possible to merge filaments in filament based methods, the required filament ‘surgery’ can be difficult. Descriptions of vortex particle methods require that viscosity be modelled explicitly. According to Cottet and Koumoutsakos [194], there are several methods by which this can be done. Firstly, Brownian motion or random walk methods, although these do not appear to be popular. Secondly, vortex core spreading. Vortex particles with vortex cores regularised with a Gaussian distribution mimic the Lamb-Helmholtz vortex. This has proven popular, although Greengard [195] suggested that naive core spreading converges to a system of equations different to the Navier-Stokes equations. Kempka and Strickland [196] claimed to have alleviated this shortcoming in 2D, and Rossi [197] suggested a scheme involving vortex splitting. The third method is particle strength exchange, as detailed by Winckelmans and Leonard [198] and Winckelmans *et al.* [189]. Here, a vortex particle transfers its vorticity to nearby vortex particles, leading to the diffusion of vorticity.

The viscous interaction of surfaces with vortex particles remains challenging, although there are methods such as that of Koumoutsakos *et al.* [199], and problems involving bluff body flows have been successfully studied by Shiels [200], Ploumhans and Winckelmans [201] and Ploumhans *et al.* [202].

Many solvers, including that presented in this thesis, neglect viscosity. However, it appears to be essential in the stability of vortex particle methods. Turbulent breakdown will eventually occur. Since inviscid flow has no minimum length-scale, the vortex particle method will be unable to represent the small scale structures. This will result in the simulation blowing up. To alleviate this, sub-grid vorticity models have been suggested [194].

A benefit of the VPM lies in the algorithmic tools available. A naive vortex particle method of N particles is of algorithmic complexity $\mathcal{O}(N^2)$. This can be reduced to $\mathcal{O}(N\log(N))$ with tree codes [203], and further reduced to $\mathcal{O}(N)$ using Greengard and Rokhlin’s fast multipole method [204]. Notes on improved implementation of the fast multipole method were given by Greengard and Rokhlin [205], Fong and Darve [206], and—for vortex particle problems—Gumerov and Duraiswami [207]. These methods create multipole expansions to approximate groups of particles, reducing the number of interactions needed. Whether the error of an expansion is acceptable is decided by a multipole acceptance criterion. For potentials and velocities (the first derivative), this is known. However, the author is unaware of multipole acceptance criterion for the second derivates of potential needed for vortex particle stretching.

A secondary advantage of vortex particle methods relates to modern computer hardware. Single instruction multiple data processors, and, in particular, graphics processing units with programmable shader pipelines have become increasingly common in recent years. Dedicated hardware can run many thousands of parallel threads in lock-step simultaneously, resulting in greater computer bandwidth than a single fast computing core. As a consequence, for appropriate problems the floating-point performance of a computer can be significantly increased. Vortex particle methods and similar gravitational or electrostatics problems are suitable for such computing methods. Examples of GPU accelerated vortex particle codes are that of Rossinelli *et al.* [208], Hu *et al.* [209] and Wu *et al.* [210] in 3D, and that of Morgenthal *et al.* [211] for pseudo-3D problems. However, the massively parallel nature is challenging to work with. Consequently, a graphics processor implementation of the fast multipole method may have a similar computational cost to a tree code, as found by Yokota and Barba [212]. Salmon and Warren [213, 214] gave hints on implementation, and Winckelmans *et al.* gave hints on implementing a vortex particle code integrated into the boundary element method [215].

The challenges of vortex particle methods are numerous. Stability can be problematic in 3D, along with computation cost. Extensive reviews of vortex particle methods were completed by Cottet and Koumoutsaks [194] and Branlard [216]. However, VPMs remain attractive when they can be made to work. Applications include wind turbine codes such as that of García *et al.*[217], with wake breakdown studied by Marten *et al.* [218], and propulsion by Alvarez and Ning [219].

Three dimensional methods are needed to resolve the dynamics of the leading-edge vortex. The commonly used unsteady vortex lattice model may be unsuitable for this challenge, requiring the use of vortex particle methods instead. These can model vortex distortion and viscosity without resorting to *ad-hoc* methods.

Having assessed a spectrum of flow physics and accompanying low-order methods, the research objectives of this thesis will be outlined in the next section.

1.2 Research objectives

This dissertation aims to further the state of the art of low-order methods for unsteady aerodynamics of finite wings by resolving uncertainty around current methods, and plugging capability gaps.

Frequency-domain unsteady lifting-line theory was developed at a time when the numerical and experimental tools for method validation were limited. Questions remain:

- How accurate is unsteady lifting-line theory in the context of practical rectangular wing planforms (for which LLT is supposedly invalid)?
- To what extent does it matter if a ULLT such as Sclavounos's is suitable for only Cheng's [93] Domains I-IV?
- Many ULLTs use simplified Prandtl-like wake models. To what extent is the wake model important?
- Are ULLTs derived for inviscid flow applicable to high Reynolds number problems?

Lifting-line theories are typically derived for inviscid flow and assume a planar wake. However, many modern applications involving HALE UAVs, MAVs and energy harvesting devices are in the low Reynolds number regime, and may include large amplitude kinematics and leading-edge vortices. This poses several questions:

- Can inviscid ULLT be applied to low Reynolds number problems?
- To what extent do linearised ULLTs provide a good solution for wings undergoing large-amplitude kinematics, involving leading-edge vortex formation? Is it possible to predict LEV formation using lifting-line theory?

Whist uncertainty in low-order methods is important, the requirement for new, time-domain methods must also be considered.

- Ideally, an analytical time-domain method should be obtained. The method should reflect the more advanced wake models available to frequency-domain problems.
- Most current methods assume a planar wake. A time-domain numerical method that includes geometric non-linearity, including non-planar wakes, should be obtained.
- Aerodynamic non-linearity is not within the capability of common low-order models. A method capable of modelling leading-edge vortices using the idea of Ramesh *et al.*'s [145] LESP criterion should be obtained.

The dissertation focuses first on the limitations and uncertainties of current unsteady lifting-line theories, before continuing onwards to new methods reflecting new capabilities. Each of these new methods uses fewer assumptions, but at the cost of greater computational requirements.

The original contributions and publications obtained whilst attempting to answer these research questions are outlined in the next section, before this introductory chapter is concluded with an outline of this dissertation in Sec. 1.4.

1.3 Original contributions and publications

The original contributions are largely represented by journal articles that are either published or in review. The contributions are as follows:

A modified version of Sclavounos' ULLT is presented A minor modification is made to Sclavounos's frequency-domain ULLT [94] to remove the dependence on known whole-wing added-mass coefficients which were previously assumed to be known in advance. This generalises the method for different kinematics, potentially including spanwise and chordwise flexibility and gusts. This improves the consistency of Sclavounos's method, and provides a more concise and easy to follow explanation of unsteady lifting-line theory for future authors - unsteady lifting-line theory literature is often mathematically dense and primarily concerned with the asymptotic nature of the method, making it hard to read. See Sec. 2.2 and Bird and Ramesh [1].

ULLT is assessed for rectangular wings in the inviscid regime In early work on ULLT, methods were not well validated, probably due to the paucity of experimental data available for comparison. In Sec. 2.3 and Bird and Ramesh [1] frequency-domain ULLT is compared to inviscid CFD results for rectangular wings at several reduced frequencies and aspect ratios. Lift and moments are considered, along with distributions with respect to span. It is shown that ULLT is a valuable tool for the analysis of rectangular wings, even though the asymptotic assumptions about wing shape are violated for rectangular wings. It is also found that frequency-domain ULLTs typically provide good results at high frequency, even if asymptotic analysis of the wake model suggests otherwise.

ULLT is assessed in the high Reynolds number regime In Section 2.3.3 and Bird and Ramesh [1] ULLT is applied to the case of an oscillating wing at high Reynolds numbers. This is an important step given that the method is derived for the non-physical inviscid regime.

A new simplified frequency-domain ULLT wake model is presented A ULLT wake model describing the streamwise component of vorticity in the wake of an oscillating wing is described in Sec. 2.2.4 and Bird and Ramesh [1]. The wake model correctly demonstrates the correct high-frequency asymptotic behaviour, in contrast to pseudosteady methods, whilst remaining relatively simple to obtain. Whilst it is of limited value for analytical problems, it doesn't require matching of some components of the outer wake. This could greatly ease the development of a numerical lifting-line theory for more general kinematics, whilst aiding an understanding of the error that such a method would introduce.

The impact of ULLT wake models is assessed The model of the wake in the outer solution is a significant challenge in the derivation of ULLTs. The results obtained with several different wake models are compared to assess the importance of the wake model in Sec. 2.3 and Bird and Ramesh [1]. This is important given the tendency of authors to use simplified wake models when creating *ad-hoc* ULLTs without understanding the limitations these models imply.

ULLT is assessed in the low Reynolds number regime Modern applications are often in the Re=10 000 regime, relevant to some of the applications mentioned in Sec. 1.1.1. Inviscid ULLTs are applied to low Reynolds number flows in Chapter 3 and in Bird *et al.* [2]. It is found that for small amplitude oscillatory kinematics of rectangular wings ULLTs tend to slightly overestimate forces, but remain useful.

A leading-edge vortex prediction method using ULLT is presented Leading-edge vortices are an important aerodynamic non-linearity that cannot be modelled by ULLT. A means to predict LEV formation within the analytical frequency-domain ULLT framework is described in Sec. 3.2. and Bird *et al.* [2]. This LESP distribution can be used to estimate the extent to which the results are useful, and whether a more advanced, more computationally expensive method is required.

Inviscid linear ULLT is assessed for problems with LEVs The results of inviscid geometrically linear ULLTs are compared to those of CFD for Re=10 000 regime problems with large oscillation amplitudes leading to leading-edge vortex formation in Chapter 3 and Bird *et al.* [2]. It is found that leading-edge vortices lead to superlinear increases in forces, reducing the overestimate ULLT typically provides at low Reynolds number. As aspect ratio reduces we find that 3D leading edge vortex structures become more stable. Hence, for whole wing forces ULLT often provides a good prediction. However, the prediction of forces at any point on the span was poor due to the strong localized effects of the LEV.

A semi-analytical time-domain ULLT is presented A method to apply frequency-domain ULLT to time-domain problems at low computational cost is described in Chapter 4 and Bird and Ramesh [220]. Current analytical time-domain methods rely on simplified wake models. The shortcomings of these wake models are demonstrated in Sec. 2.3. It is demonstrated advanced frequency-domain ULLTs can be efficient applied to time-domain problems using a combination of Fourier transforms and interpolation of frequency-domain results with respect to frequency. The method only demands that the underlying frequency-domain ULLT is linear.

A time-marching geometrically non-linear ULLT is presented A geometrically non-linear time-marching discrete-vortex based ULLT is derived in Chapter 5 and in Bird *et al.* [3]. The method uses the the large amplitude unsteady thin aerofoil of Ramesh *et al.* [102] to demonstrate how a geometrically non-linear discrete-vortex based 2D model can be integrated into a lifting-line theory, including the matching of inner 2D and outer 3D wakes.

A method to model LEV formation using the VPM is presented A means to model leading-edge vortices on 3D wings at low computational cost in comparison to CFD is described in Chapter 6 and Bird *et al.* [6]. The method uses regularized vortex particles to model the wake and leading edge vortex.

1.4 Dissertation outline

This dissertation follows the research objectives set out in Sec. 1.2 in the logical order.

In Chapter 2, a small-amplitude, frequency-domain unsteady lifting-line theory is introduced, based on the work of Sclavounos [94]. Simplified wake models are also introduced. This facilitates a Euler CFD based study to resolve several aspects of uncertainty that surround unsteady lifting-line theory. ULLT is applied to rectangular wings for which its derivation is asymptotically invalid. Its effectiveness is tested over a spectrum of oscillation frequencies and aspect ratios. The spanwise distribution of force is investigated and the wake obtained from CFD is compared to assumed form of the wake in the outer solution. It is found that ULLT provides a good solution, that the model used to model the wake matters, and that a constant correction for oscillation frequency will lead to poor results. Finally, it is compared to a high Reynolds number case. Again, ULLT provides a good solution.

Having established the utility of ULLT for the regime in which it was derived, Sclavounos's ULLT is applied to cases violating its assumptions in Chapter 3. Many modern applications are in the low Reynolds number region and feature large-amplitude kinematics. The inviscid ULLT is applied to oscillating rectangular wings at both small and large amplitudes. This allows the accuracy of the ULLT and a new means by which to predict leading-edge vortex shedding to be tested. It is found that the ULLT is useful at low Reynolds number, even when there are large leading-edge vortex structures. The force distribution with respect to span is predicted reasonably well when LEVs are not present. LEVs can be predicted using the LESP criterion applied to ULLT.

Having assessed the applicability of frequency-domain ULLT to problems for which it was derived and some for which it was not, a method to apply frequency-domain ULLTs to time-domain problems is suggested in Chapter 4 - a step in the direction of providing more low-order time-domain tools for analysing the unsteady aerodynamics of finite wings. As noted in the literature review, analytically based time-domain methods are less advanced than their frequency-domain counterparts, based on the assessment of wake models made in Chapter 2. This method, christened the ULLT / Convolution in Frequency Domain (UCoFD), is assessed for both inviscid small-amplitude problems, and a low Reynolds number problems involving LEV shedding. It is found to be effective in the former case, and to provide adequate results in the latter cases.

Chapters 2, 3 and 4 used geometrically linear lifting-line theory. A criticism of current low-order models is their linearity. A numerical lifting-line theory using a geometrically non-linear inner solution with a discrete vortex particle wake is introduced in Chapter 5. The means by which the inner solution's 2D discrete vortex particle wake can be matched with its 3D outer-domain counterpart is demonstrated. This numerical method is then applied to time-domain problems.

It had originally been hoped that the numerical ULLT of Chapter 5 would be extensible to leading-edge vortex formation. However, this did not prove to be the case. Consequently, to model aerodynamic non-linearity, a new method, named Vortex Formation on Finite Leading Edge (VoFFLE), is introduced in Chapter 6. This method combines the LESP criterion, a vortex lattice representation of the wing and a vortex particle representation of the wake to model the formation of leading-edge vortex in 3D at low computational cost compared to the CFD alternative. The ability of the method to correctly predict LEV formation in 3D is compared to that of CFD.

Chapter 7 concludes this dissertation. A summary of the research and its implications is followed by a section on recommended future work.

Appendices detail the wing-tip singularity in Guermond and Sellier's method for rectangular wings, presents some aspects of unsteady thin aerofoil theory, describes how the integrals in frequency-domain ULLT's integro-differential equation may be regularised and details the CFD used in this thesis and its validation.

Nomenclature

The main symbols and acronyms used in this thesis are listed here. Some symbols may have more than one meaning assigned to them. In these cases, the symbol will be redefined in the relevent section. Symbols not listed here are defined internally within sections.

Latin

A	coefficient in Fourier series
$\boldsymbol{A}$	interaction matrix
Æ	aspect ratio
B	coefficient in Fourier series
c	chord
$\overline{c}$	mean chord
C_l	two-dimensional lift coefficient
C_L	three-dimensional lift coefficient
C_m	two-dimensional moment coefficient
C_M	three-dimensional moment coefficient
$C(k)$	Theodorsen's function
F	three-dimensional correction strength
$\mathcal{F}$	Fourier transform
h	plunge displacement
h_0^*	non-dimensional plunge amplitude
k	chord reduced frequency
K	three-dimensional interaction kernel
L	lifting-line
$\mathcal{L}$	leading edge suction parameter
$\boldsymbol{n}$	surface normal vector
o	asymptotic order notation
O	asymptotic order notation
$\mathcal{O}$	algorithmic complexity (big O notation)
q	vortex particle velocity regularisation function
$\boldsymbol{r}$	radius vector

s	semispan
S	wing surface
t	time
Δt	time step
$t^* = tU/\bar{c}$	convective time
T	oscillation period
$\boldsymbol{u}$	velocity
U_∞	free stream velocity
v	surface velocity
$\boldsymbol{w}$	induced velocity
x	streamwise coordinate
$\boldsymbol{x}$	three-dimensional coordinate
y	spanwise coordinate
$y^* = y/s$	non-dimensional spanwise coordinate
z	vertical coordinate
x^*_m	non-dimensional reference location for pitching moment

Greek

α	angle of attack
$\boldsymbol{\alpha}$	vortex particle circulation
γ	chordwise bound vorticity distribution
Γ	bound circulation
δ	Dirac delta
ζ	spanwise coordinate
ζ	vorticity regularisation function
η	spanwise coordinate
θ	chordwise coordinate
λ	wake wavelength
Λ	vortex particle redistribution function
μ	regularisation distance
ν	span reduced frequency
ξ	streamwise variable of integration
ρ	non-dimensional radius
ρ_∞	free stream density
σ	ramp function smoothing parameter for ramp-hold-return
Σ	wake
ϕ	velocity potential

ω	angular frequency
$\boldsymbol{\omega}$	vorticity
Ω	set of LEV shedding locations

Abbreviations

CFD	Computational Fluid Dynamics
CPU	Central Processing Unit
C-ULLT	Complete ULLT (see Sec. 2.2.4)
GPU	Graphics Processing Unit
HALE	High Altitude Long Endurance
LAULLT	Large Amplitude Unsteady Lifting-Line Theory (see Chapter 5)
LAUTAT	Large Amplitude Unsteady Thin Aerofoil Theory [102]
LESP	Leading Edge Suction Parameter [145]
LDVM	LESP modulated discrete vortex method [145]
LLT	Lifting-Line Theory
MAV	Micro Air Vehicle
NACA	National Advisory Committee for Aeronautics (now NASA)
NATO	North Atlantic Treaty Organization
P-ULLT	Pseudosteady ULLT (see Sec. 2.2.4)
S-ULLT	Simplified ULLT (see Sec. 2.2.4)
UAV	Unmanned Aerial Vehicle
UCoFD	ULLT / Convolution in Frequency Domain (see Chapter 4)
ULLT	Unsteady Lifting-Line Theory
UVLM	Unsteady Vortex Lattice Method
VLM	Vortex Lattice Method
VPM	Vortex Particle Method
VoFFLE	Vortex Formation on Finite Leading Edge (see Chapter 6)

Chapter 2

Frequency-domain small-amplitude unsteady lifting-line theory

2.1 Introduction

Frequency-domain unsteady lifting-line theory is a means by which 2D unsteady aerofoil solutions, such as that of Theodorsen [56] for oscillating aerofoils and Sears [62] for oscillating gusts, can be applied to 3D problems involving finite wings. The method corrects the 2D problem to account for 3D phenomena.

As described in Sec. 1.1.4, Sclavounos's unsteady lifting-line theory [94] is currently the most advanced easily applicable analytical unsteady lifting-line theory. Guermond and Sellier [85] provided a more generally applicable theory. Their method is applicable to curved and swept wings. Sclavounos's method can only be applied to straight wings. Guermond and Sellier's method is also applicable to wings oscillating at all frequencies. The assumptions made in the derivation of Sclavounos's method mean that it is asymptotically invalid for wake wavelengths shorter than the chord scale of the wing. Finally, Guermond and Sellier express their method in more general terms than Sclavounos. Sclavounos derives his method only for pitch and plunge problems although there is no reason it cannot be more general. Unfortunately, Guermond and Sellier's method is not easily applied to the rectangular-tipped wing planforms often found in man-made aircraft. This is due to the chord distribution discontinuity at the tips. See Appendix A.1.

In this chapter, frequency-domain unsteady lifting-line theory (and lifting-line theory in general) is introduced using Sclavounos's method, with minor modifications. These modifications follow Guermond and Sellier to allow Sclavounos's ULLT to be applied to more general problems. This theory is covered in Sec. 2.2. The kernel that accounts for 3D correction is also studied in Sec. 2.2.4. This kernel is responsible for much of the complexity of ULLT. The integro-differential equation central to obtaining solutions in Sclavounos's method allows for different unsteady kernels to be investigated. Different kernels representing simplified wake models that are appealing for their application in *ad-hoc* and numerical ULLTs can therefore be studied. A new kernel that represents only the streamwise oscillating vorticity in the wake is investigated to this end.

Having introduced frequency-domain unsteady lifting-line theory and the kernel that accounts for 3D interaction, the ULLT can then be compared to Euler regime CFD (detailed in Appendix C.1) and strip theory in Sec. 2.3. The motivation for the case parameters studied is described in Sec. 2.3.1. Initially, Sclavounos's unsteady kernel is compared to CFD for rectangular wings of aspect ratios 8, 4 and 2 for both heave and leading-edge pitch kinematics. Next, the impact of the ULLT interaction kernel on predicted lift coefficient is investigated and a visual comparison of the wake prediction is made. Then the lift distribution with respect to span is investigated. Comparison of the ULLT to experiment are made in Sec. 2.3.3 before the chapter concludes in Sec. 2.4.

This chapter serves multiple purposes. It introduces frequency-domain ULLT, and the idea of the wake interaction kernel. It then assesses ULLT for rectangular wing planforms where supposedly LLT is invalid but nonetheless often applied. It investigates the importance of the wake model by comparing the results of different interaction kernels and examines the results obtained with these kernels in the very high frequency domain where they are supposedly invalid. And finally it verifies that a method derived for the non-physical Euler regime remains applicable to high Reynolds number cases.

2.2 Theoretical approach

A straight, unswept wing is immersed in an inviscid, incompressible fluid with freestream velocity U_∞. The wing is subject to an oscillating velocity boundary condition in the normal direction to the wing surface. These oscillations do not need to be constant with respect to span, although in this dissertation rigid-body pitch (α) and plunge (h) will be primarily considered. Sclavounos's frequency-domain unsteady lifting-line theory provides a method by which the forces on and flow about this wing can be obtained.

Lifting-line theory is formulated on two length-scales. Firstly, the outer domain, where span-sized elements of the geometry are considered. And secondly, the inner domain, where detailed chord-scale solutions are obtained. This can be justified by the method of separation of length-scales.

At distances from the wing on the span length-scale, where the chord-scale is comparatively negligible, the flow is insensitive to the wing geometry. The wing can be represented by a line of concentrated bound circulation $\Gamma(y)$. For the straight wing in this problem this line lies on the y-axis. Because the boundary condition on the wing is oscillating, the bound circulation $\Gamma(y)$ is also oscillating. Consequently the wing's wake, which is being convected away from the wing at the freestream velocity U_∞, has both streamwise vortic-

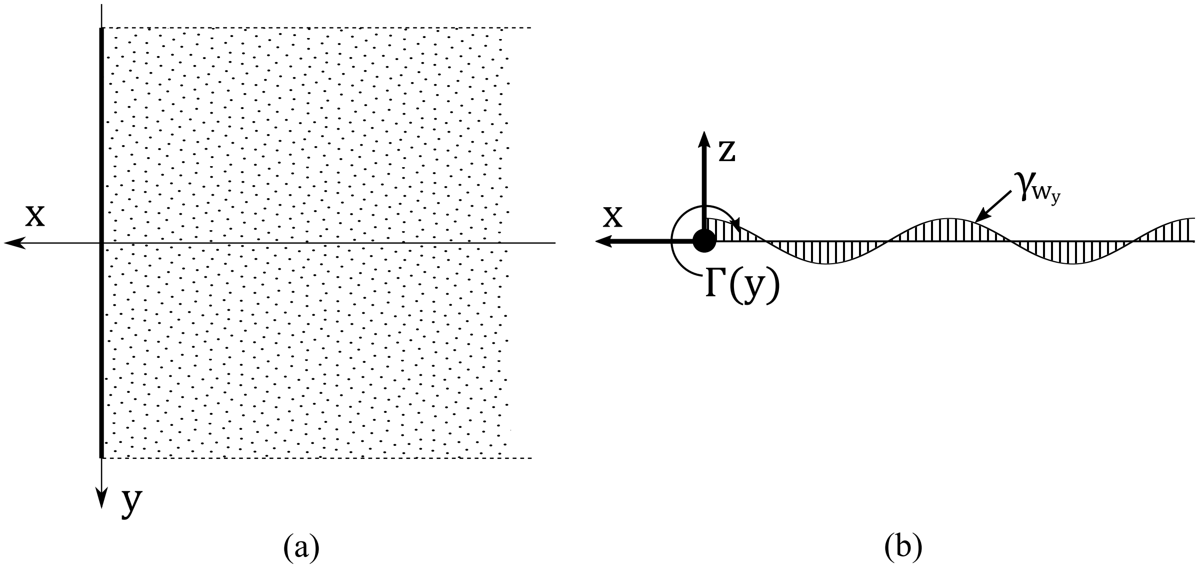

Figure 2.1: (a) Plan view of the lifting-line and its wake in the outer domain, and (b) the 2D problem in the outer domain.

ity components due to Helmholtz's theorems, and spanwise vorticity components due to Kelvin's circulation theorem. This wake is represented by a planar vortex sheet.

Closer to the wing, on distance comparable to the chord, the detailed flow is considered. This can be done using methods such as that of Theodorsen [56]. This inner solution is assumed to change slowly along the span, so using a 2D solution is valid. This 2D inner problem with the outer 3D span-scale problem can be combined using the matched asymptotic expansion method [79] to obtain an unsteady lifting-line theory.

The details of this theory will be obtained in several steps. Firstly, in Sec. 2.2.1, Sclavounos's derivation of the outer solution is reproduced. Next, the inner solution is presented for rigid-body pitch and heave in Sec. 2.2.2. The inner and outer are matched and the final lifting-line equation is obtained in Sec. 2.2.3. Finally, the kernel and the influence of the various wake models are discussed in Sec. 2.2.4.

2.2.1 The outer solution

Figure 2.1 illustrates the lifting-line and its wake based on the assumptions made in the outer domain. The chord, which is assumed to be negligible in the outer domain, has shrunk to a point.

The bound circulation of the wing can be described by as a complex quantity,

$$\Gamma(y;t) = \Gamma_0(y)e^{i\omega t}, \qquad |y| \leq s. \tag{2.1}$$

where Γ_0 is the circulation distribution at time $t = 0$, ω is the oscillation rotational frequency, y is the spanwise coordinate and s is the semispan of the wing.

The wing leaves a vortex sheet in its wake. This vortex sheet has a streamwise component γ_{w_x} caused by Helmholtz's theorems, which require that the change in the wing's bound circulation with respect to span must be trailed in to the wake, and Kelvin's theorem that results in that any change of bound vorticity be shed as spanwise wake vorticity (γ_{w_y}). On the lifting-line, at $x = 0$,

$$\gamma_{w_x}|_{x=0} = \frac{\partial \Gamma_0(y)}{\partial y} e^{i\omega t}, \tag{2.2}$$

$$\gamma_{w_y}|_{x=0} = -\frac{1}{U_\infty}\frac{\partial \Gamma}{\partial t} = -\frac{i\omega\Gamma_0(y)}{U_\infty} e^{i\omega t}. \tag{2.3}$$

The wake is convected at the freestream velocity U_∞, hence

$$\gamma_{w_{x/y}}(x, y; t) = \begin{cases} \gamma_{w_{x/y}}(0, y; t) e^{i\omega x/U_\infty}, & x \leq 0 \\ 0, & x > 0. \end{cases} \tag{2.4}$$

A two dimensional slice in the x-z plane is shown in Fig. 2.1(b). In this plane, the lifting-line appears as a point vortex, with a wake on $z = 0$, $x \leq 0$. It is here that the Kelvin condition (Eq. 2.3) is satisfied. For a bound circulation of unit amplitude, the velocity potential is given by

$$\overline{\phi^{2D}}(x, z) = \frac{1}{2\pi}\tan^{-1}\frac{z}{x} - \frac{i\omega}{2\pi U_\infty}\int_{-\infty}^{0} e^{i\omega\xi/U_\infty}\tan^{-1}\frac{z}{x-\xi}\,\mathrm{d}\,\xi \tag{2.5}$$

where ξ is a streamwise variable of integration, and the overline of $\overline{\phi^{2D}}$ indicates unit, time-free nature of the quantity. The first term of the equation represents the bound vorticity at origin, and the wake vortex sheet is represented by the integral term.

The 2D wake given in Eq. 2.5 cannot represent a 3D problem however. The streamwise vorticity, γ_{w_x}, due to Eq. 2.2 must still be included. Sclavounos includes them as the second term in the asymptotic expansion of the full outer velocity potential equation:

$$\phi(x, y, z; t) \sim \Gamma(y; t)\overline{\phi^{2D}}(x, z) - \frac{z}{2\pi}\int_{-s}^{s}\frac{\partial \Gamma(\eta; t)}{\partial \eta}K(y - \eta)\,\mathrm{d}\,\eta \tag{2.6}$$

where the kernel $K(y)$ is the 3D interaction kernel, and η is the spanwise variable of integration. The form of $K(y)$ depends on the choice of wake model, discussed in Sec. 2.2.4. The second term containing $K(y)$ represents an unsteady downwash accounting for the 3D interaction in the outer domain. It can be differentiated with respect to z to give the induced downwash due to finite wing effects. This second term is independent of x and linear in z, meaning that the downwash over a chord section is uniform in the x-z plane. Sec. 2.3 investigates and discusses the impact of this assumption on wing load prediction by comparing lift coefficients from ULLT against high-fidelity computational

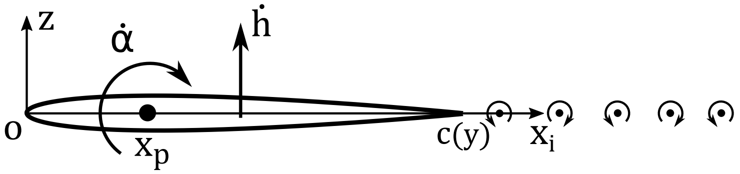

Figure 2.2: Inner domain, showing the velocities of the airfoil, pitch-axis location, chord length and spanwise shed vorticity.

fluid dynamics over a large range of frequencies.

2.2.2 The inner solution

In the inner domain, it is assumed that the span scale is much greater that the chord scale ($2s \gg c$), and that change in the flow around a chord section occurs on the span-scale, meaning that the inner problem can be considered 2D. This makes considering the detailed flow around a chord section easier. For frequency domain unsteady lifting-line theory, this 2D problem is modelled as an oscillating vertical velocity boundary condition, which can be solved using methods such as that of Theodorsen [56]. For the purposes of this dissertation, rigid-body kinematics will be emphasised. Oscillating heave and pitch oscillations can be expressed as

$$h(y,t) = h_0^*(y)c(y)e^{i\omega t} \tag{2.7}$$

$$\alpha(y,t) = \alpha_0(y)e^{i(\omega t+\psi)} \tag{2.8}$$

where h_0^* is plunge amplitude per unit chord, α_0 is pitch amplitude, ψ is the phase between plunge and pitch, and ω is the frequency of oscillation. The oscillation frequency can be non-dimensionalised either as the chord reduced frequency, k, or span reduced frequency, ν:

$$k(y) = \frac{\omega c(y)}{2U_\infty}, \tag{2.9}$$

$$\nu = \frac{\omega s}{U_\infty}. \tag{2.10}$$

For rigid-body kinematics, this problem is displayed in Fig. 2.2. Theodorsen [56] first obtained a solution for this problem. A more general solution was obtained for Küssner and Schwarz [64], by which gust response could also be obtained, using an expansion based on the oscillating pressure distribution. Alternatively, it can be expressed in terms of Ramesh *et al.*'s unsteady thin aerofoil theory [102] as in Bird and Ramesh [1]. Küessner and Schwarz's method avoids the complexity of obtaining the vorticity distribution over the chord, but Ramesh *et al.*'s method dovetails with the numerical methods used in the later chapters of the dissertation. Consequently both methods are detailed in Appendix B.

Only the results required for this chapter are presented here.

For the 2D problem of an aerofoil oscillating in rigid pitch (indicated by the subscript α) or heave (indicated by subscript h), the 2D bound circulation Γ^{2D}, 2D lift coefficient C_l^{2D} and 2D moment coefficient C_m^{2D} can be obtained as

$$\Gamma_h^{2D}(y;t) = \frac{4U_\infty h_0^*(y)c(y)e^{-ik}}{iH_0^{(2)}(k) + H_1^{(2)}(k)} e^{i\omega t} \tag{2.11}$$

$$\Gamma_\alpha^{2D}(y;t) = \frac{4U_\infty \alpha_0(y)c(y)e^{-ik}}{iH_0^{(2)}(k) + H_1^{(2)}(k)} \left(\left(x_p^* - \frac{3}{4} \right) - \frac{1}{2ik} \right) e^{i(\omega t + \psi)} \tag{2.12}$$

$$C_{l_h}(y;t) = 2\pi h_0^*(-2ikC(k) + k^2)e^{i\omega t} \tag{2.13}$$

$$C_{l_\alpha}(y;t) = 2\pi\alpha_0 \left[C(k) \left(1 - 2ik \left(x_p^* - \frac{3}{4} \right) \right) + \frac{ik}{2} + k^2 \left(x_p^* - \frac{1}{2} \right) \right] e^{i(\omega t + \psi)} \tag{2.14}$$

$$C_{m_h}(y;t) = 2\pi h_0^* \left[-2ikC(k) \left(x_m^* - \frac{1}{4} \right) + k^2 \left(x_m^* - \frac{1}{2} \right) \right] e^{i\omega t} \tag{2.15}$$

$$\begin{aligned} C_{m_\alpha}(y;t) = 2\pi\alpha_0 \Bigg[& C(k) \left(1 - 2ik \left(x_p^* - \frac{3}{4} \right) \right) \left(x_m^* - \frac{1}{4} \right) \\ & + k^2 \left(x_p^* \left(x_m^* - \frac{1}{2} \right) - \frac{1}{2} \left(x_m^* - \frac{9}{16} \right) \right) + \frac{ik}{2} \left(x_m^* - \frac{3}{4} \right) \Bigg] e^{i(\omega t + \psi)} \end{aligned} \tag{2.16}$$

where $H_0^{(2)}(z)$ and $H_1^{(2)}(z)$ are Hankel functions of the second kind, x_p^* is the non-dimensional reference location for pitching moment and x_m^* is the non-dimensional reference location for pitching moment, where for both quantities a value of 0 corresponds to the leading edge and 1 the trailing edge. $C(k)$ is Theodorsen's function, which can be defined as

$$C(k) = \frac{K_1(ik)}{K_1(ik) + K_0(ik)} \tag{2.17}$$

where K_0 and K_1 are modified Bessel functions [221].

2.2.3 Matching of the inner and outer solutions

The asymptotic expansion of the outer full potential equation (Eq. 2.6) contains an as-yet unknown distribution of bound circulation and the inner solution lacks any kind of correction for 3D effects. The inner and outer solutions must be combined to obtain a solution. The asymptotic expansion of the outer full potential equation (Eq. 2.6) models the problem as the asymptotic expansion of the 2D problem with a uniform downwash. In the inner solution this is

$$\phi(x, y, z; t) = \phi_{h/\alpha}^{2D} + F(y)(i\omega z e^{i\omega t} - \phi_{hn}^{2D}) \tag{2.18}$$

The 2D solution $\phi^{2D}_{h/\alpha}$ is corrected by a uniform downwash $F(y)i\omega z e^{i\omega t}$ and the section's reaction to this downwash $F(y)\phi^{2D}_{hn}$. The subscript hn is used to donate quantities relating to heaving with unit amplitude. This is a downwash of plunge amplitude $h_0 = h^*_0 c = F(y)$ for which the associated velocity potential is $F(y)\phi^{2D}_{hn}$ with resulting bound vorticity $F(y)\Gamma^{2D}_{hn}$. Consequently, the outer expansion of the inner velocity potential at large distances from the chord is

$$\phi(x, y, z; t) \sim \Gamma^{2D}_{h/\alpha}\overline{\phi^{2D}} + F(y)(i\omega z e^{i\omega t} - \Gamma^{2D}_{hn}\overline{\phi^{2D}}). \tag{2.19}$$

Equation 2.6 and Eq. 2.19 may now be matched. An expression for bound circulation can be obtained as

$$\Gamma(y; t) = \Gamma^{2D}_{h/\alpha}(y, t) - F(y)\Gamma^{2D}_{hn}(t). \tag{2.20}$$

which, referring back to Eq. 2.6, allows the strength of the 3D correction to be obtained:

$$F(y) = -\frac{1}{2\pi i\omega e^{i\omega t}} \int_{-s}^{s} \Gamma'(\eta)K(y - \eta)\,\mathrm{d}\,\eta. \tag{2.21}$$

From this an integro-differential equation can be obtained, similar to that of Prandtl. Substituting this expression for $F(y)$ into Eq. 2.20 gives

$$\Gamma - \frac{\Gamma^{2D}_{hn}}{2\pi i\omega} \int_{-s}^{s} \Gamma'(\eta)K(y - \eta)\,\mathrm{d}\,\eta = \Gamma^{2D}. \tag{2.22}$$

All the terms in this equation contain a common time factor $e^{i\omega t}$. A solution can be obtained by approximating the time-free bound circulation Γ_0(y) as the Fourier series

$$\Gamma_0 = 4U_\infty s \sum_{m=1}^{M} \Gamma_m \sin(m\zeta), \tag{2.23}$$

where $y = -s\cos\zeta$. For problems where both the kinematics and planform of the wing are symmetric about $y = 0$, the even m terms can be neglected. This allows a linear system to be obtained that can be solved to obtain Γ_0. The integration of Sclavounos's kernel K_C to obtain this linear system is detailed in Appendix A.2. This solution can be used to obtain the 3D correction strength $F(y)$ using Eq. 2.20, which can then be used to obtain lift and pitching moment coefficients, including 3D corrections as $C_{l/m} = C^{2D}_{l/m} - FC_{l/m_{hn}}$. The wing lift and pitching moment are

$$C_L = \frac{1}{2s\bar{c}} \int_{-s}^{s} C_l(y)c(y)\,\mathrm{d}\,y, \tag{2.24}$$

$$C_M = \frac{1}{2s\bar{c}^2} \int_{-s}^{s} C_m(y)c^2(y)\,\mathrm{d}\,y, \tag{2.25}$$

where the corrected 2D coefficients are integrated with respect to span. These integrals can be computed efficiently using type-2 Gauss-Chebyshev quadrature.

These integrals lead to a difference between the current method and that of Sclavounos. Sclavounos does not provide expressions for lift and moment coefficients with respect to span. To obtain the lift coefficient for the entire wing, Sclavounos integrates only the circulatory component of the lift, and a constant added mass coefficient, known *a priori*, is added. The method here is more similar to that used in Guermond and Sellier [85], and offers two advantages. Firstly, the added-mass coefficient does not need to be known in advance. The added mass coefficient is not trivial to compute in 3D and lifting-line theory suggests that the it should change with respect to frequency due to the dependence of $F(y)$ on frequency. Secondly, implicitly obtaining added mass allows a force distribution to be obtained with respect to span.

2.2.4 The kernel $K(y)$

The kernel $K(y)$, which represents the spanwise interaction of the inner solutions via the outer domain, was first introduced in Eq. 2.6. It must give the difference between a 2D strip theory solution and the actual 3D solution of the problem.

The simplest form of $K(y)$ comes from strip theory, where three dimensional interaction is neglected. The wake of the inner solutions continues to model the spanwise wake vorticity γ_{w_y}, but without account for the change with respect to span from any point on the span. It also neglects the streamwise vorticity γ_{w_x}, meaning that the wing tip vortices aren't included. All interaction between the inner domains is neglected, meaning the strip theory kernel K_{2D} is

$$K_{2D}(y) = 0. \tag{2.26}$$

In Prandtl's original lifting-line theory, the streamwise vorticity γ_{w_x} in the wake was accounted for in the outer domain. For steady flow, the streamwise vorticity strength is invariant with the downstream coordinate. Making this assumption results in a 'pseudosteady' kernel, which neglects the sinusoidal variation with respect to downstream coordinate given in Eq. 2.4. The resultant pseudosteady kernel K_P is equivalent to that of Prandtl:

$$K_P(y) = \frac{1}{2sy^*}, \tag{2.27}$$

where $y^* = y/s$ and the ULLT based on this kernel is abbreviated P-ULLT.

A new kernel can be obtained if the sinusoidal variation of γ_{w_x} with respect to x given by Eq. 2.4 is accounted for. Only accounting for the streamwise component of wake vorticity is simpler. It avoids the complication that, if the spanwise component of wake vorticity were to be included, it would be necessary to correct for the fact it would exist in both inner and outer domains, lest its effects be felt twice. The Biot-Savart law [51] can be applied to the streamwise vorticity field, allowing the downwash on a point of the

Table 2.1: Features of the trailing wake behind the wing (in the outer solution) for the various solution methods considered in this research.

Method	Kernel	Wake model in outer solution
Strip theory	K_{2D}	γ_{w_y}: No model γ_{w_x}: No model
P-ULLT (Pseudosteady)	K_P	γ_{w_y}: No model γ_{w_x}: constant with respect to x-coordinate
S-ULLT (Simplified)	K_S	γ_{w_y}: No model γ_{w_x}: harmonic variation in x-direction
C-ULLT (Complete)	K_C	γ_{w_y}: harmonic variation in x-direction γ_{wx}: harmonic variation in x-direction

wing at y_0 due to a section of the wing $\mathrm{d}\,y$ to be obtained as

$$\mathrm{d}\,q = -\frac{\partial \Gamma}{\partial y}\frac{1}{4\pi}\int_{-\infty}^{0} \frac{e^{\frac{i\omega\xi}{U_\infty}}(y-y_0)}{(\xi^2+(y-y_0)^2)^{\frac{3}{2}}}\,\mathrm{d}\,\xi,$$

allowing K_S to be obtained as

$$K_S(y) = \frac{1}{2sy^*}\left[\nu|y^*|K_1\left(\nu|y^*|\right) + \frac{i\pi\nu|y^*|}{2}\Big(I_1\left(\nu|y^*|\right) - L_{-1}\left(\nu|y^*|\right)\Big)\right], \tag{2.28}$$

where $I_n(x)$ and $K_n(x)$ are the modified Bessel functions of the first and second kind respectively, and $L_n(x)$ is the modified Struve function[221]. Again, this neglects variation in γ_{w_y} with respect to span in the outer solution, making it simple to obtain in both this frequency-domain ULLT and potentially in time-domain ULLTs. The ULLT based on this kernel is therefore referred to the simplified ULLT (S-ULLT).

Obtaining a kernel that accounts for both the shed streamwise vorticity γ_{w_x} and the 3D correction to the effects of the shed spanwise vorticity γ_{w_y} is more challenging. Sclavounos [94] obtained this kernel K_C as

$$K_C(y) = \frac{1}{2s}\operatorname{sgn}(y^*)\left[\frac{e^{-\nu|y^*|}}{|y^*|} - i\nu E_1(\nu|y^*|) + \nu P(\nu|y^*|)\right], \tag{2.29}$$

where $E_1(x)$ is the exponential integral[221] and

$$P(y) = \int_1^\infty e^{-yt}\left[\frac{\sqrt{t^2-1}-t}{t}\right]\mathrm{d}\,t + i\int_0^1 e^{-yt}\left[\frac{\sqrt{1-t^2}-1}{t}\right]\mathrm{d}\,t. \tag{2.30}$$

This ULLT is denoted as the complete ULLT (C-ULLT) in this research.

The different ULLT models can be compared by the components of the wake they model. This is done in Table 2.1.

An important feature of the ULLT is the high and low frequency limits of the interaction kernel. At low frequencies the unsteady solution is expected to tend to the pseudosteady solution. This is the case for all of the ULLTs but strip theory:

$$\lim_{\omega\to 0}\{K_C(y)\} = \lim_{\omega\to 0}\{K_S(y)\} = K_P(y). \tag{2.31}$$

And at high frequency, the ULLT interaction kernel ought to tend to strip theory.

$$\lim_{\omega\to\infty}\{K_C(y)\} = \lim_{\omega\to\infty}\{K_S(y)\} = K_{2D}(y) = 0. \tag{2.32}$$

The pseudosteady kernel does not do this. However, the added-mass effects in the inner solution scales as $O(k^2)$ compared to $O(k)$ for the circulatory effects. Consequently, even the P-ULLT may be expected to approach strip theory at sufficiently high oscillation frequencies.

2.3 Results

In the theory section of this chapter, a ULLT was derived following the method of Sclavounos. Multiple assumptions were made. Potential flow methods were used, meaning that inviscid, incompressible flow was assumed. The kinematics were assumed to be small and the wake assumed to be planar. These assumptions are common to many low-order models, including the inner solutions used here.

The unsteady lifting-line theory itself introduces further assumptions. A limitation common to all lifting-line theories is that the inner solution must change slowly with respect to span. This implies that, for rigid-body kinematics, a lenticular or cusped wing must be used for the LLT to be valid near the wing tips [79]. In practice, many practical wing planforms have rectangular wing tips[1]. Lenticular and cusped wings would better satisfy the assumptions of LLT, but these planforms never appear to be used in any of the applications motivating this thesis. The derivation of the ULLT also introduces further assumptions about the wake wavelength, confining Sclavounos's model, the C-ULLT, to Cheng's [93] Domains I-IV for strict asymptotic validity. However, the interaction kernel correctly tends to strip theory at very high frequencies. The same is true for the simplified streamwise vorticity S-ULLT. The pseudosteady P-ULLT may eventually tend to strip theory due to the different scaling of added-mass and circulatory effects.

From a practical perspective, the implications of these asymptotic limitations are unclear. Historically lifting-line theory has extensively been misapplied to rectangular wings and elliptic wings. For all the different wake models, the ULLTs appear to have the cor-

---

[1] Here, rectangular wing tips imply that the chord is non-zero at the very tip of the wing. Consequently, other planforms including tapered wings have rectangular tips.

rect limiting behaviour, whilst being asymptotically invalid. This results section therefore applies the ULLTs for problems involving rectangular wings oscillating at a large range of frequencies in both pitch and heave in order to understand the applicability of ULLT and the limitations of the wake models.

2.3.1 Case choice

Trying to compare low-order methods to experiment or CFD for finite wings undergoing unsteady kinematics potentially leads to a combinatorial explosion. It is not the aim of the dissertation to extensively investigate the effects of different wing planforms or kinematics. Instead, it is limited to rectangular wing planforms and rigid-body pitch and heave kinematics. Rectangular wing planforms are chosen because they are applicable to engineering problems, and, as alluded to, these are especially troublesome for lifting-line theories due the jump in chord length at the wing tips. Three aspect ratios are chosen: aspect ratios 8, 4 and 2 to represent high-, intermediate-, and low-aspect ratio cases respectively. The effectiveness of ULLT is expected to vary in accordance to these aspect ratios. When low Reynolds number cases are studied in later chapters, aspect ratios 6, 3, and 1 rectangular wings are studied to reduce the computational cost of CFD and to better reflect the low-aspect-ratio wings common at low Reynolds numbers.

For kinematics, pitch and heave problems are studied. The pitch location is about the leading edge of the wing. In this chapter, where only small amplitude oscillations are studied, the moment reference location is the mid-chord for consistency with the work of Sclavounos. This is inconsistent with later chapters where the leading edge is used as the moment reference location in order to match the pitching location for large-amplitude cases.

2.3.2 Validation of lift and moment coefficients from C-ULLT

In this section, Sclavounos's ULLT (the C-ULLT) is validated against Euler CFD for heave and leading-edge pitch. The CFD method is detailed in Appendix C.1. Lift and moment coefficients are compared in both amplitude and phase. Heave is considered first followed by leading-edge pitch. In all cases, the mean angle of attack is zero.

Heaving kinematics

Figure 2.3 shows the amplitude and phase of the whole-wing lift coefficient C_L and mid-chord moment coefficient C_M. These coefficients are normalized by both amplitude and chord reduced frequency. Amplitude normalization is possible because the ULLT is linear. Chord reduced frequency normalisation leads to results comparable to steady theory as $k \to 0$. The problem becomes equivalent to a wing moving at a constant plunge velocity. As $k \to \infty$, vorticity in the wake has no influence on the wing due to the Reimann-Lebesgue

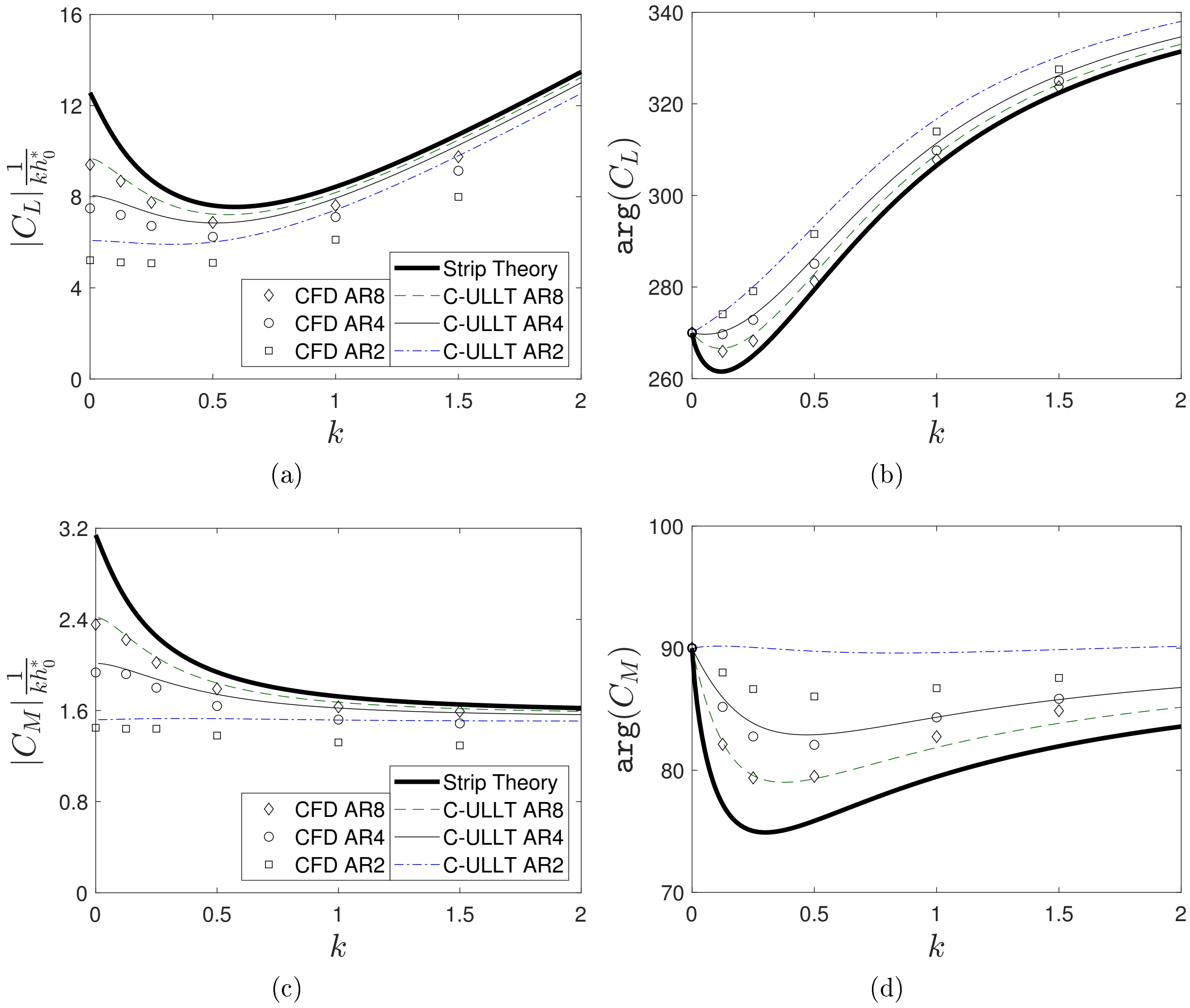

Figure 2.3: Comparison of lift and moment about mid-chord for C-ULLT, strip theory and Euler CFD for rectangular wings oscillating in heave with a zero mean angle of attack.

lemma. Physically, before any trailing wake vorticity can be convected downstream, it is cancelled the by shedding of the opposite voriticty. The CFD is displayed as points and the theories described in this chapter displayed as lines. Strip theory (Theodorsen's method) is shown in bold, with the C-ULLT results show with thinner lines.

The $|C_L|/kh_0^*$ with respect to frequency obtained from CFD shown in Fig. 2.3(a). Examining this, the normalized lift amplitude is lower for lower aspect ratio wings at all frequencies. At $k = 0$, non-infinite aspect ratios and wing planform limitations introduce error even for the steady case. For $k < 0.5$, the lift decreases with k at aspect ratios 8 and 4, whilst remaining approximately constant at aspect ratio 2. For $k > 0.5$, lift increases with respect to k. The rate of increase with respect to k is lower for lower aspect ratios suggesting the added-mass per unit span of the finite wing decreases with aspect ratio.

The complete ULLT of Sclavounos predicts the trends of the CFD. Fig. 2.3(a) shows that at aspect ratio 8 and lower reduced frequencies the prediction of the ULLT is excellent. As aspect ratio decreases, there is an over-prediction of $|C_L|$ in comparison to the CFD. At higher frequencies, the C-ULLT predicts that the lift with respect to oscillation frequency is approximately equal for all aspect ratios - the added-mass per unit span is equal. This introduces error compared to the CFD, and leads to an over-prediction of lift at high frequencies for the lower aspect ratio wings, where the C-ULLT prediction of the added mass coefficient is too high. ULLT predicts that as $k \to \infty$ the 3D effects tend to 0. This suggests that this assumption is untrue because of the choice of rectangular planforms for which lifting-line theory is not entirely valid. This could be investigated using the unsteady vortex lattice method, following the methodology of Smyth *et al.* [181].

In Fig. 2.3(b), the phase of the whole-wing lift is examined. In the limit of low frequency, CFD and the C-ULLT predict that the phase of the lift with have a lag of 90°. As k increases, the CFD and C-ULLT agree that the response depends on aspect ratio. High aspect ratios initially increase phase lag, whilst low aspect ratios decrease it. Beyond $k \approx 0.1$ lag decreases for all aspect ratios. The C-ULLT predicts phase well at low frequencies. As frequency increases, the accuracy of the prediction remains good at high aspect ratio, but the low Æ2 wing leads to error.

The amplitude of the pitching moment about the mid-chord is examined in Fig. 2.3(c). Like lift, the C-ULLT is accurate in predicting $|C_M|$ aspect ratio 8, and the accuracy of the prediction decreases with aspect ratio. Again, this is especially true at higher values of k where the C-ULLT predicts that the values of $|C_M|$ ought to converge. Instead, the CFD predicts that the lower aspect ratio wings result in lower moment coefficients.

Finally, the phase of C_M is examined in Fig. 2.3(d). The CFD shows that for all aspect ratios the phase lead initially reduces with increasing chord reduced frequency, but then starts to increase again in the region of $k = 0.5$. The C-ULLT predicts this well for the aspect ratio 8, reasonably well for the aspect ratio 4 case, but poorly for the aspect ratio 2 case.

For heaving rectangular wings, the C-ULLT can predict the results of the CFD, although accuracy is worse for the low-aspect-ratio, Æ2 case. ULLT was universally better than strip theory, which entirely neglects 3D effects leading to an often considerable overestimate of forces, and a significant phase prediction error.

Next, pitching kinematics are considered.

Pitching kinematics

As with the heaving kinematics, the C-ULLT is compared against CFD for the leading-edge pitching of rectangular wings. Results are displayed in Fig. 2.4. Unlike the heaving cases shown in Fig. 2.3, there is no normalisation with respect to frequency, although amplitude normalization is again used.

Again, $|C_L|/\alpha_0$, shown in Fig. 2.4(a) is considered first. At $k = 0$, the CFD shows that lower aspect ratio leads to reduced lift. It also shows a slight initial decrease in lift from $k = 0$ at aspect ratio 8, but an approximately flat lift slope for the lower aspect

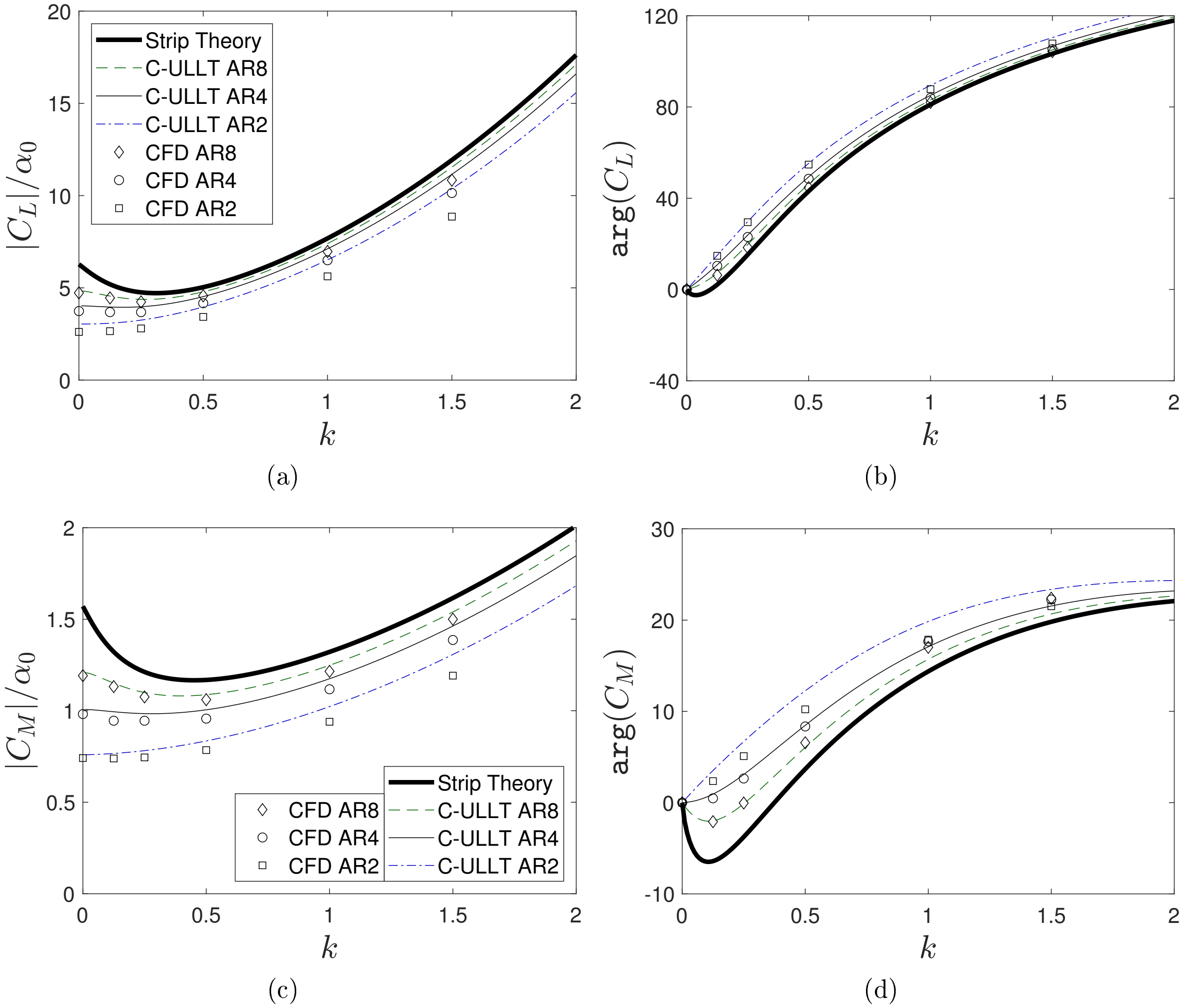

(a) (b)

(c) (d)

Figure 2.4: Comparison of the C-ULLT, strip theory and Euler CFD for rectangular wings oscillating in pitch about the leading edge. Moment coefficient is taken about the mid-chord.

ratio wings. Then, as k increases further the lift increases super-linearly. The C-ULLT reflects all of these trends, with better prediction at higher aspect ratios. Again, higher frequencies introduce errors, perhaps due to the added mass and the rectangular wing planform.

For the phase of C_L, shown in Fig. 2.4(b), the CFD results show that initially the C_L starts in phase with the kinematics, with a lead being introduced as frequency increases. The CFD predicts that lower aspect ratio results in a slightly larger phase lead. These trends are excellently predicted by the C-ULLT, although at low aspect ratio and high frequency, there is a slight over-prediction of the phase lead.

For pitching moment amplitude, shown in Fig. 2.4(c), the CFD results show lower $|C_M|$ at lower aspect ratio. The trends of the curve are correctly predicted by the C-ULLT. At low chord reduced frequency, the moment slightly reduces with respect to k for the aspect ratio 8 case, and stays approximately constant for the Æ4 and Æ2 cases. As chord reduced frequency increases further, the moment amplitude increases. For the aspect ratio 8 case, the C-ULLT remains accurate, although as aspect ratio decreases the C-ULLT increasingly over-predicts with frequency.

Finally, Fig. 2.4(d) shows the phase of the moment coefficient. The CFD and C-ULLT agree that the moment is initially in phase with the kinematics at $k = 0$. As the pitch oscillation frequency increases, the moment produced by the aspect ratio 8 wing lags the kinematics, the Æ4 wing starts to lead the kinematics slightly, and the Æ2 wing leads the kinematics more. As chord reduced frequency increases further, the phase lead increases in all cases. The lead for all wings approximately converges to the same value at $k \approx 1$, and beyond that the trend that lower aspect ratio wings have a larger phase lead reverses - the Æ8 case has the largest phase lead. C-ULLT predicts phase well at lower values of k ($k \approx\leq 0.5$) for aspect ratios 8 and 4. Error is introduced at $k = 2$. At higher frequencies, the prediction of C-ULLT worsens. It fails to predict the change in phase lead with respect to frequency that occurs in the CFD result.

The C-ULLT again predicted the CFD results well for rectangular wing pitching about their leading edge. It provided a significantly better result than strip theory, even at low aspect ratios where its accuracy was worse.

Having examined the results of the Sclavounos's C-ULLT, the error introduced by other wake models will be considered in the next section.

Influence of ULLT kernel on lift coefficient

In the last section, the C-ULLT based on the work of Sclavounos was compared to CFD results for rectangular wings oscillating in heave and pitch. It was found to provide a reasonably good estimate of both the lift and moment coefficient, with better predictions being obtained in the high aspect ratio, low chord reduced frequency regime where the

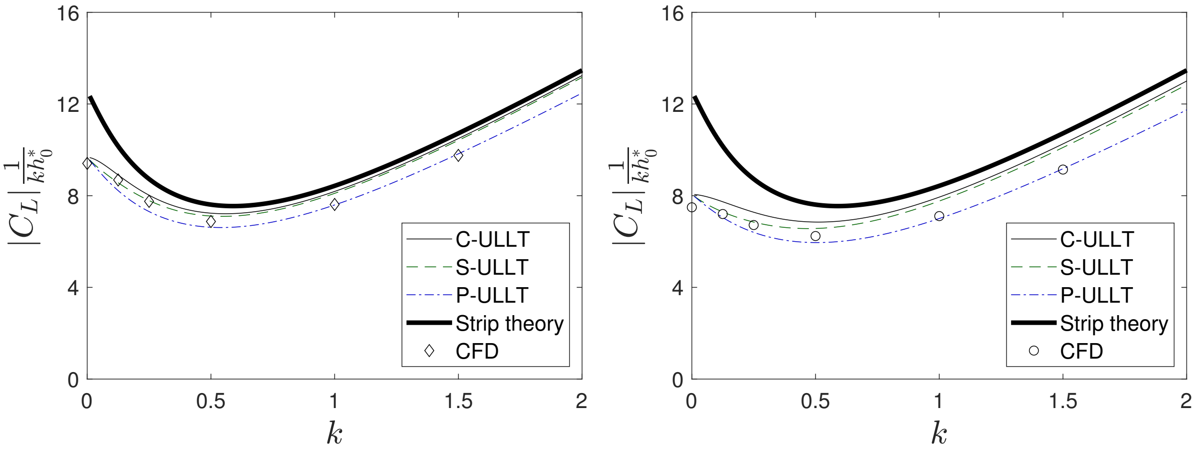

(a) Aspect ratio 8 (b) Aspect ratio 4

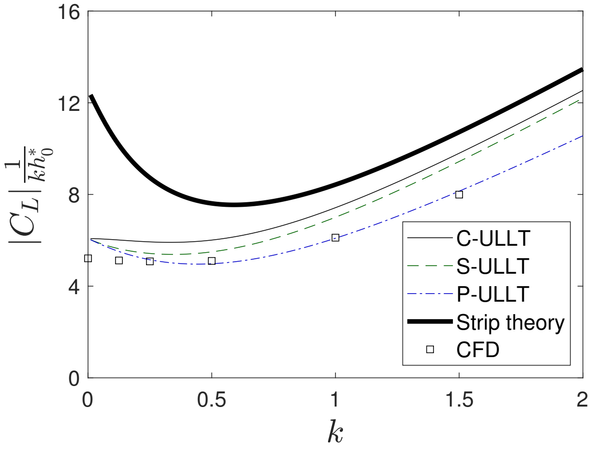

(c) Aspect ratio 2

Figure 2.5: Comparison of lift prediction from unsteady lifting-line theories for rectangular wings oscillating in heave in the Euler regime.

C-ULLT would be expected to perform best.

However, the kernel used to compute the 3D interaction of the C-ULLT, K_C, is complicated and challenging to implement (see Appendix A.2), and an analytical time-domain equivalent has not yet been obtained. In Sec. 2.2.4, alternate simplified kernels were discussed. The P-ULLT applies Prandtl's wake model to unsteady problems. Its simplicity has lead it to be used in methods such as those of Ramesh *et al.* [114] and Boutet and Dimitriadis [97]. A more complete model can be obtained by including the oscillating of the streamwise vorticity in the outer wake. This model still simplifies away the correction for the change in spanwise vorticity with respect to span, so is called the S-ULLT in this research. Such a model could be useful for numerical ULLTs. However, the impact of using these ULLTs is unclear. In this section, we compare the results of the C-ULLT, the S-ULLT and the P-ULLT to CFD to better understand the cost of simplified wake models. The lift amplitude of the models is examined in Fig. 2.5 for rectangular wings oscillating in heave.

The ULLT kernels all have the same low-frequency limit, according to Eq. 2.31. They all tend to Prandtl's result. It is therefore unsurprising that at all aspect ratios, they predict the same value of $|C_L|$.

At non-zero chord reduced frequencies, the increasingly complex kernels predict higher lift. The S-ULLT predicts higher lift than the P-ULLT, due to the Riemann-Lebesgue lemma applied to the induced downwash from the wake, and the C-ULLT predicts more lift that the S-ULLT since the change with repect ot span in wake spanwise vorticity in the wake is corrected for. All of the ULLTs show that the slope of $|C_L|/kh_0^*$ with respect to k is negative below approximately $k \approx 0.5$, after which it is positive.

Beyond $k \approx> 1$, the slope of all of the ULLT $|C_L|/kh_0^*$ curves is approximately constant. The added mass contribution to the lift is dominant - the circulatory contribution to lift for a heaving wing is of $O(k)$, but the added mass contribution is of $O(k^2)$. The C-ULLT, S-ULLT and strip theory curves converge (or appear to be in the process of converging for the Æ2 case) at high frequency. This follows the expected result of unsteady lifting-line theory. The P-ULLT appears to have a smaller slope than the other ULLTs and strip theory. The P-ULLT kernel, K_P, does not have a zero high frequency limit meaning that there is a 3D downwash correction even at very high frequency.

For Æ8 result shown in Fig. 2.5(a), the C-ULLT and S-ULLT provide an excellent prediction of CFD results for lift for $k \approx< 0.5$. The P-ULLT underestimates lift. As frequency increases further the C-ULLT and S-ULLT over-predict the CFD $|C_L|/kh_0^*$ curve. Instead, the P-ULLT provides the best match with CFD at $k \geq 1$.

A comparison of ULLTs and CFD for the aspect ratio 4 and 2 cases are shown in Fig. 2.5(b) and Fig. 2.5(c) respectively. As aspect ratio decreases, the difference between the results for the different ULLTs becomes larger.

The first difference is the initial slope of the $|C_L|/kh_0^*$ curves. The C-ULLT at $k = 0$ has a lower $|C_L|/kh_0^*$ slope than the S-ULLT and P-ULLT, which have a similar initial gradient. This is presumably due to the inclusion of spanwise vorticity in the wake of the outer solution. The slope of the C-ULLT appears to briefly increase in negative gradient before the gradient increasingly becomes positive with gradient. This feature is not found in the S-ULLT and P-ULLT results, where the gradient of the $|C_L|/kh_0^*$ only becomes more positive until a constant gradient is reached around $k \approx 1$. This effect is most prominent at low aspect ratio where the spanwise vorticity necessarily changes faster with respect to span, meaning the correction included only in the C-ULLT becomes more important.

A second difference is found in the over-prediction of $|C_L|$. ULLT appears to over-predict this for rectangular wings at low aspect ratios. The initial difference between the C-ULLT and the S-ULLT and P-ULLT results in the S-ULLT and P-ULLT better predicting the CFD result.

All of the ULLTs produce a far better result than strip theory. The difference between the strip theory solution and the true solution is frequency dependent, and all of the ULLTs could provide a reasonable estimate of this effect. In regimes where the assumptions of ULLT are best satisfied, the C-ULLT provides the best results. The S-ULLT provided better predictions than the P-ULLT in these scenarios. As frequency increased or aspect ratio decreased, error resulting from the assumptions of lifting-line theory increased, and the choice of ULLT became less important. For example, the P-ULLT appeared to give the best results at $\mathcal{R}2$ and $k > 1$. The prediction of ULLT that the lift would tend to the strip theory result appeared to be poor for rectangular wings. That the P-ULLT works best is not necessarily general. Instead, it may be better to draw the conclusion that the error introduced by the use of simplified wake models is unimportant given the error introduced by the violation of the assumptions on which LLT is based, justifying the use of simpler kernels.

The P-ULLT in some situations gave a better result than the more complete and supposedly superior ULLTs. The idea that it gave a better result due to fortune rather than any physical reason may be reinforced by examining the wake of the CFD, and the assumed outer wake forms of the ULLTs.

Comparison of wake topologies in the ULLT kernels

The ULLT improves on strip theory by correcting for the difference between the 2D solution on each strip and the wake in 3D. To do this, they model the 3D wake with varying fidelity. In this section, the assumed form of the wake used by the C-ULLT, S-ULLT and P-ULLT are compared to the results obtained using CFD. Only a single case is examined - that of the aspect ratio 4 rectangular oscillating in heave at $k = 0.5$, shown in Fig. 2.6. This case was chosen since it provides a good demonstration of the method although the relatively high reduced frequency and low aspect ratio introduce error into the ULLT solutions, most noticeably into the C-ULLT result.

To create this figure, the vortex sheet strength needed to be computed. For the ULLTs, this could be done easily based on the bound vorticity distribution and the assumed form of the wake used in their derivation. For the CFD, the wake vorticity was integrated over a line in the out of plane direction on a grid.

The C-ULLT, which includes both the oscillating spanwise and streamwise vorticity contributions in the correction, provides a good prediction of the CFD result. Some error is present, as expected, close to the wing tip. The assumed singular distribution (due to the remapped Fourier distribution) of wing-tip trailed streamwise vorticity is incorrect. In the CFD, the streamwise wake vorticity remains finite, instead spreading out. Separation on the sharp edges of the wing tip leads to additional small flow features in the CFD result. The spanwise component of wake vorticity exhibits some error with respect to phase. This is most visible in the difference in phase between the wing centre and tip. The difference

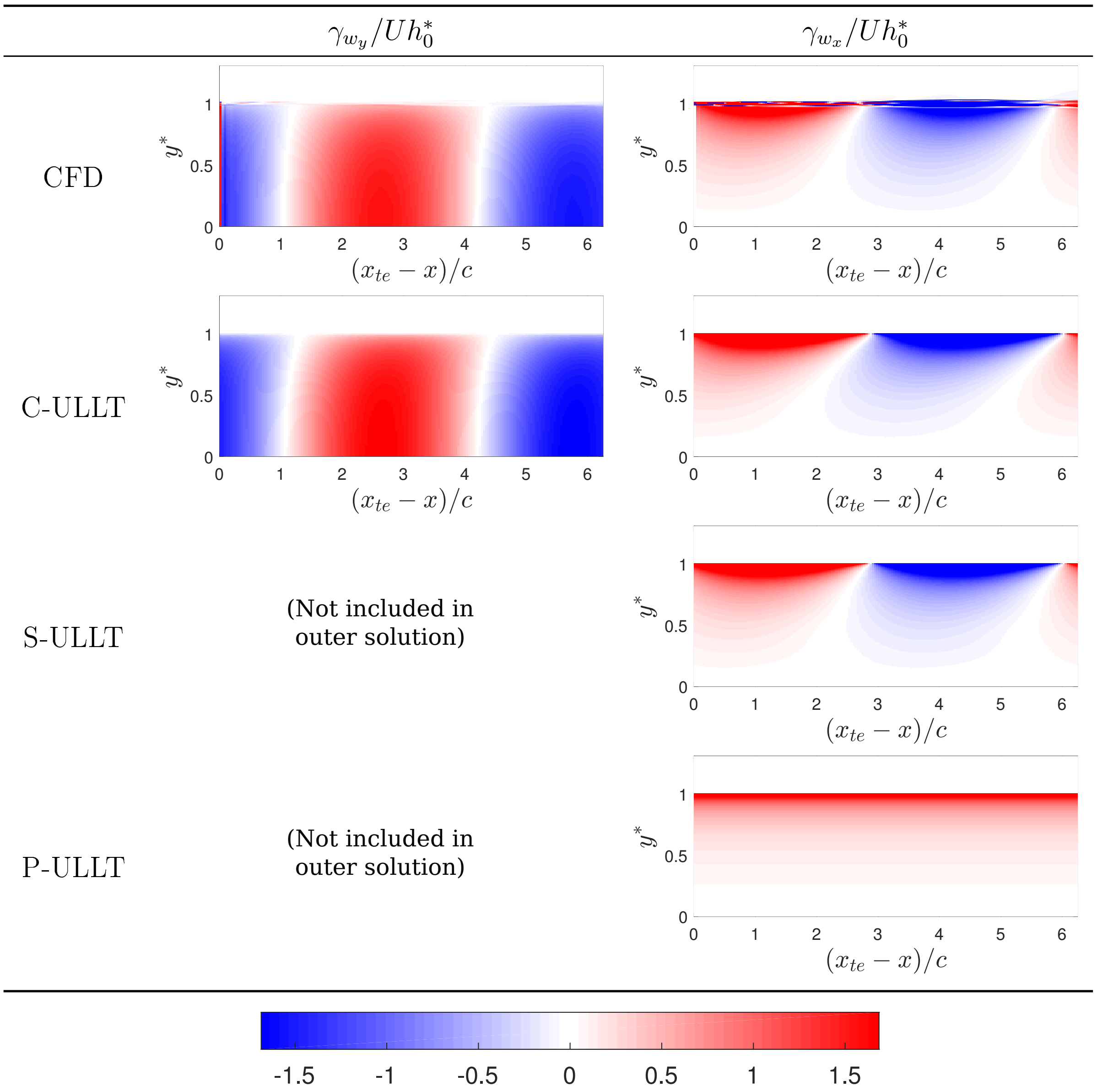

Figure 2.6: Comparison of wake vorticity density for an aspect ratio 4 wing oscillating at $k = 0.5$. The ULLT results show only the wake model assumed in the outer domain. Since the wing is shrunk to a line in the outer domain of the ULLTs, the x coordinate of the trailing edge, x_{te}, is zero for ULLTs. Shown at $t \bmod 2\pi/\omega = 0$.

predicted by the C-ULLT is larger than found in the CFD results. The reason for this is probably the relatively high chord reduced frequency. The phase of 3D correction from Sclavounos's kernel appears to introduce error as $k = 1$ is approached.

The S-ULLT is simplified by only considering the streamwise vorticity in the outer solution. It produces a similar γ_{w_x} field to the C-ULLT, albeit with a small disagreement in phase. However, where the streamwise vorticity is strongest near the wing tip this difference is very small. As stated, the S-ULLT does not model the γ_{w_y} in the outer domain, allowing the kernel to be obtained more easily. This spanwise component of wake vorticity is included in the inner solution, but only in the 2D sense - there is no 3D correction.

The streamwise component of vorticity in the assumed wake form of the P-ULLT is invariant with respect to downstream coordinate - it is pseudosteady. It matches the streamwise vorticity of the CFD very close to the wing, with the lack of variation introducing error downstream. Consequently it can still obtain reasonable results. This is especially true for long wake wavelengths when error is introduced further downstream, further away from the wing, and consequently has a reduced impact.

In this section, the variation in solution with respect to span was introduced. In the next section, the variation of the force coefficients with respect to span is considered.

Influence of ULLT kernel on spanwise lift distribution

Lifting-line theory provides not only a means to obtain more accurate predictions of forces on whole wings, but also the distribution of the forces with respect to span. In applications such as aeroelasticity where strip theory is often used, the distribution of the loads with respect to span are important. In this section these load distributions are therefore compared to the data obtained from CFD.

In previous sections it was found that the difference between strip theory and lifting-line theory lift and moment distributions varied considerably with respect to frequency. At low chord-reduced frequencies, all the ULLTs examined in this chapter converged on a single value much less than the force amplitude predicted by strip theory. At $k = 0.5$, the ULLTs disagreed due to differences in the wake models. And at high frequencies, the S-ULLT and C-ULLT tended towards strip theory. Likewise, the ULLTs have different distributions of forces due to their wake models.

To facilitate the comparison of ULLT and CFD results, the CFD simulations were processed to obtain lift and moment distributions at 8 equispaced time instances over an oscillation. A sine wave was fitted using a least-squares method to the distribution at every station measured across the span, allowing the method to account for both varying phase and amplitude with respect to span.

In this section the lift distributions will be examined for rectangular wings of Æ8, Æ4

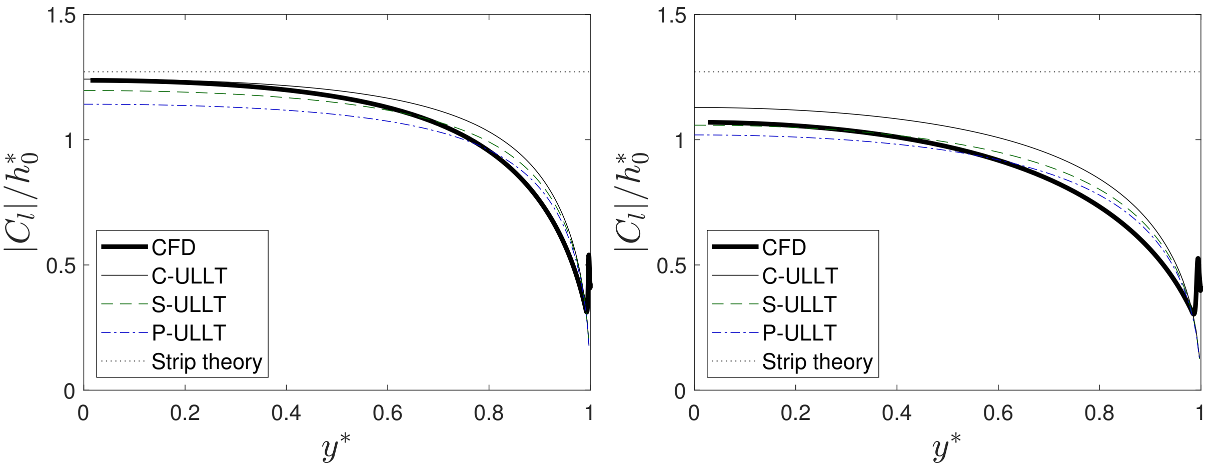

(a) Aspect ratio 8 (b) Aspect ratio 4

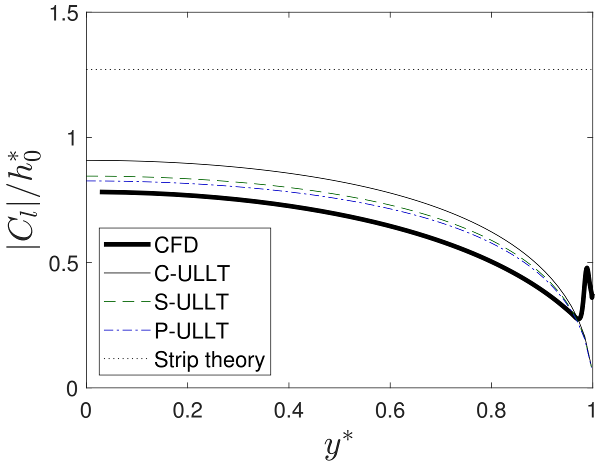

(c) Aspect ratio 2

Figure 2.7: Comparison of spanwise lift distribution from ULLTs, strip theory and Euler CFD data for wings oscillating in heave at $k = 0.125$.

and Æ2 oscillating in heave at three frequencies. Firstly, a low frequency of $k = 0.125$ - a non-zero frequency is used to differentiate the results of the ULLTs. Next, high frequency results at $k = 1.5$, where for the whole-wing forces the P-ULLT appeared to give the best results as the C-ULLT and S-ULLT tended to the strip theory solution. And finally, an intermediate frequency of $k = 0.5$. At this frequency, normalised lift-coefficients for the wings were lowest due to strong circulatory effects, and the effect of added mass had not yet to become dominant.

Low frequency behaviour

Figure 2.7 compares the lift amplitude distributions for the ULLTs, strip theory and the Euler CFD for rectangular wings oscillating in heave at $k = 0.125$.

The CFD results, shown in bold, show a mostly smooth distribution of lift, with the maximum value of $|C_l|$ found at the wing centre. This decreases smoothly away from the wing centre. The rate of decrease increases near the wing tip. At the very wing-tip, there is a spike in lift. This spike is of approximately the same width for all three aspect ratio wings, and is caused by flow separation at the sharp edges of the wing tip.

The ULLTs predict slightly different C_l curves due to the non-zero oscillating frequency and different wake models. The difference between ULLT results is small due to the low frequency. The C-ULLT predicts the most lift, followed by the S-ULLT then the P-ULLT. All the curves have very similar shapes since the interaction kernels lead to similar results at low frequencies. None of these curves are capable of predicting the wing-tip force spike.

Lifting-line theory would be expected to give the best results in the highest aspect ratio, Æ8 case. Here, the C-ULLT predicts the CFD result well at the wing centre, but error is introduced near the wing tip. As lower aspect ratios, the C-ULLT over-predicts the CFD wing-centre result. As a consequence, the S-ULLT at Æ4 and then the P-ULLT at Æ2 give the best predictions of wing centre-lift since they generally predict less lift than the C-ULLT. All of the ULLTs appear to give better results than strip theory.

High frequency behaviour

The predicted lift distribution from CFD, strip theory and ULLT for rectangular wings oscillating in heave at $k = 1.5$ is shown in Fig. 2.8.

According to literature on frequency-domain unsteady lifting-line theory [85, 92, 94], the ULLT solution should approach strip theory at high frequency. This is predicted by the C-ULLT and S-ULLT as expected (see Eq. 2.32). They match the C_l predicted by strip theory over most of the wing at Æ8 and Æ4. At aspect ratio 2, they exceed the strip theory result in the centre of the wing. At all aspect ratios, the tip effects are confined to a smaller area at the wing tip when compared to lower frequency results in Fig. 2.7. However, the C-ULLT and S-ULLT over-predict lift in comparison to CFD, and - as with whole-wing forces - the P-ULLT gives a better solution, especially at low aspect-ratio.

Intermediate frequency behaviour

Figure 2.9 shows the lift distribution for a wing oscillating at $k = 0.5$. It is in this intermediate frequency range where unsteady effects have the largest influence. At higher frequencies, added mass effects are dominant and at lower frequencies the steady solution is approached.

There is more differentiation between the different ULLTs than for the low frequency cases, but less than at high frequency. The C-ULLT and S-ULLT matches the shape

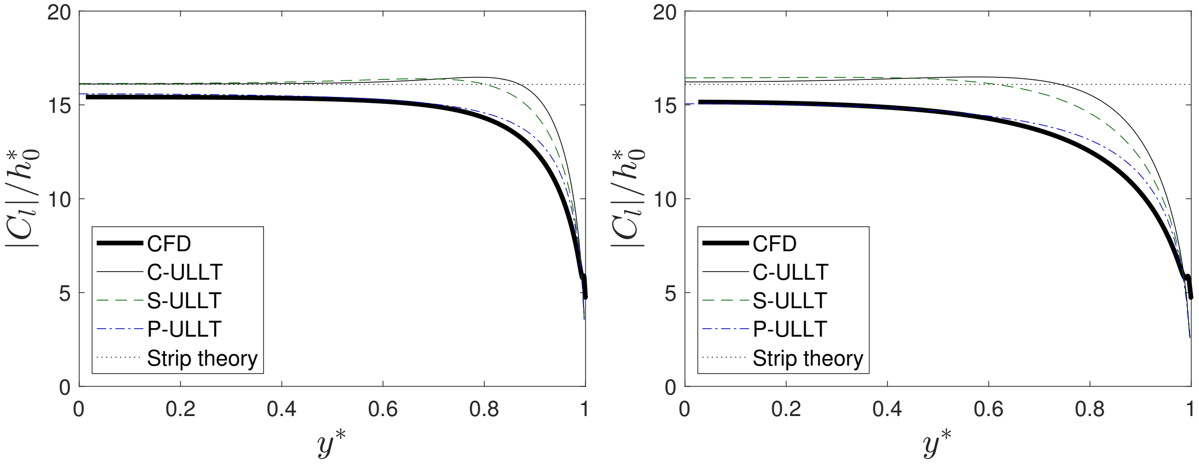

(a) Aspect ratio 8 (b) Aspect ratio 4

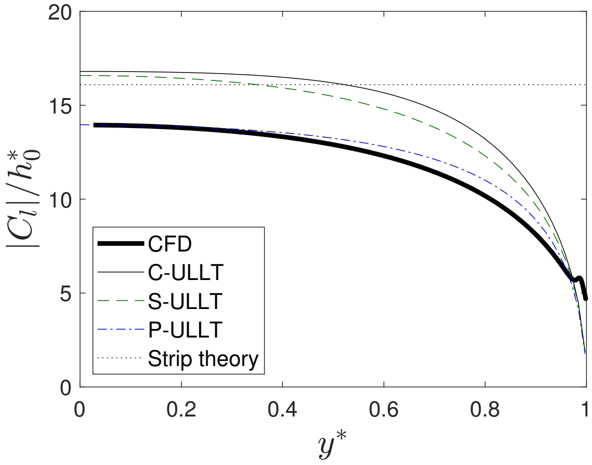

(c) Aspect ratio 2

Figure 2.8: Comparison of spanwise lift distribution from ULLTs, strip theory and Euler CFD data for wings oscillating in heave at $k = 1.5$.

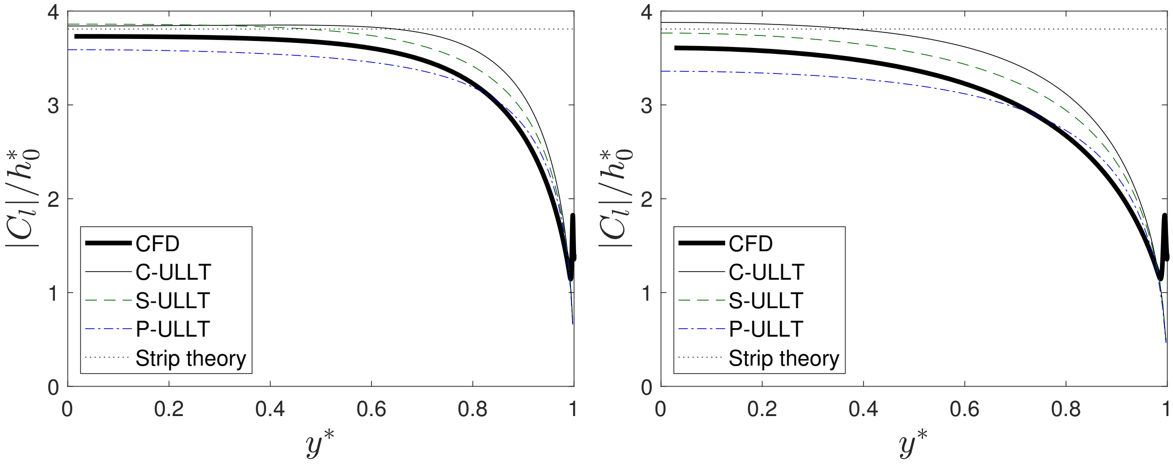

(a) Aspect ratio 8, $k = 0.5$ (b) Aspect ratio 4, $k = 0.5$

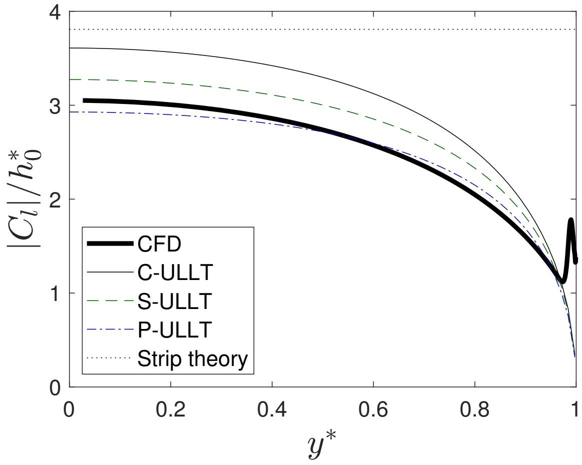

(c) Aspect ratio 2, $k = 0.5$

Figure 2.9: Comparison of spanwise lift distribution from ULLTs, strip theory and Euler CFD data for wings oscillating in heave at $k = 0.5$.

of the CFD at all aspect ratios. However, the lift amplitudes are overestimated, with overestimate increasing at low aspect ratios. The S-ULLT, which tends to predict lower values of lift than the C-ULLT, is the best predictor of the CFD result at aspect ratios 8 and 4, although it over-predicts the CFD result at Æ2.

Thus far the ULLTs have been compared to results obtained for Euler CFD. Euler CFD was designed to match the flow assumptions in the derivation of the ULLTs. However, inviscid, incompressible flow is non-physical. In the next section ULLT is compared to experimental flow to verify that it is applicable to real problems.

2.3.3 Validation with experimental data

The unsteady lifting-line theories and the Euler CFD used for comparison both assume inviscid, incompressible flow. However, such flow is non-physical. In this section, ULLT is validated against experimental data from NASA technical report 4632 [222] to confirm that ULLT remains useful for practical applications.

In the experiment, a rectangular wing of aspect ratio 10.1 undergoes pitch oscillation about the quarter chord. The wing is of span 60.62 inches and the chord is of 12 inches. The free stream velocity is $U_\infty = 100.58\,\mathrm{m\,s^{-1}}$ and angular frequency of oscillation is $\omega = 88.09\,\mathrm{rad\,s^{-1}}$, leading to a chord reduced frequency of $k = 0.133$, Reynolds number of 1.951×10^6 and Mach number of 0.288. The average angle of attack is 3.98° and the pitch amplitude is 4.35°.

At the chord reduced frequency $k = 0.133$ circulatory effects dominate. There is a difference between the C-ULLT, S-ULLT and P-ULLT, but it is small. Unsteady lifting-line theory will therefore be represented by the C-ULLT. ULLT assumes a boundary condition oscillating about zero. However, the theory is linear, making the addition of a constant non-zero contribution consistent. Here, Prandtl lifting-line theory [51, 76] is used since it is the low frequency limit of the C-ULLT. This LLT is also used to obtain an average lift for strip theory results. Figure 2.10 shows lift coefficient C_l against angle of attack for different points on the span on the wing.

Starting near the wing centre, Fig. 2.10(a) shows C_l against angle of attack at $y^* = 0.250$. The thick line shows the experimental result. The elliptic nature of the curve is due to a small phase difference between the lift and the angle of attack. Both strip theory and ULLT predict a smaller phase difference than observed, and also both over-predict the amplitude of the both the lift amplitude and average lift by a similar amount.

Figure 2.10(b) shows the results at $y^* = 0.475$. Here the amplitude and average lift obtained is similar to the more central $y^* = 0.250$ station, although the experimental C_l is more in phase with the kinematics. The overestimate of the ULLT and strip theory is smaller.

At $y^* = 0.800$, close to the tip of the wing, both the average value and amplitude of C_l

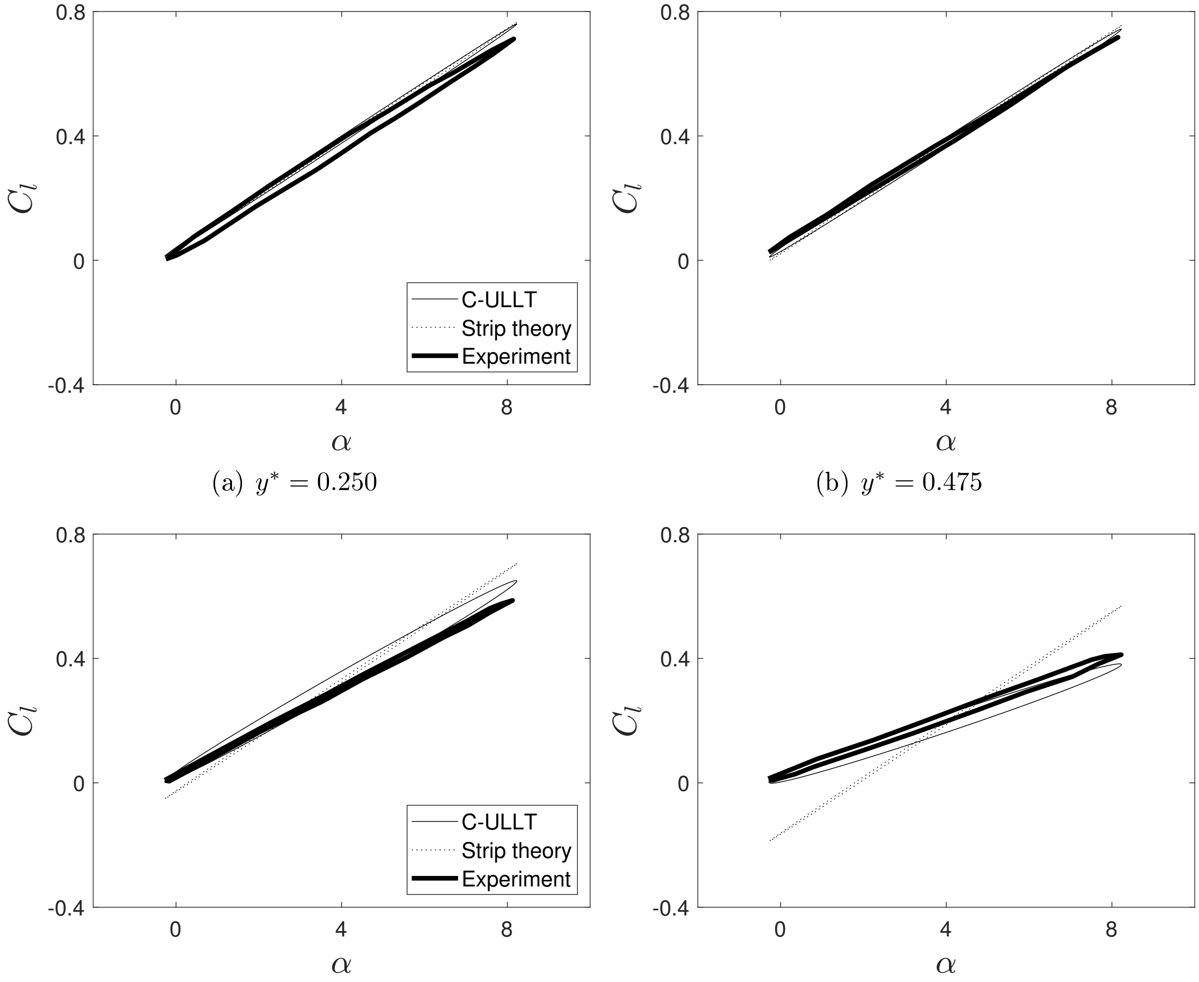

(a) $y^* = 0.250$

(b) $y^* = 0.475$

(c) $y^* = 0.800$

(d) $y^* = 0.966$

Figure 2.10: A comparison of the lift coefficient predicted by ULLT/LLT, strip theory and experiment at different spanwise locations.

are smaller. Figure 2.10(c) shows how in the experiment C_l and the kinematics are still in phase, with a larger phase difference predicted by the ULLT. The ULLT also slightly over-predicts the mean and amplitude values, but by a smaller margin than strip theory.

Finally, Fig. 2.10(d) show that in the experiment the lift amplitude and mean are now significantly reduced at $y^* = 0.966$. A phase difference has also developed. This is reflected in the ULLT results, but strip theory significantly overestimates amplitude.

2.4 Summary

This chapter has laid the groundwork for this dissertation. Unsteady lifting-line was introduced using a slightly modified version of Sclavounos's frequency-domain ULLT. Multiple wake models were introduced, including a new one based on only the streamwise vorticity in wake. The ULLTs were then compared to Euler CFD results for oscillating rectangular wings, for both lift and moment, and to visualise the assumed wake form. Finally, the Sclavounos based ULLT was applied to an experimental problem to verify its usefulness for high Reynolds number problems.

The frequency domain method introduced was based on the work of Sclavounos. It is based on potential flow, and assumes straight wings and small oscillations. It was modified slightly to allow for more general kinematics and to remove the requirement for an explicit added mass coefficient. Usefully, the ULLT results in an integro-differential equation similar to that of Prandtl. This allows different wake interaction kernels to be used.

Sclavounos suggests a complicated wake kernel that accounts for both spanwise and streamwise vorticity in the outer domain. Alternatively a pseudosteady Prandtl like kernel can be substituted, as it often is in *ad-hoc* ULLTs. In this chapter a new kernel is also introduced. This new kernel represents a wake model where only the oscillating streamwise component of vorticity is represented in the outer domain. This new ULLT is relevant because it avoids the challenge of including the spanwise vorticity in both inner and outer domain. A better understanding of this assumption is useful for those constructing numerically based ULLT where this duality can be challenging.

The C-ULLT was compared to Euler CFD results for a rectangular wing oscillating in pitch and heave. The use of a rectangular wing is particularly challenging for lifting-line theories, but represents real-world applications. The C-ULLT was found to work well for chord reduced frequencies of $k < 0.5$ and higher aspect ratios. At lower aspect ratios (eg. Æ2), unsteady lifting-line theory is less accurate, but still gives a far better result than strip theory. At higher frequencies, ULLT overestimates forces, perhaps due to the rectangular wing planform. However, it remains better or equivalent to strip theory.

Next, the different ULLT wake models and corresponding kernels were compared. The simplified, streamwise vorticity ULLT gave similar results to the Sclavounos based ULLT. The Prandtl-like pseudosteady ULLT gave an increasingly different prediction from the Sclavounos method as frequency increased. In ideal conditions, the most complex ULLT gave the best results. The other ULLTs typically predicted less lift. Consequently, for problems where ULLT is not so well suited, the simplified and pseudosteady ULLTs gave better results, although perhaps for the wrong reasons. All ULLTs gave better results than strip theory.

The assumed wake form of the different ULLTs were compared to that of the CFD. This demonstrated error in the ULLTs with respect to span. This was further investigated by examining lift distributions for different aspect ratio wings at three different heave oscillation frequencies. It could be seen that lift distribution changed with respect to oscillation frequency. As earlier, when the most complex Sclavounos based ULLT was applied to non-ideal problems, the simpler ULLTs often predicted the CFD results more accurately, again perhaps by luck. Universally ULLT remained superior to strip theory.

Finally, ULLT was applied to a high Reynolds number problem. It was found to provide good results compared to experimental data. This confirmed that the method was applicable to high Reynolds number flows.

This chapter has established the usefulness of ULLT in the Euler and high Reynolds number regime with small oscillations. However, many modern unsteady applications occur at low Reyonlds numbers with large oscillations. The applicability of frequency-domain ULLT is studied in the next chapter.

Chapter 3

Applying linearised inviscid ULLT to low-Reynolds-number, high-amplitude problems

3.1 Introduction

In the last chapter, the concept of analytical frequency-domain unsteady lifting-line theory was introduced and compared to CFD results in the Euler regime for small amplitude heave and pitch oscillation problems. Whilst these cases show that ULLT is useful for small-amplitude problems such as flutter at high Reynolds numbers, whether ULLT is useful for low-Reynolds-number, large-amplitude applications remains uncertain. It is in this regime that some of the motivations of this thesis lie, including high-altitude long-endurance aircraft, micro air vehicles and energy harvesting devices.

In this chapter, small-amplitude inviscid frequency-domain unsteady lifting-line theory is applied to small and large amplitude problems in the Reynolds number 1×10^4 regime. Large-amplitude kinematics results in leading-edge vortex structures that are not modelled by the ULLT and lead to uncertainty over loads and load distributions on the wings.

The outline of this chapter is therefore as follows. First, referring back the introduction of ULLT in Chapter 2 Sec. 2.2, a method to predict leading-edge vortex formation based on the unsteady lifting-line theory framework is suggested in Sec. 3.2. Next, the cases investigated in this chapter are outlined in Sec. 3.3. Whole-wing forces are presented in Sec. 3.4, along with the ULLT prediction of separation. For the large amplitude cases, the leading-edge vortex has a significant impact. The form of this LEV at the wing centre is examined in Sec. 3.5. Variation of wing loads with respect to span, and the relation of the loads to the leading-edge vortex structure and its variation over the wing is studied in Sec. 3.6. Finally, the chapter is summarised in Sec. 3.7.

3.2 LESP in unsteady lifting-line theory

This chapter uses the modified version of Sclavounos's frequency-domain ULLT, dubbed the C-ULLT, presented in Sec. 2.2. Sclavounos's interaction kernel, K_C is used, and no modifications are made to the method to account for the low Reynolds number conditions. This model was found to be useful for rectangular wings oscillating in inviscid incompressible flow. Whilst it worked best at higher aspect ratios and lower frequencies, the method always produced better results than strip theory where the problem is solved by applying 2D solutions to strips on the wing and summing their results. It does this by correcting 2D inner solutions to account for 3D effects.

The 2D inner solutions are corrected by a uniform downwash, leading to Eq. 2.18:

$$\phi(x, y, z; t) = \phi^{2D}_{h/\alpha} + F(y)(i\omega z e^{i\omega t} - \phi^{2D}_{hn}).$$

This allows the bound circulation distributions and wing load distributions to be found, and can also be applied to the Leading-Edge Suction Parameter (LESP) of Ramesh *et al.* [145].

The idea of the LESP criterion is recent [145]. It is used as a criterion by which leading-edge vortex shedding can be included within discrete vortex enhanced thin-aerofoil theories without having to model viscosity.

Suction is required for the flow to remain attached as it passes round the leading edge of an aerofoil. In thin aerofoil theory, this suction is measured by the leading-edge suction parameter. As detailed in Appendix B, thin aerofoil theory typically assumes a distribution of either vorticity

$$\gamma(x, y; t) = 2U_\infty \left[A_0(y; t) \frac{1 + \cos\theta}{\sin\theta} + \sum_{n=1}^{\infty} A_n(y; t) \sin(n\theta) \right]$$

in the case of Ramesh *et al.* (Eq. B.1) or pressure jump

$$\Delta C_p(x, y; t) = \left[4B_0(y) \tan\left(\frac{\theta_{ks}}{2}\right) + 8 \sum_{1}^{\infty} B_n(y) \sin(n\theta_{ks}) \right] e^{i\omega t}$$

in the case of Küssner and Schwarz (Eq. B.15).

In either case, there is a singularity at the leading edge which keeps flow attached. Physically this singularity represents the projection of the low pressure on the rounded leading edge only a the flat plate geometry used by unsteady thin aerofoil theory. For the 2D problem, the LESP, $\mathcal{L}^{2D}(t)$ can be directly related to these singular terms as

$$\mathcal{L}^{2D}(y; t) = A_0(y; t) = B_0(y) e^{i\omega t}. \tag{3.1}$$

Ramesh *et al.* [145] found that leading-edge separation occurred when a geometry and Reynolds number specific value of LESP was reached. The aerofoil can only support a maximum value of LESP, referred to as the critical value $\mathcal{L}_{crit}$. Above this, leading-edge vortex shedding occurred. This value is largely independent of particular kinematics (recent studies have shown a mild dependence on pitch rate [146]). Once $\mathcal{L}_{crit}$ has been empirically determined, typically using CFD, it can be applied to any problem's kinematics.

In this chapter, only wings undergoing rigid heave in accordance with the kinematics defined by Eq. 2.7 are considered. For such heaving kinematics this gives

$$\mathcal{L}_h^{2D}(y;t) = -2ikh_0^*(y)C(k)e^{i\omega t}. \tag{3.2}$$

This can be applied to 3D problems. For finite wings, Hirato *et al.* [172] found that the LESP was still useful for predicting LEV formation. The LESP criterion could be applied to 2D sections along the wing successfully. Here, we apply the LESP criterion by integrating it into lifting-line theory in the same way as was done for bound circulation, lift coefficient and moment coefficient.

The LESP criterion can be corrected for 3D effects following Eq. 2.18 (repeated above) as

$$\mathcal{L}(y;t) = \mathcal{L}^{2D}(y;t) - F(y)\mathcal{L}_{hn}^{2D}(y;t) \tag{3.3}$$

where $\mathcal{L}_{hn}^{2D}$ is the value of LESP for an aerofoil oscillating with unit amplitude. When this value of the LESP exceeds the critical value $|\mathcal{L}(y;t)| > \mathcal{L}_{crit}$ at any point on the span, the assumption of no LEV shedding made in the derivation of the ULLT is violated.

The formation of LEVs during large-amplitude oscillations is not the only phenomenon expected to violate the assumptions of ULLT in this chapter. The large amplitudes themselves violate the assumption that the wake is planar and that the boundary conditions representing the wing can be applied on the plane. Broken assumptions carried over from Chapter 2 include the use of rectangular and low aspect ratio wings.

3.3 Case choice

Previously, in Sec. 2.3.1, ULLT was compared against Euler CFD for small amplitude pitch and plunge kinematics. Here, ULLT is examined in the low Reynolds number Re=10 000 regime, with large amplitude oscillation.

Once again, rectangular wings are used. For leading-edge vortex formation, the geometry of the wing is important. Here, a NACA0008 aerofoil is used and the wing has squared off tips. Aspect ratios 6, 3 and 1, and the 2D case are studied. Lowering the aspect ratio used in comparison to Euler cases studied in Chapter 2 has several benefits.

Table 3.1: Case parameters

Parameter	Values
k	0.4
$\mathcal{R}$	1, 3, 6, ∞
h_0^*	0.05, 0.5, 1

Firstly, the low aspect ratios better reflect those found in applications such as micro air vehicles and insects - applications where LEV formation is important. Secondly, it reduces the computational cost of the CFD. And thirdly, it aided experimental design.

The low Reynolds number CFD used throughout this dissertation was validated against the experimental work of Shūji Ōtomo and Ignazio Maria Viola of the University of Edinburgh [2, 5, 6]. Details of the validation and the CFD are given in Appendix C.2. In the experimental design compromise had to be made in choosing the wing span in comparison to the total width of the water flume used, resulting in the use of an aspect ratio 3 wing. The NACA0008 was chosen to provide sufficient thickness for the experimental model. The experiment was also limited to heave oscillation. This chapter therefore focuses on heave kinematics.

As detailed in Appendix C.2, the CFD solved the Reynolds-Averaged Navier-Stokes (RANS) equations. Alternative methods, most notably Large Eddy Simulation (LES), are possible. However, RANS was selected because the additional fidelity of such alternatives can be wasted. As noted by Visbal [156], small perturbations in the inflow of the experimental setup require multiple phase averaged results. Recreating this in LES CFD is prohibitively expensive in terms of computational resources. Given that the CFD is being used as a reference for a comparatively simple, low-order method, RANS is sufficient.

Heave oscillations are used. The wing oscillates with a chord reduced frequency $k = 0.4$. In Chapter 2, it was found that at this chord reduced frequency unsteady vortical effects are important, significantly reducing the lift of a wing. This value of chord reduced frequency is not yet sufficiently high as to lead to the wing forces to be dominated by added-mass effects. The value of k chosen is anticipated to be challenging for unsteady lifting-line theory since wake interaction is strong.

Three oscillation amplitudes are examined. Firstly, the small amplitude of $h_0^* = 0.05$, where the wake is still approximately planar. Secondly, $h_0^* = 0.5$. Here, the wake is no longer planar, and LEV formation occurs. However, the LEVs remain close to the wing surface. Finally, large-amplitude $h_0^* = 1.0$ cases. Large LEVs form and separate from the wing surface. The case parameters used in this chapter are summarised in Table 3.1.

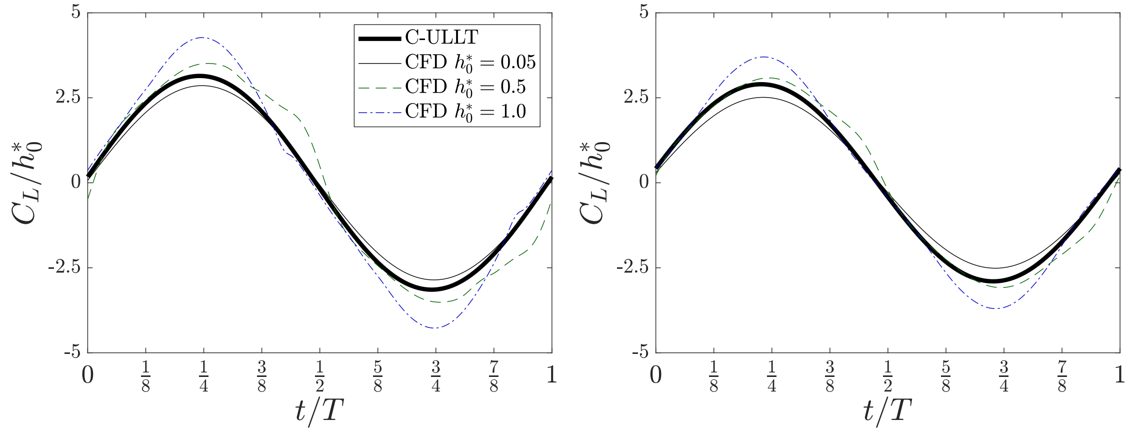

(a) 2D

(b) Aspect ratio 6

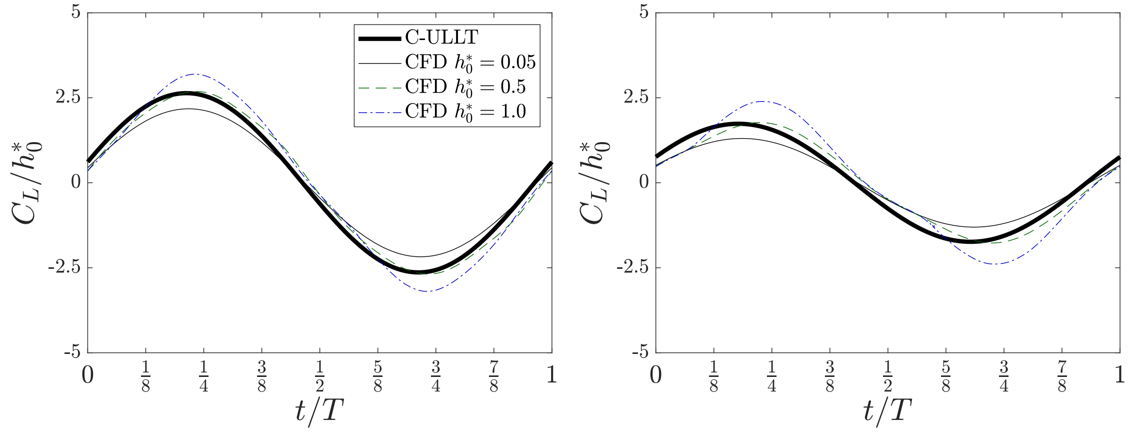

(c) Aspect ratio 3

(d) Aspect ratio 1

Figure 3.1: Comparison of the predicted lift coefficients of C-ULLT and CFD for rectangular wings oscillating in heave at various amplitudes and aspect ratios at $k = 0.4$ and Re $= 10\,000$.

3.4 Lift and moment coefficient comparison

Whole-wing forces are examined in this section before the vortex structure is examined in Sec. 3.5 and the load distribution is studied in Sec. 3.6. The whole-wing lift coefficients are shown in Fig. 3.1. The lift coefficient is normalized by oscillation amplitude. This allows the different amplitudes to be effectively compared to linear C-ULLT, highlighting the effects of aerodynamic non-linearity. Different aspect ratios are shown in different subfigures.

The 2D problem is shown first in Fig. 3.1(a). This is equivalent to a rectangular wing of infinite aspect ratio. The thick line shows the C_L/h_0^* curve of the C-ULLT (equivalent to Theodorsen for Æ$= \infty$), which is identical for all three of the amplitudes. The thinner lines of the CFD show how aerodynamic non-linearities lead to non-linear C_L scaling, and different C_L waveforms. The low amplitude $h_0^* = 0.05$ waveform is sinusoidal. Apart from the low Reynolds number, there are no additional complications beyond those of the Euler

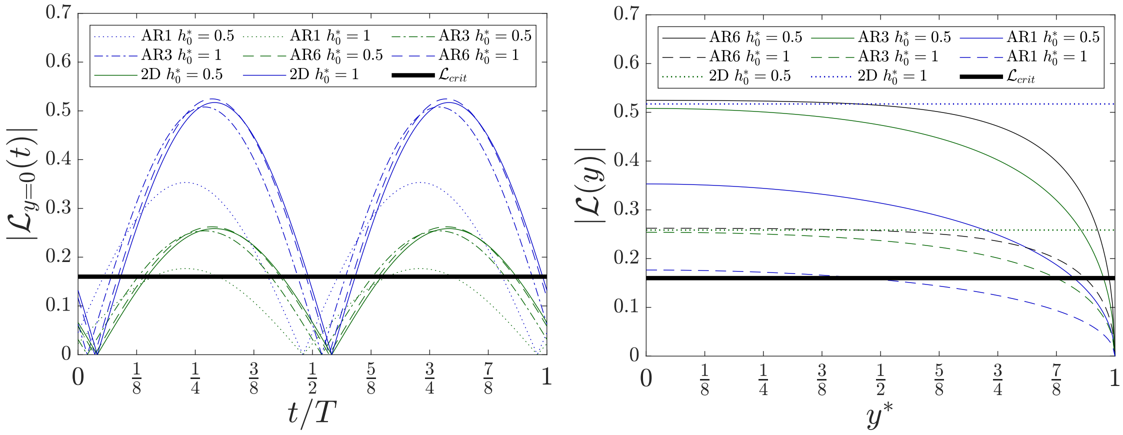

(a) LESP against time at wing centre (b) LESP amplitude spanwise distribution

Figure 3.2: Comparison of the predicted leading edge suction parameter of C-ULLT for rectangular wings oscillating in heave at various amplitudes and aspect ratios at $k = 0.4$ and Re $= 10\,000$.

cases in Chapter 2. As oscillation amplitude increases, the peak value of C_L increases super-linearly and the shape of the curve is no longer sinusoidal. At the intermediate amplitude $h_0^* = 0.5$, a leading-edge vortex forms, but it forms later than for the largest amplitude case $h_0^* = 1$. This LEV is visualised and described in Sec. 3.5. The LEV is slower to pinch off from the aerofoil meaning that the resulting lift enhancement comes later in the curve for $h_0^* = 0.5$ than for $h_0^* = 1$. This is visible in the humped shape of the $h_0^* = 0.5$ curve.

Equation 3.3 can be used to predict the value of LESP with respect to span using ULLT. The value of LESP predicted by the C-ULLT and unsteady thin aerofoil theory is shown in Fig. 3.2. The values of LESP for the $h_0^* = 0.05$ cases are not plotted since they are small and do not approach the critical value of LESP at which shedding occurs.

Fig. 3.2(a) shows the leading-edge suction parameter at the wing centre where, according to the C-ULLT for rigid-heaving rectangular wings, it is highest. Also shown is an empirically obtained critical value of LESP, $\mathcal{L}_{crit} = 0.16$. The method of Ramesh *et al.* [145] was applied to an oscillating aerofoil in 2D. The phase of the oscillation when leading-edge criticality occurred was applied to Theodorsen's method to find $\mathcal{L}_{crit}$.

Whilst a relationship can be found between the LESP against time plot shown in Fig. 3.2(a) and the C_L plot in Fig. 3.1(a), it is easy to be misled. Leading-edge vortex structures affect the flow around the aerofoil once they have formed. Neither the C-ULLT nor unsteady thin aerofoil theory model the vortex structure, and so they are are unable to account for this. This vortex structure impacts the forces on the wing even after it has been shed, so the C-ULLT and unsteady thin aerofoil have their assumptions broken for the entire oscillation, rather than just the time at which the LEV is being shed. Consequently, for evaluating validity it is better to focus on the peak value of LESP over an oscillation.

Peak LESP with respect to span is shown in Fig. 3.2(b). This also shows the extent to which $\mathcal{L}_{crit}$ is exceeded (which is related to the strength of the LEV), and that LESP varies with respect to span.

The C-ULLT was equivalent to unsteady thin aerofoil for the 2D Æ∞ problem. It can predict C_L well at small amplitudes ($h_0^* = 0.05$), albeit with a small overestimate of peak lift. At the larger amplitudes $h_0^* = 0.5$ and $h_0^* = 1$ the assumed sinusoidal C_L waveform introduces error compared to the CFD result. Additionally, it under-predicts the peak lift. However, despite the large LEVs found in the flow field for these large amplitude cases, the accuracy of the C-ULLT / Theodorsen result may still be sufficient for some applications. These results follow the conclusions of McGowan *et al.* [120].

Having examined the 2D, infinite aspect ratio case, finite-wing cases can be studied. The effects of reducing aspect ratio and increasing the importance of 3D effects are shown in Fig. 3.1(b), Fig. 3.1(c) and Fig. 3.1(d), corresponding to results for rectangular aspect ratio 6, 3 and 1 wings respectively.

The observations made in Chapter 2 for rectangular wings oscillating at small amplitude in the Euler regime are repeated here: the $h_0^* = 0.05$ CFD shows that lower aspect ratio leads to reduced lift. This trend is predicted by the C-ULLT, although as with the Euler results, it increasingly over-predicts the lift as aspect ratio reduces. For low Reynolds numbers and small amplitude problems, the advantage of ULLT over strip theory continues to be clear.

This chapter introduces larger oscillations. Like the 2D case, a super-linear increase in C_L with respect to oscillation amplitude is found, and the LEV leads to a non-sinusoidal waveform that cannot be modelled by the C-ULLT.

Examining the results of the Sclavounos-based ULLT in more detail for $h_0^* = 0.05$, it can be observed that it predicts the phase and amplitude of the C_L result well at aspect ratio 6. In Chapter 2, it was found that the 2D result and the 3D result became increasingly similar with respect to increasing chord reduced frequency until the impact of error in the added mass prediction due to rectangular planform became important at higher frequencies. Consequently, at $k = 0.4$, the C_L for the aspect ratio 6 wing is similar to that of the 2D problem. As aspect ratio decreases from Æ6 to Æ3 to Æ1, the C-ULLT prediction is in line with the results of Chapter 2. The amplitude of C_L is over-predicted, but the sinusoidal waveform prediction and phase prediction remains good. The predicted values of LESP also decrease with aspect ratio. This occurs for the same reason as the reduction in lift - the downwash due to three-dimensional effects reduces the wing loading.

As in the 2D case, increasing amplitude brings aerodynamic non-linearity, super-linear increases in lift and non-sinusoidal lift waveforms in the CFD results. The C-ULLT cannot predict these. However, the super-linear increase in lift decreases the C-ULLT's lift over-prediction for the $h_0^* = 0.05$ case. The 3D nature of the problem also appears to reduce the

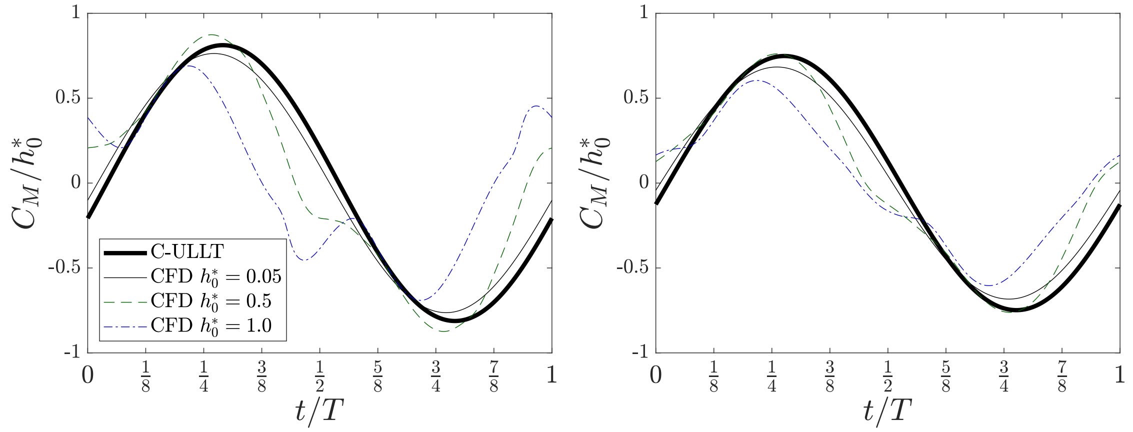

(a) 2D

(b) Aspect ratio 6

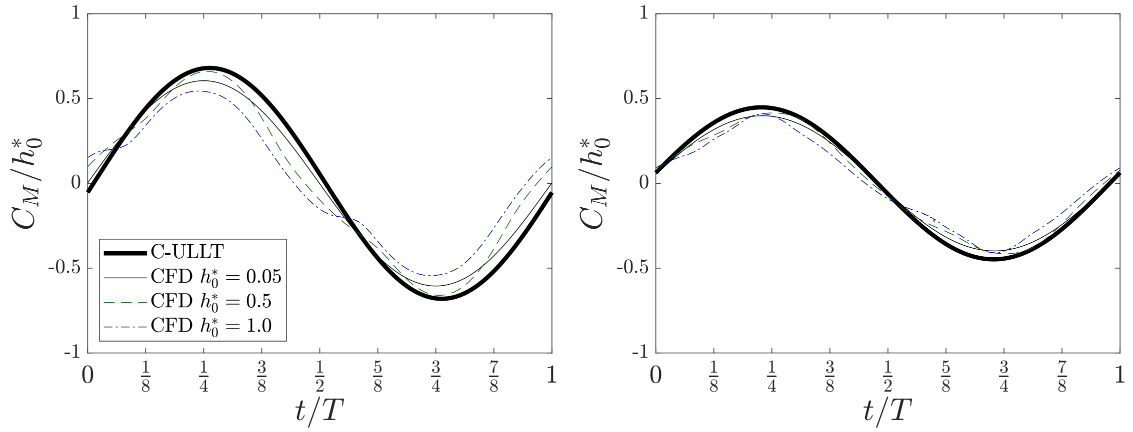

(c) Aspect ratio 3

(d) Aspect ratio 1

Figure 3.3: Comparison of the predicted mid-chord moment coefficients of C-ULLT and Re = 10 000 CFD for rectangular wings oscillating in heave at various amplitudes and aspect ratios at $k = 0.4$.

impact of aerodynamic non-linearity. As aspect ratio decreases, the C_L curves predicted by the CFD become smoother. Consequently, the C-ULLT provides a better prediction of the CFD case as Æ decreases.

Having examined the lift coefficient, the moment coefficient is examined in Fig. 3.3.

As with C_L, the 2D C_M cases shown in Fig. 3.3(a) are examined first. The low amplitude case has a sinusoidal C_M curve. As oscillation amplitude increases, the LEVs form, resulting in a non-sinusoidal curve. For the $h_0^* = 0.5$ case, the curve is initially similar to the $h_0^* = 0.05$ case, at $t/T = 1/8$, before LEV formation leads the C_M to initially increase and then drop. The C_M then briefly returns to matching the sinusoidal result before the LEV forms again in the second half of the cycle. For the even larger $h_0^* = 1$ case, the LEV forms earlier, and the subsequent loss of moment coefficient is larger.

Figure 3.3(b), Fig. 3.3(c) and Fig. 3.3(d) show the results for the aspect ratio 6, 3 and 1 wings. For the small-amplitude $h_0^* = 0.05$ the expected trend of reduced aspect ratio leading to reduced forces is present. For the large-amplitude cases, the most noticeable effect is that the increase and subsequent reduction in C_M during leading-edge vortex formation and shedding is significantly diminished as aspect ratio reduces. Finite wing effects appear to be important, even at aspect ratio 6 which produced similar results to the 2D case for C_L.

Based on the Euler results in Chapter 2, it would be expected that the C-ULLT would predict the C_M curve best for the higher aspect ratio wings for the low-amplitude $h_0^* = 0.05$ cases. For the Re$=1 \times 10^4$ results in the chapter, the accuracy of the C-ULLT is similar for all of the aspect ratios studied, over-predicting the moment amplitude slightly. At high aspect ratio there is also a small phase misprediction.

For the larger amplitude $h_0^* = 0.5$ and $h_0^* = 1$ cases, the C-ULLT provides a better prediction of the CFD at low aspect ratio where the LEV has the smallest impact. As the disturbance caused by the LEV in the CFD result gets bigger at higher aspect ratio, the amplitude and phase remain approximately correct, but the assumption of sinusoidal results is poor.

For the prediction of whole-wing forces at low Reynolds number, the C-ULLT remains useful. For small amplitudes, its utility is similar to that found in Chapter 2 for Euler regime cases. At larger amplitudes, the C-ULLT cannot model the leading-edge vortex formation or the non-planar wake. These aerodynamic non-linearities lead to non-linear change in lift and moment with respect to amplitude and non-sinusoidal C_L and C_M waveforms. The LESP criterion roughly predicts these aerodynamic non-linearities. For finite-wing problems, the deviations from the sinusoidal results due to LEVs reduces as aspect ratio reduces. Consequently, the C-ULLT still provides a good prediction.

The leading-edge vortex is critical in the non-linearity of the amplitude of C_L and C_M with respect to oscillation amplitude and the non-sinusoidal results at larger oscillation amplitudes. The form of the LEV found in the CFD results will be examined more closely in the next section.

3.5 Wing centre vorticity distribution

The leading-edge vortex leads to the non-sinusoidal C_L and C_M responses for a oscillating wing. In this section, the LEV structure at the wing centre is examined.

Figure 3.4 shows the CFD results for the non-dimensional spanwise vorticity $\omega^* = \omega_y \bar{c}/U_\infty$ at the centre of the oscillating rectangular wing where the LEV is most prominent. Results are shown for the cases with amplitude $h_0^* = 0.5$ and $h_0^* = 1$. The $h_0^* = 0.05$ is not shown because, as predicted by the LESP criterion, it does not lead to LEV formation. The instances in time show critical points on the downstroke of the wing.

The results for the 2D case are similar to that of the aspect ratio 6 cases for both amplitudes. For the intermediate amplitude $h_0^* = 0.5$ case at $t/T = 1/16$ and $t/T = 1/8$,

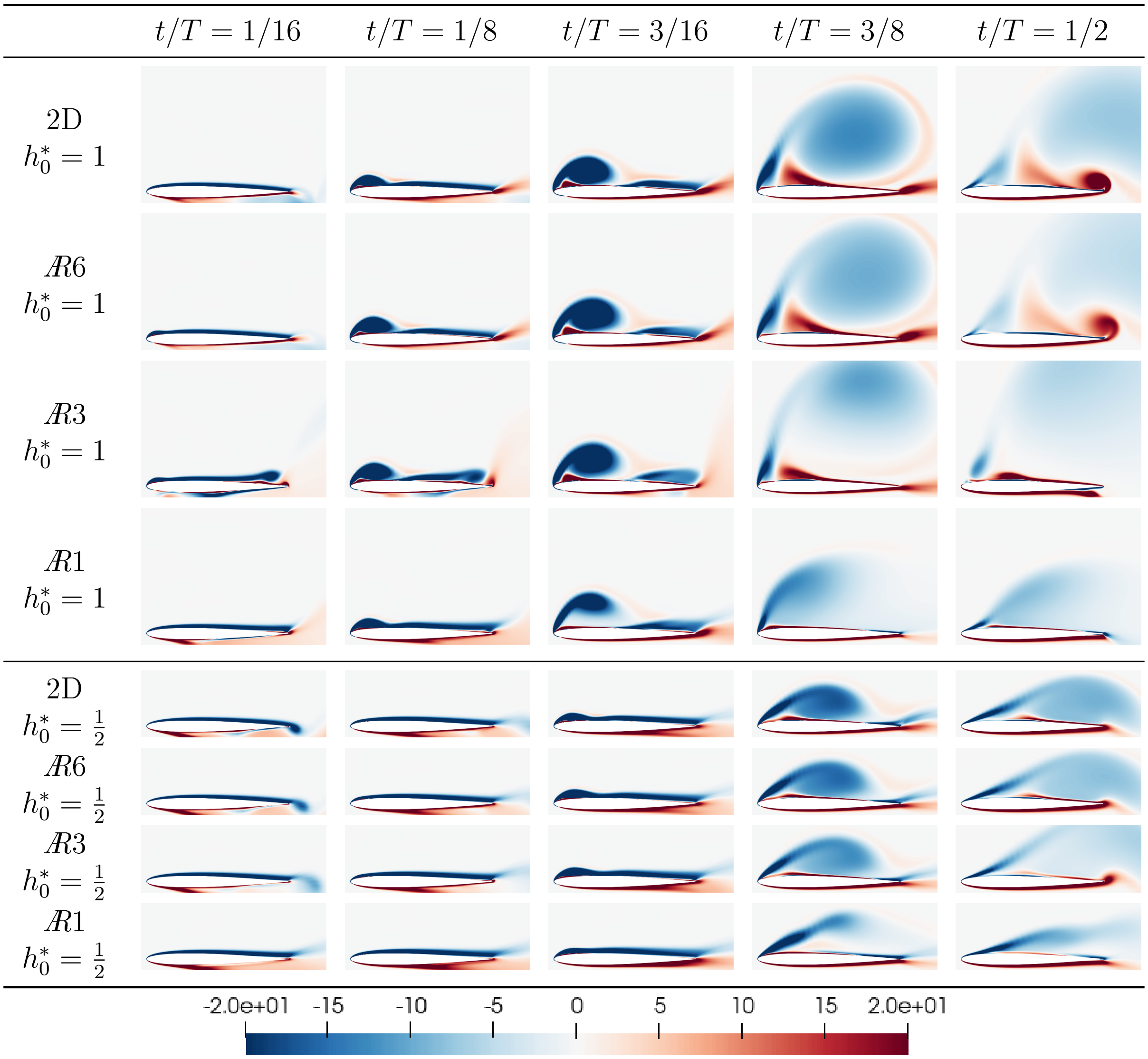

Figure 3.4: CFD results for wing centre spanwise vorticity distributions for rectangular wings oscillating in heave at $k = 0.4$ and $\mathrm{Re} = 10\,000$. The in plane vorticity is normalised as $\omega^* = \omega_y \bar{c}/U_\infty$

the boundary layer on the wing's upper surface is initially attached as the wing accelerates downwards as prescribed by the $h = h_0 \cos(\omega t)$ kinematics. The velocity of the wing is $v_z = -\omega h_0 \sin(\omega t)$. Consequently, the heave velocity increases as $t/T = 3/16$ is approached. At this velocity, the rounded profile of the wing's leading edge can no longer support the suction required to keep flow attached, and leading-edge vortex formation begins. The downstroke continues to $t/T = 3/8$, when the heave velocity is reducing. The vortex structure that has formed remains close to the aerofoil surface. The main vortex and its feeding shear layer have become prominent vortical features. The downstroke has finished at $t/T = 1/2$, ready for the upstroke (which is symmetrical to the downstroke) to begin. The vortex structure has been convected over the trailing edge and has diffused due to viscous effects. The shear layer remains attached to the leading edge and will reattach as the upstroke begins.

For the higher amplitude $h_0^* = 1$ the separation process begins earlier due to the doubling of the plunge velocity. By the time $t/T = 1/8$ the plunge velocity is already larger than at $t/T = 3/16$ in the $h_0^* = 0.5$ case, and an LEV has already formed. This LEV grows quickly, and by $t/T = 3/16$ has drawn a counter-rotating region of vorticity underneath the main vortex. Three quarters of the way through the downstroke the LEV structure has separated from the wing surface and is consequently further downstream. By the end of the downstroke at $t/T = 1/2$ the LEV has completely separated from the wing surface, and due to its size, has induced a counter vortex at the wing's trailing edge.

As the aspect ratio of the wing decreases, the leading-edge vortex in increasingly subject to 3D effects. These 3D effects weaken the LEV, keep it attached to the wing for longer and cause it to dissipate more. This in turn reduces the volatility of the forces on the wing. This is best exemplified by the aspect ratio 1, $h_0^* = 1$ result. Low aspect ratio wings also have smaller areas were the LESP is high. Figure 3.2(b) shows how the value of LESP is constant across much of the wing at aspect ratio 6, but less of the wing at aspect ratio 1. Smaller LEVs across much of the span for low aspect ratio cases results in smaller LEV induced forces.

The spanwise distribution of lift, moment and the 3D vortex structures will be examined more in the next section (Sec. 3.6).

3.6 Spanwise force distributions

In Chapter 2 (Sec. 2.3.2), the C-ULLT was able to predict force distributions with respect to span with useable accuracy compared to small-amplitude Euler CFD for cases similar to those used here. In this chapter, the C-ULLT once again is used to predict force distributions, except in the low Reynolds number regime and with large amplitude oscillation leading to leading-edge vortex structures. Figure 3.5 shows the lift and moment distribu-

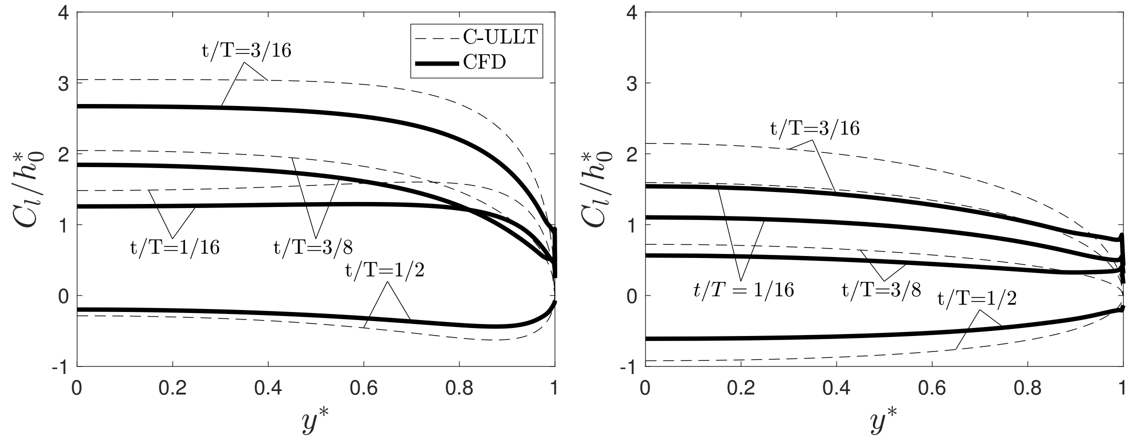

(a) Aspect ratio 6 C_l

(b) Aspect ratio 1 C_l

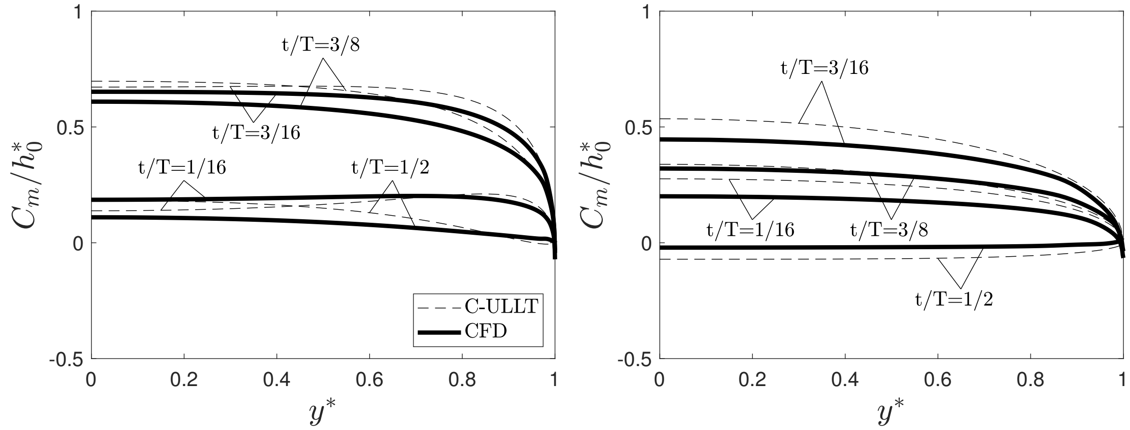

(c) Aspect ratio 6 C_m

(d) Aspect ratio 1 C_m

Figure 3.5: Comparison of the predicted lift and moment distributions of C-ULLT and CFD for rectangular wings oscillating in heave with amplitude $h_0^* = 0.05$ at $k = 0.4$ and $\mathrm{Re} = 10\,000$. Moments are taken about the mid-chord.

tions on rectangular wings of aspect ratio 6 and 1 oscillating at the small amplitude of $h_0^* = 0.05$.

The distributions of C_l and C_m are smooth for both aspect ratios. Compared to the inviscid results of Chapter 2 (Fig. 2.7), there is no spike in forces at the wing tip, although the Æ1 C_l distribution is not entirely smooth at $t/T = 3/16$. This is because the flow around the wing tip is less prone to separation at the sharp edge in the low Reynolds number regime. The overestimate of whole wing forces found in Sec. 3.4 is also present. For the aspect ratio 6 case, the C-ULLT predicts the shape of the C_l curves very well. The lift coefficient only varies significantly with respect to span very close to the wing tip, suggesting the flow is approximately 2D over most of the wing. At aspect ratio 1, the C-ULLT is expected to be less effective. This is indeed the case, with the difference in lift amplitude being particularly noticeable. The prediction of moment coefficient distribution is good at both aspect ratios, although the C-ULLT over-predicts the amplitude in comparison to the CFD results. The C-ULLT still remains useful as a tool for predicting C_l distribution at low Reynolds number and low amplitudes.

The large amplitude cases involving leading-edge vortex shedding are more challenging. Whilst the C-ULLT predicted whole-wing forces obtained from CFD well in Sec. 3.4, it cannot account for variation in the LEV with respect to span. The force distributions and Q-criterion iso-surface for the large amplitude $h_0^* = 1$ case are shown in Fig. 3.6. The Q-criterion is a means by which the vortical structure of a flow can be visualised, and is defined as $Q = \frac{1}{2}\left(\mathrm{tr}(\overline{D})^2 - \mathrm{tr}(\overline{D}^2)\right)$ where $\overline{D_{ij}} = \partial \boldsymbol{u}_i / \partial \boldsymbol{x}_j$, and here the value of $Q = 1$ is used for the iso-surface. The CFD Q-criterion and force distributions are shown at times $t/T = \{1/16, 1/8, 3/8, 1/2\}$ which correspond to the growth of the LEV as shown in Fig. 3.4.

For the aspect ratio 1 case at $h_0^* = 1$, the shape of the lift distribution is different to that of the $h_0^* = 0.05$ case. This is due to the shedding of leading-edge and tip vortices. LEV shedding is predicted by the LESP criterion obtained via the C-ULLT, but due to the pseudo-3D nature of lifting-line theory it cannot predict wing-tip vortex structures. The highest lift is found near the wing tip. The high loads are persistent, remaining even when the lift at the wing centre has reduced at $t/T = 3/8$, three quarters of the way through the downstroke. The C-ULLT fails to predict this, and the strong spanwise flow near to the wing tips is not modelled in the 2D inner solutions. The moment distribution near the tip is less smooth than suggested by the C-ULLT, but ultimately similar. Near the centre of the wing, the C_l and C_m found in the CFD results are similar to that predicted by the C-ULLT.

The prediction of load distribution by the C-ULLT is equally poor in the higher aspect ratio Æ6 case, despite the effects of the wing tip becoming less important. The wing loads can be correlated with the formation of the leading edge vortex structure visualised by the Q-criterion. At $t/T = 1/16$, just after the beginning of the downstroke, the C_l and C_m curves are still distorted by the vortex structure produced on the preceding upstroke. The vortex structures due to the downstroke first form at $t/T = 1/8$, visible on the leading edge and the wing tip. The LEV is small and attached, and only has a small impact on the lift and moment distribution, so, compared to the CFD, the predictions of C_l and C_m are reasonably good near the centre of the wing at $t/T = 1/8$. There is a spike forming near the wing tip due to the nascent tip vortex. By $t/T = 3/8$ a large LEV arch vortical structure has formed, visualised by the Q-criterion. The leg of the arch attaches to the wing surface at approximately $y^* \approx 3/4$, and is then attached to the wing corner by a conical vortex structure on the wing surface. In the C_l and C_m results, the lift and moment changes rapidly with respect to span where this vortex arch leg meets the wing surface. Outside the arch, lift is increased. Inside, it decreases. At time $t/T = 1/2$, this LEV vortex arch structure has been convected along the wing surface, and the arch legs have moved closer together. The position of the arch legs is reflected in the C_l and C_m

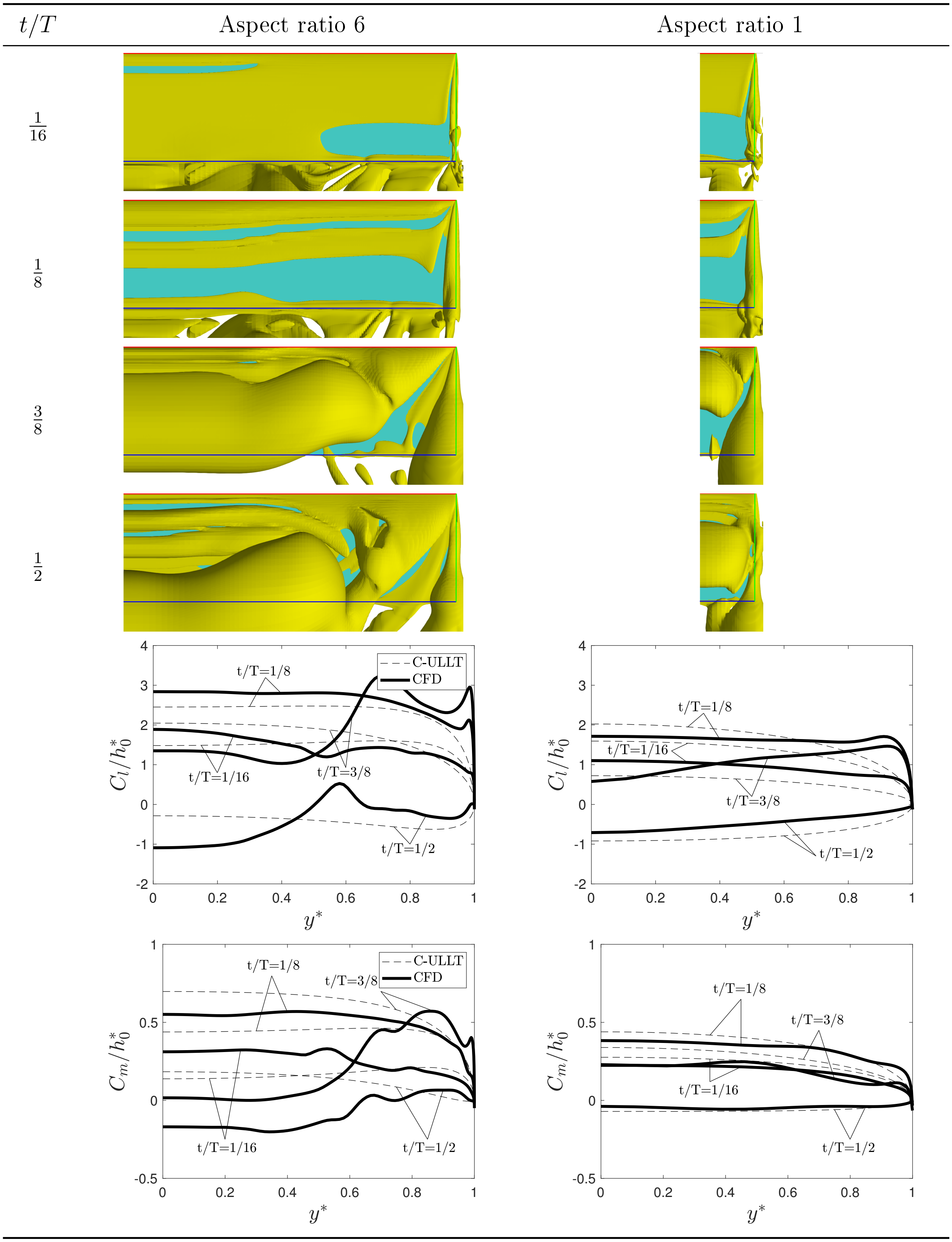

Figure 3.6: Lift distributions, moment distributions and CFD result Q-criterion isosurfaces ($Q = 1$) for a wing oscillating in heave with amplitude $h_0^* = 1$ at $k = 0.4$ and Re = 10 000. Moments are taken about the mid-chord. The leading-edge is marked in red, the trailing-edge in blue and the wing tip in green.

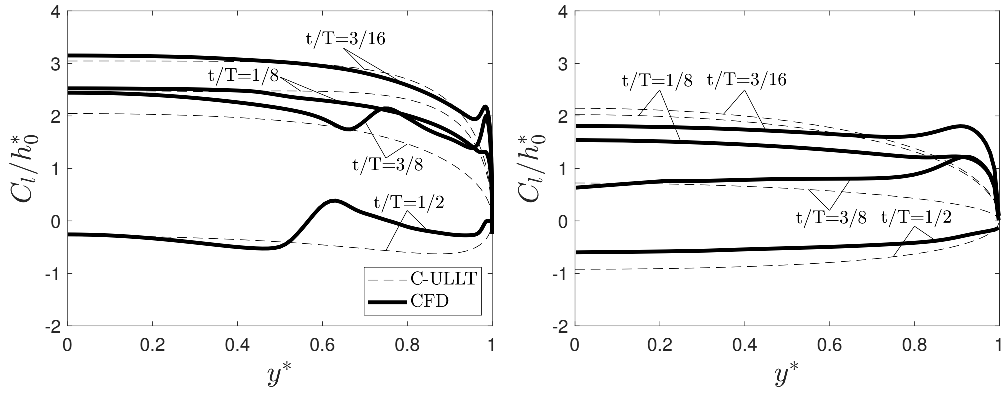

(a) Aspect ratio 6 (b) Aspect ratio 1

Figure 3.7: Comparison of the predicted lift distribution of C-ULLT and Re = 10 000 CFD for rectangular wings oscillating in heave with amplitude $h_0^* = 0.5$ at $k = 0.4$.

distributions.

Again, the C-ULLT obtained LESP correctly predicts the formation of the LEV, but is unable to predict tip vortices. However, the force distributions obtained by the C-ULLT do not reflect those found in the CFD since it is unable to model the 3D LEV arch structure. Furthermore, the arch structure deforms in 3D, making the predicted spanwise location of the LEV found using the LESP criterion less useful, and the force distributions were found to have been affected by vortex structures shed on previous oscillations. The LESP criterion was broadly useful in that LEV shedding could be predicted, but the inability of C-ULLT to model the vortex structure means it cannot provide any meaningful fidelity. Instead, it serves as an indicator that the C-ULLT predicted lift distribution is unreliable.

Finally, the lift distributions resulting from the intermediate amplitude $h_0^* = 0.5$ are examined for aspect ratios 6 and 1. The results are shown in Fig. 3.7, where the times $t/T = \{1/8, 3/16, 3/8, 1/2\}$ are shown, matching the growth of the LEV shown in Fig. 3.4.

The aspect ratio 1 case is shown in Fig. 3.7(b). For this case, the critical value of LESP, $\mathcal{L}_{crit}$, is only just exceeded at the central region of the wing, according to the C-ULLT (see Fig. 3.2(b)). Consequently, it would be expected that the LEV is small with less of an impact on the force distributions than for the higher amplitude $h_0^* = 1$ case. This appears, to some extent, to be true. As with the high amplitude case, the C-ULLT does not predict the increased lift near the wing tips, probably due to the tip vortex structure. However, this effect is diminished in comparison with the $h_0^* = 1$ where the more intense vortex structures lead to a greater localised change in lift.

Once again the aspect ratio 6 case, shown in Fig. 3.7(a), displays a more complicated lift distribution. At times $t/T = 3/8$ and $t/T = 1/2$ the impact of an LEV arch can be seen in the C_l curve. However, the impact of the arch is very much smaller than was observed for the $h_0^* = 1$ case in Fig. 3.6. At times $t/T = 1/8$ and $t/T = 3/16$, before a large LEV has formed, the C-ULLT provides a good prediction of lift distribution. The

C-ULLT again correctly predicted LEV formation, albeit with the value of critical LESP exceeded by a smaller amount, suggesting a smaller LEV. As for the Æ1 case, it would appear that this lessens the impact of the LEV on the force distribution. The values of LESP obtained from the C-ULLT can therefore be used as a rough measure of how useful the force distributions obtained using the C-ULLT are.

3.7 Summary

In this chapter small-amplitude frequency-domain inviscid unsteady lifting-line theory was applied to low Reynolds number problems for rectangular wings undergoing both small and large amplitude heave oscillations.

The Sclavounos-like ULLT introduced in Chapter 2 was used. For small amplitude oscillation problems this ULLT performed similarly in the low Reynolds number regime as in the Euler regime despite the assumption of inviscid flow being broken - it slightly overestimates whole-wing forces. A difference was present in force distribution with respect to span however. In the Euler cases of Chapter 2, separation at the tip led to a spike in lift at the wing tip. For the Reynolds number 1×10^4 cases in this chapter, this spike was mollified. Instead, there was some non-smoothness in the lift distribution at the tip.

Larger amplitude oscillation led to the formation of leading-edge vortex structures on the wings studied. This broke the assumption that the wake was planar and that all vorticity was shed from the trailing edge. For whole-wing forces, these vortex structures made the lift and moment waveforms non-sinusoidal, and changed the peak forces. This effect was strongest in 2D, but as aspect ratio decreased the effects of the vortex structure of whole-wing forces was reduced. Consequently, the ULLT provided a useful prediction, especially at low aspect ratio.

However, the ULLT was less useful in predicting the LEV-affected spanwise load distributions. The leading-edge vortex structures form an arch-like structure on the wing surface, familiar from literature. The legs of the arch meet the wing, and the lift inside and outside these legs is different. The stronger the LEV the stronger the effect. The ULLT is unable to model the formation of the LEV or its evolution, and cannot predict the change in force distributions that LEVs cause.

By combining ULLT with the leading-edge suction parameter, a means of predicting leading-edge separation and LEV formation can be obtained. This method is limited. It cannot predict the form or evolution of the LEV, or the wing-tip vortex. However, it can be used as a rough predictor of LEV strength. Consequently, it is useful for deciding whether the force distribution predicted by ULLT is useful, or whether it will be significantly impacted by the LEV. It allows the engineer to model the problem at low fidelity first, using ULLT, and use the model as a predictor of whether a method capable of modelling

LEVs is needed.

This chapter concludes the first section of this dissertation. In chapter 2, it was found that ULLT is useful for the Euler regime for which it is derived, and it was found that simplified wake models had a possibly bearable effect on the results of the ULLT. In this chapter it was found that inviscid, small-amplitude ULLT is useful in the low Reynolds number regime. It can be used for problems involving leading-edge vortices, but in these cases force distributions with respect to span are inaccurate. A method to estimate the impact of LEVs was obtained.

In the following chapters, new methods are outlined with the aim of filling gaps in the capabilities of current low-order methods. The next chapter details a linearised time-domain method aimed to address the limitations of current unsteady lifting-line theory.

Chapter 4

Applying frequency-domain ULLT to time-domain problems

4.1 Introduction

In the literature review, it was found that there was a requirement for faster time-domain methods. Research areas such as flight dynamics found the unsteady vortex lattice method restrictively slow for practical purposes. Unsteady lifting-line theory could provide a solution, allowing finite wings to be studied without the computational cost of full 3D wing/wake iteration. However, current time-domain ULLTs that avoid numerical treatment of the wake are less capable than those of the frequency domain.

Analytical time-domain unsteady lifting-line theories typically try to obtain the indicial response of a wing. As is done in 2D with Wagner's solution [52] to an impulsively started aerofoil, such a method can be combined with the Duhamel convolution integral [53] for application to arbitrary input kinematics. However, current methods depend upon a simplified wake model, reminiscent of the P-ULLT of Sec. 2.2.4. In Chapter 2, it was found that simplified wake models have a material impact on the accuracy of ULLT. Obtaining a time-domain solution with more complete wake model is challenging and an alternative is needed.

Garrick [55] showed that Theodorsen's solution [56] to the problem of oscillating aerofoils was the frequency-domain equivalent to Wagner's indicial response [52]. The difficulty of evaluating Wagner's function lead to several approximations obtained from the frequency-domain based on this fact [57, 58, 59, 60, 61]. An approximation of the more easily evaluated Theodorsen function is made in the frequency-domain and transformed to the time domain. It may be possible to apply similar techniques to ULLT. The 3D interaction strength $F(y;\omega)$ (Eq. 2.21) changes with respect to frequency and has known limiting values. However, in practice reliably approximating the locus of this function with respect to oscillation frequency is challenging. In this chapter, this problem is circumvented.

The Duhamel convolution integral convolves the indicial response with arbitrary input kinematics. The convolution theorem $g * h = \mathcal{F}^{-1}(G \cdot H)$ states that a convolution of two functions g and h can be applied as the pointwise multiplication of their respective Fourier transforms $G = \mathcal{F}(g)$ and $H = \mathcal{F}(h)$ in the frequency domain. In the context of unsteady lifting-line theory, the frequency-domain response is already known. In this chapter, it is obtained using Chapter 2's C-ULLT. Arbitrary input kinematics can be transformed to the frequency domain using a discrete Fourier transform. After convolution, an inverse Fourier transform can be applied to recover the time-domain response. The method obtained is christened the ULLT / Convolution in Frequency Domain method (UCoFD).

A more detailed explanation of this procedure, including how to avoid evaluating the C-ULLT at every frequency, will be given in the next section, Sec. 4.2. The method, combined with the C-ULLT will then be compared to CFD results in Sec. 4.3, starting with a description of time-domain cases in this chapter. A simple pitch ramp-hold-return motion is investigated in Sec. 4.3.1, followed by a heave velocity ramp that introduces some complications in Sec. 4.3.2. Many of the applications alluded to in the literature review (Sec. 1.1.1) are in the low Reynolds number regime and include large-amplitude kinematics. Such problems are studied in Sec. 4.3.3 before the summary of the chapter in Sec. 4.4.

4.2 Theory

As stated in the introduction, the ULLT / Convolution in Frequency Domain method performs the convolution of the input kinematics with the response of the wing in the frequency domain. The response of the wing with respect to angular frequency ω can be obtained using a linear frequency-domain ULLT. Whilst ULLT is computationally inexpensive compared to many time-domain methods, this convolution may require the evaluation of the response at thousands of oscillation frequencies across the entire frequency spectrum which would be computationally expensive. To avoid this, interpolation can be used.

Lifting-line theory corrects 2D solutions for 3D effects. The 2D inner solution is dominant. In Chapter 2, the lift and moment response of an aerofoil section with respect to pitch and heave are given in Eq. 2.13, Eq. 2.14, Eq. 2.15 and Eq. 2.16. Given that Theodorsen's function, $C(k)$ is of $O(1)$, these functions vary with chord reduced frequency k as $O(k)$ or $O(k^2)$ with respect to frequency. Consequently, a quadratic interpolation scheme is effective. This interpolation scheme uses weights

$$w_0(\omega) = \frac{(\omega - \omega_1)(\omega - \omega_2)}{(\omega_0 - \omega_1)(\omega_0 - \omega_2)}, \tag{4.1a}$$

$$w_1(\omega) = \frac{(\omega - \omega_0)(\omega - \omega_2)}{(\omega_1 - \omega_0)(\omega_1 - \omega_2)}, \tag{4.1b}$$

$$w_2(\omega) = \frac{(\omega - \omega_0)(\omega - \omega_1)}{(\omega_2 - \omega_0)(\omega_2 - \omega_1)}, \tag{4.1c}$$

where $\omega_0 < \omega_1 < \omega_2$ and $\omega_0 < \omega < \omega_2$ when interpolating. At high frequency, frequency-domain unsteady lifting-line tends to the 2D solution [85] where the dominant added mass effects are proportional to k^2. Consequently, extrapolation works well.

The whole-wing lift coefficient C_L or moment coefficient C_M can then be obtained as

$$C_{L/M}(\omega) = w_0(\omega)C_{L/M}(\omega_0) + w_1(\omega)C_{L/M}(\omega_1) + w_2(\omega)C_{L/M}(\omega_2). \tag{4.2}$$

This interpolation strategy is surprisingly effective. An interpolation based on 5 evaluations of the C-ULLT for an aspect ratio 4 rectangular wing is shown in Fig. 4.1. The C-ULLT was evaluated at $k = \{0.001, 0.15, 0.5, 1.2, 2.0\}$. The interpolation appears to work well despite only evaluating the C-ULLT 5 times. The error introduced by the interpolation is small compared to the difference between the C-ULLT and CFD results found in Chapter 2, Sec. 2.3.2. The inset plots show the extrapolated high frequency range. Here, the quadratic extrapolation appears to work well. Potentially interpolation with even fewer evaluated frequencies may be sufficient. However, in this chapter the chord reduced frequency set $k = \{0.001, 0.15, 0.5, 1.2, 2.0\}$ was used in all cases.

The Duhamel convolution integral has traditionally be used to combine step-response functions with arbitrary kinematics. Since it is challenging to take the frequency domain result obtained from the C-ULLT to the time-domain to obtain a step response, the UCoFD method instead transforms the input kinematics to the frequency domain. Convolution is performed in the frequency domain before an inverse Fourier transform returns the result to the time domain. For pitching kinematics $\alpha(t)$ or heaving kinematics $h(t)$ this process is defined as

$$C_{L_h}(t) = \mathcal{F}^{-1}\left(\mathcal{F}(h(t)) \cdot C_{L_h}(\omega)\right), \tag{4.3}$$

$$C_{M_h}(t) = \mathcal{F}^{-1}\left(\mathcal{F}(h(t)) \cdot C_{M_h}(\omega)\right), \tag{4.4}$$

$$C_{L_\alpha}(t) = \mathcal{F}^{-1}\left(\mathcal{F}(\alpha(t)) \cdot C_{L_\alpha}(\omega)\right), \tag{4.5}$$

$$C_{M_\alpha}(t) = \mathcal{F}^{-1}\left(\mathcal{F}(\alpha(t)) \cdot C_{M_\alpha}(\omega)\right). \tag{4.6}$$

The Fourier transforms can be computed quickly and easily using the fast Fourier transform method, for which software packages are readily available. Since such discrete

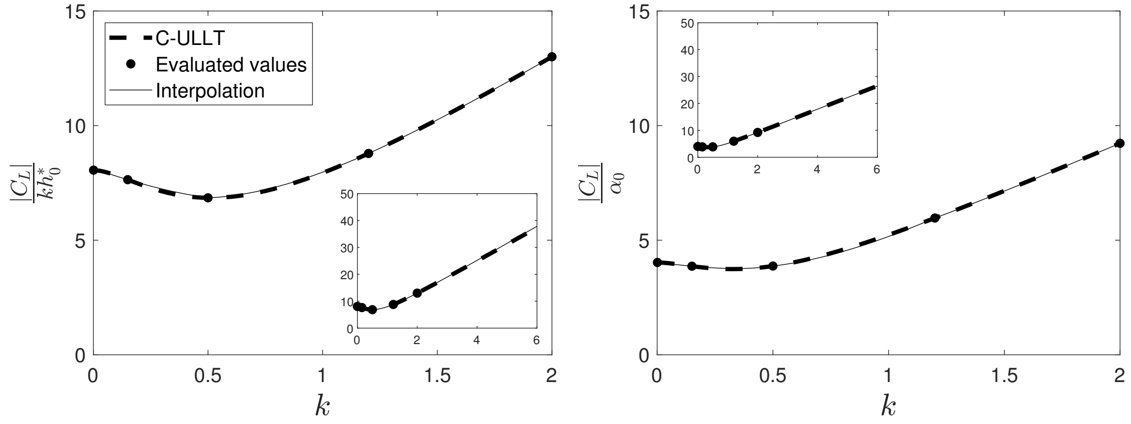

(a) Heave C_L (b) Pitch C_L

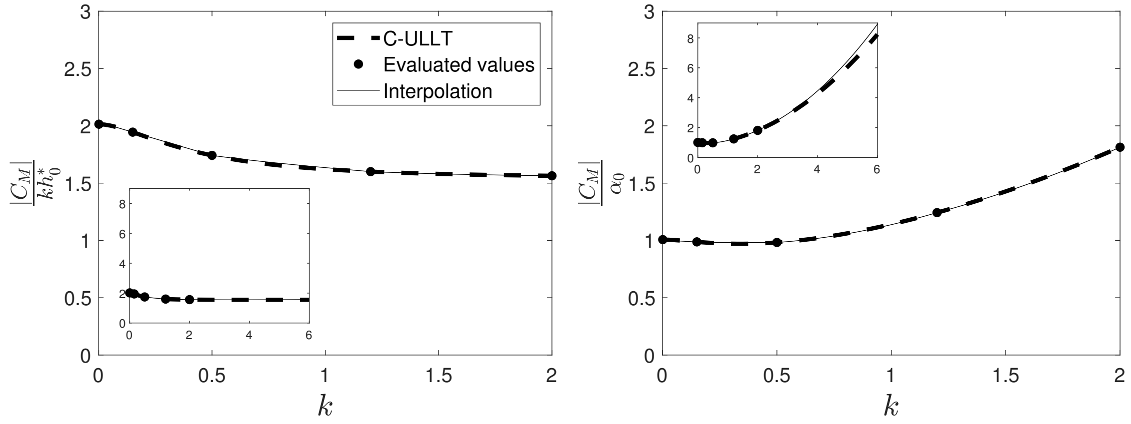

(c) Heave C_M (d) Pitch C_M

Figure 4.1: Interpolation of C-ULLT lift and moment coefficients with respect to reduced frequency for a rectangular aspect ratio 4 wing. Moments are taken about the mid-chord. Inset shows extended frequency range result. The C-ULLT was evaluated at $k = \{0.001, 0.15, 0.5, 1.2, 2.0\}$ to obtain the interpolation.

Fourier transform methods result in double sided spectrums, it is useful to note that $C_{L/M}(-\omega) = \overline{C_{L/M}(\omega)}$.

By using the fast Fourier transform to obtain the frequency-domain definition of the input kinematics, a circular convolution of the input is being computed. Consequently, the time window passed into the transform is assumed to be periodic, and the final results will also be periodic. So long as the input window is sufficiently large, this is not a problem in practice. The only caveat is that the displacement of the wing at the beginning and end of the input window should be identical. The increased input window size does not significantly effect computational cost. A discrete convolution of n points has algorithmic complexity of $\mathcal{O}(n^2)$, which is significantly greater than the $\mathcal{O}(n\log(n))$ cost of a fast Fourier transform.

4.3 Results and discussion

In this section, the UCoFD method is used to apply the C-ULLT, described in Chapter 2, to time domain problems. The results obtained are compared to those obtained by strip theory [53] and CFD. Both the Euler regime and the low Reynolds number regime (Re=10 000) are studied. The CFD setup used for the Euler cases is given in Appendix C.1, and the setup for the low Reynolds number cases given in Appendix C.2. The six cases studied in this chapter are shown in Table 4.1.

The canonical ramp-hold-return kinematics of Ol *et al.* [223] are used in all cases. These time-domain kinematics are related to flapping flight, and have tunable smoothness to control the balance of circulatory and added mass effects. The first case, Case 4.1 in Sec. 4.3.1, is a pitch ramp-hold-return in the Euler regime (Re= ∞). The kinematics are smooth and the UCoFD method can be applied without complication. Case 4.2 introduces complications in Sec. 4.3.2. The heave velocity ramp motion is non-smooth, allowing the impact of the high-frequency inaccuracy of the C-ULLT (see Chapter 2) to be investigated in the context of UCoFD. The displacement of the wing is also different at beginning and end of the input motion. Next, low Reynolds number cases representative of modern applications are investigated. Pitch ramp-heave-return motions are investigated at Re=10 000 in Sec. 4.3.3. Both small angle 3° and large angle 25° cases are investigated for wings of aspect ratio 6 and 3.

4.3.1 A returning pitch ramp in the Euler regime

The canonical pitch ramp-hold-return kinematics of Ol *et al.* can be expressed as

$$\alpha(t) = \frac{P}{a\bar{c}}\left[\frac{\cosh(aU_\infty(t-t_1)/\bar{c})\cosh(aU_\infty(t-t_4)/\bar{c})}{\cosh(aU_\infty(t-t_2)/\bar{c})\cosh(aU_\infty(t-t_3)/\bar{c})}\right]$$

Table 4.1: Cases for comparison between UCoFD, CFD and strip theory.

Case	Re	Æ	Kinematics
4.1	∞	4	Small-amplitude smooth pitch ramp-hold-return
4.2	∞	4	Small-amplitude non-smooth heave velocity ramp-hold-return
4.3a	10^4	6	Small-amplitude smooth pitch ramp-hold-return
4.3b	10^4	6	Large-amplitude smooth pitch ramp-hold-return
4.3c	10^4	3	Small-amplitude smooth pitch ramp-hold-return
4.3d	10^4	3	Large-amplitude smooth pitch ramp-hold-return

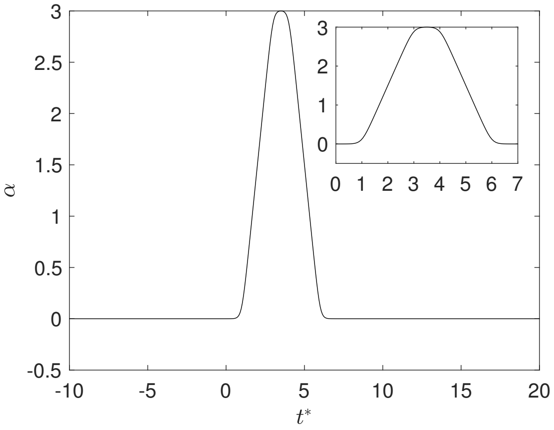

Figure 4.2: Leading edge pitch ramp-hold-return kinematics used in Case 4.1, Case 4.3a and Case 4.3c.

where $a = \pi^2/(4(t_2 - t_1)(1 - \sigma))$. Here, the ramp magnitude P is set to give $\alpha_{\max} = 3°$, and the timing parameters are set to $t_1^* = 1$, $t_2^* = 3$, $t_3^* = 4$ and $t_4^* = 6$, where $t^* = tU_\infty/\bar{c}$. The smoothness of the curve is dictated by σ, which for case 4.1 is 0.5. This value leads to smooth kinematics, as shown in Fig. 4.2. Whilst the kinematics of interest are shown in $t^* = [0, 7]$ (inset), a window of $t^* = [-10, 20]$ is used by the UCoFD method. This large window is required because, as mentioned, the Fourier transform means that a circular convolution is being computed, and the signal is assumed to be periodic. A large window avoids the problems introduced by this periodicity.

A 2048 point fast Fourier transform was applied to the input kinematics in the $t^* = [-10, 20]$ window. For Case 4.1, a rectangular wing of $\bar{c}$ =0.0762 m is used in a free stream of $U_\infty = 0.1312\,\mathrm{m\,s^{-1}}$. Consequently, the 2048 equally spaced input samples lead to a sample interval of $\Delta t \approx 0.015\,\mathrm{s}$ with a Nyquist critical frequency of $\omega_c = 2\pi/2\Delta t = 369\,\mathrm{rad\,s^{-1}}$. The corresponding critical reduced frequency is $k_c \approx 107$. This is sufficiently high to capture the input signal without aliasing, since the power of the single-sided power spectrum of the input signal has decreased from 10^{-3} at low frequency to 10^{-35} at $k_c \approx 107$.

The C-ULLT lift coefficient C_L and moment coefficient C_M responses with respect to frequency for leading-edge pitching were obtained at $k = \{0.001, 0.15, 0.5, 1.2, 2.0\}$ and quadratically interpolated. A time domain response was then obtained using the inverse

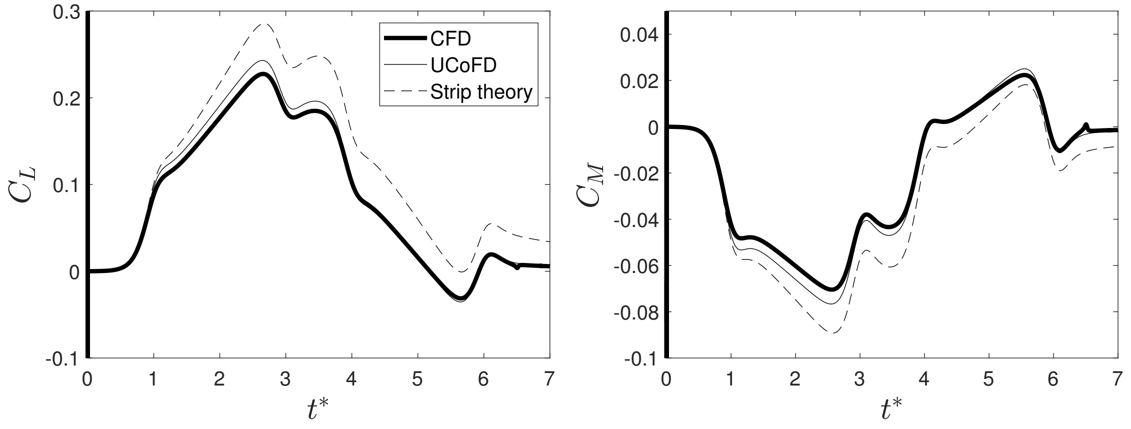

(a) C_L (b) Leading-edge C_M

Figure 4.3: Comparison of UCoFD, Euler CFD and strip theory results for Case 4.1.

fast Fourier transform. Figure 4.3 compares the results obtained with those from strip theory and CFD.

The CFD C_L response is shown in Fig. 4.3(a). The lift coefficient roughly follows the pitch angle, increasing and then returning to zero. Lift is created by two mechanisms. At times $t^* = \{1, 3, 4, 6\}$ there are sudden changes in lift. This is due to the acceleration of the wing leading to added mass effects. These times correspond to rapid changes in pitch rate. When the change in pitch rate is positive, such as at $t^* = 1$ and $t^* = 6$, there is an increase in lift. When it is negative, such as at $t^* = 3$ and $t^* = 4$, there is a decrease in lift. The second mechanism is circulatory lift. This portion of the lift is defined by the flow around the wing at any instant in time, and contributes to the overall shape of the curve. The downwash on the wing resulting from the wing's wake reduces the wing's circulatory lift. The circulatory and acceleratory added mass effects combine to create the final lift response with respect to time. The circulatory effects are differ from strip theory partially due to the 3D wake topology, shown diagrammatically in Fig. 4.4.

Early on, as the angle of attack is initially increasing, the wing sheds the starting vortex and short tip vortices, shown in Fig. 4.4(a). The starting vortex induces a large downwash on the wing, and the tip vortices are comparatively unimportant. Consequently, 3D effects are unimportant. As the kinematics continue to the hold, further spanwise vorticity is shed into the wake as shown in Fig. 4.4(b). The tip vortices becomes stronger, and 3D effects have a more significant impact on the wing forces. In Fig. 4.4(c) the return motion has began, and the circulation about the wing is decreasing. Consequently, lifting inducing spanwise vorticity is being shed into the wake. This upwash induced by this on the wing counteracts that of the 3D effects of the tip vortices. After the motion has completed in Fig. 4.4(d), a complete vortex vortex ring has been shed into the wake. The lift-inducing effects of the near-wing spanwise wake vorticity are counteracted by the streamwise vorticity wake vorticity only present in 3D.

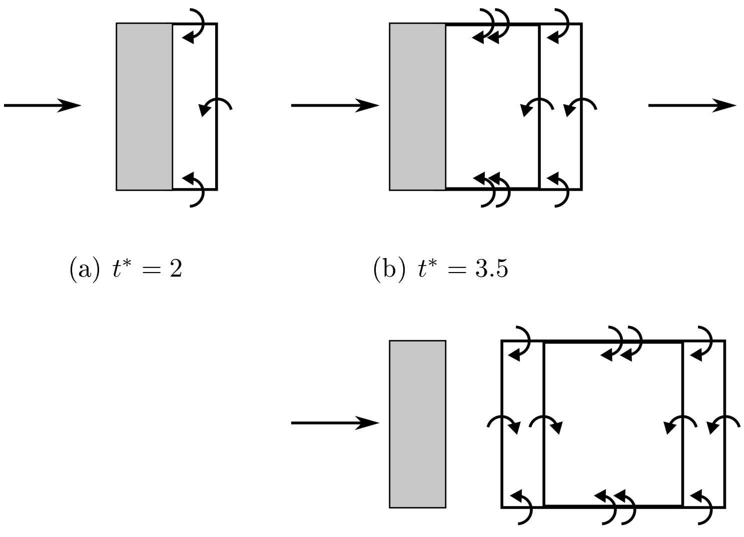
(a) $t^* = 2$ (b) $t^* = 3.5$ (c) $t^* = 5$

(d) $t^* = 7$

Figure 4.4: A plan view of a wing undergoing a pitch ramp-hold-return motion and its wake.

The UCoFD method predicts the shape of the C_L curve well. The lift peak is slightly overestimated.This is consistent with the frequency domain results for the C-ULLT in Sec. 2.3.2 where at aspect ratio 4 lift was slightly overestimated at all frequencies. The lift overestimate at $t^* = 1$ reflects how the ULLT overestimates the effects of added mass. The ongoing overestimate is due to the ULLT overestimating circulatory lift. Comparatively, strip theory over-predicts the peak lift significantly, and is incorrect by an order of magnitude at $t^* = 7$. When the wing is accelerating rapidly, for instance at $t^* = 1$, the strip theory and UCoFD results match. This is because the underlying frequency-domain ULLT solution tends to strip theory at high frequency. As time continues, there is large difference between the solution of strip theory and ULLT. This is because of the importance of 3D effects at low frequency. Since the wing is static after $t^* \approx 6$, the rapid return to zero lift found in the CFD and UCoFD results can be attributed to the circulatory effects and the difference between the 2D wake model of strip theory and the 3D wake of the finite wing.

Figure 4.3(b) compares the moment coefficient predicted by the CFD, UCoFD and strip theory. Again, the C_M curve is the result of the sum of circulatory and acceleratory effects. The acceleratory effects lead to rapid changes in C_M at $t^* = \{1, 3, 4, 6\}$. The circulatory effects lead to the overall shape of the curve. The UCoFD method matches the CFD result well, except for the overestimate of peak moment coefficient. This is consistent with the frequency domain results of Chapter 2. Once again, the strip theory significantly overestimates the peak moment coefficient and fails to return to zero by $t^* = 7$.

This case satisfies the assumptions made in the derivation of C-ULLT and the requirements of the UCoFD method. The kinematics were smooth, avoiding high frequency components, and the start pitch angle matched the end pitch angle.

The next case, Case 4.2, is more challenging for two reasons. Firstly, the smoothness parameter, σ, is altered to obtain less smooth ramp-heave-return motion. The C-ULLT in Chapter 2 performed worse at high frequency, so this may reduce the accuracy of the UCoFD results. Secondly, a heave velocity ramp is used, and the start and end points of the ramp do not match. A return ramp must be introduced.

4.3.2 A non-returning heave velocity ramp in the Euler regime

Case 4.2, studied in this section, is a heave velocity ramp-hold-return defined by the canonical kinematics of Ol *et al.* [223]. The net displacement is non-zero.

The heave velocity is defined as

$$\dot{h} = \frac{P}{a}\left[\frac{\cosh(aU_\infty(t-t_1)/\bar{c})\cosh(aU_\infty(t-t_4)/\bar{c})}{\cosh(aU_\infty(t-t_2)/\bar{c})\cosh(aU_\infty(t-t_3)/\bar{c})}\right],$$

where $a = \pi^2/(4(t_2-t_1)(1-\sigma))$ and P set to give $\dot{h}_{\max} = -0.05\bar{c}$. Once again, the time parameters are set to $t_1^* = 1$, $t_2^* = 3$, $t_3^* = 4$ and $t_4^* = 6$. The smoothness parameter σ is set as $\sigma = 0.888$. Consequently, the curve is less smooth than that used for Case 4.1 in Sec. 4.3.1.

Due to the periodic assumption introduced by the Fourier transform, the discontinuity introduced by the difference between the start and end displacement of the kinematics must be mitigated. A smooth return function should be inserted. Here, a quadratic function is used. This is given by

$$g(t) = \begin{cases} 1, & \text{if } t \leq t_{s_0} \\ 1 - 2\left(\frac{t-t_{s_0}}{t_{s_1}-t_{s_0}}\right)^2, & \text{if } t_{s_0} < t \leq (t_{s_0}+t_{s_1})/2 \\ 2\left(\frac{t_{s_1}-t}{t_{s_1}-t_{s_0}}\right)^2, & \text{if } (t_{s_0}+t_{s_1})/2 < t \leq t_{s_1} \\ 0, & \text{if } t > t_{s_1} \end{cases}. \tag{4.7}$$

This can be combined with the original kinematics $h(t)$ to give a function that returns to zero $h'(t) = h(t)g(t)$. Like Case 4.1, the kinematics are in $t^* = [0, 7]$ but a window of $t^* = [-10, 35]$ is used by the UCoFD method. The ramp is inserted after the window of interest, with $t_{s_0}^* = 10$ and $t_{s_1}^* = 20$. By placing it shortly after the kinematics, any effects resulting from the return ramp have a large period of time to decay before the kinematics begin again.

The kinematics defined by $h'(t)$ are applied to a rectangular aspect ratio 4 wing with geometry and flow conditions matching those used in Case 4.1 using the UCoFD method.

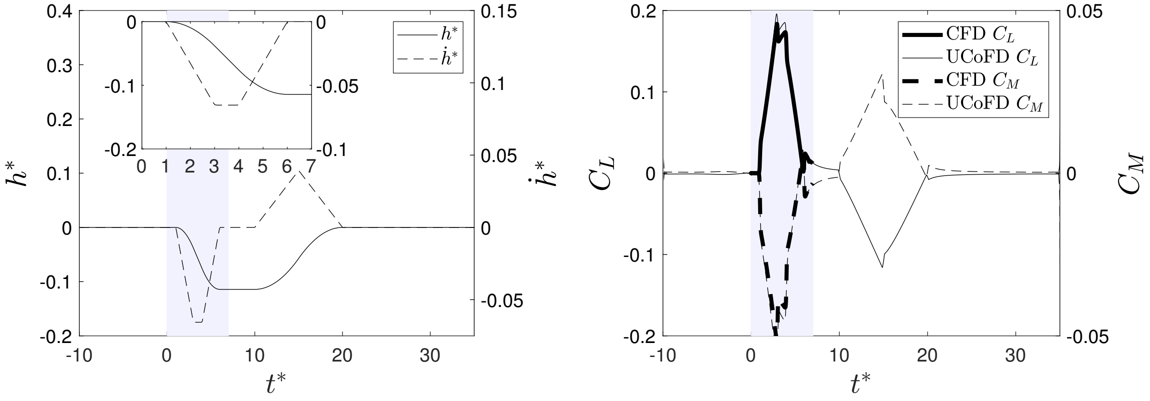

(a) Heave kinematics (b) Force coefficients

Figure 4.5: Heave ramp-heave-return kinematics and results for Case 4.2. More detailed C_L and C_M results are shown in Fig. 4.6. Region of interest highlighted.

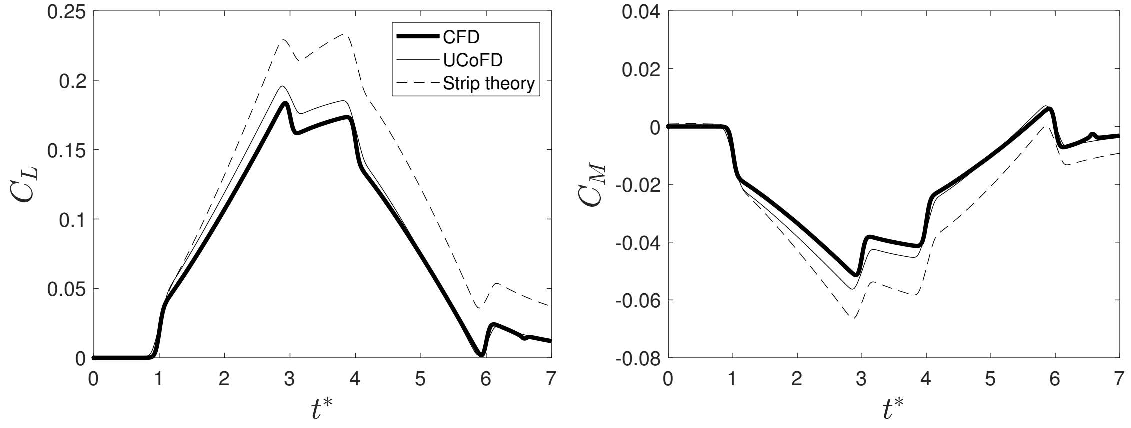

(a) C_L (b) C_M

Figure 4.6: Comparison of UCoFD, Euler CFD and strip theory results for an aspect ratio 4 rectangular wing undergoing a non-smooth heave velocity ramp manoeuvre in Case 4.2.

2048 samples were used for the discrete Fourier transform. The input kinematics and force coefficients obtained are shown in Fig. 4.5.

The kinematics, depicted in Fig. 4.5(a), show the heave velocity ramp in $t^* = [0, 7]$ (inset). The non-zero displacement at $t^* = 7$ is returned to zero by the return ramp in $t^* = [10, 20]$. This avoids a step in the kinematics between $t^* = 35$ and $t^* = -10$. In Fig. 4.5(b) the impact of the return ramp can be seen. Even after the return ramp has finished at $t^* = 20$ the force and moment coefficients are still decaying to zero.

Figure 4.6 shows the lift and moment coefficients in the time interval of interest. As in Case 4.1, the CFD results roughly follow the input kinematics, increasing, plateauing and returning to zero. The sudden jumps in C_L and C_M at times $t^* = \{1, 3, 4, 6\}$ are due to acceleratory effects. The overall shape and slow decay in forces at $t^* = 7$ are due to circulatory effects.

The ULLT / convolution in frequency domain method predicts the CFD results with good accuracy. As with Case 4.1, the method correctly obtains the shape of curve but slightly overestimates amplitude. The underlying C-ULLT was less accurate at high frequency (see Sec. 2.3.2). However the accuracy of the UCoFD method around the rapid changes in input remains good, despite their correspondence to the high frequency components of the input signal. Once again, UCoFD provides a significantly more accurate solution than the strip theory when compared to the CFD results.

Case 4.1 and Case 4.2 demonstrate how the UCoFD method can be used to apply the frequency-domain C-ULLT to time-domain small-amplitude problems in the Euler regime, where the assumptions of the UCoFD method and the C-ULLT are met. The method consistently provided better results than strip theory. Case 4.3 applies the method to low Reynolds cases large amplitudes, violating the assumptions of the method.

4.3.3 Large-amplitude pitch ramp-hold-return at Re=10 000

Micro air vehicles, unmanned aerial vehicles and energy harvesting devices require aerodynamic solutions in the low Reynolds number, high-amplitude regime (see Chapter 1, Sec. 1.1.1). So far in this chapter, Euler regime, small-amplitude kinematics cases have been investigated. These are consistent with assumptions made in the derivation of the C-ULLT and the UCoFD method. The potential flow model assumes inviscid incompressible flow, and the UCoFD method and C-ULLT both assume linearity. In this section, these assumptions are violated.

These assumptions were violated in Chapter 3 using the C-ULLT for oscillating rectangular wings. For whole-wing forces, it was found that the C-ULLT over-predicted the CFD results at low amplitude. As amplitude increased, the CFD results show how the formation of leading-edge vortices lead to a super-linear increase in force with respect to oscillation amplitude. The C-ULLT prediction of force distribution was useful at low-amplitude, but for large amplitude cases the LEV structure caused significant changes in force distribution which the C-ULLT did not model. The formation of LEV structures could be predicted using the LESP criterion.

In this section, Cases 4.3a-d are studied. These are time-domain pitch ramp-hold-return problems, with two aspect ratios and two amplitudes studied. Case 4.3a and Case 4.3c feature aspect ratio 6 and 3 wings pitching to 3° and returning. Consequently they are a time-domain equivalent of the small amplitude cases of Chapter 3. They investigate the effects of the low Reynolds number regime without the complications of LEV shedding.

Cases 4.3b and 4.3d study a larger amplitude 25° pitch ramp-heave-return intended to lead to LEV shedding. Unlike Chapter 3, pitching is studied. These cases verify whether linear ULLT based methods are still applicable in the time domain. Force distribution is not studied since this is already known to be poorly predicted by ULLT in the presence

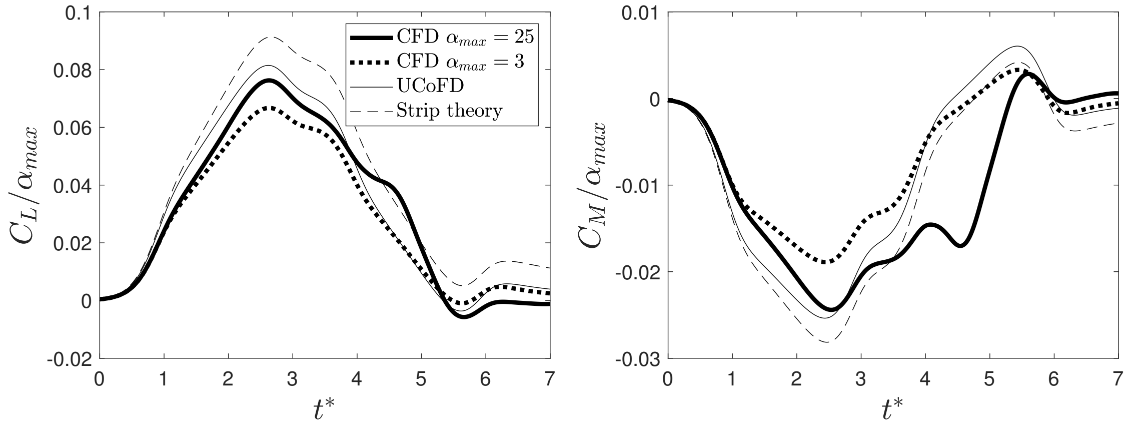

(a) Aspect ratio 6 C_L (b) Aspect ratio 6 C_M

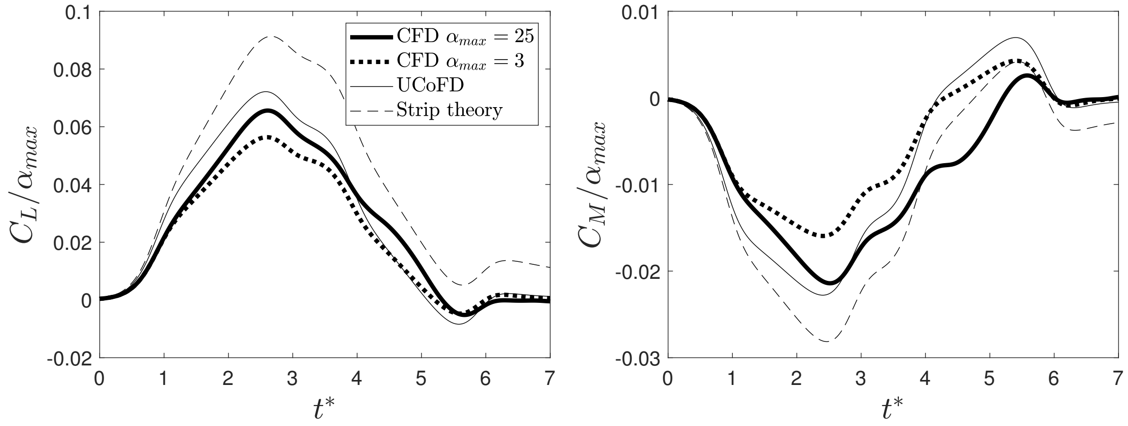

(c) Aspect ratio 3 C_L (d) Aspect ratio 3 C_M

Figure 4.7: Comparison of UCoFD, CFD and strip theory results for Cases 4.3a-d, featuring aspect ratio 6 and 3 rectangular wings undergoing a smooth pitch ramp manoeuvre to angles of attack of 25° and 3° at a Reynolds number of 10 000.

of LEVs.

The CFD methods of Chapter 3, detailed in Appendix C.2, are used again. Aspect ratio 6 (Case 4.3a and Case 4.3b) and 3 (Case 4.3c and Case 4.3d) wings with chord $\bar{c} = 0.1\,\mathrm{m}$ and a NACA0008 aerofoil section are studied in a free stream of $U_\infty = 0.1\,\mathrm{m\,s^{-1}}$ at a Reynolds number of 10 000.

The kinematics are similar to those of Case 4.1 in Sec. 4.3.1. The wing undergoes leading-edge pitching to a maximum pitch angle of $\alpha_{\max} = 3°$ (Cases 4.3a and 4.3c) and $\alpha_{\max} = 25°$ (Cases 4.3b and 4.3d). Smooth kinematics are used with $\sigma = 0.5$. As with Case 4.1 and 4.2, the time parameters are set to $t_1^* = 1$, $t_2^* = 3$, $t_3^* = 4$ and $t_4^* = 6$.

Figure 4.7 shows the normalised lift and moment coefficients obtained using CFD and the UCoFD method for Case 4.3a-d. The amplitude 3° and 25° are plotted together for comparison, and the UCoFD method is represented by a single curve since the method is linear. The distinct curves obtained in the CFD are due to aerodynamic non-linearities.

For the aspect ratio 6 cases, the results are shown in Fig. 4.7(a) for lift and Fig. 4.7(b) for moments. Unsteady lifting-line theory assumes high aspect ratio wings. In Chapter 2, it was found that the C-ULLT worked best for higher aspect ratio wings in the small amplitude Euler regime, and in Chapter 3 this was also the case in the Re=10 000 regime for small amplitude oscillation. The UCoFD method predicts the shape of both the C_L and C_M curves well compared to CFD, but over-predicts the peak lift and moment. The over-prediction of peak lift is larger than found in the Euler cases, and also larger than those found for oscillating cases in Chapter 3. The over-prediction in lift is much smaller than is suggested by strip theory however.

For the larger amplitude cases, the UCoFD results are the same due to the assumption of linearity. In Chapter 3, it was found that the forces increased super-linearly with amplitude. For the 25° pitch angle, the CFD results show that this is also the case here. The shape of the C_L and C_M curve are altered, most noticeably at $t^* \approx 4.5$. This is caused by the leading-edge vortex. Figure 4.8 shows the how the LEV forms as the angle of attack increases, pinching off at approximately $t^* = 4.5$ before being convected over the surface of the wing as the pitch angle reduces. For a more detailed analysis, see Chapter 3 Sec. 3.5. The UCoFD method does not model the LEV and is consequently unable to reflect the change in the force curves that it causes. However, the increase in peak force due to the LEV reduces the prior over-prediction of the C_L and C_M by the UCoFD method. Once again, the UCoFD method produces a far superior result to strip theory.

Similar results are obtained for Case 4.3c and Case 4.3d at aspect ratio 3. The force results for these cases are shown in Fig. 4.7(c) and Fig. 4.7(d). For the 3° amplitude case (Case 4.3c), the UCoFD method over-predicts peak lift and moment, although the predicted C_L and C_M curve shapes are correct. For the Case 4.3d, where the wing pitches to 25°, the LEV changes the shape and amplitude of the force curves. In Chapter 3, finite wing effects appeared to stabilise the LEV structure, leading to a reduced change in forces as the LEV separated from the wing surface. Similar stabilisation is visible in Fig. 4.8. The CFD results show a reduced change in forces at $t^* \approx 4.5$, suggesting this is also true for pitch ramp-hold-return kinematics. Once again, the LEV leads to a larger peak lift, reducing the over-prediction of the UCoFD method. Strip theory still provided a comparatively poor result.

4.4 Summary

In this chapter, a method to apply linear frequency-domain unsteady lifting-line theory to time domain problems was described. The Unsteady Lifting-Line Theory / Convolution in Frequency Domain (UCoFD) method uses Fourier transforms to obtain a frequency domain representation of the input kinematics. The convolution of this and the response obtained from an interpolated frequency-domain ULLT are then taken before the results

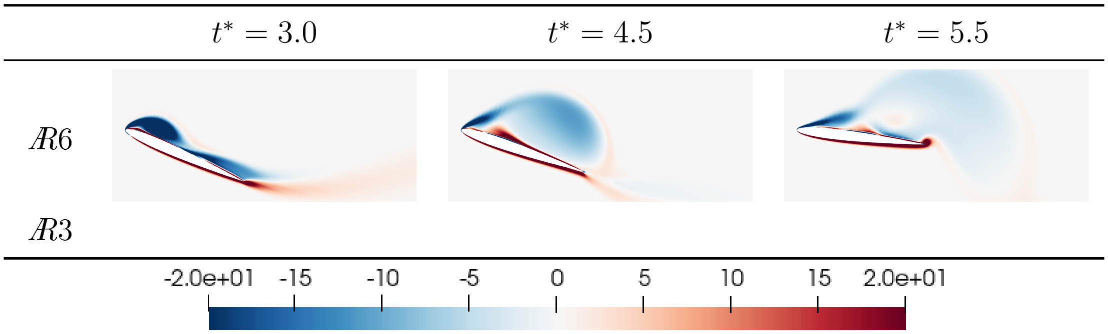

Figure 4.8: Non-dimensionalised spanwise vorticity $\omega_y c/U$ at the wing root of aspect ratio 6 and 3 wings, obtained from CFD at a Reynolds number of 10 000 in Case 4.3b and Case 4.3d.

are returned to the time-domain by an inverse Fourier transform.

The computational cost of the method is low. A quadratic interpolation scheme allows the ULLT response with respect to frequency to be obtained with good accuracy using only a few evaluations of whichever frequency-domain ULLT is being used. In this chapter the C-ULLT introduced in Chapter 2 was used, but the method does not depend upon the details of the underlying ULLT. This interpolation is also reusable since it is independent of the input kinematics. A fast Fourier transform can be used to transform the input kinematics to the frequency domain and the inverse transform is used to return the results back to the time domain. Technically, this results in a circular convolution, which assumes the input and output are periodic. In practice, this has little influence on the results and provides superior $\mathcal{O}(n \log(n))$ scaling.

In the results section, the UCoFD method was compared to CFD and strip theory. In the Euler regime, the UCoFD method could easily be applied to smooth pitch ramp-hold-return problems, providing good results, especially compared to strip theory. For a less smooth heave velocity ramp, the UCoFD method provided good results again, despite the higher frequency inaccuracy of the C-ULLT found in Chapter 2. This case also demonstrated how a return ramp should be inserted to obtain matching start and end displacements.

Some of the applications detailed in the literature review of Chapter 1 demand low Reynolds number and sometimes large-amplitude results. The UCoFD was therefore compared to CFD results for a wing undergoing a pitch manoeuvre at a Reynolds number of 10 000. The lift was overestimated for small amplitudes, and the method was unable to model the effects of leading-edge vortices. However, it provided much better results than strip theory.

The UCoFD method is useful for applications where displacements are small and the kinematics are known in advance. In the next chapter, these restrictions are removed through the formulation of a geometrically non-linear time-marching unsteady lifting-line theory.

Chapter 5

Large-amplitude time-domain ULLT

5.1 Introduction

In the last chapter (Chapter 4), a method for applying frequency-domain Unsteady Lifting-Line Theory (ULLT) to time-domain problems was obtained. It was found to work well for small-amplitude Euler-regime time-domain cases, and did not depend upon the detailed nature of the underlying ULLT. However, the method has inherent limitations. The Fourier transforms require that the underlying frequency-domain ULLT is linear. For small amplitude problems, this is appropriate. For larger amplitude cases, and cases with aerodynamic non-linearities, it is not. The method also requires that the input kinematics are known in advance. For applications such as time-marching flight dynamics solvers, this is problematic.

In this chapter, a new unsteady lifting-line theory is described which alleviates these problems using numerical methods. This is made possible by discarding the analytical wake models that have so far been central to this dissertation, and replacing them with numerical approximations. The justification for this is given by Guermond and Sellier [85], who describe mathematically how the common part of the wake in both the inner and outer solution must be cancelled. Numerically, this was originally investigated by Devinant [112] who formulated a linearised time-marching ULLT method.

This chapter expands on this work through the integration of geometrically non-linear inner solutions, allowing for wake self-convection and non-planar wakes. The Large-Amplitude Unsteady Thin-Aerofoil Theory (LAUTAT) of Ramesh *et al.* [102] is used for this purpose. This allows the ULLT described in this chapter to model large-amplitude geometrically non-linear problems, and contains the groundwork necessary for the integration of leading-edge vortex shedding methods such as Ramesh *et al.* [145]. This new lifting-line theory is therefore described as Large-Amplitude Unsteady Lifting-Line Theory (LAULLT).

The outline of this chapter is as follows. The new theory is outlined in Sec. 5.2, with

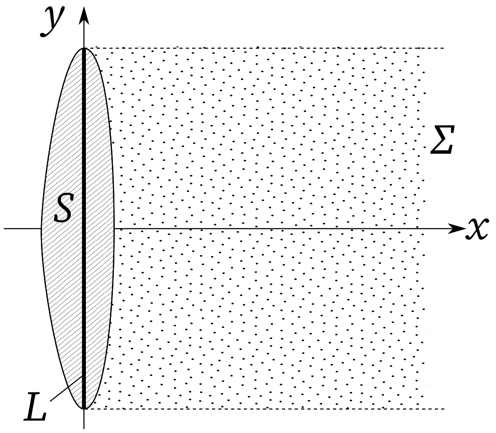

Figure 5.1: A wing with surface S and its wake with surface Σ. The wing surface can be reduced to a lifting-line L.

the inner solution (based on the work of Ramesh *et al.* [145]) described in Sec. 5.2.1 and the outer solution in Sec. 5.2.2. The time-marching algorithm is described in Sec. 5.2.3. The LAULLT is compared to CFD, the C-ULLT of Chapter 2 and the UCoFD method of Chapter 4 in the results section (Sec. 5.3). Euler-regime pitch and heave manoeuvres are investigated along with a low Reynolds number regime, large amplitude pitch ramp-hold-return manoeuvre. The chapter is summarised in Sec. 5.4

5.2 Theory

As in Chapter 2, a straight, high aspect ratio wing is immersed in an inviscid, incompressible free stream moving with velocity U_∞ in the x direction. This is shown in Fig. 5.1, along with the wake of the wing, Σ.

For lifting-line theory to be applied, the wing is assumed to be of high aspect ratio, meaning that the span is much greater than the chord, $2s/c \gg 1$. In Chapter 2, the separation of length scales was introduced. Separation of length scales allows a problem with two sufficiently different length scales to be modelled as two simplified interacting problems. On the span length scale the chord is negligible, and the wing can be modelled as a (lifting-)line, L. On the chord length scale, the 2D problem changes slowly with respect to span, making it effectively 2D. This results in an outer span-scale 3D problem, and an inner chord-scale 2D problem. These must interact for a solution to be obtained.

In Chapter 2, it was described how the inner and outer solution of a linear frequency-domain ULLT interact with each other through a wake integral that allowed a 3D correction to be applied to the 2D inner solution. This was achieved through an integral (Eq. 2.21) which acted on a wake model described by a kernel K (Sec. 2.2.4). This idea can be physically interpreted with the aide of Fig. 5.2. Note that the outer solution uses the coordinate system $\boldsymbol{x}' = \{x', y', z'\}$ where $y = y'$.

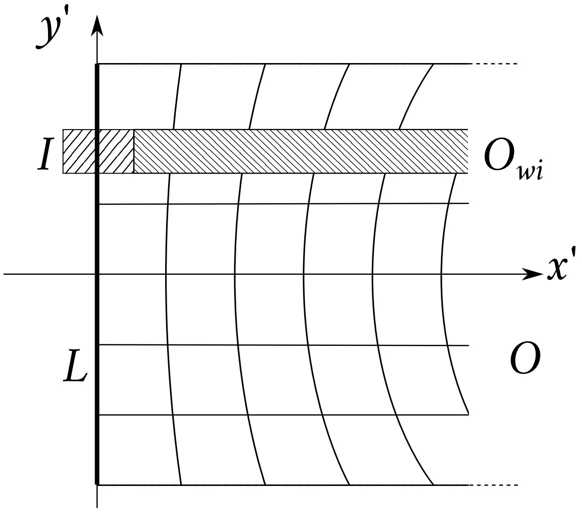

Figure 5.2: A representation of the wing as a lifting-line L and its wake.

The figure shows the lifting-line L representing the wing in the outer domain. The wake as modelled in the outer domain is $O \cup O_{wi}$. At a point $\boldsymbol{x}_S$ on the span S in I, the 2D problem is being considered. In the outer solution, this point lies on the lifting-line at $x' = 0$, and is referred to as $\boldsymbol{x}'_S$. The chord section modelled by this 2D inner solution within the inner domain I of radius c, and it has a 2D wake that is convected downstream into O_{wi}. The inner solution and outer solution match in O_{wi}. The outer domain neglects the detail of the lifting-line in I, but models the entire outer wake $O \cup O_{wi}$.

The downwash on the point M on the wing surface S can be expressed as

$$\mathbf{w}(\boldsymbol{x}_S; t) = \mathbf{w}_{in}(\boldsymbol{x}_S; t) + \mathbf{w}_{out}(\boldsymbol{x}_S; t), \tag{5.1}$$

where $\mathbf{w}_{in}$ is the downwash from the domain I (the 2D bound vorticity and near wake) and $\mathbf{w}_{out}$ is downwash due to $O \cup O_{wi}$.

Lifting-line theory reduces the cost of 3D interaction by only evaluating the downwash due to $\mathbf{w}_{out}(\boldsymbol{x}_S)$ on the lifting-line. For the high frequency capable method of Guermond and Sellier [85] for oscillatory problems, a sinusoidal downwash is used, meaning

$$\mathbf{w}_{out}(\boldsymbol{x}_S; t) = \left\{ \begin{matrix} 0 \\ 0 \\ \mathbb{R}(e^{-i\bar{k}x}(\mathbf{w}_{wi}(\boldsymbol{x}'_S; t) + \mathbf{w}_O(\boldsymbol{x}'_S; t))) \end{matrix} \right\}, \tag{5.2}$$

where $\bar{k}$ is the mean chord reduced frequency, $\mathbf{w}_{wi}$ is the downwash due to the wake in O_{wi} and $\mathbf{w}_O$ the downwash due to O. In lifting-line theory, the outer correction to downwash can vary with respect to the chord-wise coordinate, but is only evaluated at one point in the outer domain, M_0.

In this chapter, a large-amplitude time-domain solution is sought. This means that the $\mathbf{w}_{out}(\boldsymbol{x}'_S;t)$ obtained from small-amplitude wake models cannot be used. Likewise, the oscillatory inner solution assumed in Eq. 5.2 is inappropriate. Assuming oscillatory kinematics in the inner solution can be avoided by instead assuming uniform downwash $\mathbf{w}_{out}(\boldsymbol{x}_S;t) = \mathbf{w}_{wi}(\boldsymbol{x}'_S;t) + \mathbf{w}_O(\boldsymbol{x}'_S;t)$. Whilst this technically limits the asymptotic validity of the method, it was found that the practical implications of doing this were minimal in Chapter 2.

The velocity induced by the inner 2D domain $I \cup O_{wi}$ on a point $\boldsymbol{x}_S$ in I is

$$\mathbf{w}_{2D}(M;t) = \mathbf{w}_b(\boldsymbol{x}_S;t) + \mathbf{w}_I(\boldsymbol{x}_S;t) + \mathbf{w}_{wi}(\boldsymbol{x}_S;t) = \mathbf{w}_{in}(\boldsymbol{x}_S;t) + \mathbf{w}_{wi}(\boldsymbol{x}_S;t), \tag{5.3}$$

where $\mathbf{w}_b$ is the downwash induced by the bound vorticity of the chord section inself, $\mathbf{w}_I$ is the effect of wake vorticity in I and $\mathbf{w}_{wi}$ is the effect of wake vorticity in the inner domain that has been convected downstream into the area represented in the outer wake as O_{wi}. If the downwash $\mathbf{w}_{out}$ due the wake as modelled in the outer domain $O \cup O_{wi}$ were to be summed it would also include O_{wi}. O_{wi} would be accounted for twice, once in the inner domain and once in the outer domain. To match the inner and outer solutions, the outer limit of the inner domain must therefore be subtracted from the solution:

$$\mathbf{w}(\boldsymbol{x}_S) = \mathbf{w}_{2D}(\boldsymbol{x}_S) + \mathbf{w}_{out}(\boldsymbol{x}'_S) - \mathbf{w}_{wi}(\boldsymbol{x}'_S) + o(1/\text{Æ}), \tag{5.4}$$

where $o(1/\text{Æ})$ is the error resulting from this. For swept or curved wings additional terms are needed - see Guermond and Sellier [85].

5.2.1 Inner solution

The inner solution solves the detailed 2D problem of flow about the aerofoil. In Chapters 2, 3 and 4, planar frequency-domain unsteady thin aerofoil theory was used. This had a close form solution, but cannot account for large-amplitude kinematics. In this chapter, Ramesh *et al.*'s [102] Large Amplitude Unsteady Thin Aerofoil Theory is used. It interacts with the outer solution via the discrete vortex based wake model, described in Sec. 5.2.2. The exact method of the inner solution is unimportant for LAULLT, and the theory could potentially be substituted for any discrete vortex shedding unsteady aerofoil theory such as those of Yan et al. [101], Katz and Plotkin [51], and McCune et al. [224]. This section contains a minimal explanation of LAUTAT in the context of LAULLT. For more a more detailed explanation, see Ramesh *et al.* [102].

The inner solution is evaluated at N_{inner} evenly distributed points over the span of the wing. The i^{th} inner solution is located at $y = y_i$ on L where $y_i < y_{i+1}$ for $i = 0, 1, ..., N_{\text{inner}}$, and exists in the x-z plane. A point in the ith inner solution is therefore at $\{x, y_i, z\}$. Each inner solution can be considered in isolation except for the corrective downwash accounting

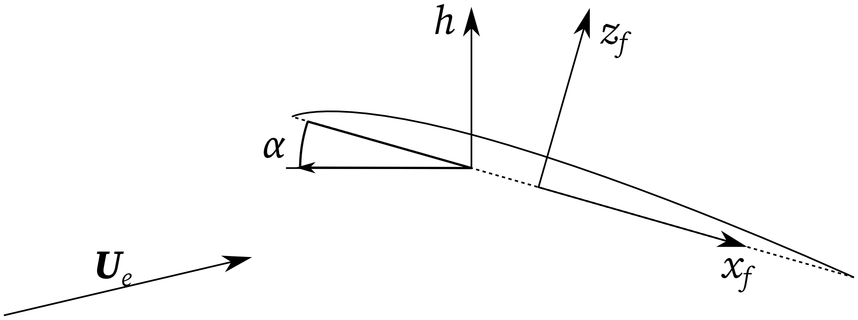

Figure 5.3: The aerofoil frame coordinate system. The camber line of the aerofoil is shown.

for 3D effects $\mathbf{w}_{out}(x, y_i) - \mathbf{w}_{wi}(x, y_i)$ (see Eq. 5.4) to obtain an effective free stream velocity $\boldsymbol{U}_e$:

$$\boldsymbol{U}_e(y_i; t) = \mathbf{U}_\infty + \mathbf{w}_{out}(y_i) - \mathbf{w}_{wi}(y_i), \tag{5.5}$$

where the velocities are in the x-z plane. For consistency among the inner solutions, the true free stream velocity $\mathbf{U}_\infty$ is used.

The inner solution is in the x-z plane at y_i on the span. The aerofoil is described using a local coordinate system shown in Fig. 5.3. The chord is on $x_f \in [-c(y_i)/2, c(y_i)/2]$, with leading edge located at $x_f = -c(y_i)/2$. As with the thin aerofoil presented in Appendix B.1, the bound spanwise vorticity distribution over the chord $\gamma_b(y_i; t)$ is described a Fourier series and a leading edge singularity,

$$\gamma_b(y_i; t) = 2|\mathbf{U}_\infty| \left(A_{i,0}(t) \frac{1 + \cos(\theta)}{\sin(\theta)} + \sum_{n=1} A_{i,n}(t) \sin(n\theta) \right), \tag{5.6}$$

where $x_f = c(y_i)\cos(\theta)/2$, and A_n are unknown time-varying coefficients. As in Chapter 3, the A_0 can be linked to the leading-edge suction parameter $\mathcal{L}$ [145], although this fact is not used in this chapter. The coefficients A_n can be obtained as

$$A_{i,0}(t) = -\frac{1}{\pi} \int_0^\pi \frac{W(\theta)}{|\mathbf{U}_\infty|} \, d\theta, \tag{5.7}$$

$$A_{i,0}(t) = \frac{2}{\pi} \int_0^\pi \frac{W(\theta)}{|\mathbf{U}_\infty|} \cos(n\theta) \, d\theta \quad \text{for } n > 0, \tag{5.8}$$

where $W(\theta, y_i; t)$ is the downwash on the aerofoil in the aerofoil coordinate system due to the sum of the free stream velocity, the movement of the aerofoil and the flow induced by vorticity in the 2D solution's wake.

The wake of each inner solution is modelled using discrete vortex particles in 2D, with a new vortex particle being generated at each time step. This allows a time-domain solution to be obtained, and avoids assumptions about the wake geometry. An illustration of this wake is shown in Fig. 5.4. The m^{th} vortex particle of the i^{th} inner solution is at coordinate

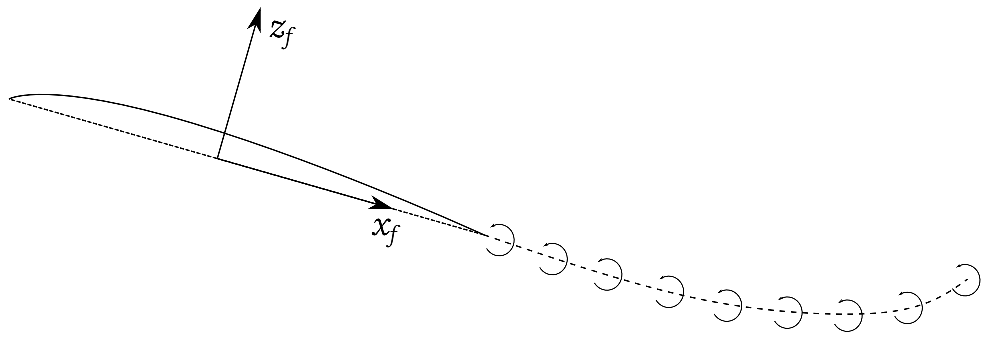

Figure 5.4: The wake of the aerofoil in the inner solution is represented using discrete vortex particles. The aerofoil camber line is shown.

$\boldsymbol{x}^p_{i,m} = \{x^p_{i,m}, z^p_{i,m}\}$ and has circulation $\Gamma^p_{i,m}$. The induced velocity on a point $\{x, z\}$ by the mth discrete vortex can be expressed as

$$\begin{Bmatrix} \frac{\partial \phi^p_{i,m}}{\partial x} \\ \frac{\partial \phi^p_{i,m}}{\partial z} \end{Bmatrix} = \frac{\Gamma^p_{i,m}}{2\pi} \frac{1}{(x - x^p_{i,m})^2 + (z - z^p_{i,m})^2} \begin{Bmatrix} z - z^p_{i,m} \\ x^p_{i,m} - x \end{Bmatrix}, \tag{5.9}$$

where $\phi^p_{i,m}(x, z; y_i)$ is the 2D velocity potential field in the x-z plane of the mth particle of the ith inner solution. Combining this with the kinematics and effective free stream velocity allows the local downwash to be obtained as

$$W(x_f, y_i; t) = \dot{h}\cos\alpha - \mathbf{U}_e \cdot \begin{Bmatrix} \sin\alpha \\ \cos\alpha \end{Bmatrix} - \frac{\dot{\alpha} c}{2}\left(x_f - \left(x^*_m - \frac{1}{2}\right)c\right) - \frac{\partial \phi^p_i}{dz_f}, \tag{5.10}$$

where $\dot{\alpha}$ and $\dot{h}$ are the time derivatives of the pitch and heave displacements of the aerofoil and $\phi^p_i = \sum_m \phi^p_{i,m}$ is the velocity potential due to the particles in the wake. Again, x^*_p is non-dimensionalised pitching location introduced in Chapter 2.

The wake is allowed to convect freely at each time-step. A forward Euler scheme is used:

$$\boldsymbol{x}^p_{i,m}|_{t+\Delta t} = \boldsymbol{x}^p_{i,m}|_t + \begin{Bmatrix} \frac{\partial \phi_i}{dx} \\ \frac{\partial \phi_i}{dz} \end{Bmatrix} \Delta t, \tag{5.11}$$

where t is time, Δt is the time step and $\partial\phi_i$ is the velocity potential field of the ith inner solution, and is the sum of the potentials of the aerofoil bound vorticity, the free stream and the wake particles. At every time step, a new vortex particle is shed into the wake to satisfy the Kelvin condition on the aerofoil. The mth particle is placed at time t is located at

$$\boldsymbol{x}^p_{i,m}|_t = \begin{cases} \boldsymbol{x}^p_{i,te}|_t + \frac{2\Delta t}{3}\left(\boldsymbol{U}_e + \dot{\boldsymbol{x}}^p_{i,te}|_t\right), & \text{if } m = 0 \\ \boldsymbol{x}^p_{i,te}|_t + \frac{2}{3}(\boldsymbol{x}^p_{i,m-1}|_t - \boldsymbol{x}^p_{i,te}|_t), & \text{otherwise} \end{cases}, \tag{5.12}$$

where $\boldsymbol{x}_{i,te}|_t$ is the coordinate of the trailing edge of the aerofoil in the ith inner solution at time t, and $\dot{\boldsymbol{x}}^p_{i,te}|_t$ its velocity. The strength of the new vortex particle is obtained using the Kelvin condition as

$$\Gamma_i(t) + \sum_{m=0} \Gamma^p_{i,m} = 0, \tag{5.13}$$

where $\Gamma_i(t)$ is the bound circulation about the ith inner solution. The can be obtained using the bound vorticity coefficients:

$$\Gamma_i(t) = \frac{|\mathbf{U}_\infty| c(y_i)}{2} \pi \left(A_{i,0} + \frac{A_{i,1}}{2} \right), \tag{5.14}$$

The normal force on the aerofoil in the ith inner solution can be computed as

$$\begin{aligned} C_n(y_i;t) = \frac{2}{|\mathbf{U}_\infty|} \Bigg[& \left(\boldsymbol{U}_e \cdot \begin{Bmatrix} \cos\alpha \\ -\sin\alpha \end{Bmatrix} + \dot{h} \sin\alpha \right) \left(A_{i,0} + \frac{1}{2} A_{i,1} \right) \\ & + c \left(\frac{3}{4} \dot{A}_{i,0} + \frac{1}{4} \dot{A}_{i,1} + \frac{1}{8} \dot{A}_{i,2} \right) \Bigg] + \frac{2}{c|\boldsymbol{U}_\infty|^2} \int_{-c/2}^{c/2} \frac{\partial \phi^p_i}{\partial x_f} \gamma_b(x_f; y_i, t)\, dx_f, \end{aligned} \tag{5.15}$$

and the leading-edge suction force as

$$C_s(y_i;t) = 2\pi A^2_{i,0}. \tag{5.16}$$

From C_n and C_s the lift coefficient of any inner solution can be found as

$$C_l(y_i;t) = C_n \cos\alpha + C_s \sin\alpha. \tag{5.17}$$

5.2.2 The outer wake

In the outer solution, the inner solutions must be interpolated to obtain a wake. From this wake a correction to account for 3D effects can be obtained.

The outer wake is based on the discrete vortex particle wake of the inner solutions. Coordinates in the inner domain $\boldsymbol{x} = \{x, z\}$ are mapped to the outer domain $\boldsymbol{x}' = \{x', y', z'\}$ as

$$\begin{Bmatrix} x' \\ y' \\ z' \end{Bmatrix} = \begin{Bmatrix} x_i - x_{i,te} \\ y_i \\ z_i - z_{i,te} \end{Bmatrix}, \tag{5.18}$$

where the subscript i, te indicates the trailing edge coordinate of the ith inner solution.

Having transformed the coordinates of the vortex particles into the outer domain, a vortex lattice representing the 3D wake is constructed. This is shown in Fig. 5.5.

The inner solutions are solved in lock-step, and consequently have the same number of wake vortex particles. The mth vortex particle across all i wakes can be interpolated using a cubic spline [225]. For $y < y_0$ or $y > y_N$ the cubic spline is linearly extrapolated.

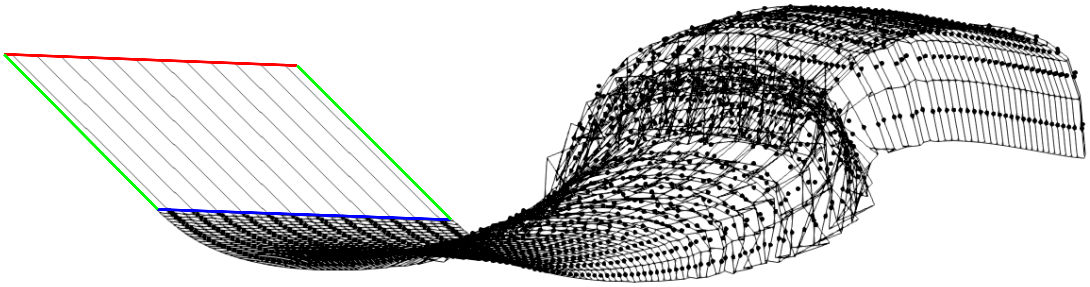

Figure 5.5: The vortex particles of the inner solutions are transformed to the outer domain and interpolated. Inner solution chord lines included for illustrative effect. The locations of the leading edge, trailing edge and wing tips are shown in red, blue and green respectively.

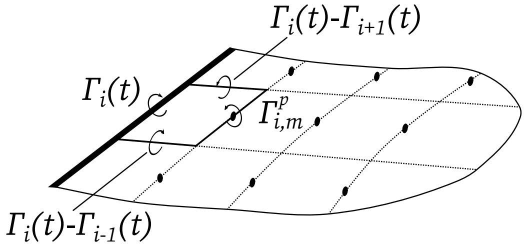

Figure 5.6: Assembly of the wake vortex lattice.

This allows a vortex lattice to be assembled, shown in Fig. 5.6. Vortex filaments intersect the location $\boldsymbol{x}^{p'}$, matching their circulation. The vortex wake implicitly satisfies both Helmholtz's theorems and Kelvin's theorem.

The vortex lattice vertices are obtained by evaluating the splines obtained by interpolation of the coordinates of the mth vortex particles for all inner solutions at $y = \{-s, (y_0 + y_1)/2, (y_1 - y_2)/2, ..., (y_{N-1} + y_N)/2, s\}$, creating a grid of points. The grid is extended to include the lifting-line bound vorticity.

The Biot-Savart law [51] can be used integrate the induced velocity on the lifting-line at y_i to obtain $\mathbf{w}_{out}(M_0)$. Since the lifting-line is straight, the influence of the vortex filaments on the line $x = z = 0$ can be ignored.

To obtain the 3D correction $\boldsymbol{w}_{wi}$ is also needed. This computation is similar to evaluation of velocity due to the wake in the inner solution, except that the outer coordinates are used.

$$\mathbf{w}_{wi}(M_0) = \begin{Bmatrix} \sum_{m=0}^{M} \frac{-\Gamma_{i,p}}{2\pi} \frac{z'_{i,m}}{x'^2_{i,m}+z'^2_{i,m}} \\ 0 \\ \sum_{m=0}^{M} \frac{\Gamma_{i,p}}{2\pi} \frac{x'_{i,m}}{x'^2_{i,m}+z'^2_{i,m}} \end{Bmatrix}. \tag{5.19}$$

Having obtained $\mathbf{w}_{out}$ and $\mathbf{w}_{wi}$, the a new effect free stream $\boldsymbol{U}_e$ can be computed for each inner solution according to Eq. 5.5.

To compute the whole-wing force coefficients, the lift distribution across the wing is interpolated using cubic splines and then integrated.

$$C_L(t) = \frac{1}{2s\bar{c}} \int_{-s}^{s} C_l(y;t)c(y)\, dy. \tag{5.20}$$

5.2.3 Algorithm

A time marching-algorithm is used to obtain a solution. It is as follows:

1. Construct the wake in the outer solution by interpolating the inner solutions.
2. Compute 3D correction downwash according to Eq. 5.4 to obtain $\boldsymbol{U}_e$.
3. Place new vortex particles and solve the inner solution.
4. Perform convection of vortex particles for time-step.
5. Return to step 1.

The inner solutions can be considered individually for the purpose of placing new particles, solving, and convecting the wake. The new vortex particles are within a radius of $O(c)$ of the chord section, and so can be considered with domain I. This justifies solving the inner solutions independently.

It is important to distinguish the method from the aesthetically similar unsteady vortex lattice method. In the LAULLT, self-convection occurs in the inner solution. The induced velocity of the vortex lattice is only evaluated on the lifting-line on the outer solution. Consequently for N_{inner} inner solutions and M vortex particles the cost of self-convection on each step of LAULLT is $\mathcal{O}(N_{\text{inner}}M^2)$. This compares to $\mathcal{O}(N^2M^2)$ for a UVLM for a N by M lattice. The freedom of the wake is constrained, but this comes with the benefit that the LAULLT is comparatively robust.

Compared to the UCoFD method of Chapter 4, the algorithmic complexity of LAULLT is high. To simulate a given period of time $t_{\max}$, the number of steps and therefore wake particles scales as $t_{\max}/\Delta t$. This results in a total complexity of $\mathcal{O}(1/\Delta t^3)$ for naive wake convection, or $\mathcal{O}(1/\Delta t^2)$ if wake self-convection is neglected or the fast multipole method [204] is applied. In comparison, the complexity of the UCoFD method is far lower, with the fast Fourier transform scaling as $\mathcal{O}(1/\Delta t \log(1/\Delta t))$.

5.2.4 Limitations

The LAULLT shares some of the same limitations as the lifting-line theory presented in Chapter 2. It assumes that the wing is straight and of high aspect ratio, and that the inner solution is varying slowly with respect to span. Technically it ought not to be applied to rectangular or elliptic wings. The method assumes inviscid, incompressible flow, although this limitation could be partially avoided with substitution of the inner solution. The method also assumes all vorticity is shed from the trailing edge of the wing.

5.3 Results and discussion

The results obtained using LAULLT are compared to the results obtained from CFD, and to linearised lifting-line theories presented in Chapter 2 and Chapter 4. In previous chapters, it was usually found that the moment coefficient prediction of ULLT was as good as or better than lift coefficient prediction. Therefore, this chapter focuses on lift coefficient results.

The results are separated into three sections. Firstly, the LAULLT is applied to Euler-regime heave oscillation problems, with results compared to those from the C-ULLT of Chapter 2 in Sec. 5.3.1. These cases verify the similarity of the different lifting-line theories. The Euler CFD used for comparison in this section is detailed in Appendix C.1.

Next, small-amplitude time-domain cases is examined in Sec. 5.3.2. The pitch and heave cases from Chapter 3 are repeated, allowing comparison to the UCoFD method. These demonstrate the applicability of the LAULLT to time-domain problems.

Finally, LAULLT is applied to large-amplitude low Reynolds number cases in Sec. 5.3.3. The large-amplitude allows the non-linearity of the LAULLT to be demonstrated. The low Reynolds number CFD setup detailed in Appendix C.2 is used for comparison. Comparison to the CFD also shows a shortcoming of the LAULLT method - it cannot model the leading-edge vortices that are common in large amplitude cases.

5.3.1 Small-amplitude oscillating Euler regime problems

The large-amplitude unsteady lifting-line theory aims to expand on the capabilities of the C-ULLT introduced in Chapter 2, and the UCoFD method (which, as presented, is based on the C-ULLT) introduced in Chapter 4. It should therefore be capable of producing similar results to both methods when confined to problems where the small amplitude assumption is valid. In this section, the LAULLT is compared to the C-ULLT for a problem of a wing oscillating in heave. For all these cases, the LAULLT was run for enough oscillations of the wing for convergence to occur.

The heave oscillation of rectangular wings is considered, with the kinematics defined in Chapter 2 as $h(t) = h_0^* c e^{i\omega t}$ (Eq. 2.7). The lift coefficient with respect to time is shown in Fig. 5.7 for four cases. Rectangular wings of aspect ratios 8 and 2 are studied at chord reduced frequencies $k = 0.125$ and $k = 1.5$

Figure 5.7(a) shows the results obtained for an aspect ratio 8 wing oscillating at a low chord reduced frequency, $k = 0.125$. The low frequency and high aspect ratio mean that the C-ULLT is expected to perform well (see Chapter 2). The LAULLT was modelled

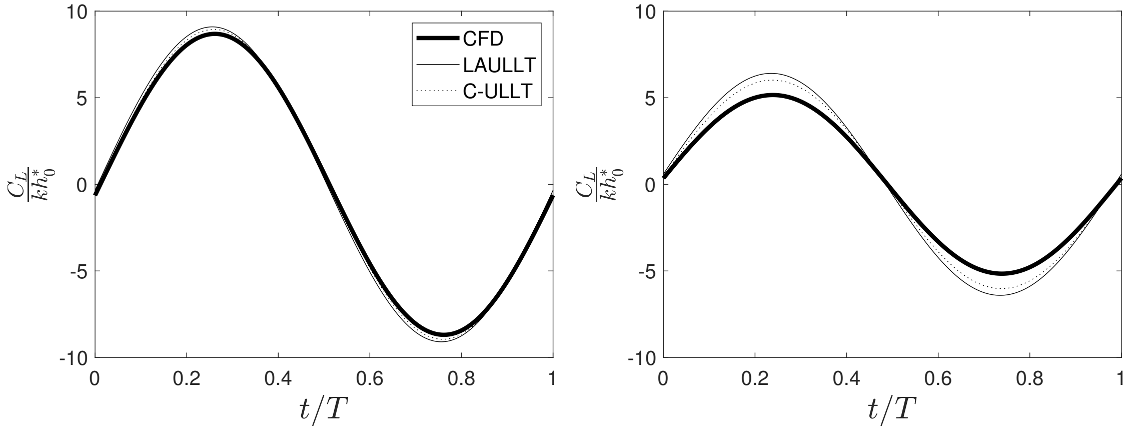

(a) Aspect ratio 8, $k = 0.125$ (b) Aspect ratio 2, $k = 0.125$

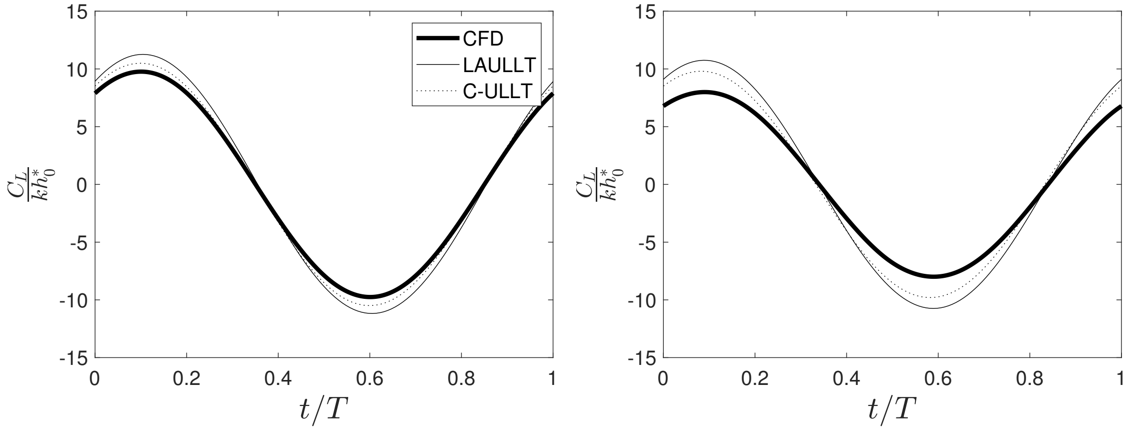

(c) Aspect ratio 8, $k = 1.5$ (d) Aspect ratio 2, $k = 1.5$

Figure 5.7: Comparison of Euler CFD, LAULLT and C-ULLT results for rectangular wings oscillating in heave.

with a non-dimensional timestep $\Delta t^* = 0.025$, and 32 equally spaced inner solutions. The LAULLT matches the C-ULLT well and is almost exactly sinusoidal. Both low-order methods slightly overestimate the lift-amplitude of the CFD. The LAULLT over-predicts lift amplitude by 5% and 17% for the aspect ratio 8 case and aspect ratio 2 case respectively.

In Chapter 2 Sec. 2.3.2, it was found that the C-ULLT over-predicted the lift amplitude of low aspect ratio rectangular wings. This effect can be also be seen in Fig. 5.7(b). The LAULLT obtains a similar result, predicting a slightly higher oscillation amplitude than the C-ULLT. For this case, the LAULLT used the same timestep $\Delta t^* = 0.025$ and 8 inner solutions across the span of the wing.

The difference between the LAULLT and C-ULLT predictions grows at high chord reduced frequency $k = 1.5$, shown in Fig. 5.7(c), despite the high aspect ratio. The reason for this is the high-frequency performance of the large-amplitude unsteady thin-aerofoil theory used in the inner solution. As chord-reduced frequency increases a smaller time-step is required in order to obtain good results. Here, $\Delta t^* = 0.01$ is used. In the LAULLT method, the cancellation of the effects of $\mathbf{w}_{out}(M_0) - \mathbf{w}_{wi}(M_0)$ can be numerically troublesome. The singular nature of vortex elements used in the wake result in both terms scaling as $1/r$ where r is the radius from the wing. The nearest wake elements to the wing are at a distance proportional to Δt. Consequently, the magnitude of the induced downwash is $O(1/\Delta t)$. The subtraction of the floating-point representations of these large downwashes introduces numerical errors as Δt becomes small. Additionally, the numerical cost of the solution increases as $O(1/\Delta t^3)$ if naive methods are used for convection in the inner domain. Consequently, the lift amplitude error of the LAULLT is 15%. At aspect ratio 2 and $k = 1.5$, shown in Fig. 5.7(d), the LAULLT slightly over-predicts the C-ULLT again. Both over-predict the results obtained by CFD, as expected (see Sec. 2.3.2). This time, then amplitude error of the LAULLT is 34%.

For small-amplitude frequency-domain problems, the LAULLT is capable of producing similar results to the analytical C-ULLT studied in Chapter 2. The time-step used must be adjusted to obtain good results for higher frequency problems. However, too small a time step introduces numerical and computational cost difficulties.

LAULLT is formulated in and intended for the time domain. In the next section, LAULLT is compared to the UCoFD method of Chapter 4 for small-amplitude time-domain problems in the Euler regime.

5.3.2 Small-amplitude time-domain Euler regime problems

In Chapter 4, small-amplitude time-domain problems in the Euler regime were evaluated using the UCoFD method, which allowed the frequency-domain C-ULLT of Chapter 2 to be applied to time-domain problems. The LAULLT amplitude is applied to these same problems, referred to as Case 4.1 and Case 4.2 in Table 4.1.

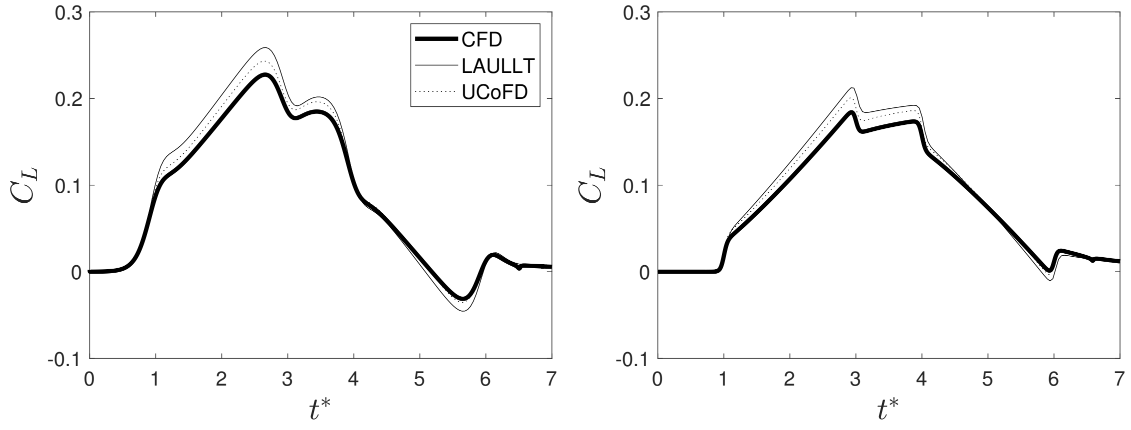

(a) A smooth leading-edge pitch ramp-hold-return motion (b) A non-smooth heave velocity ramp-hold-return motion

Figure 5.8: Comparison of Euler CFD, LAULLT and UCoFD results for aspect ratio 4 rectangular wings undergoing ramp-hold-return kinematics.

The lift coefficient results from CFD, LAULLT and UCoFD for Case 4.1 and Case 4.2 are shown in Fig. 5.8.

Case 4.1 was initially analysed in Sec. 4.3.1 using the UCoFD method. An aspect ratio 4 rectangular wing undergoes a leading-edge pitch ramp-hold-return motion in the Euler regime. The amplitude is small (3°), and the kinematics are smooth, as shown in Fig. 4.2. Figure 5.8(a) shows the lift prediction of LAULLT for these same kinematics compared to the results of CFD and UCoFD.

As for the oscillation cases, the LAULLT model, which used 16 inner solutions and a time-step $\Delta t^* = 0.025$, slightly over-predicts the UCoFD results and over-predicts the CFD result by a larger margin. However, it predicts the shape of the C_L curve well and, unlike the UCoFD method, can be integrated into solvers where the kinematics are not known in advance.

A similar result is observed in the results of Case 4.2, shown in Fig. 5.8(b). The LAULLT over-predicts lift in comparison to the CFD and UCoFD method. Once again, at time-step of $\Delta t^* = 0.025$ is used. In the last section, Sec. 5.3.1, it was found that small time-steps are required for higher frequency kinematics. For the lift-spikes present here, which represent the high-frequency component of the kinematics input signal, the LAULLT appears to provide a good solution nonetheless. The UCoFD method required special treatment of the kinematics to avoid non-zero final displacements. In comparison, the LAULLT method is simple to apply.

So far, this chapter has concentrated on small amplitude kinematics. Larger amplitude kinematics, supposedly an advantage of the LAULLT over UCoFD, are studied in the next section.

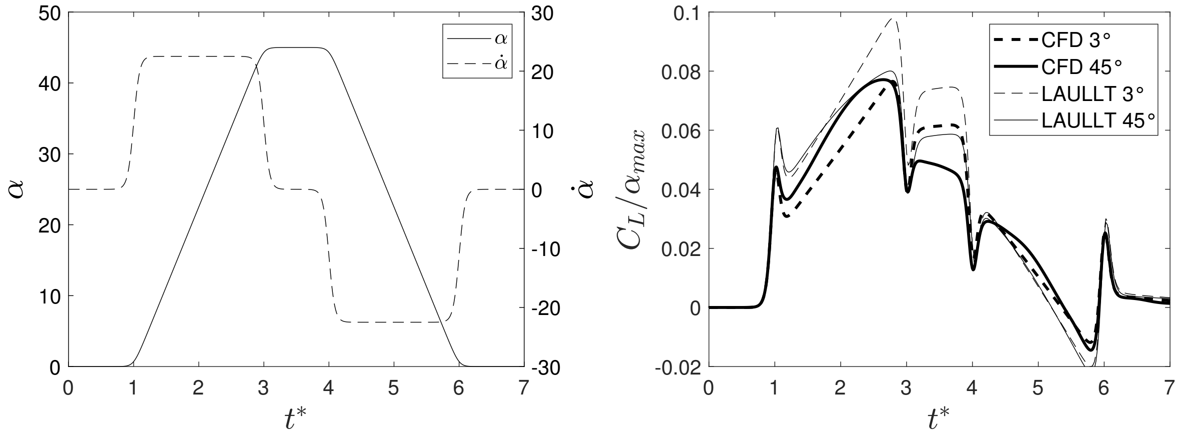

(a) Leading edge pitch kinematics

(b) Lift coefficient

Figure 5.9: The kinematics and whole wing lift for a wing undergoing a pitch ramp-hold-return manoeuvre at two amplitudes at Re = 10 000.

5.3.3 Large-amplitude time-domain low Reynolds number problems

In Sec. 5.3.1 and Sec. 5.3.2 the LAULLT was compared to CFD and small-amplitude lifting-line theory results for small amplitude problems in the Euler regime. To solve for the aerodynamics in research areas such as micro air vehicles, unmanned aerial vehicles or energy harvesting devices, solutions for low Reynolds number, high amplitude problems are required. A Reynolds number 10 000 case is considered in this section at small and large amplitude.

A non-smooth pitch ramp is considered. As in Chapter 4, it is defined by the canonical pitch ramp motion of Ol *et al.* [223], expressed as

$$\alpha(t) = \frac{P}{a\bar{c}}\left[\frac{\cosh(aU_\infty(t-t_1)/\bar{c})\cosh(aU_\infty(t-t_4)/\bar{c})}{\cosh(aU_\infty(t-t_2)/\bar{c})\cosh(aU_\infty(t-t_3)/\bar{c})}\right]$$

where $a = \pi^2/(4(t_2 - t_1)(1-\sigma))$. Here P set to give $\alpha_{\max} = 3°$ for the small-amplitude problem and $\alpha_{\max} = 45°$ for the large amplitude problem. The timing parameters are set to $t_1^* = 1$, $t_2^* = 3$, $t_3^* = 4$ and $t_4^* = 6$, where $t^* = tU_\infty/\bar{c}$. Both the kinematics and the results from the LAULLT are compared to those from CFD in Fig. 5.9.

The kinematics are displayed in Fig. 5.9(a). The pitch ramp-hold-return pivots about the leading edge of the wing. The kinematics are non-smooth, resulting in large angular accelerations $\ddot{\alpha}$. These are reflected in the lift coefficient obtained, displayed in Fig. 5.9(b).

The dashed lines represent the lower amplitude kinematics with a maximum pitch angle of 3°. The LAULLT solution accurately reproduces the shape of the CFD result, but overestimates the magnitude of the C_L curve. This is consistent with previous results. The UCoFD method over-predicted lift for a low Reynolds number time-domain case in

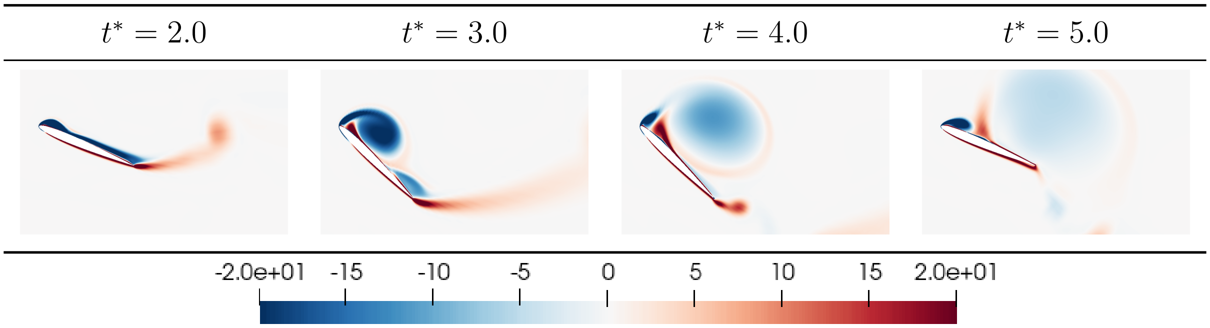

Figure 5.10: Normalised spanwise vorticity $\omega_y c/U$ for a rectangular aspect ratio 6 wing pitching to 45° at Re = 10 000.

Sec. 4.3.3, and the LAULLT has over-predicted the C-ULLT and UCoFD methods in this chapter.

The solid lines show the results obtained for a ramp to 45°. The initial spike at $t^* = 1$ is due to the acceleration of the wing combined with the effect of added mass. At both amplitudes, the LAULLT overestimates the magnitude of this spike, although normalised lift coefficient $C_L/\alpha_{\max}$ matches for both amplitudes. This is consistent with results of the CFD for both amplitudes. As the pitch angle increases, the C_L increases. For the small amplitude case, the rate of increase is approximately constant until the end of the initial ramp motion at $t^* = 3$. For the 45° case, the rate of increase decreases as the maximum angle of attack is reached. This is the result of geometric non-linearity in the LAULLT. As a result, the LAULLT approximately matches the shape of the CFD results. However, the CFD results suggest that the normalized lift coefficient $C_L/\alpha_{\max}$ of both cases should approximately match at time $t^* = 3$. This is not the case in the LAULLT results since the method does not model the leading-edge vortex.

The leading-edge vortex that forms in the CFD result for the large amplitude case is displayed in Fig. 5.10. The visualisation displays the normalised spanwise vorticity at the wing centre. For a more detailed discussion of the leading-edge vortex, see Chapter 3, Sec. 3.5.

Geometric non-linearity leads to a reduction in lift at high angles of attack, as observed in the LAULLT results. At large pitch angles, the normal force is no longer acting solely in the lift direction. However, large-amplitude kinematics are often accompanied by leading-edge vortices. As established in Chapter 3, these lead to a super-linear increase in lift with respect to kinematics amplitude. These effects interact such that the peak lift obtained in the CFD result is approximately similar for both the small amplitude and large amplitude problems.

The LEV leads to a reduction in the $C_L/\alpha_{\max}$ in the CFD result in the hold phase of the kinematics between $t^* = 3$ and $t^* = 4$. In small amplitude 3° CFD result, the lift stays constant. For the large amplitude case, the lift decreases due to the detachment of the

LEV from the wing. The LAULLT results do not reflect this phenomenon.

The LAULLT over-predicts lift at low Reynolds number in comparison to CFD. For large-amplitude case, it includes the effects of geometric non-linearity. However, such cases often include leading-edge vortices which are not included in the LAULLT.

5.4 Summary

A time-domain unsteady lifting-line theory including geometric non-linearities was formulated by combining Ramesh *et al.*'s large-amplitude unsteady thin-aerofoil theory with lifting-line theory. The discrete vortex based wake of the 2D inner solutions were matched in the outer 3D domain using a vortex lattice constructed at each time step. The time-marching solution makes the theory easy to apply to problems where the kinematics are not known in advance, such as that of flight dynamics.

The theory, named Large-Amplitude Unsteady Lifting-Line Theory (LAULLT) was compared to CFD, and to the C-ULLT and UCoFD method introduced in Chapter 2 and Chapter 4 respectively. For Euler regime small-amplitude problems it obtains similar results to the linearised C-ULLT and UCoFD methods.

LAULLT was also compared to CFD results for leading-edge pitching problems in the low Reynolds number Re = 10 000 regime. As is consistent with results in previous chapters, the LAULLT over-predicted the CFD result for lift for a small-amplitude (3°) ramp-hold-return motion. For a larger amplitude, 45° ramp-hold-return, the LAULLT includes some features of the CFD result. It successfully included a loss of lift resulting from large angle of attack. However, the LAULLT does not model the LEV found in the CFD result. This LEV has a significant impact on the lift of the wing, leading to a difference between the CFD and LAULLT results.

Ramesh *et al.* [102] expanded upon the LAUTAT model to include leading-edge vortex shedding using the Leading Edge Suction Parameter [145] (see Chapter 3). The natural next step in the evolution of the LAULLT model is to use the LEV-capable 2D solution, using a second wake to represent the LEV in the outer domain. Unfortunately this is numerically unstable, perhaps due to the rapid change in bound vorticity with respect to span withing the confines of a Guermond and Sellier [85] based framework. To include 3D LEV phenomena, a truly 3D method is required.

In the next chapter, a 3D method capable of modelling the LEV is consequently introduced.

Chapter 6

A method to include the leading-edge vortex

6.1 Introduction

The leading-edge vortex has featured heavily in this dissertation. It is an aerodynamic non-linearity resulting from flow separation at the leading-edge of a wing. The resulting shear layer rolls up on itself to form a large vortex structure capable of significantly altering the wing's aerodynamics. The LEV structure was first encountered in Chapter 3, where the predictions of frequency-domain unsteady lifting-line theory were at best worsened in the presence in the LEV, as in the case of whole-wing forces, or at worst rendered useless, as in the case of force distributions.

Linearity, both with respect to geometry and aerodynamic phenomena, was assumed in Chapters 2-4. These assumptions allow ULLT to be more easily formulated, and the computational cost of analysis reduced. In Chapter 5, the assumption of geometric linearity was removed with the formulation of a Large Amplitude Unsteady Lifting-Line Theory (LAULLT). However, with large-amplitude kinematics comes LEVs. It was originally intended that the LAULLT would be extended to include LEVs using the leading-edge suction parameter to determine separation. However, this was unsuccessful, partially because of the highly three-dimensional nature of the LEV structure on finite wings. A 3D solution is needed.

The Unsteady Vortex Lattice Method (UVLM) is a popular method for 3D analysis of unsteady wing aerodynamics. The wing and wake are represented by a lattice of vortex filaments that implicitly satisfies Helmholtz's theorems and the Kelvin condition. However, the UVLM alone cannot model the leading-edge vortex due to the assumption of inviscid, incompressible flow. LEV formation is a viscous phenomenon.

For unsteady thin-aerofoil theory, also based on potential flow, this problem has been overcome through the leading-edge suction parameter of Ramesh *et al.* [145], introduced in Chapter 3. An aerofoil leading edge can only provide so much suction to keep flow attached for a given geometry and Reynolds number. This suction can be linked to the vorticity or pressure distribution of the aerofoil to create a leading-edge vortex shedding criterion. These models have been used successfully in 2D.

In 3D, the validity of the LESP criterion has been verified by Hirato *et al.* [172]. It was applied to finite wings as an extension of the UVLM, where a leading-edge wake formed the LEV [187]. However, the UVLM introduces challenges. The nature of the problem makes the solution prone to numerical instability, especially at the core of the leading-edge vortex. Correcting for the extreme vortex distortion is challenging. If LEV shedding could be successfully completed, the merger of the LEV into the trailing-edge wake vortex rings is a viscous phenomenon. With the UVLM modelling LEVs, only short-running simulations could be obtained.

Vortex particles provide an alternative to vortex filaments. Winckelmans *et al.* [189] recommend that in situations where the limitations of vortex filaments become noticeable, vortex particles be used instead. This approach is taken in this chapter.

A vortex lattice wing is combined with leading-edge and trailing-edge vortex lattice near wakes. These wakes are converted to regularised vortex particles a short distance from the wing. The LESP is used to determine flow criticality at the leading edge and the vortex particle wake is allowed to freely convect. The solution is stabilised by redistribution of vortex particles making the method semi-Lagrangian. The method obtained was named the Vortex Formation on Finite Leading Edge or VoFFLE method.

The chapter begins with theory in Sec. 6.2. The semi-Lagrangian vortex particle method is described in Sec. 6.2.1 and vortex filaments are introduced in Sec. 6.2.2. The vortex filaments are combined into a vortex lattice capable of modelling the wing geometry and near wake in Sec. 6.2.3. A key aspect of the model is the determination of wake vorticity strength. For the trailing-edge wake this is determined using the Kutta condition. For the leading-edge wake, this is determined using the LESP criterion. The process of determining the vorticity of the wing and wakes is outlined in Sec. 6.2.4, before the time-stepping algorithm and implementation details are described in Sec. 6.2.5. Having described the method, the results obtained are detailed in Sec. 6.3. First, the solutions obtained from CFD, VoFFLE and UVLM for the trailing-edge wake of a wing oscillating in heave are studied in Sec. 6.3.1. This case verifies that VoFFLE correctly models unsteady wake evolution. In Sec. 6.3.2, the VoFFLE method is used to model the leading-edge vortex and compared to CFD results. The chapter is summarised in Sec. 6.4.

6.2 Theory

In Chapter 5, singular vortex particles were used to model the wake of an aerofoil in 2D. For 3D problems, vortex particle theory becomes more complicated. It must account for vortex stretching, and regularisation is required for stability and convergence. As the Lagrangian vortex particle field distorts, it must be periodically redistributed. This vortex particle theory is described in Sec. 6.2.1.

The wing and near wake are represented using the unsteady vortex lattice method. The wake vortex lattice is converted into vortex particles a short distance from the wing. Section 6.2.2 describes the vortex filaments and Sec. 6.2.3 describes the vortex lattice structure. The vorticity distribution of wake and the wing is described in Sec. 6.2.4, and the time-marching procedure in Sec. 6.2.5.

6.2.1 Vortex particles

Vortex particles represent a vortical fluid element with a vector valued circulation $\boldsymbol{\alpha}$ which is the integral of vorticity $\boldsymbol{\omega}$ within the volume. In this dissertation they were first encountered in Chapter 5, where the wake of an aerofoil was represented using singular vortex particles. For singular vortex particles, the circulation of the volume represented by a particle acts from a point. Consequently, the discretised vorticity field $\tilde{\boldsymbol{\omega}}$ represented by a set of vortex particles can be described as

$$\tilde{\boldsymbol{\omega}}(\boldsymbol{x};t) = \sum_{m}^{M} \boldsymbol{\alpha}_m^p(t)\delta(\boldsymbol{x} - \boldsymbol{x}_m^p(t)), \tag{6.1}$$

where the effects of M singular particles with circulation $\boldsymbol{\alpha}_m^p$ and position $\boldsymbol{x}_m^p$ are summed. The singular nature of the vortex particles is described with the 3D Dirac delta function, $\delta(\boldsymbol{x})$. It is important to note that the true vorticity field $\boldsymbol{\omega}(\boldsymbol{x};t)$ and the discretised field are different $\tilde{\boldsymbol{\omega}}(\boldsymbol{x};t)$ are different. According to Helmholtz's theorems, the true field is divergence free but the discretised field is not. However, the resulting velocity $\boldsymbol{u}(\boldsymbol{x})$ is divergence free in both cases.

For free wakes the vortex particles are free to convect at the local velocity

$$\frac{d\boldsymbol{x}_m^p}{dt} = \boldsymbol{u}(\boldsymbol{x}_m^p). \tag{6.2}$$

The circulation of the vortex particles also changes with respect to time to match the stretching and contraction of an equivalent vortex filament. This change is described as

$$\frac{d\boldsymbol{\alpha}_m^p}{dt} = \nabla\boldsymbol{u}(\boldsymbol{x}_m^p)\cdot\boldsymbol{\alpha}_m^p. \tag{6.3}$$

The velocity of induced by vortex particles can be described as

$$\boldsymbol{u}(\boldsymbol{x};t) = -\sum_{m}^{M} \frac{q\left(\frac{|\boldsymbol{x}-\boldsymbol{x}_m^p|}{\mu}\right)}{|\boldsymbol{x}-\boldsymbol{x}_m^p|^3} (\boldsymbol{x}-\boldsymbol{x}_m^p) \times \boldsymbol{\alpha}_m^p \tag{6.4}$$

where, for singular particles, $q_{\text{singular}} = 1$. Evidently, for singular particles as $|\boldsymbol{x}-\boldsymbol{x}_m^p| \to 0$, the induced velocity $\boldsymbol{u}(\boldsymbol{x};t) \to \infty$. The vortex stretching term consequently also singular. This can be troublesome for the numerical stability, so instead of singular particles regularised particles with regularisation distance ('radius') μ are used.

Instead of concentrating the circulation of the volume represented by the vortex particle at a singular point, regularised particles assume a distribution of vorticity $\zeta(\rho)$, normalised by the regularised particle's radius μ:

$$\tilde{\boldsymbol{\omega}}(\boldsymbol{x};t) = \sum_{m}^{M} \frac{\boldsymbol{\alpha}_m^p(t)}{\mu^3} \zeta\left(\frac{\boldsymbol{x}-\boldsymbol{x}_m^p(t)}{\mu}\right). \tag{6.5}$$

For singular particles, this $\zeta_{\text{singular}}(\rho) = \rho^3 \delta(\boldsymbol{x}-\boldsymbol{x}_m^p(t))$. Most regularisation functions are radially symmetric. This makes it convenient to introduce the radius vector $\boldsymbol{r}$ and the regularised radius $\rho = |\boldsymbol{r}|/\mu$.

As discussed in literature review Sec. 1.1.9, regularised particles are also preferable for their convergence characteristics. So long as the regularised particles overlap, the discretised vorticity field $\tilde{\boldsymbol{\omega}}$ is approximately solenoidal. For Euler problems, the convergence of regularised vortex particle methods was proven by Beale and Majda [191], meaning as the radius of the particles shrink the solution obtained tends to the true Navier-Stokes solution. In practice, regularised particles make it easier to achieve stable, long-running simulations.

For Eq. 6.4, used to obtain the velocity induced by a vortex particle field, a velocity regularisation function $q(\rho)$ is required. For regularised particles this obtained as

$$q(\rho) = \int_0^\rho \zeta(\xi)\xi^2 \, d\xi, \tag{6.6}$$

$$\zeta(\rho) = \frac{1}{\rho^2}\frac{dq}{d\rho}(\rho). \tag{6.7}$$

Writing an expression for the vortex stretching equation, Eq. 6.3, is less straightforward. Three equivalent equations can be written for the true vorticity field $\boldsymbol{\omega}$. However, for the discretised field $\tilde{\boldsymbol{\omega}}$ these forms are no longer equivalent. Consequently, Winckelmans and Leonard [198] and Cottet and Koumoutsakos [194] describe three schemes for the interaction of vortex particles: classical, mixed and transpose. No one scheme is 'superior'. In this dissertation, the transpose scheme is used since it conserves the total vorticity of the problem. This transpose scheme can be described as

$$\frac{d\boldsymbol{\alpha}_m^p}{dt} = \sum_n \frac{1}{\mu^3}\left(q(\rho_{nm})\frac{\boldsymbol{\alpha}_m^p \times \boldsymbol{\alpha}_n^p}{\rho_{nm}^3} + \frac{1}{|\boldsymbol{r}_{nm}|^2}\left(3\frac{q(\rho_{nm})}{\rho_{nm}^3} - \zeta(\rho_{nm})\right)(\boldsymbol{\alpha}_m^p \cdot (\boldsymbol{r}_{nm} \times \boldsymbol{\alpha}_n^p))\boldsymbol{r}_{nm}\right) \tag{6.8}$$

where $\boldsymbol{r}_{nm}$ is the vector between the two particles $\boldsymbol{x}_m - \boldsymbol{x}_n$, and ρ_{nm} is $|\boldsymbol{r}_{nm}|/\mu$.

Some regularisation functions are more common. Winckelmans and Leonard [198] and Winckelmans *et al.* [189] list some well studied regularisations, but for the results obtained in this chapter, Gaussian regularisation is used. This is defined as

$$4\pi\zeta_{\text{gaussian}}(\rho) = \sqrt{\frac{2}{\pi}}e^{-\rho^2/2} \tag{6.9}$$

$$4\pi q_{\text{gaussian}}(\rho) = \operatorname{erf}(\rho/\sqrt{2}) - \rho\zeta_{\text{gaussian}}(\rho) \tag{6.10}$$

were $\operatorname{erf}(x)$ is the error function as described by Olver et al. [221].

Having defined the induced velocity, vortex stretching, and regularisation, a Lagrangian solution, where the particles convect at the local velocity, can be defined. Lagrangian solutions may be sufficient for problems where the wake does not distort significantly. However, the purpose of this chapter is to simulate problems where vortical effects are strong. This can be challenging.

The leading-edge vortex results in significant vortex stretching. As a consequence, the vortex particles representing the wake either spread apart or bunch together. Bunched particles introduce unnecessary computational cost, whereas overly stretched particles can be spread too far apart. The discretised vorticity field $\tilde{\boldsymbol{\omega}}$ becomes non-solenoidal if the particles no longer over-lap, resulting in the true vorticity field $\boldsymbol{\omega}$ being poorly approximated. This can lead to numerical instability. Redistribution of the vortex particles can alleviate this problem.

A poorly distributed set of vortex particles can be replaced by a set of vortex particles placed on the vertices of an equally spaced grid. In this chapter, a spacing of $2\mu/3$ is used. The proper equal spacing of the new vortex particles ensures proper representation of the vorticity field. The circulation of each of the new particles is defined by a redistribution function $\Lambda_{3D}(2\boldsymbol{r}/3\mu)$. This 3D function can be obtained from a 1D redistribution function $\Lambda(r/\mu)$ as $\Lambda_{3D} = \Lambda(|2\boldsymbol{r}_{nm}\cdot\boldsymbol{e}_x|/3\mu)\Lambda(|2\boldsymbol{r}_{nm}\cdot\boldsymbol{e}_y|/3\mu)\Lambda(|2\boldsymbol{r}_{nm}\cdot\boldsymbol{e}_z|/3\mu)$, where $\boldsymbol{e}_x$, $\boldsymbol{e}_y$ and $\boldsymbol{e}_z$ are the Cartesian basis vectors. Again there are multiple possible distribution schemes, some of which are described in Winckelmans *et al.* [189]. For the results obtained in this dissertation a redistribution scheme that conserves moments up to the third order is used:

$$\Lambda(\rho) = \begin{cases} \frac{1}{2}(1-\rho^2)(2-\rho), & \text{if } 0 \leq \rho \leq 1 \\ \frac{1}{6}(1-\rho)(2-v)(3-\rho), & \text{if } 1 \leq \rho \leq 2 \\ 0, & \text{otherwise} \end{cases} \tag{6.11}$$

Applying the redistribution scheme allows the nth new particle's circulation to be obtained from the M particles of the original field as

$$\boldsymbol{\alpha}_n^p = \sum_m^M \boldsymbol{\alpha}_m^p \Lambda(\boldsymbol{r}_{nm}) \tag{6.12}$$

In this dissertation the redistribution scheme is not applied at every time step. The method is therefore semi-Lagrangian.

6.2.2 Vortex filaments

Vortex filaments are lines representing vortex tubes of circulation. The filament's circulation per unit length is described as Γ^f. If a filaments is of constant strength along its length and it forms a ring, it representes a divergence free discretised vorticity field $\tilde{\boldsymbol{\omega}}$. The Biot-Savart law can be used to evaluate the velocity induced on a point by a straight singular vortex filament fragment [51]

$$\boldsymbol{u}(\boldsymbol{x}) = \frac{\Gamma^f}{4\pi} \frac{\boldsymbol{r}_0 \cdot (\hat{\boldsymbol{r}}_1 - \hat{\boldsymbol{r}}_2)}{|\boldsymbol{r}_1 \times \boldsymbol{r}_2|^2} \boldsymbol{r}_1 \times \boldsymbol{r}_2 \tag{6.13}$$

where, if $\boldsymbol{x}_s$ and $\boldsymbol{x}_e$ are the start and end of a vortex filament fragment respectively, $\boldsymbol{r}_0 = \boldsymbol{x}_e - \boldsymbol{x}_s$, $\boldsymbol{r}_1 = \boldsymbol{x} - \boldsymbol{x}_s$ and $\boldsymbol{r}_2 = \boldsymbol{x} - \boldsymbol{x}_e$. $\hat{\boldsymbol{r}}$ indicates the unit radius vector.

Like the singular vortex particles described in the previous Sec. 6.2.1, the described filament is singular and consequently can be numerically problematic. For vortex particles, regularisation was simple. The induced velocity due to a regularised filament is harder to evaluate and requires integration along its length. To do this the filament is converted to similarly regularised particles, effectively applying a midpoint rule based quadrature. The conversion is displayed in Fig. 6.1, where particles are evenly spaced at distance $\Delta \boldsymbol{x}^p$. This distance is chosen to ensure the particles are overlapping according to the regularisation radius μ as

$$\Delta \boldsymbol{x}^p = \frac{\boldsymbol{x}_e - \boldsymbol{x}_s}{\text{ceil}\left(|\boldsymbol{x}_e - \boldsymbol{x}_s|/\mu\right) + 1}, \tag{6.14}$$

where any error is similar to that introduced by the discretisation of the vorticity field

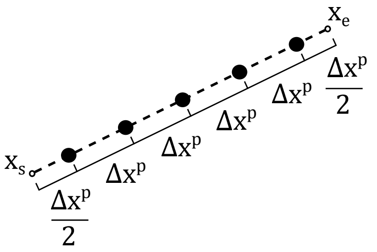

Figure 6.1: Placement of vortex particles equivalent to a vortex filament

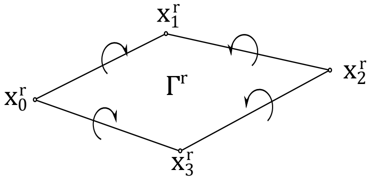

Figure 6.2: A vortex ring

modelled using vortex particles. Each new particle has circulation

$$\boldsymbol{\alpha}^p = \Gamma^f \frac{\boldsymbol{x}_e - \boldsymbol{x}_s}{\operatorname{ceil}\left(|\boldsymbol{x}_e - \boldsymbol{x}_s|/\mu\right) + 1}. \tag{6.15}$$

The conversion to vortex particles is used for the regularised interaction of the vortex lattice with the wake, and for conversion of vortex filaments into the vortex particle wake.

6.2.3 Vortex rings and vortex lattices

Vortex filaments are assembled into vortex lattices. This implicitly satisfies both the Kelvin condition and Helmholtz's theorems. A quadrilateral vortex ring is shown in Fig. 6.2. It is composed of four straight vortex filament fragments, arranged end to end. They share the same vorticity per unit length Γ^r. The velocity induced by the ring can be computed using Eq. 6.13.

The vortex rings comprise part of a larger vortex lattice. The lattice inherits the useful properties of the individual rings. A surface can be represented by vortex rings, although care must be taken, as detailed in Roesler and Epps [103]. A lattice representing a surface is shown in Fig. 6.3. An equispaced grid represents the surface, with the spacing related to the time-step and the free stream velocity U_∞ as $\Delta t = c/(JU_\infty)$, where J is the number of wing vortex rings in the streamwise direction [103]. The rings are set a quarter of their length back from the leading-edge of the surface. To represent the surface, a non-penetration boundary condition is applied at the centre of the ring.

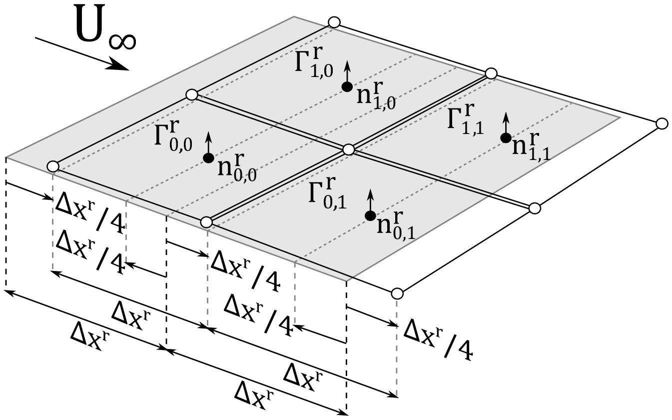

Figure 6.3: A vortex lattice representing a surface. The surface is shown in gray.

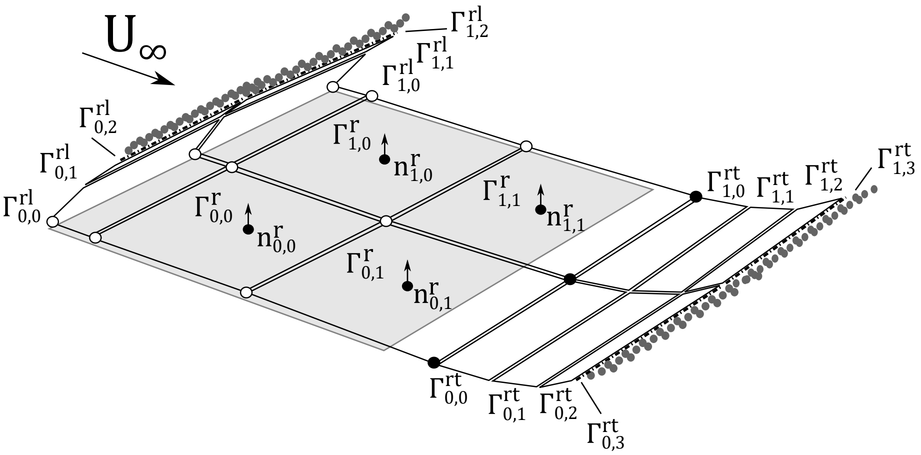

Figure 6.4: The vortex lattice representing the wing with both the leading and trailing edge wakes. The white circles represent the constrained surface geometry and the black circles represent vertices where wing geometry is reapplied on each timestep. Small lattice buffer regions are shown before the wakes are converted into vortex particles. Grey circles represent vortex particles and the dot-dashed lines represent the edge of a vortex ring that has partially been transformed into vortex particles.

6.2.4 The leading and trailing edge wake

Regularised vortex particles were introduced in Sec. 6.2.1, filaments in Sec. 6.2.2 and lattices in Sec. 6.2.3. In this section the means to make them work in concert is described.

As mentioned in Sec. 6.2.3, the wing is represented by a vortex lattice. The near leading-edge wake and trailing edge wake are also represented by vortex lattices. However, these are converted to vortex particles a short distance from the wing as described in Sec. 6.2.2. This idea is depicted in Fig. 6.4.

The vertices of the wing-surface vortex lattice have their position with respect to time defined by the wing's kinematics. Wake vertices are free to convect at the local velocity. The vertices on the wing's trailing edge are wake vertices are part of the wake and allowed to convect. However, the trailing-edge geometry is reimposed at every time-step.

The near wakes are represented by vortex lattices, before being converted into vortex particles. This method was pioneered by Willis *et al.* [177], where this region was referred to as a buffer. The buffer region is required to ensure that, when computing new wing strengths, the interaction between wing and wake is consistent. By converting filaments into particles, the vortex particle wake becomes an extension of the lattice. The lattice continues to satisfy the Kelvin condition on the wing surface, where new vorticity is introduced to the problem. However, the wake lattices only have net-zero circulation when combined with the particle wakes.

Having described the geometric discretisation of the wing and wakes at a point in time, its evolution and the means to obtain ring strengths must be described. The evolution of the wake will be described first.

The free nodes (those not represented with a white circle in Fig. 6.4) are free to convect at their local velocity. This local velocity is the sum of the free stream and the induced velocities due to the wakes. On each time-step, the wake vortices convect away from the wing, shown in Fig. 6.5(a) to Fig. 6.5(b). Consequently, the leading edge vortex rings adjacent to the wing, with strengths $\Gamma^{rl}_{i,j=0}$, will stretch. These rings are split in two, with new vertices inserted a third of the way from the wing edge to the far vertices of the element to be split, shown in Fig. 6.5(c). The ring strength $\Gamma^{rl}_{i,new}$ must be computed at every time-step. For the trailing edge wake, the vertices at the intersection of the wing lattice and wake lattice are allowed to convect, as depicted by the black circle markers in Fig. 6.5. At each time step, a new row of vortex rings is appended the trailing-edge wake, allowing the trailing-edge geometry to be reimposed in Fig. 6.5(c). The vortex ring strengths $\Gamma^{rt}_{i,\mathrm{new}}|_{t+\Delta t} = \Gamma^{r}_{i,J}|_{t}$.

At the leading edge, this scheme is similar to that used for the LEV modelling LDVM method of Ramesh *et al.* [145]. In 3D this scheme was also used by Hirato *et al.* [187]. It has the advantage that it takes account of both convection and wing motion.

The vortex ring strengths on the wing, $\Gamma^{r}_{i,j}$ must still be obtained along with those on newest row of the leading-edge vortex lattice $\Gamma^{rl}_{i,\mathrm{new}}$. As noted, at the trailing edge the ring strength is obtained from that of adjacent wing ring on the previous step. It does not need to be computed.

The leading-edge vortex does not always have vorticity, since leading-edge separation does not always occur. By default, when a leading-edge shear layer is not being shed, $\Gamma^{rl}_{i,\mathrm{new}} = \Gamma^{rl}_{i,0}$, and only the wing vortex ring strengths need to be computed. This case is considered first.

When only solving the wing vortex ring strengths, $\Gamma^{r}_{i,j}$, a linear system obtained by velocity non-penetration boundary condition on the wing can be solved. At a collocation

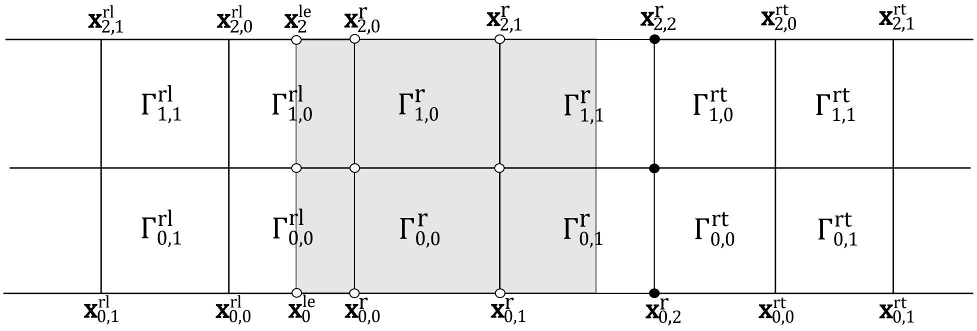

(a) Wake at t

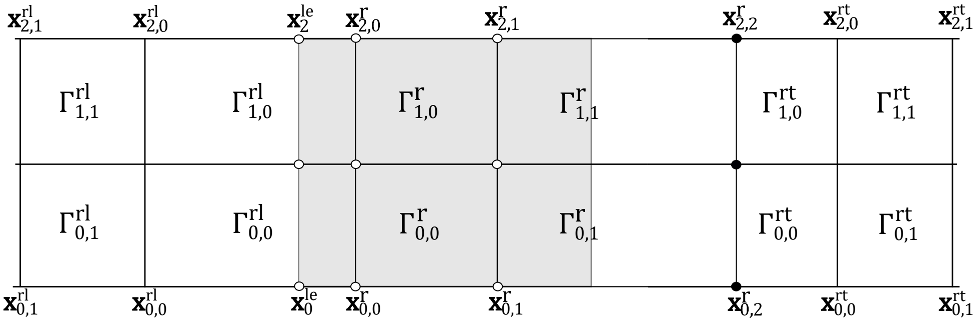

(b) Wake at $t + \Delta t$ before splitting

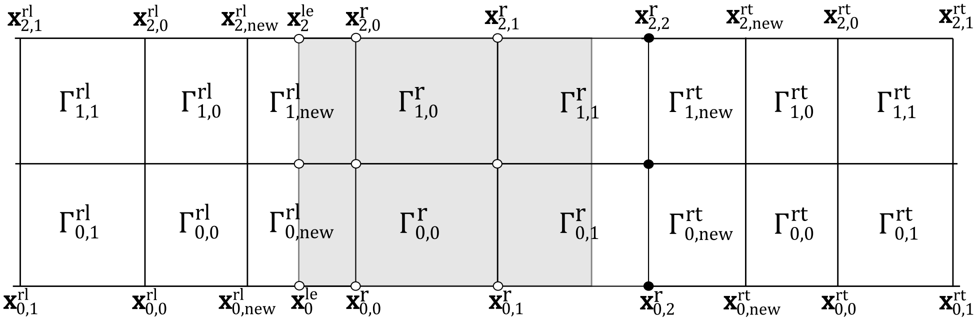

(c) Wake at $t + \Delta t$ after splitting

Figure 6.5: Splitting lattice to introduce new rings. The wakes are unrolled for illustrative purposes.

point at the centre of a wing vortex lattice cell,

$$\{\boldsymbol{u}_{\text{wing}} \cdot \boldsymbol{n}\} = \{\boldsymbol{u}_{\text{ext}} \cdot \boldsymbol{n}\} + [\boldsymbol{A}]\{\Gamma^r\} \tag{6.16}$$

where $\boldsymbol{u}_{\text{wing}}$ is the wing surface velocity and $\boldsymbol{n}$ is the wing surface normal shown as $\boldsymbol{n}^r_{i,j}$ in Fig. 6.4. The velocity induced on the wing by the free stream and the free wake is $\boldsymbol{u}_{\text{ext}}$. The velocity influence of the vector of wing lattice wing strengths $\{\Gamma^r\}$ is given through multiplication with the influence matrix $[\boldsymbol{A}]$. This follows the standard UVLM model, as described by Katz and Plotkin [51].

Having obtained $\Gamma^r_{i,j}$ assuming that a leading-edge vortex is not being shed, leading-edge criticality must be tested. This is done using the LESP criterion introduced in Chapter 3. If a the leading-edge suction $\mathcal{L}$ exceeds the limiting value $\mathcal{L}_{crit}$, separation occurs. In Chapter 3, this was linked to the leading-edge singularity in vorticity A_0, or pressure B_0 from thin aerofoil theory. Here, the singularity is not analytically defined and must be recovered from the observation that the strength of the vortex ring at $j = 0$ on the wing surface (corresponding to the leading-edge rings) has vorticity primarily linked to the singularity.

Following Aggarwal [188], the following relation is obtained

$$\Gamma_{LEi\ \text{crit}} = \frac{\mathcal{L}_{\text{crit}} U_\infty c \left[\cos^{-1}\left(1 - \frac{2\Delta x_i}{c_i}\right) + \sin\left(\cos^{-1}\left(1 - \frac{2\Delta x_i}{c_i}\right)\right)\right]}{1.13} \tag{6.17}$$

where Γ_{LEi} is the vorticity per unit length of the ith leading edge vortex filament of the wing vortex lattice and $\Gamma_{LEi\text{crit}}$ is the limiting value. Δx^r is the spacing of the vortex lattice in the chordwise direction (see Fig. 6.3), and c_i is the wing chord. The factor of 1.13 can be obtained from comparing a 2D UVLM method to the LAUTAT method found in Chapter 5 Sec. 5.2.1. This result matches that of Hirato *et al.* [187].

The strength of the leading edge filament Γ_{LEi} is

$$\Gamma_{LEi} = \begin{cases} \Gamma^r_{i,0} - \Gamma^{rl}_{i,\text{new}}, & \text{when} |\Gamma^r_{i,0}| < \Gamma_{LEi\text{crit}} \\ \pm\Gamma_{LEi\text{crit}} = \Gamma^r_{i,0} - \Gamma^{rl}_{i,\text{new}}, & \text{otherwise.} \end{cases} \tag{6.18}$$

where $\Gamma^{rl}_{i,\text{new}} = \Gamma^{rl}_{i,0}$ when the LEV is not being shed. The LESP criterion therefore allows the identification of locations where the leading edge vortex is shed, and then allows the ring strength $\Gamma^{rl}_{i,\text{new}}$ to be obtained via a linear system.

If the criterion is active for a set of leading-edge wake rings Ω the system can be solved as

$$\{\boldsymbol{u}_{\text{wing}} \cdot \boldsymbol{n}\} = \{\boldsymbol{u}_{\text{ext}-\Omega} \cdot \boldsymbol{n}\} + [\boldsymbol{A}]\{\Gamma\} + [\boldsymbol{A}_\Omega]\{\Gamma_{li,0}\} \tag{6.19}$$

where $\boldsymbol{u}_{\text{ext}-\Omega}$ is the induced velocity $\boldsymbol{u}_{\text{ext}}$, which includes the wake influences and free stream, minus the influence of the rings in Ω. An LEV at one point on the wing influences the leading-edge suction at other points on the span. Theoretically, Ω must therefore be obtained iteratively. In practice it was observed that Ω usually oscillates between two possible solutions. For the results obtained in this dissertation, it is assumed that the initial Ω obtained from Eq. 6.16 is correct.

6.2.5 Algorithm and implementation

In this section, the time-marching algorithm and implementation details are described.

The time-marching algorithm is as follows:

1. Convect the free wake according to the local velocity using a regularised representation of the wing and wake. Redistribute wake if required.
2. Split the leading-edge vortex rings adjacent to the leading edge, giving the new rings strength equal to the original unsplit ring.
3. Split the vortex ring adjacent to the trailing edge in the trailing-edge wake and assign it the same strength as adjacent trailing-edge wing surface vortex ring.
4. Convert part of the wake vortex lattice sheets into vortex particles.
5. Solve for the wing surface vortex ring strengths, assuming no leading edge shedding.
6. The set of leading edge locations where the shedding criterion is activated is Ω. Recalculate the wing surface ring strengths on this assumption.

Some implementation details are needed. The most numerically expensive aspect of the current VoFFLE method is the wake self convection. Naive implementations of this N-body problem require $\mathcal{O}(N^2)$ operations, compared to $\mathcal{O}(N\log(N))$ for tree codes [203] or $\mathcal{O}(N)$ for fast multipole methods [204]. The graphics processing unit (GPU) can also be used to accelerate computation [208, 209, 210, 212]. For small numbers of particles, the use of GPU acceleration is more beneficial than advanced algorithms. According to Yokota and Barba [212], naive GPU accelerated methods are fastest below ~ 25000 particles. The difficulty of implementing the fast multipole method efficiently for parallel computation results in its advantages never materialising in practice in comparison to tree codes. No open-source, cross-OS, cross-hardware-vendor accelerated vortex particle method code was available. Consequently, the CVortex code [226] was written, including Julia-language wrappers available in the Julia general library repository. This code implements the N-body naively for multiple vortex particle regularisation methods, and includes a parallel sparse octtree particle insertion method for multiple particle redistribution methods.

The VoFFLE method scales poorly. The regularisation distance μ is effectively the resolution of the solution. To double the resolution infers that eight times the particles are required and that the time-step should be halved. Consequently, the scaling is of $O(\mu^{-7})$ for the naive N-body solution. For a fast multipole method based solution, the scaling would be of $O(\mu^{-4})$.

For particle convection, Winckelmans *et al.* [215] stated that 'a Euler scheme is simply not acceptable', suggesting the use second-order Adams-Bashforth scheme. The creation of new vortex particles makes the use of Adams-Bashforth scheme difficult, so a second-order Runge-Kutta scheme is used for the results obtained in this chapter. Higher order schemes were investigated but tangible benefits were not observed.

The particle redistribution scheme introduces vortex particles every time it is used. Many of these particles have negligible vorticity, but if kept will greatly inflate the computational cost of the method. Consequently, it is conventional to remove vortex particles with a vorticity under some threshold, redistributing their circulation through the entire vorticity field. In CVortex, this threshold is implemented as a tunable fraction of $\sum_m^M |\boldsymbol{\alpha}_m|/M$, with $0.25\sum_m^M |\boldsymbol{\alpha}_m|/M$ used for the results presented here.

6.3 Results

In this section the VoFFLE method is compared against CFD results for two cases. Firstly, a large-amplitude heave case featuring an aspect-ratio 3 wing, where LEVs are not modelled. A long-running simulation demonstrates how the VoFFLE method can correctly model the trailing-edge wake and its evolution. Unsteady vortex lattice methods are included to demonstrate equivalence for these problems. Secondly, Case 4.3c, originally presented in Chapter 4 Sec. 4.3.3, is revisited. This shows how the VoFFLE method can predict the phenomena involved in LEV formation and separation on a finite wing.

For both cases, rectangular aspect ratio 3 wings with a NACA0008 section are used. The geometry and CFD at Re=10 000 is described in Appendix C.2. In the VoFFLE method, the wing is represented by a vortex lattice. The lattice has 21 rings chordwise and 45 ring across the span. These are equispaced. Following Roesler and Epps [103], a time-step of $\Delta t = 0.05$ is used. A second-order Runge-Kutta scheme is used for convection. The regularisation distance is set to $\mu = 1.5U_\infty\Delta t$, following Ramesh *et al.* [145]. A similar setup is used for the unsteady vortex lattice methods in Sec. 6.3.

VoFFLE results in this chapter were computed without wake relaxation or viscosity schemes. A desktop computer was used with an AMD FX-8320E processor and AMD RX Vega 56 graphics processor, with results computed in single precision using the CVortex library. This is compared to CFD computed according to the method in Appendix C.2 on the Cirrus UK National Tier-2 HPC service at EPCC, with 144 Intel Broadwell cores.

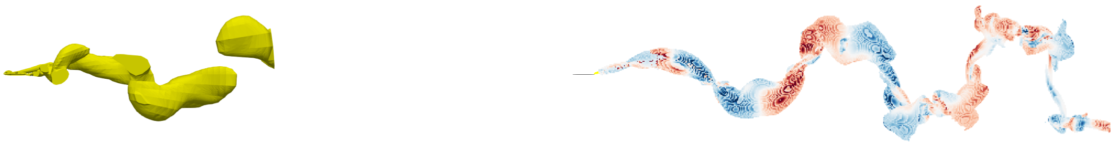

(a) CFD side view

(b) VoFFLE side view

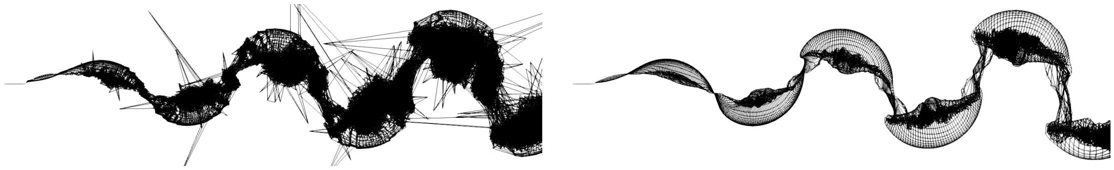

(c) Singular UVLM side view

(d) Regularised UVLM side view

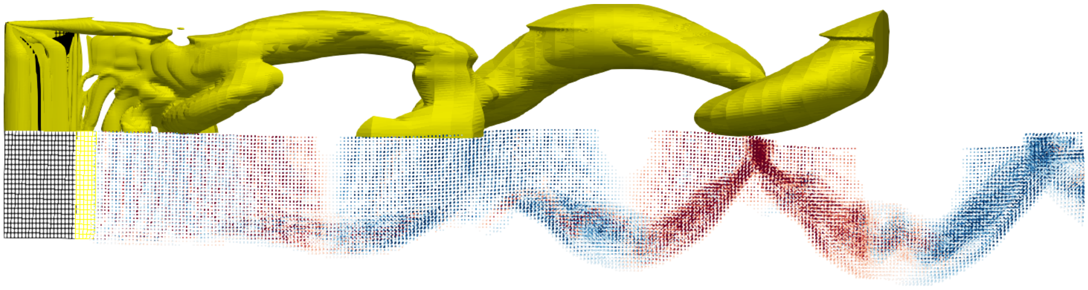

(e) CFD / VoFFLE composite plan view

Figure 6.6: A comparison of CFD, VoFFLE and UVLM wake evolution for an aspect ratio 3 wing oscillating in heave with amplitude $h_0^* = 0.5$ and chord reduced frequency $k = 0.4$. The CFD is visualised with a $Q = 0.01$ iso-surface.

6.3.1 Trailing-edge wake

This section shows a comparison of the wake of VoFFLE method, CFD, and regularised and singular unsteady vortex lattice methods. Leading-edge vortex shedding is turned off in the VoFFLE method, and the parameters are set according to Sec. 6.3. Particle redistribution is performed every 10 time-steps.

An aspect ratio 3 wing oscillates in heave at amplitude $h_0^* = 0.5$ and chord reduced frequency $k = 0.4$. Unlike Chapter 3, the kinematics are defined as $h = h_0^* c \sin(\omega t)$. The wakes of these models are shown after 4 oscillations, at $t = 4T$, in Fig. 6.6.

Figures 6.6(a-d) show a side view of the vortex structure in the wakes of the CFD, VoFFLE method, convectional UVLM and regularised-filament UVLM. Excluding the LEV present in the early portion of the CFD result, the wake geometry of the CFD and the vortex element methods (VoFFLE, UVLMs) is similar. Figure 6.6(e) shows a composite of the CFD and VoFFLE results. The VoFFLE method is capable of correctly modelling the geometry of the vortex rings in the wake.

A benefit of vortex element methods is shown by Fig. 6.6(a). The domain of the CFD is limited. It is unable to model the far wakes of the vortex element methods. The VoFFLE method (Fig. 6.6(b)) and the regularised-filament UVLM (Fig. 6.6(d)) produce the cleanest results, with the VoFFLE method only modelling the vortex cores in the wake vortex rings. Vortex particles with negligible vorticity are removed. The advantage of regularised vortex elements are clear on comparison of the singular and regularised UVLM in Fig. 6.6(c) and Fig. 6.6(d) respectively. The singular filament UVLM leads to spuriously placed filaments. Should one of these filaments interact with the wing, the simulation would become unstable.

The VoFFLE method did not provide useful estimates of wing forces based on the UVLM pressure distribution method of Katz and Plotkin [51]. Force distributions are therefore not presented in this chapter.

For trailing-edge wake simulations, the VoFFLE method matched the wake geometry of the CFD results and the UVLM methods whilst remaining well behaved. The UVLM methods are suitable for trailing-edge wakes. However, under large distortion, such as in LEVs, the filaments are unable to correctly model the geometry of the problem. In the next section a leading-edge vortex problem will be studied using the VoFFLE method.

6.3.2 Leading-edge vortex

Case 4.3, originally studied in Sec. 4.3.3, describes a rectangular aspect ratio 3 wing undergoing leading-edge pitch ramp-hold-return kinematics. The wing has a NACA0008 aerofoil of chord $\bar{c} = 0.1\,\mathrm{m}$ and squared off wing tips, is immersed in a free stream of velocity $U_\infty = 0.1\,\mathrm{m\,s^{-1}}$ for a Reynolds number of Re=10 000. The pitch angle is defined using the ramp-hold-return kinematics of Ol *et al.* [223] as

$$\alpha(t) = \frac{P}{a\bar{c}}\left[\frac{\cosh(aU_\infty(t-t_1)/\bar{c})\cosh(aU_\infty(t-t_4)/\bar{c})}{\cosh(aU_\infty(t-t_2)/\bar{c})\cosh(aU_\infty(t-t_3)/\bar{c})}\right]$$

where $a = \pi^2/(4(t_2-t_1)(1-\sigma))$. P is set to give $\alpha_{\max} = 25°$, and the timing parameters are set to $t_1^* = 1$, $t_2^* = 3$, $t_3^* = 4$ and $t_4^* = 6$. The smoothing parameter is set to $\sigma = 0.5$.

The VoFFLE method parameters are described in Sec. 6.3. The LEV leads to significant distortion, so the particle redistribution scheme described in Sec. 6.2.1 is applied to the vortex-particle wake on even numbered time-steps, making the method semi-Lagrangian. Following Chapter 3, a critical value of the leading-edge suction parameter $\mathcal{L}_{crit} = 0.16$ is used. On the desktop PC described in Sec. 6.2.5, this setup required 74 s for 7 s of simulation time, excluding I/O operations. At the end of the simulation, there were approximately 36 000 particles in the wake. In comparison, the CFD setup described in Sec. C.2 required 2200 CPU core hours on the CIRRUS computing service. The VoFFLE method did not require pre-processing and the output files describing the flow are small in comparison to those generated by CFD.

The CFD and VoFFLE method are compared using vorticity iso-surfaces and wing-centre spanwise vorticity plots. The iso-surface of vorticity $|\boldsymbol{\omega}^*| = |\boldsymbol{\omega}\bar{c}/U_\infty| = 1$ is shown in

Fig. 6.7. In Chapter 3, the Q-criterion was used to visualise vortexes. Here, the vorticity magnitude is used. This demonstrates the lack boundary layer on the VoFFLE wing surface in comparison to the CFD.

The vorticity magnitude iso-surface is shown at for points in time, $t^* = \{3, 4, 5, 6\}$. The pitch ramp-hold-return can be compared to Fig. 4.2, which depicts the kinematics for Case 4.1. The kinematics are similar to those used here, except that maximum pitch angle is 3° rather than 25°. The pitch ramp starts at $t^* = 1$. The first visualisation at $t^* = 3$ is at the end of the ramp, at approximately $\alpha \approx 25°$. The second point $t^* = 4$ is at the end of the hold period, still at approximately $\alpha \approx 25°$. The pitch angle reduces by $t^* = 5$ to $\alpha \approx 12.5°$. At $t^* = 6$, the angle of attack has returned to zero.

At $t^* = 3$, the CFD shows a tip vortex extending from the leading-edge corner downstream and a leading-edge separation bubble. In the VoFFLE method, the tip vortex is present, but only behind the trailing edge. The tip separation is not modelled in the VoFFLE method to avoid numerical instability. The leading-edge separation bubble is also present. As in the CFD, it is larger at the centre of the wing, getting smaller towards the tip. However, the size at the centre of the wing is over-predicted.

The pitch angle stays approximately constant between $t^* = 3$ and $t^* = 4$, at approximately 25°. The CFD predicts that an LEV has formed. Again, the size of the structure is larger at the centre of the wing, and it tapers to nothing at the leading-edge corners. Separation is also present in the VoFFLE method. This is more clearly visible in the vorticity cross section shown in Fig. 6.8, studied later. The LEV has rolled up on itself less than found in the CFD results, and has convected further downstream.

The pitch angle is reducing rapidly at $t^* = 5$. The CFD result shows how the LEV has detached from the leading-edge corners of the wing, and is being convected over the wing surface. It has formed the arch structure familiar from literature and Chapter 3, Fig. 3.6. A similar phenomenon occurs in the VoFFLE result. The LEV is no longer attached to the leading-edge corners and has formed an arch structure. However, the VoFFLE result predicts it is further downstream than found in CFD.

At $t^* = 6$, the CFD shows the LEV structure has separated from the wing and has been convected downstream. A similar phenomenon is shown in the VoFFLE result, but again the arch structure is further downstream than predicted by the CFD.

The VoFFLE method, though not in exact agreement with the CFD, was able to predict LEV formation and separation. The LEV formed at approximately the correct time, and had the correct variation with respect to span. Whilst the form of the LEV structure predicted was not identical to that found in the CFD, it still detached from the leading-edge corners and formed an arch structure. This was successfully carried into the wake.

The VoFFLE method correctly captured some key features of the problem. Impor-

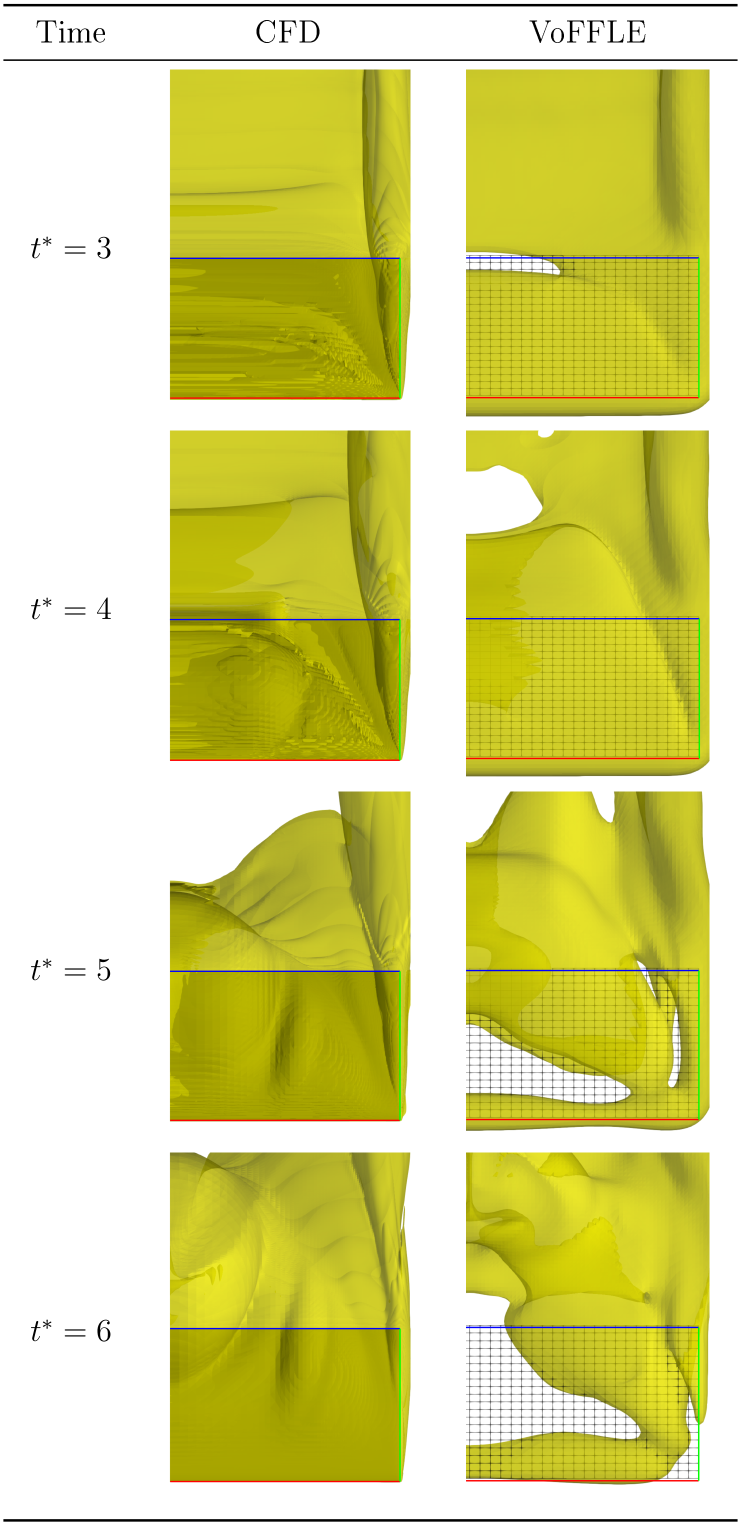

Figure 6.7: A comparison of CFD and VoFFLE vorticity magnitude iso-surfaces for $|\boldsymbol{\omega}\bar{c}/U_\infty| = 1$ for an aspect ratio 3 wing undergoing pitch 25° ramp-hold-return motion. The leading edge, trailing edge and wing tip are shown in red, blue and green respectively.

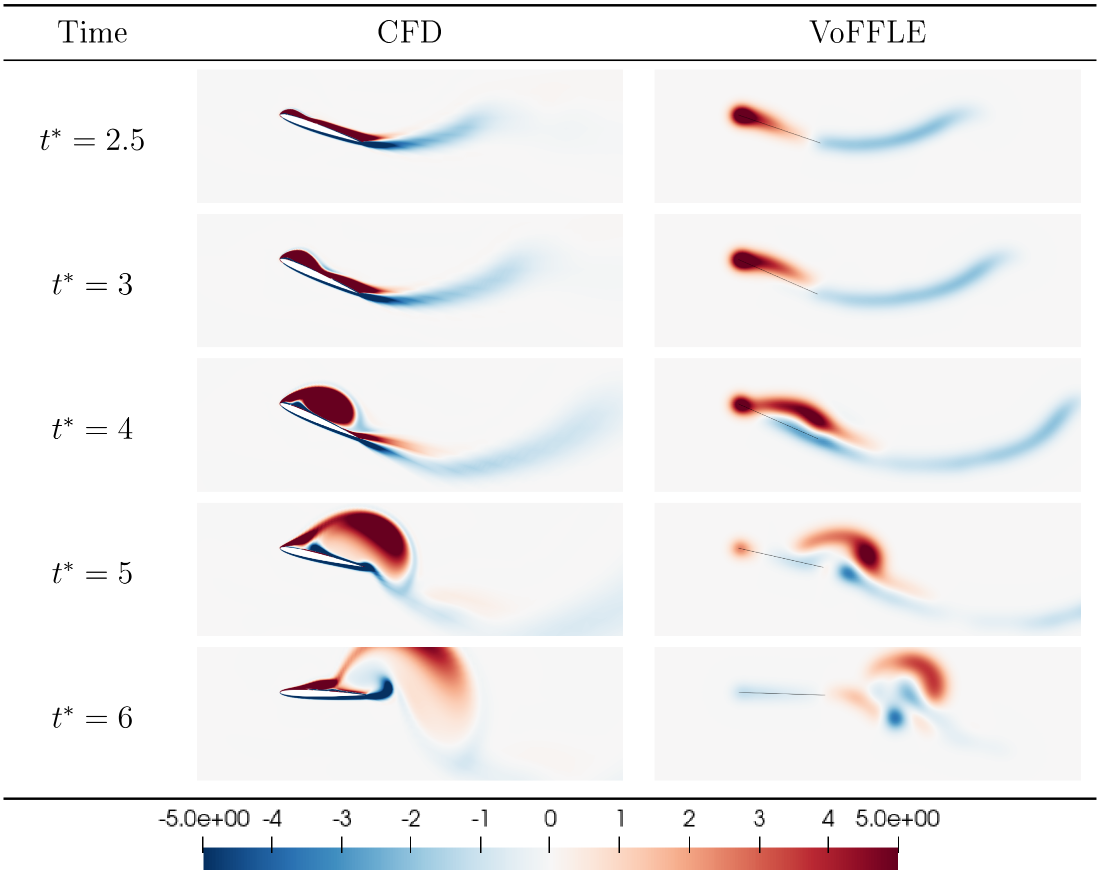

Figure 6.8: A comparison of CFD and VoFFLE normalised spanwise vorticity $\omega_y \bar{c}/U_\infty$ at the centre of an aspect ratio 3 wing undergoing a 25° pitch ramp-hold-return motion.

tantly, the LEV could be completely shed from the wing. This is shown in an examination of the vorticity at the wing centre, visualised in Fig. 6.8. The figure shows the $t^* = 2.5$ and the times shown in Fig. 6.7 ($t^* = \{3, 4, 5, 6\}$).

The first instance is at $t^* = 2.5$, prior to LEV formation. The lower 'resolution' of the VoFFLE method is visible, with regularisation distance being comparable to that of the assumed-negligible wing thickness. The wake of the VoFFLE method is modelled as inviscid, and the semi-Lagrangian vortex particle method results in very little diffusion of the vorticity. The wake of the CFD diffuses more because of the low Reynolds number. The geometry of the trailing-edge wakes match well.

At $t^* = 3$ and $t^* = 4$, the growth of the LEV is visible in the CFD results. The VoFFLE method LEV does not stay attached to the wing, instead being convected downstream. At both times, the trailing edge wake of both methods match well.

The pinch-off of the LEV predicted by the CFD is visible at time $t^* = 5$. This has occurred earlier in the VoFFLE result, and the VoFFLE result suggests the LEV has been convected further downstream. Once again, the trailing-edge wake geometries are in good agreement, although the VoFFLE method is less diffusive.

At $t^* = 6$, the LEV has been convected behind the wing in both methods. In the VoF-

FLE method, this cross section shows the mixing of the LEV with the trailing-edge wake. The VoFFLE method does not model viscosity, so the LEV structure cannot correctly merge with the trailing-edge wake. The wake model becomes numerically unstable.

6.4 Summary

In this chapter, a method to model leading-edge vortex structure at comparatively low computational cost was described, overcoming a limitation of the methods described in Chapter 2, Chapter 4 and Chapter 5. The method combined a vortex lattice representation of the wing with semi-Lagrangian regularised vortex particle wakes. The leading-edge suction parameter of Ramesh *et al.* [145] was used to modulate leading-edge vortex shedding.

The Vortex Formation on Finite Leading Edge (VoFFLE) method could successfully model a problem involving leading-edge vortices approximately 10 000 faster[1] than the CFD used for comparison, requiring minimal pre-processing. The VoFFLE correctly predicted separation at the leading edge, and the formation of an LEV. The LEV was pinned at the leading-edge corners until it separated from the wing surface, forming an arch structure that was convected into the wake. Very little diffusion occurred in the wake and the geometry of the trailing-edge wake agreed well with that from CFD.

This concludes the third new method described in this dissertation. In Chapter 4, a time-domain method was described. It was limited by the requirement that the kinematics be known *a priori*, and that linear geometric and aerodynamic models used. In Chapter 5, a geometrically non-linear time-marching method was introduced, alleviating two of these problems. In this chapter, a more general model, capable of modelling an aerodynamic non-linearity was introduced. This dissertation is concluded in the next chapter.

---

[1] Based on the assumption that a desktop PC is equivalent to approximately 10 Intel Broadwell Xeon cores.

Chapter 7

Conclusions

This chapter concludes the dissertation by summarising the main outcomes of this research in Sec. 7.1. The key contributions of this work along with associated publications were given in the introductory chapter, Chapter 1, in Sec. 1.3, and are not repeated here. Following the summary, some suggestions for possible future work are made in Sec. 7.2.

7.1 Summary

This dissertation, on low-order methods for the unsteady aerodynamics of finite wings, reviewed literature and set out key contributions and research questions in Chapter 1. Here, a summary of the answers to these research questions is given.

7.1.1 Theoretical developments

This dissertation started with a chapter on an analytical frequency-domain unsteady lifting-line theory. The method was based on the work of Sclavounos [94] since it represents the most general frequency-domain unsteady lifting-line theory available that can be applied to rectangular wings. The ULLT was modified to generalise the inner solution and avoid the requirement that the three-dimensional added-mass term be known in advance. Additionally, another 3D wake interaction kernel was derived, that represented only the streamwise component of the oscillating wake sheet.

The ULLT and the different wake models were compared against data obtained from Euler CFD for rectangular wings oscillating in heave and pitch at aspect ratios 8, 4, and 2. It was found that ULLT with Sclavounos's interaction kernel obtained good results for both lift and moment coefficients. The streamwise vorticity only kernel introduced small errors. The pseudosteady, Prandtl-like wake model kernel introduced larger errors at intermediate frequencies. At high frequencies it matched the CFD best, but this is likely luck related to rectangular wing planform.

All the kernels tended towards the 2D results at high frequency - supposedly the correct solution, even if the wake model introduced error. In practice, strict asymptotic applicability of the wake model to correct high frequency limit did not seem to matter. The main impact of the simplified wake models appeared at lower chord reduced frequencies.

Whilst the ULLTs tended towards the 2D solution at high frequency, as ULLT suggests they should, the CFD results used for comparison did not. Lifting-line theory is technically not applicable to the rectangular wings. The consequence of this appears to be that the added-mass obtained from lifting-line theory at high frequency was incorrect.

The ULLT also provided good results for spanwise force distributions, although the moment distribution was generally more accurate than the lift distribution. Error was introduced, as expected, near to the rectangular wing tips.

Chapter 2 finished with the comparison of the ULLT to experimental data, for a high-aspect-ratio wing oscillating in pitch about a non-zero average pitch angle. The ULLT accurately predicted the lift coefficient of the wing.

In Chapter 3, the same ULLT was applied to low Reynolds number CFD for rectangular wings oscillating at both small and large amplitudes. It was found that the ULLT provided useful solutions for the Re=10 000 small-amplitude problems, predicting both the moment and lift amplitudes (including spanwise distribution) with reasonable accuracy. The accuracy was not so good as for the Euler cases, but remained useful.

Larger amplitude kinematics resulted in the wings shedding leading-edge vortices. Chapter 3 included a method, based on Ramesh *et al.*'s [145] concept of the leading edge suction, to predict leading-edge vortex shedding on finite wings. The method was able to correctly predict LEV shedding, although not with significant fidelity.

When large-amplitude kinematics caused LEVs to be shed, ULLT remained useful as a means to measure the whole-wing forces. On finite wings, the LEV forms an arch structure. Compared to 2D, this stabilises the LEV, leading to less irregular forces. This effect is stronger at lower aspect ratios. As aspect ratio decreased, the force waveforms become more sinusoidal. Consequently, the ULLT, which assumes sinusoidal results, predicted them better. At higher aspect ratio, the ULLT could correctly predict the amplitude of the force waveforms, but could not predict the shape.

LEVs are especially disruptive with respect to force distributions. LEVs lead to rapid changes in force distribution with respect to span in the vicinity of the LEV. Since the ULLT does not model the LEV, it cannot predict these. However, the LESP criterion combined with the ULLT at least provides a means by which to predict that the ULLT prediction will be poor.

Chapter 2 and Chapter 3 concentrated on assessing a current unsteady lifting-line theory and its applicability. Frequency-domain ULLT was found to be a useful tool even when the assumptions on which it is based were violated, and as such could be applied to problems facing modern engineers. However, the need for time-domain tools was set out in Chapter 1. Chapter 4 delivers the first of these.

In Chapter 4, a new method by which frequency-domain ULLT could be applied to time-domain problems was obtained. Past methods either relied on expensive numerical models of the wake, or analytical methods which required simplified Prandtl-like wake models. By applying frequency-domain ULLT to time-domain problems, the new method could employ a more complex wake model whilst remaining primarily analytical.

The method, named ULLT / Convolution in Frequency Domain (UCoFD), transformed the input kinematics to the frequency domain using the Fourier transform. Here, it undergoes convolution with the results of the frequency-domain problem before the inverse Fourier transform is applied. To avoid having the evaluated a frequency-domain ULLT at every frequency, an interpolation scheme is introduced. This scheme requires only a few frequency-domain ULLT evaluations to obtain a good approximation.

This scheme was applied to time-domain cases. For a small-amplitude pitching case, it obtained good results. A return ramp kinematic had to be inserted to apply the method to a heave-velocity ramp which finished with non-zero displacement. Again, UCoFD obtained good results. Finally, the UCoFD method was applied to pitch ramps at low Reynolds numbers. The conclusions as to its applicability were similar to those found for frequency-domain ULLTs in Chapter 3.

The UCoFD method obtained good results, but has shortcomings. The method is linear (and this must be the case for the Fourier transform and inverse Fourier transform). The method also assumes that the problem's kinematics are known in advance. For flight dynamics problems which combine aerodynamics, control and structural dynamics, this may be a problem. To overcome these obstacles, numerical methods must be employed, as detailed in the next section.

7.1.2 Numerical simulations

Numerical methods are used to obtain an unsteady lifting-line theory where geometric non-linearity can be introduced and the kinematics do not need to be known in advance in Chapter 5. A time-marching ULLT is derived. The inner 2D solution is based on Ramesh *et al.*'s large-amplitude unsteady thin-aerofoil theory [102]. This method includes geometric non-linearities by using a discrete vortex particle based wake. The outer solution uses a vortex lattice based wake, with a matching technique used to avoid singularities.

The method, christened Large-Amplitude Unsteady Lifting-Line Theory (LAULLT), was applied to several problems. For small-amplitude oscillating problems, similar results were obtained compared to the frequency-domain C-ULLT of Chapter 2. For a small-amplitude heave velocity ramp-hold-return problem, it obtained similar results to UCoFD. A large-amplitude, low-Reynolds-number pitching problem showed how LAULLT could resolve the effects of geometric non-linearity, but was limited by its inability to model the leading-edge vortex.

It had been hoped that LAULLT would be extensible to include leading-edge vortices, but this did not seem to be possible, with the extended method being numerically unstable on LEV formation. Whilst some possible extensions to the method are suggested in Sec. 7.2.2, it can be effectively argued that to model LEVs, fully 3D methods are needed. Such a method is presented in Chapter 6.

The Vortex Formation on Finite Leading Edge (VoFFLE) method, combines a vortex lattice wing, Ramesh *et al.*'s LESP criterion [145] for LEV shedding prediction and a regularised vortex particle leading- and trailing-edge wake. The vortex particle wakes solve many of the problems of vortex lattice wakes, and allow LEVs to be shed.

The VoFFLE method allows leading-edge vortices to be modelled in 3D at low computational cost in comparison to CFD. The GPU accelerated naive implementation used in this dissertation allowed a case to be solved at approximately one ten-thousandth of the computational cost of the equivalent CFD case.

The VoFFLE method proved capable of predicting LEVs and captured the important features in 3D. It allowed the simulation of an LEV detaching from the wing surface during a pitch ramp-hold-return motion. Suggestions for further development of the VoFFLE method are made in Sec. 7.2.5.

7.2 Recommendations for future work

All good things come to an end (that includes PhDs). Inevitably, potentially fruitful avenues of research must be abandoned either for lack of time or to obtain a cohesive dissertation. This section details possible research topics that I regret that I have not been able to investigate myself.

7.2.1 Frequency-domain ULLT

Chapter 2 detailed frequency-domain unsteady lifting-line theory. The inner solution was based around problems similar to that of Theodorsen [56], and were limited to inviscid solutions. As a consequence, error is introduced by applying them to low Reynolds number problems.

Taha and Rezaei [74] formulated a viscous extension to Theodorsen's problem using triple-deck boundary layer theory, providing better results at low Reynolds numbers. This non-linear theory could be integrated into a frequency-domain ULLT to obtain better results for viscous small-amplitude problems.

7.2.2 LAULLT

In Chapter 5, the large amplitude unsteady lifting-line theory was explained. The potential of this method is that it does not depend on any particular 2D inner solution, so long as there is a discrete vortex particle wake. This allows more advanced inner solutions to be substituted in.

Inner solutions that model LEVs, the boundary layer and dynamics stall could be introduced. This is not without challenges. Introducing LEV using Ramesh et al.'s LDVM [145] using a second wake in the outer domain failed. Such a model blows up on LEV formation for reasons that are unclear. The model would be unable to model the complex 3D nature of LEV structures, but 'good' is the enemy of 'good enough', especially in the context of low-order models.

A second possible expansion is based on the work of Chapter 2, where a simplified outer wake model that modelled only the streamwise components of vorticity was investigated. This wake introduced error compared to the complete wake model, but the error may well be acceptable in many circumstances.

Avoiding the requirement that the spanwise vorticity exist in both the inner and outer domain may prove liberating with respect to kinematics. Close to the wing, at distances of $O(\bar{c})$ the spanwise vorticity could exist within only the inner wake. After that they could exist in outer wake. This could allow kinematics out of the plane of the inner solutions.

7.2.3 Application of methods to gust and flexing wing problems

All methods described in the PhD were applied to pitching and heaving wing kinematics. Modelling gusts is challenging to set up and validate in CFD, and for the problems motivating the PhD, Kay *et al.* [136] pointed out that turbulence and pitching are similar. Nonetheless, most methods on this PhD are applicable to gust problems.

The models could also be applied to wings flexing in both the spanwise and chordwise directions. Spanwise flexing reflects the kinematics of flexible wings for aeroelastic problems. Chordwise flexing approximates the flexing of biological bodies.

Finally, this PhD was primarily concerned with rectangular wings. Whilst rectangular wing tips are overwhelmingly popular in man-made flight, they do not represent the wings found in nature. Non-rectangular wing tips should be investigated.

7.2.4 Guermond and Sellier's ULLT

Guermond and Sellier ULLT [85] is notable for its applicability to all frequencies and swept, curved wings. This PhD is only concerned with straight wings, but it is likely that methods for non-straight planforms will be required in the future. A frequency-domain

ULLT for such problems is needed. This could be integrated into the UCoFD method of Chapter 4 to obtain time-domain solutions.

For straight wings, some notes on the implementation of Guermond and Sellier's method are given in Appendix A.1.

7.2.5 VoFFLE

The VoFFLE method has significant potential, although multiple surmountable hurdles stand in its way. The chief among these is obtaining forces.

Wing loads were not presented in Chapter 7 since the implementation method based on the UVLM of Katz and Plotkin [51] provided poor results. The reasons for this were unclear.

Secondly, VoFFLE, as presented in this dissertation, lacks viscosity. This is essential for long term evolution of the LEV and wake, and for the viscous phenomenon of vortex ring merging. Viscosity is needed to represent the viscosity of the flow itself and also to represent sub-grid viscosity. Particle strength exchange schemes can be used. Viscosity in the particle strength exchange scheme only impacts particles that are close together. Consequently, viscosity can be implemented with relative ease for a cost of $\mathcal{O}(N\log(N))$ using space-filling curves or octtrees, or $\mathcal{O}(N)$ using the Fast Multipole Method.

Another notable omission from VoFFLE is tip separation. Tip separation is problematic without viscosity and causes the model to blow up. Tip separation should be added, and a tip separation parameter, similar to the LESP criterion should be considered. This may be essential for the modelling of elliptic wings where the tip vortex and leading edge vortex interact in a different manner than for the rectangular wings investigated in this dissertation.

Finally, there are several methods that could be used to accelerate the code, making it applicable to larger problems. Firstly, a treecode or fast multipole method could be used to accelerate wake interaction, allowing for larger or faster simulations. Secondly, a pFFT method [178] could be used to reduce the cost of solving the wing's surface vorticity distribution. And thirdly a non-uniform wake redistribution method could be used to reduce the fidelity of the wake away from the wing, potentially also improving the stability of the method.

Appendix A

Frequency-domain ULLT

A.1 Guermond and Sellier

Guermond and Sellier's [85] ULLT is the only unsteady lifting-line theory uniformly valid over the entire frequency domain (some ULLTs fail to consider their validity at high frequencies or overstate their validity). It is also valid for curved and swept wings. Unfortunately, the method is challenging both to understand and to implement.

In this appendix, the singularities encountered when applying their method to a rectangular wing are demonstrated, before a suggestion for a means to apply the method in a manner reminiscent of Prandtl. Firstly however, Guermond and Sellier's theory must be introduced, albeit simplified for straight wings. Note that some symbols are redefined here.

A wing is oscillating with frequency ω with small amplitude. Flow is in the positive X direction with velocity U_∞. The span of the wing is in the Y direction, with the lifting line L on $X = 0$. Non-dimensionalised coordinates are defined:

$$X = cx$$
$$Y = sy$$
$$V = sv$$

where c is the chord of the rectangular wing, s is the semispan of the wing and V and v are coordinates in the downstream direction. Consequently, the wing is in $-1 < y < 1$ and $-0.5 < x < 0.5$. The angular frequency can also be described in terms of reduced frequencies:

$$\overline{k} = \omega \overline{c}/(2U_\infty)$$

$$\nu = \omega s / U_\infty$$

The ULLT is considered in terms of the acceleration potential $\mathbf{\Psi} = -p/\rho_\infty$. This too is non-dimensionalised:

$$\mathbf{\Psi} = U_\infty^2 \psi. \tag{A.1}$$

Guermond and Sellier set up the following asymptotic expression for the upwash velocity over the span of the wing:

$$w(x,y) = \mathscr{K}_0[\![\psi]\!] + \frac{1}{\text{Æ}}\mathscr{K}_1[\![\psi]\!] + o\left(\frac{1}{\text{Æ}}\right), \tag{A.2}$$

where $[\![\psi]\!]$ is the jump in acceleration potential across the wing surface. Physically interpreted, the upwash $w(x,y)$ (equal to the vertical velocity of the wing) is the sum of the two-dimensional effects (zeroth order expansion term $\mathscr{K}_0$) and some three dimensional effects (first order term $\mathscr{K}_1$), with error of order $o(1/\text{Æ})$.

Simplified for straight wings, these operators are

$$\mathscr{K}_0[\![\psi]\!] = -\frac{1}{2\pi}\text{F.P.}\int_{-c(y)/2}^{c(y)/2}\left[\frac{1}{x-\xi} - 2i\bar{k}e^{-2ik(x-\xi)}\text{F.P.}\int_{-\infty}^{x-\xi}\frac{e^{2i\bar{k}\tau}}{\tau}d\tau\right][\![\psi]\!](\xi,y)d\xi, \tag{A.3}$$

where F.P. indicates the Hadamard finite part integral, and

$$\begin{aligned}\mathscr{K}_1[\![\psi]\!] = e^{-2i\bar{k}x}\Big\{ &- i\nu\frac{\mathcal{G}(y)}{2\pi}\int_{-\infty}^{0}\frac{e^{i\nu v}}{v}dv + \frac{1}{4\pi}\text{F.P.}\int_{-1}^{1}\frac{\mathcal{G}(\eta)}{(y-\eta)^2}d\eta \\ &- \frac{i\nu}{4\pi}\text{F.P.}\int_{-\infty}^{0}e^{i\nu v}\Big[\text{F.P.}\int_{-1}^{1}\frac{\mathcal{G}(\eta)}{(y-\eta)^2}\Big[1+\frac{v}{\sqrt{v^2+(y-\eta)^2}}\Big]d\eta\Big]dv\Big\}.\end{aligned}$$

$\mathcal{G}(y)$ is effectively the bound vorticity with a modified phase:

$$\mathcal{G}(\eta) = \int_{-c/2}^{c/2} e^{2ik\xi}[\![\psi]\!](\xi,\eta)\,d\xi = \Gamma(\eta)e^{ikc(\eta)} \tag{A.4}$$

The Hadamard finite part integral discards the infinite part of a hyper-singular integral. For educational purposes, it is often introduced as the derivative of the Cauchy principal value (C.P.V.) integral:

$$\text{F.P.}\int_a^b \frac{w(x)f(x)}{(x-s)^2}dx = \frac{d}{ds}\text{C.P.V.}\int_a^b\frac{w(x)f(x)}{x-s}dx.$$

It can be regularised as

$$\text{F.P.}\int_a^b\frac{f(t)}{(t-x)^2}dt = \lim_{\varepsilon\to 0^+}\left\{\int_a^{x-\varepsilon}\frac{f(t)}{(t-x)^2}dt + \int_{x+\varepsilon}^b\frac{f(t)}{(t-x)^2}dt - \frac{f(x+\varepsilon)+f(x-\varepsilon)}{\varepsilon}\right\}.$$

This will be simplified and applied to the problem of a rectangular wing in the next section. In the subsequent section, an indirect means of solution in the spirit of Prandtl will be proposed.

A.1.1 Direct solution for a rectangular wing

For illustrative purposes, we first follow the direct method of solution suggested by Guermond and Sellier to obtain the pressure jump distribution $\llbracket\psi\rrbracket$ for a rectangular wing. This will demonstrate the limitations of the direct method.

The system Eq. A.2 can be solved in a triangular manner. Hence to obtain $\llbracket\psi_1\rrbracket$ we must first invert

$$\mathscr{K}_0\llbracket\psi_0\rrbracket = w(x,y),$$

to obtain ψ_0, followed by inverting

$$\mathscr{K}_0\llbracket\psi_1\rrbracket = -\mathscr{K}_1\llbracket\psi_0\rrbracket.$$

Hence to order $o(1/\textit{\AE})$,

$$\llbracket\psi\rrbracket = \mathscr{K}_0^{-1}\left[w(x,y) - \frac{1}{\textit{\AE}}\mathscr{K}_1\llbracket\psi_0\rrbracket\right] + o\left(\frac{1}{\textit{\AE}}\right). \tag{A.5}$$

The inversion of operator $\mathscr{K}_1$ is a classical problem. Whilst Guermond and Sellier direct readers to an inversion derived from Theodorsen presented in Ashley and Landahl [69], the Küssner-Schwarz general solution provides a method less dependent upon challenging integrals. See Appendix B.2.

With the knowledge that we only need to evaluate operator $\mathscr{K}_1\llbracket\psi_0\rrbracket$ on a rectangular wing, the operator can be further simplified. This removes the finite-part integrals.

$$\begin{aligned}\mathscr{K}_1\llbracket\psi_0\rrbracket = \frac{e^{-2i\bar{k}x}\mathcal{G}(\llbracket\psi_0\rrbracket)}{2\pi}&\Bigg\{\frac{1}{y^2-1} - \\ &\frac{i\nu}{2}\int_{-\infty}^{0} e^{i\nu v}\left[\frac{2}{y^2-1} + \sqrt{\frac{1}{(y-1)^2}+\frac{1}{v^2}} + \sqrt{\frac{1}{(y+1)^2}+\frac{1}{v^2}} + \frac{2}{v}\right]dv\Bigg\},\end{aligned} \tag{A.6}$$

where $\mathcal{G}(\llbracket\psi_0\rrbracket)$, constant with respect to span for $\llbracket\psi_0\rrbracket$, can be obtained easily from the Küssner-Schwarz general solution. The semi-infinite oscillatory integral can be evaluated either using truncated Filon quadrature or a suitable double-exponential transform.

Having obtained $\llbracket\psi\rrbracket$, forces can be obtained. Alternatively, one can obtain lift and moment coefficient directly from Küssner-Schwarz using the modified downwash $w(x,y) - \mathscr{K}_1\llbracket\psi_0\rrbracket/\textit{\AE}$.

Guermond and Sellier's method has two main drawbacks. The lesser of these is the algebraic effort required to obtain even the relatively simple first order operator $\mathscr{K}_1$ in terms of non-singular integrals. The larger problem is the form of the first order operator—

namely the $1/(y^2-1)$ term. This means the 3D downwash has $\lim_{y\rightarrow\pm 1} = \infty$. Whilst it is expected that square wing-tips will be problematic, this singular integral means that the integral of the lift coefficient with respect to span is divergent. Consequently, the direct method is of limited use for rectangular wings.

Although Prandtl-Glauert lifting-line theory does not encounter this problem since the downwash is not evaluated at the wing tip, it is known that lifting-line theory is problematic in the vicinity of non-cusped or non-lenticular wing-tips. This is emphasised by Van Dyke [79]. Van Dyke explains how the tip shape of the wing is of vital importance. The discontinuity of squared wing tips can lead to singular integrals. The solution of lifting-line theory obtained for elliptical wing tips is also asymptotically invalid at the wing tip, but the weakly singular integral at least leads to a finite solution.

In the next section, the way in which Prandtl-Glauert limit the possible solutions is emulated, such that non-singular solutions can be obtained.

A.1.2 Indirect solution

To obtain a solution by a Prandtl-like method, one can first rearrange the expansion Eq. A.2 for the downwash similarly to the direct solution:

$$[\![\psi]\!] = \mathscr{K}_0^{-1}(w(M)) - \frac{1}{\text{Æ}}\mathscr{K}_0^{-1}\left(\mathscr{K}_1[\![\psi]\!]\right) + o\left(\frac{1}{\text{Æ}}\right),$$

which is different to the triangularly-solved expression used in the direct solution (Eq. A.5). The substitution of $[\![\psi_0]\!] \rightarrow [\![\psi]\!]$ is permissible because

$$[\![\psi]\!] = [\![\psi_0]\!] + \frac{1}{\text{Æ}}[\![\psi_1]\!] + o\left(\frac{1}{\text{Æ}}\right),$$

meaning that,

$$\frac{1}{\text{Æ}}\mathscr{K}_1\left([\![\psi]\!]\right) = \frac{1}{\text{Æ}}\mathscr{K}_1\left([\![\psi_0]\!]\right) + \frac{1}{\text{Æ}^2}\mathscr{K}_1\left([\![\psi_1]\!]\right) + o\left(\frac{1}{\text{Æ}^2}\right),$$

resulting in a difference of $o(1/\text{Æ})$ in comparison to the direction solution given in Eq. A.5.

Next observe that $\mathscr{K}_1$ is only an operator on $[\![\psi]\!]$ via $\mathcal{G}(y)$ for straight wings. Additionally, if $\mathcal{G}$ is applied to both sides of the equation, G_{2D} ($\mathcal{G}$ applied to the 2D solution) can be separated out from the first order terms because $\mathcal{G}$ is a linear operator.

$$\mathcal{G}([\![\psi]\!]) = \mathcal{G}(\mathscr{K}_0^{-1}(w(M))) - \frac{1}{\text{Æ}}\mathcal{G}\big(\mathscr{K}_0^{-1}\left(\mathscr{K}_{1G}(\mathcal{G}([\![\psi]\!]))\right)\big), \tag{A.7}$$

where $\mathscr{K}_{1G}$ indicates the operator $\mathscr{K}_1$ which takes a $\mathcal{G}(y)$ distribution as its argument. To solve for downwash, we can approximate the solution of $\mathcal{G}(\llbracket\psi\rrbracket)$ with a Fourier series:

$$\mathcal{G}(\llbracket\psi\rrbracket) = \sum_{n}^{\infty} G_n \sin(n\theta),$$

$$y = -s\cos(\zeta),$$

where G_n are complex. Substituting this gives

$$\sum_{n}^{\infty} G_n \sin(n\zeta) = G_{2D} - \frac{1}{\AE} \sum_{n}^{\infty} \left[G_n \mathcal{G}\left(\mathscr{K}_0^{-1}\left(\mathscr{K}_{1G}\left(\sin(n\zeta)\right)\right)\right)\right] \tag{A.8}$$

which is a linear problem similar in spirit to that of Prandtl [76]. The difference between this solution, and Guermond and Sellier's direct method is of $o(1/\AE)$.

A.2 Regularising Sclavounos's interaction kernel

Sclavounos's unsteady lifting-line theory is attractive because it applies to the frequency range for which finite wing effects are of importance, but evaluating the integral in the integro-differential equation can be challenging. This appendix details the means to do this. The relevant integro-differential is repeated here from Eq. 2.22:

$$\Gamma - \frac{\Gamma_{hn}^{2D}}{2\pi i\omega} \int_{-s}^{s} \Gamma'(\eta) K(y-\eta)\,\mathrm{d}\,\eta = \Gamma^{2D},$$

where the bound circulation Γ can approximated by a Fourier series $\Gamma_0 = 4U_\infty s \sum_{m=1}^{M} \Gamma_m \sin(m\xi)$ and the spanwise coordinate $y = s\cos(\xi)$ for $\xi \in [0, \pi]$.

There are multiple kernels described in the thesis. The most challenging to integrate is that of Sclavounos, the kernel $K_C(y)$. This is given by Sclavounos and Eq. 2.29 as

$$K_C(y) = \frac{1}{2}\mathrm{sgn}(y)\left[\frac{e^{-\nu|y|}}{|y|} - i\nu E_1(\nu|y|) + \nu P(\nu|y|)\right],$$

where $\nu = \omega/U_\infty$, U_∞ is the free stream velocity, $E_1(x)$ is the exponential integral as defined in Olver *et al.*[221], and

$$P(y) = \int_1^\infty dt\, e^{-yt}\left[\frac{\sqrt{t^2-1}-t}{t}\right] + i\int_0^1 dt\, e^{-yt}\left[\frac{\sqrt{1-t^2}-1}{t}\right].$$

Both the $1/y$ and the E_1 terms contain singularities. Consequently, it is desirable to have a regularised form of

$$\mathscr{I} = \int_{-s}^{s} d\eta \frac{d\Gamma_0(\eta)}{dy} K_C(y-\eta),$$

where the symbol $\mathscr{I}$ is locally defined for the purpose of this appendix. Substituting the variable of integration, the following is obtained

$$\mathscr{I} = -\int_0^\pi d\xi \frac{d\Gamma(\eta)}{d\xi} K(y-\eta),$$

where

$$\frac{d\Gamma_0(\xi)}{d\xi} = 4U_\infty s \sum_{m=1}^{M} \Gamma_m m \cos(m\xi).$$

The integral $\mathscr{I}$ can be further be decomposed into three integrals as

$$\mathscr{I} = \mathscr{I}_1 + \mathscr{I}_2 + \mathscr{I}_3,$$

where

$$\mathscr{I}_1 = -\int_0^\pi d\xi \frac{d\Gamma_0(\eta)}{d\xi} \frac{1}{2} \frac{e^{-\nu|y-\eta|}}{y-\eta}, \tag{A.9}$$

$$\mathscr{I}_2 = \int_0^\pi d\xi \frac{d\Gamma_0(\eta)}{d\xi} \frac{1}{2} \operatorname{sgn}(y-\eta) i\nu E_1(\nu|y-\eta|), \tag{A.10}$$

$$\mathscr{I}_3 = -\int_0^\pi d\xi \frac{d\Gamma_0(\eta)}{d\xi} \frac{1}{2} \operatorname{sgn}(y-\eta) \nu P(\nu|y-\eta|). \tag{A.11}$$

These integrals will be considered separately. The simpler integrals $\mathscr{I}_1$ and $\mathscr{I}_3$ will be considered first in Sec. A.2.1 and Sec. A.2.2. This will be followed by the more challenging integral $\mathscr{I}_2$ in Sec. A.2.3.

A.2.1 The $\mathscr{I}_1$ integral

The integral $\mathscr{I}_1$ can be simplified to

$$\mathscr{I}_1 = -2U_\infty s \sum_{m=1}^{M} \Gamma_m k \left[\int_0^\pi d\xi \cos(m\xi) \frac{e^{-\nu|y-\eta|}}{y-\eta} \right],$$

where $1/(y-\eta)$ can be identified as the singular part, singular at $\eta = y = s\cos(\xi_s)$. This can be evaluated using the singularity subtraction method as

$$\mathscr{I}_1 = -2U_\infty s \sum \Gamma_m k \int_0^\pi d\xi \frac{1}{y-\eta} \left(\cos(m\xi) e^{-\nu|y-\eta|} - \cos(m\xi_s) \right), \tag{A.12}$$

which can now be evaluated numerically. The quadrature should be split at ξ_s due to the discontinuous derivative.

A.2.2 The $\mathscr{I}_3$ integral

The integral $\mathscr{I}_3$ can be evaluated with relative ease since $P(y)$ is not singular. Consequentially it is possible to numerically evaluate

$$\mathscr{I}_3 = -2U_\infty s\nu \sum_{m=1}^{M} \Gamma_m m \left[\int_0^\pi d\xi \cos(m\xi) \mathrm{sgn}(y-\eta) P(\nu|y-\eta|) \right]$$

directly, splitting the quadrature about $\eta = y$.

A.2.3 The $\mathscr{I}_2$ integral

The integral $\mathscr{I}_2$ is more challenging than $\mathscr{I}_1$ and $\mathscr{I}_3$, and the primary reason for the inclusion of this appendix. Repeating $\mathscr{I}_2$,

$$\mathscr{I}_2 = \int_0^\pi d\xi \frac{d\Gamma_0(\eta)}{d\xi} \frac{1}{2} \mathrm{sgn}(y-\eta) i\nu E_1(\nu|y-\eta|),$$

which can be evaluated as a summation

$$\mathscr{I}_2 = 2U_\infty s i\nu \sum_{m=1}^{M} \Gamma_m m \left[\int_0^\pi d\xi \cos(k\xi) \mathrm{sgn}(y-\eta) E_1(\nu|y-\eta|) \right].$$

This is singular, but singularity subtraction cannot easily be applied. Instead, an intermediate form is required. Two possible intermediates are suggested here, useful for verification purposes. The first method uses the derivative of the exponential integral, and the second uses a series expansion form.

$\mathscr{I}_2$ using the $E_1(z)$ derivative definition

The exponential integral derivative is

$$\frac{dE_1(z)}{dz} = -\frac{e^{-z}}{z}.$$

This allows the following indefinite integrals to be defined:

$$\int dx\ E_1(x) = xE_1(x) - e^{-x} + C,$$
$$\int dx\ E_1(-x) = xE_1(-x) + e^{x} + C,$$

where C is a constant of integration. This can be used to evaluate an integral with a singularity at $x = 0$ in the Cauchy sense

$$\int_a^b dx\, \mathrm{sgn}(x)E_1(|x|) = \lim_{\varepsilon \to 0^+} \left(\left[-xE_1(-x) - e^x\right]_a^{-\varepsilon} + \left[xE_1(x) - e^{-x}\right]_\varepsilon^b \right),$$

where $a < 0 < b$. This limit $\lim_{\varepsilon \to 0^+}(\varepsilon E_1(\varepsilon)) = 0$. As a consequence this evaluates as

$$\int_a^b dx\, \mathrm{sgn}(x)E_1(|x|) = aE_1(-a) + e^a + bE_1(b) - e^{-b}.$$

This does not yet have the complexity of the original integral $\mathscr{I}_2$. Some substitution is in order. We require $x = \nu(y - \eta)$, and substitute for ξ again. Consequently, $x = \nu(y - s\cos(\xi))$ and $dx = \nu s \sin(\xi)\; d\xi$. This gives the integral

$$\int_a^b dx\, \mathrm{sgn}(x)E_1(|x|) = \nu s \int_0^\pi d\xi\, \mathrm{sgn}(y - s\cos(\xi))E_1(\nu|y - s\cos(\xi)|)\sin(\xi),$$

where, to satisfy the limits, $b = \nu(y - s\cos(\pi)) = \nu(y + s)$ and $a = \nu(y - s)$

$$\nu s \int_0^\pi d\xi\, \mathrm{sgn}(y - s\cos(\xi))E_1(\nu|y - s\cos(\xi)|)\sin(\xi) = \\ \nu(y-s)E_1(-\nu(y-s)) + e^{\nu(y-s)} + \nu(y+s)E_1(\nu(y+s)) - e^{-\nu(y+s)}.$$

Combining this with the singularity subtraction method allows a regularised integral to be obtained. The rather cumbersome expression for this is:

$$\begin{aligned}\mathscr{I}_2 = 2U_\infty s i \nu \sum_{m=1}^{M} \Gamma_m m \Bigg[& \\ & \int_{\xi_s}^{\pi} d\xi\; E_1(\nu(y - s\cos(\xi)))\sin(\xi) \left(\frac{\cos(m\xi)}{\sin(\xi)} - \frac{\cos(m\xi_s)}{\sin(\xi_s)} \right) - \\ & \int_0^{\xi_s} d\xi\; E_1(\nu(s\cos(\xi) - y))\sin(\xi) \left(\frac{\cos(m\xi)}{\sin(\xi)} - \frac{\cos(m\xi_s)}{\sin(\xi_s)} \right) + \\ \frac{\cos(m\xi_s)}{\nu s \sin(\xi_s)} & \left(\nu(y-s)E_1(-\nu(y-s)) + e^{\nu(y-s)} + \nu(y+s)E_1(\nu(y+s)) - e^{-\nu(y+s)} \right) \Bigg].\end{aligned} \tag{A.13}$$

$\mathscr{I}_2$ using the expansion definition of $E_1(z)$

$\mathscr{I}_2$ can also be tackled by identifying and extracting the singular part of E_1. The following identity is from Abramowitz and Stegun 5.1.11 [227]:

$$E_1(z) = -\gamma - \ln(z) - \sum_{n=1}^{\infty} \frac{(-1)^n z^n}{n n!}$$

where the singularity in E_1 is logarithmic. This can separated in the integral:

$$\begin{aligned}
\mathscr{I}_2 &= 2U_\infty s i \nu \sum_{m=1}^{M} \Gamma_m m \left[\int_0^\pi d\xi \cos(m\xi) \mathrm{sgn}(y-\eta) E_1(\nu|y-\eta|) \right] \\
&= 2U_\infty s i \nu \sum_{m=1}^{M} \Gamma_m m \Bigg[\int_0^\pi d\xi \cos(m\xi) \mathrm{sgn}(y-\eta) \left(E_1(\nu|y-\eta|) + \ln(\nu|y-\eta|) \right) \\
&\qquad\qquad - \int_0^\pi d\xi \cos(m\xi) \mathrm{sgn}(y-\eta) \ln(\nu|y-\eta|) \Bigg]
\end{aligned}$$

The integral $\int dx \ln(x) = x\ln(x) - x + C$ is well known. Swapping the variable of integration allows the following to be obtained

$$\begin{aligned}
&\int_0^\pi d\xi \;\ln(|\nu(y-\eta)|)\nu s \sin(\xi) = \\
&\qquad \nu(y+s)\ln(\nu(y+s)) - \nu(y+s) - \nu(y-s)\ln(-\nu(y-s)) + \nu(y-s)
\end{aligned}$$

This provides another means by which to regularise the integral $\mathscr{I}_2$, obtained as

$$\begin{aligned}
\mathscr{I}_2 = 2U_\infty s i \nu \sum_{m=1}^{M} \Gamma_m m \Bigg[& \\
& \int_0^\pi d\xi \cos(m\xi) \mathrm{sgn}(y-\eta) \left(E_1(\nu|y-\eta|) - \ln(\nu|y-\eta|) \right) \\
& - \int_0^\pi d\xi \;\nu s \sin(\xi) \ln(\nu|y-\eta|) \left(\mathrm{sgn}(y-\eta) \frac{\cos(k\xi)}{\nu s \sin(\xi)} - \mathrm{sgn}(0) \frac{\cos(m\xi_s)}{\nu s \sin(\xi_s)} \right) \\
& - \frac{\mathrm{sgn}(0)\cos(k\xi_s)}{\nu s \sin(\xi_s)} \Big(\nu(y+s)\ln(\nu(y+s)) - \nu(y+s) \\
& - \nu(y-s)\ln(-\nu(y-s)) + \nu(y-s) \Big) \Bigg] \qquad \text{(A.14)}
\end{aligned}$$

where once again care must be taken to use separate quadratures either side of the singularity.

Appendix B

Unsteady thin aerofoil theory

The unsteady aerodynamics of wings is grounded in the seminal works of Theodorsen [56], Sears [62], Wagner [52] and Küssner [54]. These consider the unsteady flow about a thin aerofoil using potential flow theory.

In this thesis we use lift and moment results obtained from Theodorsen's theory in the derivation of lifting-line theory, and also present the results for the leading edge suction. These results are obtained for pitching and heaving motions, although there is no reason why more general kinematics could not used.

Here, the derivation of the lift, moment and leading edge suction is presented by two means. Firstly, the solution of Ramesh based on a Glauert-Fourier vorticity distribution of bound vorticity on a thin aerofoil. This can be easily related to the large amplitude unsteady thin aerofoil theory with a discrete vortex particle wake used as the inner solution in Chapter 5. Secondly, Küssner and Schwarz's general solution is presented, since it is less mathematically challenging in many cases.

B.1 Glauert-Fourier vorticity distribution series solution

Following Ramesh *et al.* [102], a thin aerofoil in unsteady flow can have its bound vorticity distribution described as a Glauert-Fourier series

$$\gamma(x_i;t) = 2U_\infty \left[A_0(t)\frac{1+\cos\theta}{\sin\theta} + \sum_{n=1}^{\infty} A_n(y,t)\sin(n\theta) \right] \tag{B.1}$$

θ transforms the spanwise coordinate as $x_i = 0.5c(1-\cos\theta)$ where x_i is in [0, 1] (see Fig. 2.2), and A_0, $A_1 ... A_N$ are time-dependent Fourier coefficients.

The A_0 term is singular at the leading edge. This is required to turn flow round the sharp leading edge found in thin aerofoil theory. It is related to the suction peak caused by the turn, and has found significance as the Leading-Edge Suction Parameter of Ramesh *et al.* [145]. Technically, this distribution does perfectly satisfy the Kutta condition since, for unsteady cases, there may be non-zero vorticity at the trailing edge.

Several quantities are of interest. The bound circulation Γ, the lift coefficient C_l and the moment coefficient C_m. These can be expressed in terms of the first few values of A_i and its derivative with respect to time, $\dot{A}_i$:

$$\Gamma(t) = U_\infty c\pi \left(A_0 + \frac{A_1}{2}\right), \tag{B.2}$$

$$C_l(t) = 2\pi \left[A_0 + \frac{1}{2}A_1 + \frac{c}{U_\infty}\left(\frac{3}{4}\dot{A}_0 + \frac{1}{4}\dot{A}_1 + \frac{1}{8}\dot{A}_2\right)\right], \tag{B.3}$$

$$\begin{aligned} C_m(t) = 2\pi \Bigg[& A_0\left(x_m^* - \frac{1}{4}\right) + \frac{A_1}{2}\left(x_m^* - \frac{1}{2}\right) + \frac{A_2}{8} \\ & + \frac{c}{U_\infty}\left(\frac{3\dot{A}_0}{4}\left(x_m^* - \frac{7}{12}\right) + \frac{\dot{A}_1}{4}\left(x_m^* - \frac{11}{16}\right) + \frac{\dot{A}_2}{8}\left(x_m^* - \frac{1}{2}\right) + \frac{\dot{A}_3}{64}\right)\Bigg], \end{aligned} \tag{B.4}$$

where $x_m^* \in [0,1]$ is the non-dimensional reference location for pitching moment. Ramesh [75] obtained the coefficients for Theodorsen's problem as

$$\begin{aligned} A_0 &= C(k)\frac{W_{3qc}}{U_\infty} - \frac{\dot{\alpha}c}{4U_\infty}, \\ A_1 &= \frac{\dot{\alpha}c}{2U_\infty} - 2\frac{W_{3qc}}{U_\infty}(C(k) - e^{-ik}S(k)), \\ A_{2\ldots N} &= (-1)^n 2ikS(k)\frac{W_{3qc}}{U_\infty}Q_n, \end{aligned} \tag{B.5}$$

where $C(k)$ is Theodorsen's function (Eq. 2.17),

$$C(k) = \frac{K_1(ik)}{K_1(ik) + K_0(ik)},$$

and S(k) is the Sears function,

$$S(k) = \frac{1/ik}{K_1(ik) + K_0(ik)}, \tag{B.6}$$

where $K_0(z)$ and $K_1(z)$ are modified Bessel functions of the second kind, as defined by Olver *et al.* [221]. The terms $Q_n(k)$ are wake coefficients,

$$Q_n(k) = \int_0^\infty e^{-ik\cosh\zeta}e^{-n\zeta}d\zeta \tag{B.7}$$

and W_{3qc} is the normal downwash at the aerofoil three-quarter chord location. This is obtained from the kinematics as

$$W_{3qc} = U_\infty \alpha - \dot{h} - \dot{\alpha} c \left(x_p^* - \frac{3}{4} \right) \tag{B.8}$$

Using the expressions rigid for body pitch and plunge (Eq. 2.7 and Eq. 2.8) and downwash (Eq. B.8), the normal downwash on the aerofoil at the three-quarter chord point can be obtained for heave and pitch respectively as

$$W^{2D}_{3qc,h}(t) = -2iU_\infty k h_0^* e^{i\omega t} \tag{B.9}$$

$$W^{2D}_{3qc,\alpha}(t) = U_\infty \left[1 - 2ik \left(x_p^* - \frac{3}{4} \right) \right] \alpha_0 e^{i(\omega t + \psi)} \tag{B.10}$$

This allows the bound circulation (Eq. 2.11 and Eq. 2.11), lift coefficient (Eq. 2.13 and Eq. 2.14) and moment coefficient (Eq. 2.15 and Eq. 2.16) to be found.

B.2 Küssner and Schwarz's general solution

Unlike the Glauert-Fourier vorticity distribution method described in the previous section, it is most convenient to derive this general solution for an aerofoil in $x \in [-c/2, c/2]$, where c is the chord. At the leading edge $x = -c/2$ and at the trailing edge $x = c/2$. This aerofoil coordinate can also be described in terms of θ_{ks} as $x = c\cos(\theta_{ks})/2$. The aerofoil is undergoing small amplitude harmonic oscillation. These can be defined by a complex deformation shape $z_0(x)$

$$z = Re(z_0(x)e^{i\omega t}), \tag{B.11}$$

where ω is angular frequency and t is time. This can be used to obtain the upwash v_0 on the aerofoil:

$$v_0(x) = U_\infty \frac{dz}{dx} + \frac{dz}{dt} = \left(i\omega - U_\infty \frac{d}{dx} \right) z_0(x), \tag{B.12}$$

or the v_0 expression can be given directly for gust problems such as that of Sears [62]. This can also be expressed as a Fourier series

$$v_0(\theta_{ks}) = -U_\infty \left(P_0 + 2\sum_{n=1}^{\infty} P_n \cos(n\theta_{ks}) \right) e^{i\omega t}, \tag{B.13}$$

where

$$P_n = -\frac{1}{U_\infty \pi e^{i\omega t}} \int_0^\pi d\theta_0 \; v_0(\theta_0) \cos(n\theta_0) \text{ for } n \geq 0. \tag{B.14}$$

The pressure distribution across the foil can then be found as

$$\Delta C_p = \left[4B_0 \tan\left(\frac{\theta_{ks}}{2}\right) + 8\sum_{1}^{\infty} B_n \sin(n\theta_{ks})\right] e^{i\omega t}, \tag{B.15}$$

where

$$\begin{aligned} B_0 &= C(k)(P_0 + P_1) - P_1 \\ B_n &= \frac{ik}{2n}P_{n-1} + P_n - \frac{ik}{2n}P_{n+1} \end{aligned} \tag{B.16}$$

This allows the lift and mid-chord moment coefficients to be found as

$$C_l = \frac{L}{\frac{1}{2}\rho_\infty U_\infty^2 c} = 2\pi\left((P_0 + P_1)C(k) + (P_0 - P_2)\frac{ik}{2}\right)e^{i\omega t}, \tag{B.17}$$

$$C_{m\frac{1}{2}} = \frac{M_{\frac{1}{2}}}{\frac{1}{2}\rho_\infty U_\infty^2 c^2} = \frac{\pi}{2}\left(P_0 C(k) - P_1(1 - C(k)) - (P_1 - P_3)\frac{ik}{4} - P_2\right)e^{i\omega t}, \tag{B.18}$$

where the chord reduced frequency $k = \omega c/(2U)$, $C(k)$ is the Theodorsen function (Eq. 2.17), and $H_0^{(2)}$ and $H_1^{(2)}$ are Hankel functions of the second kind defined in Olver *et al.* [221].

For the total bound vorticity Newman [68] gives

$$\Gamma = \frac{-4U_\infty e^{-ik}}{\omega\pi}\frac{1}{iH_0^{(2)}(k) + H_1^{(2)}(k)}\int_0^\pi \sqrt{\frac{\cos(\theta_0) - 1}{\cos(\theta_0) + 1}}\sin(\theta_0)v_0(\theta_0)d\theta_0, \tag{B.19}$$

allowing the following to be obtained:

$$\Gamma = \frac{4iU_\infty^2 e^{-ik}}{\omega}\frac{P_0 - P_1}{iH_0^{(2)}(k) + H_1^{(2)}(k)}e^{i\omega t}. \tag{B.20}$$

A less traditional characteristic value is the leading edge suction parameter introduced by Ramesh *et al.* [145]. This can be obtained directly from the leading edge pressure singularity as

$$\mathcal{L}(t) = B_0 e^{i\omega t} \tag{B.21}$$

Fung [70] provides a good explanation of this theory for both Theodorsen-like and Sears-like problems, albeit for an aerofoil of chord $c = 2$ only.

Appendix C

Computational fluid dynamics

C.1 Euler CFD

Computational fluid dynamics simulations were completed for the validation of Euler regime problems in this thesis and related journal articles. This was completed using the open-source CFD toolbox OpenFOAM. For all of these cases, the method of solution and meshes were identical. The author acknowledges the work of Kiran Ramesh for the CFD method, and the generous support of the Cirrus UK National Tier-2 HPC service at EPCC (http://www.cirrus.ac.uk) and the ARCHIE-WeSt High Performance Computer (www.archie-west.ac.uk) based at the University of Strathclyde.

The following paragraph is based on the original text of Kiran Ramesh from Bird and Ramesh [1].

OpenFOAM was used to analyse unsteady incompressible Euler problems. Heave and pitch kinematics were applied to a body-fitted, structured computational mesh, and the finite volume method was used to solve the time-dependent governing equations. The time derivatives were discretized with a second-order backward implicit scheme, and second-order limited Gaussian integration schemes are used for the gradient, divergence and Laplacian terms. The pressure implicit with splitting of operators (PISO) algorithm implements pressure-velocity coupling. Laminar flow is considered with kinematic viscosity set to zero. The moving wing is represented by a slip boundary condition.

In all cases, a rectangular wing with a NACA0004 wing section was used. This aerofoil section was chosen to match the thin wing assumption often employed by methods in this thesis. Three aspect ratios (8, 4, and 2) were considered. Only half the wing was meshed since the problems considered were symmetric about the wing centre. Cylindrical O-meshes were constructed with 160 cells around the wing section, with increased resolution near the leading and trailing edges. In the wall-normal direction the far-field extends 20 chord lengths in all directions around the aerofoil section with 115 cells in this region. The aspect ratio 8, 4 and 2 wings have 218, 199 and 87 cells respectively over the semispan of

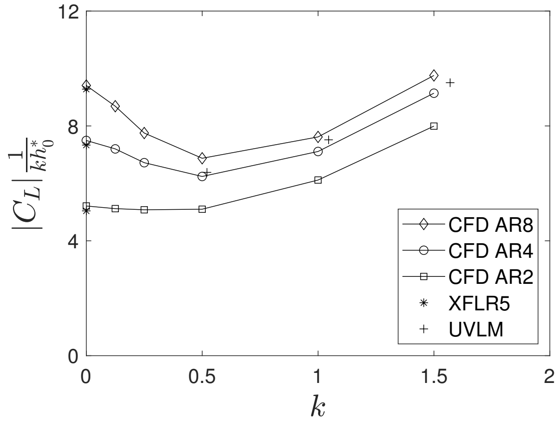

Figure C.1: Comparison of the lift coefficients obtained from CFD, the XFLR5 steady panel method and the UVLM for a heaving rectangular wing.

the wing, with increased resolution near the tip. The spanwise domain extends 100 cells beyond the wingtip, corresponding to 5 chord lengths.

Using the finite volume method to study Euler regime problems is theoretically challenging for two reasons. Firstly, there is no inherent vorticity generation mechanism in Euler CFD, with vorticity generated by numerical error at sharp edges. And secondly, inviscid flows have no minimum length scale, making it difficult to verify that the mesh is sufficiently well refined.

In practice, CFD can provide a good solution to Euler problems, as verified by a steady 3D panel method and unsteady vortex lattice data. The Euler CFD method can be compared to the steady 3D panel method code of XFLR5. For the panel method, the chord section was discretized into 60 panels with a cosine distribution increasing resolution at the leading and trailing edges. For the aspect ratio 8, 4 and 2 wings, the span was discretised into 60, 45 and 40 panels were used respectively, with cosine distributions used higher resolution near the wing tips. The unsteady vortex lattice data is based on the work of Lee [228] as reproduced in Sclavounos [94]. These results are shown in Fig. C.1

For the steady case at chord reduced frequency $k \to 0$, the XFLR5 panel method is in good agreement with the CFD at all aspect ratios. This verifies that the CFD method correctly models the Kutta condition at the trailing edge and that transport of the wing-tip vortex is successful.

The UVLM solution of Lee [228] only provides data for the aspect ratio 4 case, and assumes that the wing is thin. Despite differences in the modelled geometry, the UVLM and CFD are in agreement at all values of chord reduced frequencies studied.

C.2 Low Reynolds number CFD

For many practical problems comparison to the Euler regime is inappropriate, and low Reynolds number results are needed. To enable this, the OpenFOAM CFD toolbox was once again used. The author acknowledges the work of Kiran Ramesh for the CFD method, and the generous support of the Cirrus UK National Tier-2 HPC service at EPCC (http://www.cirrus.ac.uk).

The CFD was designed to be validated against experiments carried out by Shūji Ōtomo and Ignazio Maria Viola at the University of Edinburgh. Rectangular wings of aspects ratios of 6, 3 and 1 were used. An aspect ratio 3 wing was used for the experimental validation. A NACA0008 aerofoil was used chosen to ensure a sufficiently thick aerofoil for the experiment.

The numerical method used in the CFD is described in Sec. C.2, and validation against the experiments of Ōtomo and Viola in Sec. C.2.

CFD numerical method

The following paragraph is based on the original text of Kiran Ramesh from Bird et al. [2].

The OpenFOAM CFD toolbox was used to solve the incompressible Reynolds-Averaged Navier-Stokes equations. As with the Euler method, heave and pitch kinematics were applied to a body-fitted, structured computational mesh, and the finite volume method was used to solve the time-dependent governing equations. The transient terms were discretized with a backward implicit scheme, and limited Gaussian integration schemes were applied to the gradient, divergence and Laplacian terms. Pressure-velocity coupling was achieved using the pressure implicit with splitting of operators (PISO) algorithm, and the Spalart-Allmaras (SA) model [229] was used for turbulent closure. The SA model has previously been successfully applied to unsteady, separated flows at Re=1×10^4 such as those in the work of McGowan *et al.* [120] and Ramesh *et al.* [145]. The original SA model's trip terms were turned off, and the effects of the effects of the turbulence model confined to the shed vortical structures and wake.

Rectangular wings with a NACA0008 section, squared off wing tips and a chord of $\overline{c}$ =0.1 m were used. Only half the wing was meshed due to the flow symmetry about the wing centre, and an O-mesh topology with increased leading and trailing edge resolution was used to discretise the chord into 116 cells. Aspect ratios 6, 3 and 1 were considered with discretised with 211, 105 and 35 cells of the semispan of the wing respectively. The domain extended 4 chords beyond the wing tip in the spanwise direction, discretised with an average spacing of 21 cells per chord length. The cell spacing in the wall-normal direction on the wing started at 1.5×10^{-5} m at the wall to obtain a $y^+ < 1$. This mesh extends a distance of 11.5 chord lengths with an average density of 16.3 cells per chord

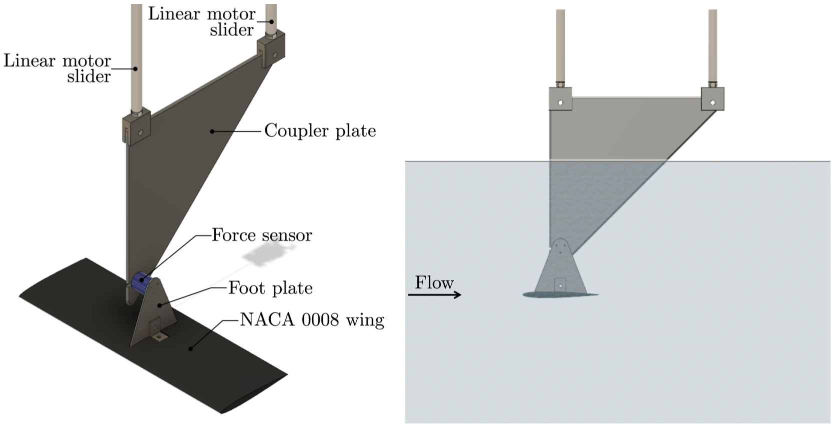

(a) Detailed view (b) Side view

Figure C.2: Test section and experimental setup

length. For the simulations, a free stream velocity U_∞ of $0.1\,\mathrm{m\,s^{-1}}$ was used in a fluid with kinematic viscosity $1 \times 10^{-6}\,\mathrm{m\,s^{-2}}$.

Validation against experiment

The CFD was validated against an experiment performed in the water flume at the University of Edinburgh.

The following three paragraphs are based on the original text of Shūji Ōtomo from Bird et al. [2]

The aspect ratio 3 wing was 3D printed. The free stream velocity was fixed at $0.1\,\mathrm{m\,s^{-1}}$, matching the value used for the CFD resulting in a Reynolds number of 1×10^4. The heaving foil rig consists of two linear motors (LinMot, PS01-23x80F-HP-R20) connected with each other via a linkage system and a coupler plate. This is shown in Fig. C.2.

A six-axis force/torque sensor (ATI Inc., Nano-17 IP68), mounted between the coupler plate and the foot plate, was used to conduct direct force measurements. The sensor is capable of measuring forces in the plane of the wing cross section up to $\pm 25\,\mathrm{N}$, $\pm 35\,\mathrm{N}$ in the orthogonal direction, and moments up to $\pm 250\,\mathrm{N\,m}$ around the three axes. The forces are measured with a resolution of 1/160 N and the moments with a precision of 1/32 N m. LabVIEW was used to both trigger the prescribed motor kinematics and to record the forces using a DAQ board for synchronised data measurement. The forces were sampled at 10 kHz, and filtered in three steps. A fourth-order Butterworth low-pass filter with a cutting frequency of 75 Hz was followed by smoothing with a 200 points moving average before a sixth-order Chebyshev II low-pass filter with −20 dB attenuation in the stopband was applied. This method can preserve load spikes. Phase-averaging is applied for 20 periods.

Flowfield analysis is performed using Particle Image Velocimetry (PIV). A double pulsed Nd:YAG laser (New Wave Research, Solo PIV, 532 nm, 200 mJ) was used to illu-

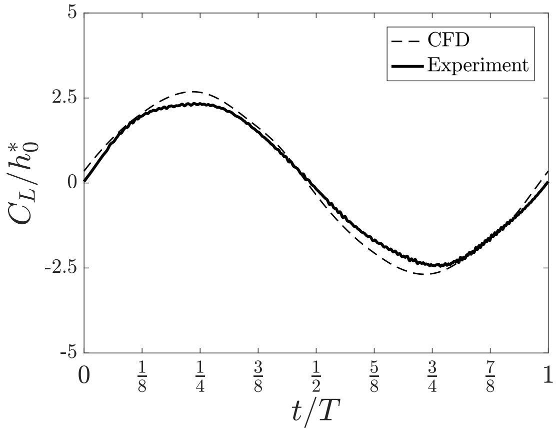

Figure C.3: Comparison of the lift coefficients obtained from CFD and experiment for a plunging rectangular aspect ratio 3 wing for $h_0^* = 0.5$ and $k = 0.4$.

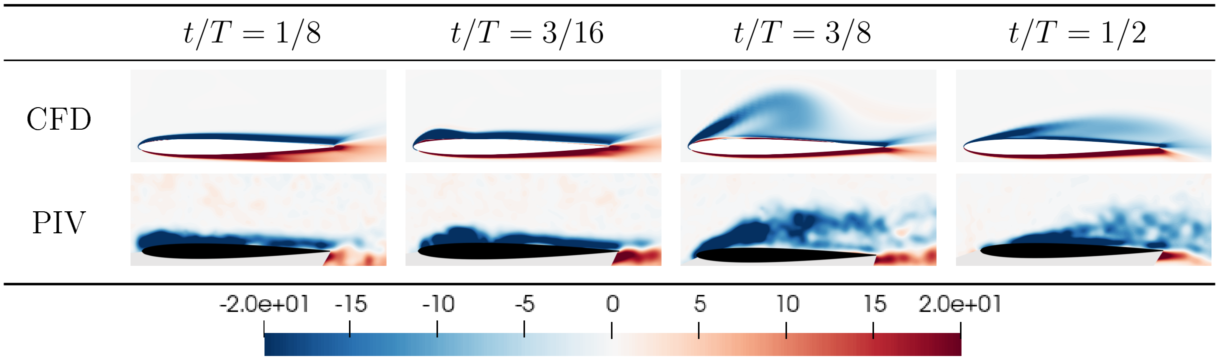

Figure C.4: Comparison of experimental and CFD quarter span vorticity distributions for rectangular aspect ratio 3 wings oscillating in heave at $k = 0.4$ and $h_0^* = 0.5$.

minate the plane at 1/4 of the span of the wing, with silver coated hollow glass spheres (Potters Industries, 10 µm) used as seeding. Images are obtained with CCD camera (IMPERX, B2020 equipped with Nikon 50 mm lens) with a resolution of 2056 pix × 2060 pix. Velocity vectors are computed using adaptive multi-pass cross-correlation, with a first interrogation window of 64 pix × 64 pix, and a final interrogation window of 32 pix × 32 pix, and an overlap of 50% (DaVis, LaVision Inc.) The Gaussian filtered PIV data was phase-averaged over 30 periods.

The case of the aspect ratio 3 rectangular wing oscillating ($h = h_0 c \cos(\omega t)$) with non-dimensional amplitude $h_0^* = h_0 c = 0.5$ at a chord reduced frequency of $k = 0.4$ was used for validation. At this chord-reduced frequency unsteady effects are important, but the frequency is not so high as to cause the forces to be dominated by added mass effects. The amplitude is sufficiently large to cause the formation of leading-edge vortex structures. Figure C.3 shows a comparison of the lift coefficient obtained using CFD and experiment. The spanwise vorticity at the quarter span point is shown in Fig. C.4 at times $t/T = [1/8, 3/16, 3/8, 1/2]$. These are critical times that show the development of the LEV.

The CFD predicts the lift coefficient obtained using the experiment well. The PIV flow visualisation matches that obtained from CFD. In both methods, the formation of the LEV is visible between $t/T = 1/8$ and $t/T = 3/16$. At time $t/T = 3/8$, matching flow features can be seen, including the angle of the leading-edge shear layer and the approximate shape of the LEV region. At the bottom of the downstroke at $t/T = 1/2$, both CFD and experiment show that the vortex structure has been convected downstream, whilst remaining attached to the surface of the wing.

Bibliography

[1] H. J. A. Bird and K. Ramesh, “Unsteady lifting-line theory and the influence of wake vorticity on aerodynamic loads,” *Theoretical and Computational Fluid Dynamics*, jul 2021.

[2] H. J. A. Bird, K. Ramesh, S. Ōtomo, and I. M. Viola, “Usefulness of inviscid linear unsteady lifting-line theory for viscous large-amplitude problems,” *AIAA Journal*, 2021. Accepted.

[3] H. J. A. Bird and K. Ramesh, “Applying frequency-domain unsteady lifting-line theory to time-domain problems,” *AIAA Journal*, 2021. In review.

[4] H. J. A. Bird and K. Ramesh, “Theoretical and computational studies of a rectangular finite wing oscillating in pitch and heave,” in *6th European Conference on Computational Mechanics (ECCM 6) 7th European Conference on Computational Fluid Dynamics (ECFD 7)*, International Centre for Numerical Methods in Engineering, June 2018.

[5] H. J. A. Bird, S. Otomo, K. Ramesh, and I. M. Viola, “A geometrically non-linear time-domain unsteady lifting-line theory,” in *AIAA Scitech 2019 Forum*, American Institute of Aeronautics and Astronautics, Jan 2019.

[6] H. J. A. Bird, K. Ramesh, S. Ōtomo, and I. M. Viola, “Leading edge vortex formation on finite wings using vortex particles,” in *AIAA Scitech 2021 Forum*, American Institute of Aeronautics and Astronautics, Jan 2021.

[7] DreamWorks Animation, Columbus 81 Productions, and Pacific Data Images, “Bee movie.” Film, Paramount Home Entertainment, 2007.

[8] “A Russian military build-up on Ukraine’s border prompts alarm,” *The Economist*, vol. 439, April 2021.

[9] “St Louis and federal courts mull a controversial surveillance programme,” *The Economist*, vol. 439, no. 9241, 2021.

[10] I. Boudway, "Medical drone startup to begin COVID vaccine delivery in April," *Bloomberg News*, Feb. 2021. Accessed online 21/04/2021.

[11] R. Neate, "Drone deliveries soar in rural scotland during coronavirus outbreak," *The Guardian*, May 2020. Accessed online 21/04/2021.

[12] C. K. Gilmore, M. Chaykowsky, and B. Thomas, *Autonomous Unmanned Aerial Vehicles for Blood Delivery: A UAV Fleet Design Tool and Case Study.* RAND CORP, 2020.

[13] Federal Aviation Administration, "Package delivery by drone (part 135)," 2019. Accessed 21/04/2021.

[14] J. Gonzalo, D. López, D. Domínguez, A. García, and A. Escapa, "On the capabilities and limitations of high altitude pseudo-satellites," *Progress in Aerospace Sciences*, vol. 98, pp. 37–56, Apr 2018.

[15] R. Cellan-Jones, "Facebook's drones - made in britain." `http://www.bbc.co.uk/news/technology-36855168`, July 2016. Accessed: 27/04/2018.

[16] E. Gurdus, "A 'super cell tower' in the stratosphere: Aerovironment and softbank's 5g vision." `https://www.cnbc.com/2018/09/13/aerovironment-and-softbanks-5g-vision-cell-tower-in-the-stratosphere.html`, Oct. 2018.

[17] S. Trimble, "Wildfire monitoring role eyed for haps, hale aircraft." `https://aviationweek.com/awindefense/wildfire-monitoring-role-eyed-haps-hale-aircraft-0`, Oct. 2019. Accessed 02/10/2019.

[18] W. Williams and M. Harris, "The challenges of flight-testing unmanned air vehicles," in *Systems Engineering, Test & Evaluation Conference, Sydney Australia*, 2002.

[19] "Unsteady aerodynamic response of rigid wings in gust encounters," tech. rep., North Atlantic Treaty Organisation Science and Technology Organisation, 2020. RTO-TR-AVT-282.

[20] A. R. Jones and O. Cetiner, "Overview of NATO AVT-282: Unsteady aerodynamic response of rigid wings in gust encounters," in *AIAA Scitech 2020 Forum*, American Institute of Aeronautics and Astronautics, Jan 2020.

[21] T. E. Noll, J. M. Brown, M. E. Perez-Davis, S. D. Ishmael, G. C. Tiffany, and M. Gaier, "Investigation of the helios prototype aircraft mishap," tech. rep., National Aeronautics and Space Administration, 2004.

[22] J. Murua, *Flexible Aircraft Dynamics with a Geometrically-Nonlinear Description of the Unsteady Aerodynamics.* PhD thesis, Imperial College London, May 2012.

[23] W. Su and C. E. S. Cesnik, “Nonlinear aeroelasticity of a very flexible blended-wing-body aircraft,” *Journal of Aircraft*, vol. 47, pp. 1539–1553, Sep 2010.

[24] W. Su and C. E. S. Cesnik, “Dynamic response of highly flexible flying wings,” *AIAA Journal*, vol. 49, pp. 324–339, Feb 2011.

[25] R. J. S. Simpson, *Unsteady Aerodynamics, Reduced-Order Modelling, and Predictive Control in Linear and Nonlinear Aeroelasticity with Arbitrary Kinematics.* phdthesis, Imperial College London, 2016.

[26] J. R. Jones and C. E. S. Cesnik, “Preliminary flight test correlations of the x-HALE aeroelastic experiment,” *The Aeronautical Journal*, vol. 119, pp. 855–870, July 2015.

[27] P. J. González, F. J. Silvestre, M. de Freitas Virgilio Pereira, Z. Y. Pang, and C. E. S. Cesnik, “Loop-separation control for very flexible aircraft,” *AIAA Journal*, vol. 58, pp. 3819–3834, Sep 2020.

[28] C.-S. Chang, D. H. Hodges, and M. J. Patil, “Flight dynamics of highly flexible aircraft,” *Journal of Aircraft*, vol. 45, pp. 538–545, Mar 2008.

[29] X. Changchuan, Y. Lan, L. Yi, and Y. Chao, “Stability of very flexible aircraft with coupled nonlinear aeroelasticity and flight dynamics,” *Journal of Aircraft*, vol. 55, pp. 862–874, Mar 2018.

[30] H. Hesse and R. Palacios, “Reduced-order aeroelastic models for dynamics of maneuvering flexible aircraft,” *AIAA Journal*, vol. 52, pp. 1717–1732, Aug 2014.

[31] Z. Wang, P. C. Chen, D. D. Liu, and D. T. Mook, “Nonlinear-aerodynamics/nonlinear-structure interaction methodology for a high-altitude long-endurance wing,” *Journal of Aircraft*, vol. 47, pp. 556–566, Mar 2010.

[32] F. J. Silvestre, A. B. G. Neto, R. M. Bertolin, R. G. A. da Silva, and P. Paglione, “Aircraft control based on flexible aircraft dynamics,” *Journal of Aircraft*, vol. 54, pp. 262–271, Jan 2017.

[33] M. J. Patil and D. H. Hodges, “Flight dynamics of highly flexible flying wings,” *Journal of Aircraft*, vol. 43, pp. 1790–1799, Nov 2006.

[34] C. M. Shearer and C. E. S. Cesnik, “Nonlinear flight dynamics of very flexible aircraft,” *Journal of Aircraft*, vol. 44, pp. 1528–1545, Sep 2007.

[35] L. Liu, T. Kim, and K. L. Lai, “Efficient analysis of HALE aircraft structure for static aeroelastic behavior,” *Journal of Aerospace Engineering*, vol. 30, p. 04016075, Jan 2017.

[36] M. Ritter, P. Teixeira, and C. E. Cesnik, “Comparison of nonlinear aeroelastic methods for maneuver simulation of very flexible aircraft,” in *2018 AIAA/ASCE/AHS/ASC Structures, Structural Dynamics, and Materials Conference*, American Institute of Aeronautics and Astronautics, Jan 2018.

[37] F. Afonso, J. Vale, É. Oliveira, F. Lau, and A. Suleman, “A review on non-linear aeroelasticity of high aspect-ratio wings,” *Progress in Aerospace Sciences*, vol. 89, pp. 40–57, Feb 2017.

[38] “Experimental and computational investigations in low reynolds number aerodynamics, with applications to micro air vehicles (mavs),” tech. rep., North Atlantic Treaty Organization Science and Technology Organization, 2007. RTO-TR-AVT-101.

[39] W. Su, S. S.-M. Swei, and G. G. Zhu, “Optimum wing shape of highly flexible morphing aircraft for improved flight performance,” *Journal of Aircraft*, vol. 53, pp. 1305–1316, sep 2016.

[40] C. S. Beaverstock, B. K. S. Woods, J. H. S.-M. Fincham, and M. I. Friswell, “Performance comparison between optimised camber and span for a morphing wing,” *Aerospace*, vol. 2, no. 3, pp. 524–554, 2015.

[41] E. Livne and T. A. Weisshaar, “Aeroelasticity of nonconventional airplane configurations-past and future,” *Journal of Aircraft*, vol. 40, pp. 1047–1065, Nov 2003.

[42] M. Hansen, J. Sørensen, S. Voutsinas, N. Sørensen, and H. Madsen, “State of the art in wind turbine aerodynamics and aeroelasticity,” *Progress in Aerospace Sciences*, vol. 42, pp. 285–330, Jun 2006.

[43] A. B. Rostami and M. Armandei, “Renewable energy harvesting by vortex-induced motions: Review and benchmarking of technologies,” *Renewable and Sustainable Energy Reviews*, vol. 70, pp. 193–214, Apr 2017.

[44] C. P. Ellington, C. van den Berg, A. P. Willmott, and A. L. R. Thomas, “Leading-edge vortices in insect flight,” *Nature*, vol. 384, pp. 626–630, Dec 1996.

[45] “Unsteady aerodynamics for micro air vehicles,” tech. rep., North Atlantic Treaty Organization Science and Technology Organisation, 2010. RTO-TR-AVT-149.

[46] "Characterization of bio-inspired micro air vehicle dynamics," tech. rep., North Atlantic Treaty Organization Science and Technology Organisation, 2015. RTO-TR-AVT-184.

[47] "Extensions of fundamental flow physics to practical mav aerodynamics," tech. rep., North Atlantic Treaty Organization Science and Technology Organization, 2016. RTO-TR-AVT-202.

[48] J. A. Garcia, "Numerical investigation of nonlinear aeroelastic effects on flexible high-aspect-ratio wings," *Journal of Aircraft*, vol. 42, pp. 1025–1036, jul 2005.

[49] R. Palacios and C. Cesnik, "Static nonlinear aeroelasticity of flexible slender wings in compressible flow," in *46th AIAA/ASME/ASCE/AHS/ASC Structures, Structural Dynamics and Materials Conference*, American Institute of Aeronautics and Astronautics, apr 2005.

[50] B. Hallissy and C. Cesnik, "High-fidelity aeroelastic analysis of very flexible aircraft," in *52nd AIAA/ASME/ASCE/AHS/ASC Structures, Structural Dynamics and Materials Conference*, American Institute of Aeronautics and Astronautics, apr 2011.

[51] J. Katz and A. Plotkin, *Low Speed Aerodynamics*. Cambridge University Press, 2 ed., 2001.

[52] H. Wagner, "Über die entstehung des dynamischen auftriebes von tragflügeln," *ZAMM - Zeitschrift für Angewandte Mathematik und Mechanik*, vol. 5, no. 1, pp. 17–35, 1925.

[53] G. J. Leishman, *Principles of Helicopter Aerodynamics*. Cambridge University Press, 2006.

[54] H. G. Küssner, "Zusammenfassender bericht über den instationären auftrieb von flügeln," *Luftfahrtforschung*, 1936.

[55] I. E. Garrick, "On some reciprocal relations in the theory of nonstationary flows," tech. rep., NACA, 1938.

[56] T. Theodorsen, "General theory of aerodynamic instability and the mechanism of flutter," Tech. Rep. 496, NACA, 1935.

[57] R. T. Jones, "The unsteady lift of a wing of finite aspect ratio," tech. rep., National Advisory Committee for Aeronautics, 1940.

[58] W. P. Jones, "Aerodynamic forces on wings in non-uniform motion," tech. rep., Aeronautical Research Council, 1945.

[59] E. Dowell, "A simple method for converting frequency-domain aerodynamics to the time domain," Tech. Rep. NASA TM-81844, National Aeronautics and Space Administration, 1980.

[60] H. Dunn, "An analytical technique for approximating unsteady aerodynamics in the time domain," tech. rep., National Aeronautics and Space Administration, 1980. NASA Technical Paper 1738.

[61] R. Vepa, "On the use of pade approximants to represent unsteady aerodynamic loads for arbitrarily small motions of wings," in *14th Aerospace Sciences Meeting*, American Institute of Aeronautics and Astronautics, Jan 1976.

[62] W. R. Sears, "Some aspects of non-stationary airfoil theory and its practical application," *Journal of the Aeronautical Sciences*, vol. 8, pp. 104–108, Jan 1941.

[63] T. V. Karman and W. Sears, "Airfoil theory for non-uniform motion," *Journal of the Aeronautical Sciences*, vol. 5, pp. 379–390, Aug 1938.

[64] H. G. Küssner and I. Schwarz, "The oscillating wing with aerodynamically balanced elevator," tech. rep., National Advisory Committee for Aeronautics, 1941.

[65] R. Isaacs, "Airfoil theory for flows of variable velocity," *Journal of the Aeronautical Sciences*, vol. 12, pp. 113–117, Jan 1945.

[66] J. M. Greenberg, "Airfoil in sinusoidal motion in a pulsating stream," tech. rep., NACA, June 1947.

[67] R. L. Bisplinghoff, H. Ashley, and R. R. Halfman, *Aeroelasticity.* Addison-Wesley Publishing, 1955.

[68] J. N. Newman, *Marine Hydrodynamics.* MIT University Press Group Ltd, 1977.

[69] H. Ashley and M. T. Landahl, *Aerodynamics of Wings and Bodies.* Dover Publications Inc., 1985.

[70] Y. C. Fung, *An Introduction to the Theory of Aeroelasticity.* Dover Publications, 1993.

[71] M. E. Goldstein and H. Atassi, "A complete second-order theory for the unsteady flow about an airfoil due to a periodic gust," *Journal of Fluid Mechanics*, vol. 74, pp. 741–765, apr 1976.

[72] H. M. Atassi, "The sears problem for a lifting airfoil revisited - new results," *Journal of Fluid Mechanics*, vol. 141, pp. 109–122, apr 1984.

[73] B. P. Epps and B. T. Roesler, "Vortex sheet strength in the sears, küssner, theodorsen, and wagner aerodynamics problems," *AIAA Journal*, pp. 1–16, Jan 2018.

[74] H. Taha and A. S. Rezaei, "Viscous extension of potential-flow unsteady aerodynamics: the lift frequency response problem," *Journal of Fluid Mechanics*, vol. 868, pp. 141–175, Apr 2019.

[75] K. Ramesh, "On the leading-edge suction and stagnation-point location in unsteady flows past thin aerofoils," *Journal of Fluid Mechanics*, vol. 886, Jan 2020.

[76] L. Prandtl, "Applications of modern hydrodynamics to aeronautics," tech. rep., NACA, 1923. Rep. 116.

[77] F. W. Lanchester, *Aerodynamics, constituting the first volume of a complete work on aerial flight.* London, A. Constable & Co., 1907.

[78] M. Van Dyke, *Perturbation Methods in Fluid Mechanics.* Parabolic Press, 1975.

[79] M. Van Dyke, "Lifting-line theory as a singular-perturbation problem," *Journal of Applied Mathematics and Mechanics*, vol. 28, pp. 90–102, Jan 1964.

[80] J. K. Thurber, "An asymptotic method for determining the lift distribution of a swept-back wing of finite span," *Communications on Pure and Applied Mathematics*, vol. 18, pp. 733–756, nov 1965.

[81] H. K. Cheng, "Lifting-line theory of oblique wings," *AIAA Journal*, vol. 16, pp. 1211–1213, nov 1978.

[82] T. Kida and Y. Miyai, "An alternative treatment of lifting-line theory as a perturbation problem," *Zeitschrift für angewandte Mathematik und Physik ZAMP*, vol. 29, pp. 591–607, Jul 1978.

[83] J.-L. Guermond, "A generalized lifting-line theory for curved and swept wings," *Journal of Fluid Mechanics*, vol. 211, p. 497, Feb 1990.

[84] J.-L. Guermond, "A systematic formula for the asymptotic expansion of singular integrals," *ZAMP Journal of Applied Mathematics and Physics*, vol. 38, pp. 717–729, Sep 1987.

[85] J.-L. Guermond and A. Sellier, "A unified unsteady lifting-line theory," *Journal of Fluid Mechanics*, vol. 229, p. 427, Aug 1991.

[86] J. Weissinger, "The lift distribution of swept-back wings," tech. rep., National Advisory Committee for Aeronautics, 1947.

[87] E. Reissner, "Note on the theory of lifting surfaces," *Proceedings of the National Academy of Sciences*, vol. 35, pp. 208–215, apr 1949.

[88] R. T. Jones, "The unsteady lift of a finite wing," tech. rep., National advisory committee for aeronautics, 1939.

[89] T. V. Holten, "The computation of aerodynamic loads on helicopter blades in forward flight using the method of the acceleration potential," tech. rep., Delft University of Technology, 1975.

[90] T. V. Holten, "Some notes on unsteady lifting-line theory," *Journal of Fluid Mechanics*, vol. 77, p. 561, Oct 1976.

[91] E. C. James, "Lifting-line theory for an unsteady wing as a singular perturbation problem," *Journal of Fluid Mechanics*, vol. 70, p. 753, Aug 1975.

[92] A. R. Ahmadi and S. E. Widnall, "Unsteady lifting-line theory as a singular perturbation problem," *Journal of Fluid Mechanics*, vol. 153, p. 59, Apr 1985.

[93] H. K. Cheng, "On lifting-line theory in unsteady aerodynamics," tech. rep., University of Southern California Los Angeles Department of Aerospace Engineering, 1976.

[94] P. D. Sclavounos, "An unsteady lifting-line theory," *Journal of Engineering Mathematics*, vol. 21, no. 3, pp. 201–226, 1987.

[95] L. Dragos, "The theory of oscillating thick wings in subsonic flow. lifting line theory," *Acta Mechanica*, vol. 54, pp. 221–238, Mar 1985.

[96] H. K. Cheng and L. E. Murillo, "Lunate-tail swimming propulsion as a problem of curved lifting line in unsteady flow. part 1. asymptotic theory," *Journal of Fluid Mechanics*, vol. 143, p. 327, June 1984.

[97] J. Boutet and G. Dimitriadis, "Unsteady lifting line theory using the wagner function for the aerodynamic and aeroelastic modeling of 3d wings," *Aerospace*, vol. 5, p. 92, sep 2018.

[98] P. J. Baddoo, "Lightning solvers for potential flows," *Fluids*, vol. 5, p. 227, Nov 2020.

[99] R. C. Lock and B. R. Williams, "Vicous-inviscid interactions in external aerodynamics," *Progress in Aerospace Sciences*, vol. 24, no. 2, pp. 51–171, 1987.

[100] M. Drela, "XFOIL: An analysis and design system for low reynolds number airfoils," in *Lecture Notes in Engineering*, pp. 1–12, Springer Berlin Heidelberg, 1989.

[101] Z. Yan, H. E. Taha, and M. R. Hajj, “Geometrically-exact unsteady model for airfoils undergoing large amplitude maneuvers,” *Aerospace Science and Technology*, vol. 39, pp. 293–306, Dec 2014.

[102] K. Ramesh, A. Gopalarathnam, J. R. Edwards, M. V. Ol, and K. Granlund, “An unsteady airfoil theory applied to pitching motions validated against experiment and computation,” *Theoretical and Computational Fluid Dynamics*, vol. 27, pp. 843–864, Jan 2013.

[103] B. T. Roesler and B. P. Epps, “Discretization requirements for vortex lattice methods to match unsteady aerodynamics theory,” *AIAA Journal*, vol. 56, pp. 2478–2483, Jun 2018.

[104] P. Devinant and T. Gallois, “Swept and curved wings: a numerical approach based on generalized lifting-line theory,” *Computational Mechanics*, vol. 29, pp. 322–331, Oct 2002.

[105] J. C. Sivells and R. H. Neely, “Method for calculating wing characteristics by lifting-line theory using nonlinear section lift data,” tech. rep., National Advisory Committee for Aeronautics, 1947.

[106] W. O. Valarezo and V. D. Chin, “Method for the prediction of wing maximum lift,” *Journal of Aircraft*, vol. 31, pp. 103–109, jan 1994.

[107] S. Gallay and E. Laurendeau, “Nonlinear generalized lifting-line coupling algorithms for pre/poststall flows,” *AIAA Journal*, vol. 53, pp. 1784–1792, Jul 2015.

[108] H. Ben-Gida, R. Gurka, and D. Weihs, “Leading-edge vortex as a high-lift mechanism for large-aspect-ratio wings,” *AIAA Journal*, vol. 58, pp. 2806–2819, jul 2020.

[109] D.-G. Caprace, P. Chatelain, and G. Winckelmans, “Lifting line with various mollifications: Theory and application to an elliptical wing,” *AIAA Journal*, vol. 57, pp. 17–28, Jan 2019.

[110] P. J. Phlips, R. A. East, and N. H. Pratt, “An unsteady lifting line theory of flapping wings with application to the forward flight of birds,” *Journal of Fluid Mechanics*, vol. 112, p. 97, Nov 1981.

[111] M. R. A. Nabawy and W. J. Crowthe, “A quasi-steady lifting line theory for insect-like hovering flight,” *PLOS ONE*, vol. 10, p. e0134972, Aug 2015.

[112] P. Devinant, “An approach for unsteady lifting-line time-marching numerical computation,” *International Journal for Numerical Methods in Fluids*, vol. 26, pp. 177–197, Jan 1998.

[113] M. Parenteau, F. Plante, E. Laurendeau, and M. Costes, "Unsteady coupling algorithm for lifting-line methods," in *55th AIAA Aerospace Sciences Meeting*, American Institute of Aeronautics and Astronautics, Jan 2017.

[114] K. Ramesh, T. P. Monteiro, F. J. Silvestre, A. Bernardo, G. aes Neto, T. de Souza Siqueria Versiani, and R. G. A. da Silva, "Experimental and numerical investigation of post-flutter limit cycle oscillations on a cantilevered flat plate," in *International Forum on Aeroelasticity and Structural Dynamics 2017*, June 2017.

[115] S. Backaert, P. Chatelain, and G. Winckelmans, "Vortex particle-mesh with immersed lifting lines for aerospace and wind engineering," *Procedia IUTAM*, vol. 18, pp. 1–7, 2015.

[116] D.-G. Caprace, G. Winckelmans, and P. Chatelain, "An immersed lifting and dragging line model for the vortex particle-mesh method," *Theoretical and Computational Fluid Dynamics*, 2020.

[117] O. Sugar-Gabor, "A general numerical unsteady non-linear lifting line model for engineering aerodynamics studies," *The Aeronautical Journal*, vol. 122, pp. 1199–1228, Jun 2018.

[118] W. J. McCroskey, "The phenomenon of dynamic stall," tech. rep., NASA, Mar. 1981.

[119] W. J. McCroskey, "Unsteady airfoils," *Annual Review of Fluid Mechanics*, vol. 14, pp. 285–311, Jan 1982.

[120] G. Z. McGowan, K. Granlund, M. V. Ol, A. Gopalarathnam, and J. R. Edwards, "Investigations of lift-based pitch-plunge equivalence for airfoils at low reynolds numbers," *AIAA Journal*, vol. 49, pp. 1511–1524, Jul 2011.

[121] M. V. Ol, L. Bernal, C.-K. Kang, and W. Shyy, "Shallow and deep dynamic stall for flapping low reynolds number airfoils," *Experiments in Fluids*, vol. 46, pp. 883–901, Apr 2009.

[122] S. Ōtomo, S. Henne, K. Mulleners, K. Ramesh, and I. M. Viola, "Unsteady lift on a high-amplitude pitching aerofoil," *Experiments in Fluids*, vol. 62, dec 2020.

[123] S. I. Benton and M. R. Visbal, "Effects of leading-edge geometry on the onset of dynamic stall," *AIAA Journal*, vol. 56, pp. 4195–4198, Oct 2018.

[124] A. Widmann and C. Tropea, "Parameters influencing vortex growth and detachment on unsteady aerodynamic profiles," *Journal of Fluid Mechanics*, vol. 773, pp. 432–459, May 2015.

[125] M. R. Visbal, "High-fidelity simulation of transitional flows past a plunging airfoil," *AIAA Journal*, vol. 47, pp. 2685–2697, Nov 2009.

[126] D. J. Garmann and M. R. Visbal, "Numerical investigation of transitional flow over a rapidly pitching plate," *Physics of Fluids*, vol. 23, p. 094106, sep 2011.

[127] K. O. Granlund, M. V. Ol, and L. P. Bernal, "Unsteady pitching flat plates," *Journal of Fluid Mechanics*, vol. 733, sep 2013.

[128] R. M. H. Beckwith and H. Babinsky, "Impulsively started flat plate flow," *Journal of Aircraft*, vol. 46, pp. 2186–2189, nov 2009.

[129] C. W. P. Ford and H. Babinsky, "Lift and the leading-edge vortex," *Journal of Fluid Mechanics*, vol. 720, pp. 280–313, Feb 2013.

[130] C. W. P. Ford and H. Babinsky, "Impulsively started flat plate circulation," *AIAA Journal*, vol. 52, pp. 1800–1802, aug 2014.

[131] P. R. R. J. Stevens, H. Babinsky, F. Manar, P. Mancini, A. R. Jones, T. Nakata, N. Phillips, R. J. Bomphrey, A. C. Gozukara, K. O. Granlund, and M. V. Ol, "Experiments and computations on the lift of accelerating flat plates at incidence," *AIAA Journal*, vol. 55, pp. 3255–3265, oct 2017.

[132] M. R. Visbal and D. J. Garmann, "Investigation of spanwise end effects on dynamic stall of a pitching wing section," *Journal of Aircraft*, vol. 56, pp. 2118–2130, Nov 2019.

[133] I. Andreu-Angulo, H. Babinsky, H. Biler, G. Sedky, and A. R. Jones, "Effect of transverse gust velocity profiles," *AIAA Journal*, vol. 58, pp. 5123–5133, Dec 2020.

[134] H. Biler, G. Sedky, A. R. Jones, M. Saritas, and O. Cetiner, "Experimental investigation of transverse and vortex gust encounters at low reynolds numbers," *AIAA Journal*, vol. 59, pp. 786–799, Mar 2021.

[135] K. Mulleners, P. Mancini, and A. R. Jones, "Flow development on a flat-plate wing subjected to a streamwise acceleration," *AIAA Journal*, vol. 55, pp. 2118–2122, Jun 2017.

[136] N. J. Kay, P. J. Richards, and R. N. Sharma, "Effect of turbulence and sinusoidal pitching on low-reynolds-number lift," *AIAA Journal*, vol. 58, pp. 2377–2387, Jun 2020.

[137] A. M. Young and A. S. M. Smyth, "Gust–airfoil coupling with a loaded airfoil," *AIAA Journal*, vol. 59, pp. 773–785, Mar 2021.

[138] D. Darakananda and J. D. Eldredge, “A versatile taxonomy of low-dimensional vortex models for unsteady aerodynamics,” *Journal of Fluid Mechanics*, vol. 858, pp. 917–948, Nov 2018.

[139] J. Katz, “A discrete vortex method for the non-steady separated flow over an airfoil,” *Journal of Fluid Mechanics*, vol. 102, p. 315, Jan 1981.

[140] M. A. Jones, “The separated flow of an inviscid fluid around a moving flat plate,” *Journal of Fluid Mechanics*, vol. 496, pp. 405–441, Dec 2003.

[141] T. Sarpkaya, “An inviscid model of two-dimensional vortex shedding for transient and asymptotically steady separated flow over an inclined plate,” *Journal of Fluid Mechanics*, vol. 68, p. 109, Mar 1975.

[142] S. A. Ansari, R. Żbikowski, and K. Knowles, “Non-linear unsteady aerodynamic model for insect-like flapping wings in the hover. part 1: Methodology and analysis,” *Proceedings of the Institution of Mechanical Engineers, Part G: Journal of Aerospace Engineering*, vol. 220, pp. 61–83, Feb 2006.

[143] C. E. Brown and W. H. Michael, “Effect of leading-edge separation on the lift of a delta wing,” *Journal of the Aeronautical Sciences*, vol. 21, pp. 690–694, Oct 1954.

[144] S. Michelin and S. G. L. Smith, “An unsteady point vortex method for coupled fluid–solid problems,” *Theoretical and Computational Fluid Dynamics*, vol. 23, pp. 127–153, May 2009.

[145] K. Ramesh, A. Gopalarathnam, K. Granlund, M. V. Ol, and J. R. Edwards, “Discrete-vortex method with novel shedding criterion for unsteady aerofoil flows with intermittent leading-edge vortex shedding,” *Journal of Fluid Mechanics*, vol. 751, pp. 500–538, Jun 2014.

[146] K. Ramesh, K. Granlund, M. V. Ol, A. Gopalarathnam, and J. R. Edwards, “Leading-edge flow criticality as a governing factor in leading-edge vortex initiation in unsteady airfoil flows,” *Theoretical and Computational Fluid Dynamics*, vol. 32, pp. 109–136, Aug 2018.

[147] J. Deparday and K. Mulleners, “Critical evolution of leading edge suction during dynamic stall,” *Journal of Physics: Conference Series*, vol. 1037, p. 022017, jun 2018.

[148] J. Deparday and K. Mulleners, “Modeling the interplay between the shear layer and leading edge suction during dynamic stall,” *Physics of Fluids*, vol. 31, p. 107104, oct 2019.

[149] P. Freymuth, “Visualizing the connectivity of vortex systems for pitching wings,” *Journal of Fluids Engineering*, vol. 111, no. 2, p. 217, 1989.

[150] J. H. J. Buchholz and A. J. Smits, “On the evolution of the wake structure produced by a low-aspect-ratio pitching panel,” *Journal of Fluid Mechanics*, vol. 546, p. 433, Dec 2005.

[151] J. H. J. Buchholz and A. J. Smits, “The wake structure and thrust performance of a rigid low-aspect-ratio pitching panel,” *Journal of Fluid Mechanics*, vol. 603, Apr 2008.

[152] K. D. V. Ellenrieder, K. Parker, and J. Soria, “Flow structures behind a heaving and pitching finite-span wing,” *Journal of Fluid Mechanics*, vol. 490, pp. 129–138, Sep 2003.

[153] K. Parker, K. D. von Ellenrieder, and J. Soria, “Using stereo multigrid DPIV (SMD-PIV) measurements to investigate the vortical skeleton behind a finite-span flapping wing,” *Experiments in Fluids*, vol. 39, pp. 281–298, May 2005.

[154] P. Blondeaux, F. Fornarelli, L. Guglielmini, M. S. Triantafyllou, and R. Verzicco, “Numerical experiments on flapping foils mimicking fish-like locomotion,” *Physics of Fluids*, vol. 17, p. 113601, Nov 2005.

[155] N. Chiereghin, S. Bull, D. J. Cleaver, and I. Gursul, “Three-dimensionality of leading-edge vortices on high aspect ratio plunging wings,” *Physical Review Fluids*, vol. 5, Jun 2020.

[156] M. R. Visbal, “Unsteady flow structure and loading of a pitching low-aspect-ratio wing,” *Physical Review Fluids*, vol. 2, Feb 2017.

[157] T. O. Yilmaz, M. Ol, and D. Rockwell, “Scaling of flow separation on a pitching low aspect ratio plate,” *Journal of Fluids and Structures*, vol. 26, pp. 1034–1041, Aug 2010.

[158] T. O. Yilmaz and D. Rockwell, “Three-dimensional flow structure on a maneuvering wing,” *Experiments in Fluids*, vol. 48, pp. 539–544, Oct 2009.

[159] T. O. Yilmaz and D. Rockwell, “Flow structure on finite-span wings due to pitch-up motion,” *Journal of Fluid Mechanics*, vol. 691, pp. 518–545, Dec 2011.

[160] M. R. Visbal, T. O. Yilmaz, and D. Rockwell, “Three-dimensional vortex formation on a heaving low-aspect-ratio wing: Computations and experiments,” *Journal of Fluids and Structures*, vol. 38, pp. 58–76, Apr 2013.

[161] M. R. Visbal and D. J. Garmann, “Dynamic stall of a finite-aspect-ratio wing,” *AIAA Journal*, vol. 57, pp. 962–977, Mar 2019.

[162] M. R. Visbal and D. J. Garmann, “Mitigation of dynamic stall over a pitching finite wing using high-frequency actuation,” *AIAA Journal*, vol. 58, pp. 51–60, Jan 2020.

[163] M. R. Visbal and D. J. Garmann, “Effect of sweep on dynamic stall of a pitching finite-aspect-ratio wing,” *AIAA Journal*, vol. 57, pp. 3274–3289, Aug 2019.

[164] A. Spentzos, G. N. Barakos, K. J. Badcock, B. E. Richards, F. N. Coton, R. A. M. Galbraith, E. Berton, and D. Favier, “Computational fluid dynamics study of three-dimensional dynamic stall of various planform shapes,” *Journal of Aircraft*, vol. 44, pp. 1118–1128, jul 2007.

[165] W. Shyy, H. Aono, S. Chimakurthi, P. Trizila, C.-K. Kang, C. Cesnik, and H. Liu, “Recent progress in flapping wing aerodynamics and aeroelasticity,” *Progress in Aerospace Sciences*, vol. 46, pp. 284–327, Oct 2010.

[166] R. R. Harbig, J. Sheridan, and M. C. Thompson, “The role of advance ratio and aspect ratio in determining leading-edge vortex stability for flapping flight,” *Journal of Fluid Mechanics*, vol. 751, pp. 71–105, Jun 2014.

[167] W. Shyy, P. Trizila, C.-K. Kang, and H. Aono, “Can tip vortices enhance lift of a flapping wing?,” *AIAA Journal*, vol. 47, pp. 289–293, Feb 2009.

[168] J. M. Birch and M. H. Dickinson, “Spanwise flow and the attachment of the leading-edge vortex on insect wings,” *Nature*, vol. 412, pp. 729–733, Aug 2001.

[169] M. H. Dickinson, “Wing rotation and the aerodynamic basis of insect flight,” *Science*, vol. 284, pp. 1954–1960, Jun 1999.

[170] D. Lentink and M. H. Dickinson, “Rotational accelerations stabilize leading edge vortices on revolving fly wings,” *Journal of Experimental Biology*, vol. 212, pp. 2705–2719, Jul 2009.

[171] S. S. Bhat, J. Zhao, J. Sheridan, K. Hourigan, and M. C. Thompson, “Effects of flapping-motion profiles on insect-wing aerodynamics,” *Journal of Fluid Mechanics*, vol. 884, Dec 2019.

[172] Y. Hirato, M. Shen, A. Gopalarathnam, and J. R. Edwards, “Flow criticality governs leading-edge-vortex initiation on finite wings in unsteady flow,” *Journal of Fluid Mechanics*, 2020. Submitted for publication.

[173] V. M. Falkner, "The solution of lifting-plane problems by vortex-lattice theory," tech. rep., Aeronautical research council, 1947.

[174] C. R. dos Santos and F. D. Marques, "Lift prediction including stall, using vortex lattice method with kirchhoff-based correction," *Journal of Aircraft*, pp. 1–5, Sep 2017.

[175] D. J. Pate and B. J. German, "A surface vorticity panel method," *AIAA Journal*, vol. 56, pp. 4645–4656, Dec 2018.

[176] J. Hess and A. Smith, "Calculation of potential flow about arbitrary bodies," *Progress in Aerospace Sciences*, vol. 8, pp. 1–138, 1967.

[177] D. J. Willis, J. Peraire, and J. K. White, "A combined pFFT-multipole tree code, unsteady panel method with vortex particle wakes," *International Journal for Numerical Methods in Fluids*, vol. 53, pp. 1399–1422, Mar. 2007.

[178] J. Phillips and J. White, "A precorrected-FFT method for electrostatic analysis of complicated 3-d structures," *IEEE Transactions on Computer-Aided Design of Integrated Circuits and Systems*, vol. 16, no. 10, pp. 1059–1072, 1997.

[179] J. Murua, R. Palacios, and J. M. R. Graham, "Applications of the unsteady vortex-lattice method in aircraft aeroelasticity and flight dynamics," *Progress in Aerospace Sciences*, vol. 55, pp. 46–72, Nov. 2012.

[180] R. J. S. Simpson, R. Palacios, and J. Murua, "Induced-drag calculations in the unsteady vortex lattice method," *AIAA Journal*, vol. 51, pp. 1775–1779, Jul 2013.

[181] A. S. M. Smyth, A. M. Young, and L. D. Mare, "Effect of three-dimensional geometry on harmonic gust–airfoil interaction," *AIAA Journal*, vol. 59, pp. 737–750, feb 2021.

[182] B. Nelson and J.-S. Kouh, "The aerodynamic analysis of a rotating wind turbine by viscous-coupled 3d panel method," *Applied Sciences*, vol. 7, pp. 551–566, May 2017.

[183] A. S. Smyth, A. M. Young, and L. D. Mare, "The effect of 3D geometry on unsteady gust response, using a vortex lattice model," in *AIAA Scitech 2019 Forum*, American Institute of Aeronautics and Astronautics, Jan 2019.

[184] M. Parenteau and É. Laurendeau, "Nonlinear frequency-domain solver for vortex lattice method," *AIAA Journal*, vol. 56, pp. 2242–2251, Jun 2018.

[185] T. Lambert and G. Dimitriadis, "Induced drag calculations with the unsteady vortex lattice method for cambered wings," *AIAA Journal*, vol. 55, pp. 668–672, Feb 2017.

[186] R. Mukherjee and A. Gopalarathnam, “Poststall prediction of multiple-lifting-surface configurations using a decambering approach,” *Journal of Aircraft*, vol. 43, no. 3, pp. 660–668, 2006.

[187] Y. Hirato, M. Shen, A. Gopalarathnam, and J. R. Edwards, “Vortex-sheet representation of leading-edge vortex shedding from finite wings,” *Journal of Aircraft*, pp. 1–15, Apr 2019.

[188] S. Aggarwal, “An invicid numerical method for unsteady flows over airfoils and wings to predict the onset of leading edge vortex formation,” Master’s thesis, North Carolina State University, 2013. Retrieved 05/06/2020.

[189] G. Winckelmans, R. Cocle, L. Dufresne, and R. Capart, “Vortex methods and their application to trailing wake vortex simulations,” *Comptes Rendus Physique*, vol. 6, pp. 467–486, May 2005.

[190] D. Wee, Y. M. Marzouk, F. Schlegel, and A. F. Ghoniem, “Convergence characteristics and computational cost of two algebraic kernels in vortex methods with a tree-code algorithm,” *SIAM Journal on Scientific Computing*, vol. 31, pp. 2510–2527, Jan 2009.

[191] J. T. Beale and A. Majda, “Vortex methods. i. convergence in three dimensions,” *Mathematics of Computation*, vol. 39, pp. 1–1, Sep 1982.

[192] G.-H. Cottet, P. Koumoutsakos, and M. L. O. Salihi, “Vortex methods with spatially varying cores,” *Journal of Computational Physics*, vol. 162, pp. 164–185, jul 2000.

[193] R. Cocle, G. Winckelmans, and G. Daeninck, “Combining the vortex-in-cell and parallel fast multipole methods for efficient domain decomposition simulations,” *Journal of Computational Physics*, vol. 227, pp. 9091–9120, Nov 2008.

[194] G.-H. Cottet and P. D. Koumoutsakos, *Vortex Methods*. Cambridge University Press, 2004.

[195] C. Greengard, “The core spreading vortex method approximates the wrong equation,” *Journal of Computational Physics*, vol. 61, pp. 345–348, Nov 1985.

[196] S. Kempka and J. Strickland, “A method to simulate viscous diffusion of vorticity by convective transport of vortices at a non-solenoidal velocity,” tech. rep., Sandia National Laboratories, Aug 1993.

[197] L. F. Rossi, “Resurrecting core spreading vortex methods: A new scheme that is both deterministic and convergent,” *SIAM Journal on Scientific Computing*, vol. 17, pp. 370–397, Mar 1996.

[198] G. Winckelmans and A. Leonard, "Contributions to vortex particle methods for the computation of three-dimensional incompressible unsteady flows," *Journal of Computational Physics*, vol. 109, pp. 247–273, Dec 1993.

[199] P. Koumoutsakos, A. Leonard, and F. Pépin, "Boundary conditions for viscous vortex methods," *Journal of Computational Physics*, vol. 113, pp. 52–61, jul 1994.

[200] D. Shiels, *Simulation of controlled bluff body flow with a viscous vortex method.* PhD thesis, California Institute of Technology, 1998.

[201] P. Ploumhans and G. Winckelmans, "Vortex methods for high-resolution simulations of viscous flow past bluff bodies of general geometry," *Journal of Computational Physics*, vol. 165, pp. 354–406, Dec 2000.

[202] P. Ploumhans, G. Winckelmans, J. Salmon, A. Leonard, and M. Warren, "Vortex methods for direct numerical simulation of three-dimensional bluff body flows: Application to the sphere at re=300, 500, and 1000," *Journal of Computational Physics*, vol. 178, pp. 427–463, May 2002.

[203] J. Barnes and P. Hut, "A hierarchical o(n log n) force-calculation algorithm," *Nature*, vol. 324, pp. 446–449, Dec 1986.

[204] L. Greengard and V. Rokhlin, "A fast algorithm for particle simulations," *Journal of Computational Physics*, vol. 135, pp. 280–292, Aug 1997.

[205] L. Greengard and V. Rokhlin, "A new version of the fast multipole method for the laplace equation in three dimensions," *Acta Numerica*, vol. 6, p. 229, Jan 1997.

[206] W. Fong and E. Darve, "The black-box fast multipole method," *Journal of Computational Physics*, vol. 228, pp. 8712–8725, dec 2009.

[207] N. A. Gumerov and R. Duraiswami, "Efficient FMM accelerated vortex methods in three dimensions via the lamb-helmholtz decomposition," *Journal of Computational Physics*, vol. 240, pp. 310–328, May 2013.

[208] D. Rossinelli, M. Bergdorf, G.-H. Cottet, and P. Koumoutsakos, "GPU accelerated simulations of bluff body flows using vortex particle methods," *Journal of Computational Physics*, vol. 229, pp. 3316–3333, May 2010.

[209] Q. Hu, N. A. Gumerov, and R. Duraiswami, "GPU accelerated fast multipole methods for vortex particle simulation," *Computers & Fluids*, vol. 88, pp. 857–865, Dec 2013.

[210] K. Wu, N. Truong, C. Yuksel, and R. Hoetzlein, "Fast fluid simulations with sparse volumes on the GPU," *Computer Graphics Forum*, vol. 37, pp. 157–167, May 2018.

[211] G. Morgenthal, A. S. Corriols, and B. Bendig, "A GPU-accelerated pseudo-3d vortex method for aerodynamic analysis," *Journal of Wind Engineering and Industrial Aerodynamics*, vol. 125, pp. 69–80, Feb 2014.

[212] R. Yokota and L. Barba, "Comparing the treecode with FMM on GPUs for vortex particle simulations of a leapfrogging vortex ring," *Computers & Fluids*, vol. 45, pp. 155–161, Jun 2011.

[213] J. K. Salmon and M. S. Warren, "Fast parallel tree codes for gravitational and fluid dynamical n-body problems," *The International Journal of Supercomputer Applications and High Performance Computing*, vol. 8, pp. 129–142, Jun 1994.

[214] J. K. Salmon and M. S. Warren, "Skeletons from the treecode closet," *Journal of Computational Physics*, vol. 111, pp. 136–155, Mar 1994.

[215] G. S. Winckelmans, J. K. Salmon, M. S. Warren, A. Leonard, and B. Jodoin, "Application of fast parallel and sequential tree codes to computing three-dimensional flows with the vortex element and boundary element methods," *ESAIM: Proceedings*, vol. 1, pp. 225–240, 1996.

[216] E. Branlard, *Wind Turbine Aerodynamics and Vorticity-Based Methods.* Springer, 2017.

[217] N. R. García, J. N. Sørensen, and W. Z. Shen, "A quasi-3d viscous-inviscid interaction code:q3uic," *Journal of Physics: Conference Series*, vol. 555, p. 012041, Dec 2014.

[218] D. Marten, C. O. Paschereit, X. Huang, M. Meinke, W. Schröder, J. Müller, and K. Oberleithner, "Predicting wind turbine wake breakdown using a free vortex wake code," *AIAA Journal*, vol. 58, pp. 4672–4685, Nov 2020.

[219] E. J. Alvarez and A. Ning, "Development of a vortex particle code for the modeling of wake interaction in distributed propulsion," in *2018 Applied Aerodynamics Conference*, American Institute of Aeronautics and Astronautics, Jun 2018.

[220] H. J. A. Bird, S. Ōtomo, K. Ramesh, and I. M. Viola, "A geometrically non-linear time-domain unsteady lifting-line theory," *AIAA Journal*, 2021.

[221] F. W. Olver, D. W. Lozier, R. F. Boisvert, and C. W. Clark, *NIST Handbook of Mathematical Functions Paperback and CD-ROM.* Cambridge University Press, 2010.

[222] R. A. Piziali, “2-d and 3-d oscillating wing aerodynamics for a range of angles of attack including stall,” tech. rep., NASA, 1994.

[223] M. Ol, A. Altman, J. Eldredge, D. Garmann, and Y. Lian, “Résumé of the AIAA FDTC low reynolds number discussion group's canonical cases,” in *48th AIAA Aerospace Sciences Meeting Including the New Horizons Forum and Aerospace Exposition*, American Institute of Aeronautics and Astronautics, Jan 2010. AIAA 2010-1085.

[224] J. E. McCune, C.-M. G. Lam, and M. T. Scott, “Nonlinear aerodynamics of two-dimensional airfoils in severe maneuver,” *AIAA Journal*, vol. 28, pp. 385–393, Mar 1990.

[225] W. H. Press, S. A. Teukolsky, W. T. Vetterling, and B. P. Flannery, *Numerical Recipes in C*. Cambridge University Press, 2 ed., 1992.

[226] H. J. A. Bird, “Cvortex.” `https://github.com/hjabird/cvortex`, 2020.

[227] M. Abramowitz and I. Stegun, *Handbook of Mathematical Functions: With Formulas, Graphs, and Mathematical Tables*. Dover Publications, 1965.

[228] C. S. Lee, “A numerical method for the solution of the unsteady lifting problem of rectangular and elliptic hydrofoils,” Master’s thesis, MIT Dept. of Ocean Engineering, 1977.

[229] P. Spalart and S. Allmaras, “A one-equation turbulence model for aerodynamic flows,” in *30th Aerospace Sciences Meeting and Exhibit*, American Institute of Aeronautics and Astronautics, Jan 1992. AIAA Paper 1992-0439.